Multiwavelength studies of classical novae

Elias Aydi

April 2018

A thesis submitted in partial fulfillment for the
degree of Doctor of Philosophy
in
Astronomy

Department of Astronomy
University of Cape Town

Supervisors: Dr. Shazrene Mohamed and Prof. Patricia Whitelock

Abstract

Classical novae are transient astronomical events resulting from an eruption on the surface of an accreting white dwarf in interacting binary stars, namely cataclysmic variables. These eruptions and their progenitors are ideal astronomical events/objects to study a variety of interesting topics, such as mass-transfer mechanisms, binary evolution, and thermonuclear and radiative emission processes. Novae share some general observational characteristics during their eruption phases, yet each nova is new and can show unique light-curve and spectral developments. Therefore, carrying out detailed multiwavelength studies of individual novae is important to provide an holistic picture of the eruption development with the ultimate aim of a general understanding of the physical mechanisms involved in nova eruptions, as well as the structure and evolutionary condition of their progenitors.

This dissertation presents detailed multiwavelength studies of three nova events, namely V5852 Sgr, SMCN 2016-10, and V407 Lup, as a series of chapters (papers). Our data were collected using several ground-based and space telescopes including: high- and medium-resolution optical spectroscopy from SALT, SOAR, and FLOYDS, optical and near-infrared photometry from IRSF, OGLE and SMARTS, UV and X-ray data from *Swift*, *Chandra*, and *XMM-Newton*.

In the second chapter, we present an optical and infrared study of the unusual nova V5852 Sgr. This nova is a moderately fast nova showing features of the Fe II spectroscopic type. The light-curve development is unique, showing a combination of several light-curve classes. Estimates of the distance and measurements of the line velocities suggest that the nova might be associated with the Sagittarius stream. If so, it would be the first nova to be discovered in a dwarf spheroidal galaxy.

The third chapter presents a multiwavelength study of the very fast nova SMCN 2016-10a. The fast light-curve development suggests that the system hosts a massive white dwarf ($\gtrsim 1.25\,\mathrm{M}_{\odot}$), in good agreement with the high temperature of the super-soft X-ray emission and the turn-on/turn-off time of the super-soft state. At the distance of the Small Magellanic Cloud our measurements suggest that SMCN 2016-10a is the brightest nova in the Small Magellanic Cloud and one of the brightest novae on record, with an absolute maximum magnitude of ~ -10.5 in the V-band.

Chapter four is a multiwavelength study of nova V407 Lup. With a light-curve decline time $t_2 \leq 2.9\,\mathrm{d}$, this is one of the fastest known examples and the white dwarf is possibly more massive than $1.25\,\mathrm{M}_{\odot}$. Our set of optical, UV, and X-ray data suggest that this system is an intermediate-polar cataclysmic variable based essentially on the presence of two periodicities (3.57 h and 565 s) in the light-curves. These periodicities are attributed to the orbital period of the binary and rotational period of the white dwarf. The late optical spectra (taken from day 165 post-eruption) show narrow and moving lines of He II and O VI, possibly associated with accretion regions within the binary system. This, along with the X-ray light-curves and spectra, suggest that the accretion probably resumed around 168 days post-eruption.

These studies are modest, yet essential steps in the quest for a better understanding of nova eruptions. They also demonstrate the importance of multiwavelength follow-up of novae for constraining the physical parameters of the eruption, the ejecta, and the properties of the progenitor. In the era of large all-sky surveys, such as the All-Sky Automated Survey for Supernovae and eventually the Large Synoptic Survey Telescope which have been and are ex-

pected to find a large number of optical transients and classical novae, similar multiwavelength follow-up will play a crucial role for initially identifying these transient events and further understanding their physical behaviour.

Acknowledgements

I would like to express my deep and sincere gratitude to my supervisors, Dr. Shazrene Mohamed and Prof. Patricia Whitelock for giving me the opportunity to conduct this project and for all the support which made this research work possible. Thank you for believing in me, for your patience, and for providing invaluable guidance throughout my three years of studies. I also wish to extend my thank you to Dr. David Buckley who gave me the opportunity to conduct part of this research using SALT data and for his support during my last year of PhD.

To my parents, there is no words to describe my appreciation for all the support, motivation, and sacrifices you have made to put me in the position that I am in today. Thank you for your unconditional love. To my elder sisters Lara and Madeleine, I am very grateful for all the love, care and continuous support to complete my PhD degree. To Atieh and Assaad, you were brothers to me, thank you for all that you have done. I would like to thank each member of my bigger family, particularly Salam, Nicolas, Esperance, Fifi, and Roula for all their love and support.

I would like to thank my friends Abir, Philipus, Vanessa, Brenda, Itumeleng, Mokhine, Sulona, Nicola, Silvia, Tibisay, and Dheni for the beautiful moments I had in Cape Town. This journey was much easier with all of you by my side. Thank you to all of my office-mates, Blaise, Mike, Zwido, Blaine, Eli, Daniel, and Laure for sharing this journey with me and for the valuable discussion we had at our office.

I would like to thank my friends back home: Oliver, Maya, Jad, Mira, Mitri, Marc, Ziad, Hala, Elias, for visiting me here in Cape Town and for their genuine support. I also would like to thank Isabelle, George, Rizkallah, Kirsten, and Rami for their visits to Cape Town.

I am grateful to the advice and guidance of Dr. Nicola Clementel during my first two years of PhD. I would like to acknowledge Dr. Marissa Kotze and Dr. Enrico Kotze for all their advices during these three years and Dr. Brent Miszalski, Dr. Alexei Kniazev, Dr. Margaretha Pretorius for all their help in this work. I would like to thank Prof. Ted Williams and Prof. Petri Vaisanen for the opportunity they gave me to work at the SAAO and at SALT. I would like to thank Ms. Linda Tobin, Ms. Natalie Jones, and all the SAAO staff who made this place feels like a second home. A special thank you to Jacky for all her help during my three years of stay at SAAO.

I would like to acknowledge Prof. Patrick Woudt for his guidance and I would like to thank all the members of the Astronomy Department at UCT for sharing this journey with me.

I would like to acknowledge all my collaborators who were part of this work for their contributions and for all what I have learned from them throughout my PhD studies.

I would like to thank the three examiners who gave useful and constructive comments, which improved the content of the thesis.

To my family.

Declaration of Authorship

The work presented in this thesis was done in collaboration with various people who provided some of the data and in some cases contributed to the analysis and discussion. This thesis contains research that has already been published or submitted for publication:

1. Chapter 2 (paper I) entitled "V5852 Sgr: an unusual nova possibly associated with the Sagittarius stream" has been published in the Monthly Notices of Royal Astronomical Society Journal; **E. Aydi**, P. Mróz, P. A. Whitelock, S. Mohamed, Ł. Wyrzykowski, A. Udalski, P. Vaisanen, T. Nagayama, M. Dominik, A. Scholz, H. Onozato, R. E. Williams, S. T. Hodgkin, S. Nishiyama, M. Yamagishi, A. M. S. Smith, T. Ryu, A. Iwamatsu, and I. Kawamata, 2016, MNRAS, 461, 1529.

   We present an optical and near-infrared (NIR) study of the classical nova V5852 Sgr including optical spectroscopy from the Southern African Large telescope (SALT), optical photometry from the Optical Gravitational Lensing Experiment (OGLE), and near-infrared JHK photometry from the IR survey facility (IRSF) telescope. I did all the analysis and write-up of the spectroscopic observations and the discussion and conclusions (Sections 2.1, 2.3, and 2.4). I also did the light-curve analysis and I have contributed to the distance estimation (Sections 2.2.3 and 2.2.4). The analysis and the write-up of the OGLE and IRSF JHK photometry and the reddening estimation (Sections 2.2.1, 2.2.2, and parts of Section 2.2.4) were done by P. Mróz, P. Whitelock, and T. Nagayama. R. E. Williams provided constructive comments on the spectral analysis and line identification. P. Mróz, P. A. Whitelock, S. Mohamed, Ł. Wyrzykowski, A. Udalski, P. Vaisanen, T. Nagayama, M. Dominik, A. Scholz, H. Onozato, R. E. Williams, S. T. Hodgkin, S. Nishiyama, M. Yamagishi, A. M. S. Smith, T. Ryu, A. Iwamatsu, and I. Kawamata provided very constructive comments on my draft of the paper.

   These observations showed an unusual behaviour of the eruption and they offered us a good understanding of its different aspects. We also managed to derive an estimate of the distance to the system and its location which associates the nova with the trailing stream of the Sagittarius dwarf spheroidal galaxy. If so, it is the first nova to be detected from that, or from any dwarf spheroidal galaxy.

2. Chapter 3 (paper II) entitled "Multiwavelength observations of nova SMCN 2016-10a — one of the brightest novae ever observed" has been published in the Monthly Notices of Royal Astronomical Society Journal; **E. Aydi**, K. L. Page, N. P. M. Kuin, M. J. Darnley, F. M. Walter, P. Mróz, D. A. H. Buckley, S. Mohamed, P. Whitelock, P. Woudt, S. C. Williams, M. Orio, R. E. Williams, A. P. Beardmore, J. P. Osborne, A. Kniazev, V. A. R. M. Ribeiro, A. Udalski, J. Strader, and L. Chomiuk, 2018, MNRAS, 474, 2679.

   We present a multiwavelength study of the classical nova SMCN 2016-10a including optical spectroscopy and spectropolarimetry from SALT, Las Cumbres Observatory, and Southern

Astrophysical Research (SOAR) telescope, optical and NIR photometry from the Small and Medium Research Telescope System (SMARTS) and OGLE, X-ray and ultraviolet data from *Swift* satellite. I did all the analysis and write-up of the sections related to the optical and NIR observations and the general discussion and conclusions (Sections 3.1, 3.2, 3.3, 3.6, and 3.7). The analysis and write-up of the *Swift* X-ray (Section 3.4) and ultraviolet (Section 3.5) observations were done by K. L. Page and N. P. M. Kuin, respectively. M. J. Darnley has contributed the FLOYDS spectra and the spectral energy distribution plots. F. M. Walter and P. Mróz contributed the SMARTS and OGLE photometry, respectively. J. Strader and L. Chomiuk provided the SOAR spectroscopy. R. E. Williams provided constructive comments on the spectral analysis and line identification.

J. P. Osborne, D. A. H. Buckley, S. Mohamed, P. Whitelock, K. L. Page, N. P. M. Kuin, M. J. Darnley, F. M. Walter, P. Mróz, P. Woudt, S. C. Williams, M. Orio, R. E. Williams, A. P. Beardmore, A. Kniazev, V. A. R. M. Ribeiro, A. Udalski, J. Strader, and L. Chomiuk provided very constructive comments on my draft of the paper.

The present observational set is one of the most comprehensive for any nova event in the Small Magellanic Cloud. This set of data allowed us to constrain the properties of the nova (mass of the WD, evolutionary state of the secondary, ejecta velocities) and its classification. The optical observations led us to the main conclusion of the paper that this event might be the brightest nova eruption ever observed.

3. Chapter 4 (paper III) entitled "Multiwavelength observations of V407 Lupi (ASASSN-16kt) — a very fast nova erupting in an intermediate-polar" has been submitted to the Monthly Notices of Royal Astronomical Society Journal; **E. Aydi**, M. Orio, A. P. Beardmore, J.-U. Ness, K. L. Page, N. P. M. Kuin, F. M. Walter, D. A. H. Buckley, S. Mohamed, P. Whitelock, J. P. Osborne, J. Strader, L. Chomiuk, M. J. Darnley, A. Dobrotka, A. Kniazev, B. Miszalski, and N. Ospina (submitted to MNRAS).

   We present a multiwavelength study of the classical nova V407 Lup. The chapter includes optical spectroscopy from SALT and SOAR, optical and near-infrared photometry from SMARTS, X-ray and UV data from *Swift*, *XMM-Newton*, and *Chandra* satellites. I did all the write-up and most of the analysis of the sections related to the optical, NIR observations, and high-resolution X-ray observations and the general discussion and conclusions (Sections 4.1, 4.2, 4.3, 4.4, 4.5, and 4.6). M. Orio and J-U. Ness contributed the *Chandra* and *XMM-Newton* data, respectively and carried out the high-resolution X-ray modelling. The periodograms of the X-ray and ultraviolet photometry were done by A. P. Beardmore. The analysis and write-up of the *Swift* X-ray (Section 4.4.2) and ultraviolet (Section 4.4.3) data were done by K. L. Page and N. P. M. Kuin, respectively. F. M. Walter contributed the SMARTS photometry. J. Strader and L. Chomiuk contributed the SOAR spectroscopy.

   J. P. Osborne, D. A. H. Buckley, S. Mohamed, P. Whitelock, M. Orio, A. P. Beardmore, J.-U. Ness, K. L. Page, N. P. M. Kuin, F. M. Walter, J. Strader, L. Chomiuk, M. J. Darnley, A.

Dobrotka, A. Kniazev, B. Miszalski, and N. Ospina provided very constructive comments on my draft of the paper.

The optical, X-ray and UV light-curves show two periodicities of 3.57 h and 565 s from around 168 days post-eruption. These are presumably due to the orbital period of the binary and spin period of the white dwarf and are typical characteristics seen in intermediate-polar cataclysmic variables. The SALT high-resolution spectroscopy revealed the emergence of narrow and moving He II lines, also characteristics of magnetic cataclysmic variables. Based on the peak temperature of the SSS emission ($\sim$80 eV) and the time taken for the optical brightness to fade by 2 magnitudes (t_2 $\leq$2.9 d), we conclude that the mass of the WD is in the range of 1.1 – 1.3 $M_{\odot}$. The optical and X-ray data show strong evidence for accretion resuming, probably as early as 168 days post-eruption, while the X-ray supersoft source is still on, possibly extending its duration.

Each of these chapters contains all the information to be read independently.

I confirm that I have been granted permission by the University of Cape Town's Doctoral Degrees Board to include the following publications in my PhD thesis, and where co-authorships are involved, my co-authors have agreed that I may include the publications:

1. **E. Aydi**, P. Mróz, P. A. Whitelock, S. Mohamed, Ł. Wyrzykowski, A. Udalski, P. Vaisanen, T. Nagayama, M. Dominik, A. Scholz, H. Onozato, R. E. Williams, S. T. Hodgkin, S. Nishiyama, M. Yamagishi, A. M. S. Smith, T. Ryu, A. Iwamatsu, I. Kawamata, "V5852 Sgr: an unusual nova possibly associated with the Sagittarius stream", 2016, MNRAS, 461, 1529.

2. **E. Aydi**, K. L. Page, N. P. M. Kuin, M. J. Darnley, F. M. Walter, P. Mróz, D. A. H. Buckley, S. Mohamed, P. Whitelock, P. Woudt, S. C. Williams, M. Orio, R. E. Williams, A. P. Beardmore, J. P. Osborne, A. Kniazev, V. A. R. M. Ribeiro, A. Udalski, J. Strader, L. Chomiuk, "Multiwavelength observations of nova SMCN 2016-10a — one of the brightest novae ever observed", 2018, MNRAS, 474, 2679.

3. **E. Aydi**, M. Orio, A. P. Beardmore, J.-U. Ness, K. L. Page, N. P. M. Kuin, F. M. Walter, D. A. H. Buckley, S. Mohamed, P. Whitelock, J. P. Osborne, J. Strader, L. Chomiuk, M. J. Darnley, A. Dobrotka, A. Kniazev, B. Miszalski, and N. Ospina "Multiwavelength observations of V407 Lupi (ASASSN-16kt) — a very fast nova erupting in an intermediate-polar" (submitted to MNRAS).

SIGNATURE: E. A. **DATE**: 20 April 2018

STUDENT NAME: Elias Aydi **STUDENT NUMBER**: AYDELI001

Plagiarism Declaration

I, Elias Aydi, know the meaning of plagiarism and declare that all of the work in the document, save for that which is properly acknowledged, is my own.

Contents

List of Figures

List of Tables

Chapter 1

Literature review

1.1 Introduction

"Guest stars" were observed by ancient East Asian astronomers back to 500 BCE, brightening suddenly in the night sky before fading slowly (Stephenson, 1976). In the west, they were called *Stellae novae*, which translates from Latin into "new stars", as they appeared as new stars in the night sky. At the present time, we know very well that these "new stars" are not "new" at all. They are actually eruptions that take place on the remnants of evolved stars and are known nowadays as ***novae***. Historically, novae represented three distinct classes of stellar eruption that modern astronomers are able to distinguish using photometric and spectroscopic observations. Very broadly, these are dwarf novae[1], classical novae (CNe), and supernovae[2]. While the three types of eruption are characterized by different ranges of eruption brightness (Δm, the magnitude change of the star, is approximately $\Delta m \sim 2-5$ for dwarf novae, $\Delta m \sim 8-14$ for classical novae, and $\Delta m > 15$ for supernovae), it was very difficult for early astronomers to distinguish between them. Compared to the other two types of novae, CNe lie in the middle when it comes to rate of occurrence and energy output; supernovae are the most energetic and dwarf novae are the most frequently occurring.

CNe are stellar eruptions resulting from thermonuclear reactions on the surface layers of a white dwarf (WD) that is accreting matter from a star like our Sun in a close, interacting binary system (Bode & Evans, 2008). Due to the eruption, the brightness of the system increases by 8 up to 14 mag in a matter of a few days, followed by a gradual decrease over a timescale of a few

[1] A dwarf nova is a sudden increase of luminosity of a cataclysmic variable system resulting from instability in its accretion disk. More precisely, it is a "release of gravitational energy due to a temporary increase in the mass-transfer rate through the disk" (Warner, 1995).

[2] Supernovae are stellar eruptions due to either the gravitational collapse of the core of an evolved massive star (core-collapse supernovae; see, e.g., Woosley & Janka 2005) or a nuclear fusion re-ignition in a white dwarf (accreting matter from a close companion, leading to an explosion of the white dwarf (Supernovae type Ia; see, e.g., Hillebrandt & Niemeyer 2000; Hillebrandt et al. 2013).

weeks up to months. A few years later the system returns to its initial pre-eruption brightness. During the eruption a large amount of material (between 10^{-6} and 10^{-4} $M_{\odot}$) is ejected at high speeds with a typical velocity of about 1000 km s^{-1}, enriching the interstellar medium (ISM) with heavy elements and rare isotopes. Although novae have been observed and studied extensively, a complete understanding of their eruption, the nuclear and radiative processes involved, and the physical mechanisms that operate during the eruption, is still a work in progress. Many nova properties and established theories about their eruption have been questioned, particularly in the last 10 years or so. This is largely due to the improvement and new availability of all-sky surveys, high-resolution, high-sensitivity observations, and simultaneous multiwavelength observations provided by ground-based and space telescopes. The massive improvement in the theoretical modelling and computational techniques and tools have also changed the landscape. These new techniques serve as an important tool to test the different nova eruption models.

While the observational and theoretical techniques are improving and with the increase of nova discoveries, an ever better interpretation of these enigmatic events can be foreseen and this field is expected to continue to prosper in the next few decades.

Why we study novae?

The large interest that novae have received from astronomers throughout the years is not arbitrary at all. Studying novae is linked to a better understanding of the abundances of elements in the Galaxy, stellar population synthesis, the evolution of binary systems, stellar thermonuclear processes, and the star formation history of galaxies. They also serve as valuable laboratories to study the physics of accretion onto compact objects such as WDs, the formation of emission/absorption lines and radiative processes in moving ejecta, high-energy emitting shocks, common-envelope processes, and dust condensation in circumstellar material.

CNe and recurrent novae (see Section 1.3.3) are suggested to be progenitors of type Ia supernovae via the single-degenerate scenario (see, e.g., Hoyle & Fowler 1960; Hillebrandt et al. 2013 and references therein). Type Ia supernovae have been the focus of astrophysicists and cosmologists for the last few decades especially because they provide evidence for the theory of the accelerating expansion of the Universe (see, e.g., Riess et al. 1998; Perlmutter 1999 and references therein). This is due to the fact that type Ia supernovae are standardizable candles which can be used to estimate distances, unlike core-collapse supernovae. Despite extensive studies of type Ia supernovae, their origin is yet to be fully understood and while many scenarios have been proposed, the single-degenerate channel is still one of the candidate progenitor routes for type Ia supernovae. Therefore, studying classical and recurrent novae can give important clues to understand the origins of type Ia supernovae.

CNe enrich the ISM with heavy elements, of course on a smaller scale when compared to supernovae. They are also considered one of the main sources of lithium in the Universe (see, e.g., Tajitsu et al. 2015) and other CNO isotopes such as ^{13}C, ^{15}N, and ^{17}O which are formed through nuclear reactions during the eruption. They also contribute to the dust budget in the ISM (see e.g. Gehrz et al. 1998; Evans & Gehrz 2012).

Importance of studying novae at many wavelengths

Despite their importance, systematic multiwavelength studies of CNe are still lacking. It was only recently that multiwavelength studies of CNe (see, e.g., Shore et al. 2013; Schwarz et al. 2015; Bode et al. 2016; Shore et al. 2016; Darnley et al. 2016; Li et al. 2017; Mason et al. 2018) have become feasible with a large array of ground-based and space telescopes. These provide an opportunity to carry out simultaneous observations throughout the electromagnetic spectrum. One of the most interesting aspects of CNe events is that they emit in all the bands of the electromagnetic spectrum, from radio to gamma-ray, through a variety of physical and radiative processes. Therefore observing and following up these events in multiple bands is essential for a better understanding of the origin of the different emission processes.

Aim and context of this work

This work presents a multiwavelength study of three classical nova events that occurred on 2015 March 15 (V5852 Sgr), 2016 September 24 (V407 Lup), and 2016 October 9 (SMCN 2016-10a). While nova SMCN 2016-10a occurred in (or possibly in the direction of) the Small Magellanic Cloud, the other two occurred in the Galaxy. The three studies are papers that have been either published or submitted to the Monthly Notices of Royal Astronomical Society (MNRAS) and they present comprehensive, detailed studies of each of these events where we derive their properties and interpret their behaviour with the aim of a better understanding of classical nova eruptions in general. While each nova shows unique properties and development during its eruption, detailed multiwavelength studies of individual novae are essential to assist us in interpreting the physics underlying their behaviour.

1.2 CNe: a sub-class of cataclysmic variables

1.2.1 Definition

CNe are the result of eruptions that take place on the surface of WDs in interacting binary systems, namely "Cataclysmic Variables" (CVs). These are close binary systems (orbital period of the order of a few hours) consisting of an accreting WD (the primary star) and a companion that typically fills its Roche lobe (the secondary star; Warner 1995). In this section I will give a brief description of the WD stars (the primary), the secondary star, the progenitors of CVs, the Roche lobe, and the mass-transfer/ -accretion mechanisms.

1.2.2 The white dwarf

Low and intermediate mass stars ($M \lesssim 8-10$ M$_\odot$) spend most of their lifetime on the main-sequence of the Hertzsprung-Russell Diagram (HR; see Fig. 1.1), burning H in their core into He. During this stage there is an equilibrium between the outward radiation pressure force generated by the nuclear fusion and the inward gravitational forces. When the H is consumed in the core, the star

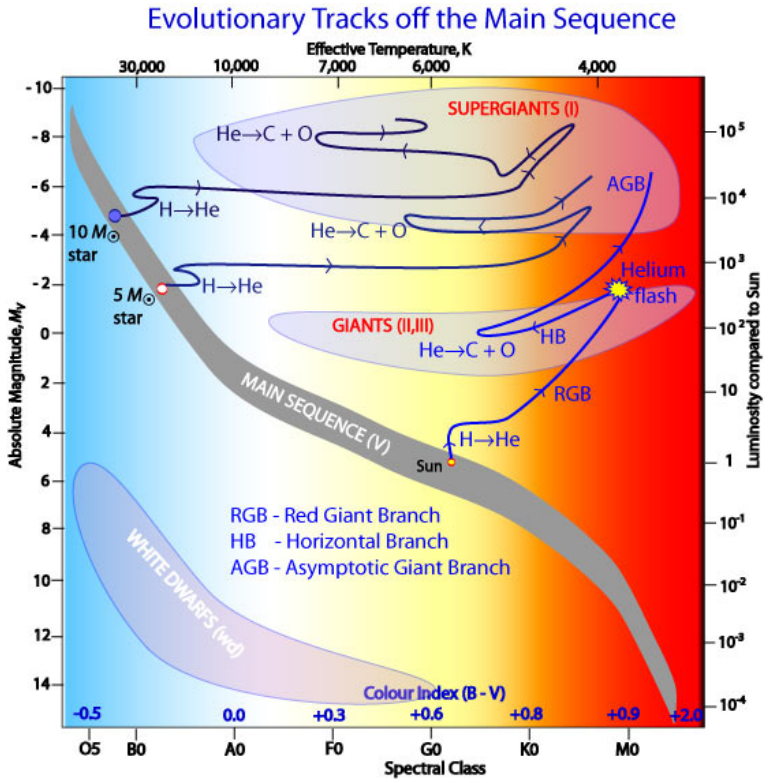

Figure 1.1: The evolutionary track of a solar-like star on the Hertzsprung-Russell Diagram. Credit: Illustration: Robert Hollow, Commonwealth Science and Industrial Research Organization (CSIRO), Australia, adapted by Carin Cain.

leaves the main-sequence and starts burning H in a shell surrounding the inert He core. This causes an increase in the size of the star to hundreds of times its initial radius, turning it into a red giant (RG). During this phase, the necessary conditions (temperature $\sim 10^8$ K and density $\sim 10^6$ kg m^{-3}) are established for the nuclear fusion of He into heavier elements, such as C, N, O and even Ne and Mg, to occur in the core of the star. Once the He is exhausted in the core, the star starts burning He in a shell surrounding the CO core and surrounded by the H burning envelope. At this stage the star moves toward the Asymptotic Giant Branch (AGB) of the HR diagram where it loses a good share of its mass through slow stellar winds and pushes its outer layers into the surrounding space. At the tip of the AGB, a star might undergo a series of periodic pulsations showing a periodic variation in optical and near-infrared (NIR) magnitudes on timescales of the order of ~ 1 year and losing mass at a rate of $\sim 10^{-7} - 10^{-4}$ M$_\odot$ yr^{-1} (see, e.g., Bowen 1988; Whitelock, Feast & van Leeuwen 2008). The expelled material, ionized by the hot core at the centre, becomes visible as a planetary nebula: a luminous Cloud of gas with the previous core of the red giant (not always visible) at the centre. This hot and luminous core evolves to become a WD after the nebula dissipates slowly with time (see, e.g., Shapiro & Teukolsky 1986; Koester & Chanmugam 1990).

The WD has a mass of the order of that of the Sun and a size of order of that of the Earth, hence it is a very dense, compact object (see Fig. 1.2). Unlike stars during their main-sequence phase, WDs do not fuse nuclei in their cores. However, it is electron-degeneracy pressure that keeps

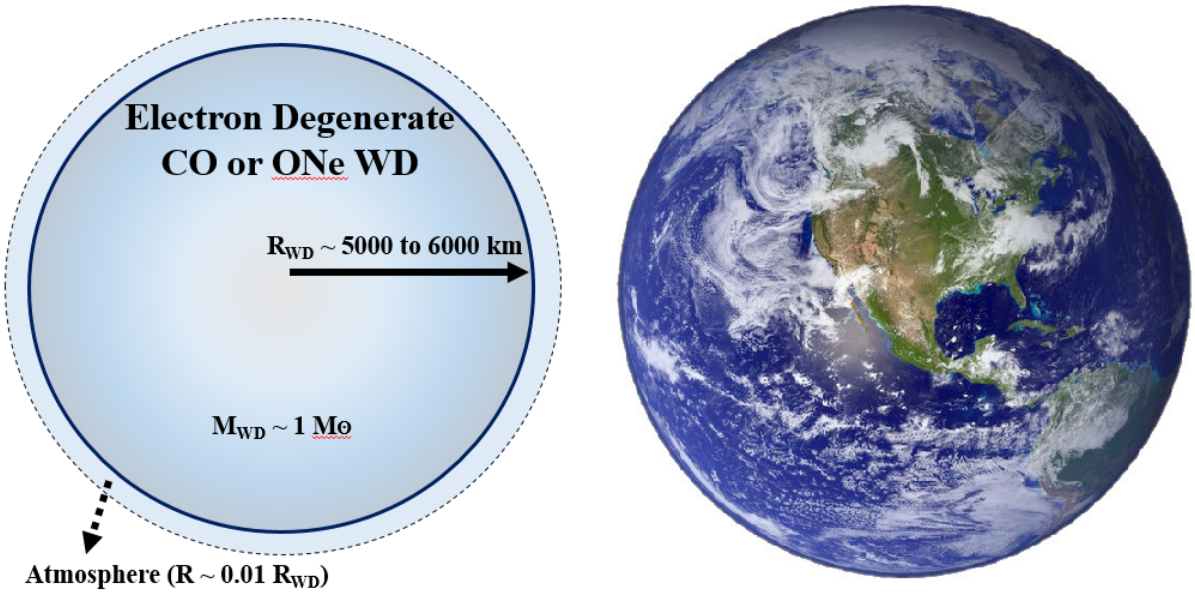

Figure 1.2: A schematic illustration of a one solar mass white dwarf in comparison with the Earth.

the WD from collapsing under its own gravity. More precisely, according to the Pauli exclusion principle, no two electrons can occupy the same quantum state simultaneously. For this reason, if the mass of the WD is less than $\sim 1.44\,\mathrm{M}_{\odot}$ (see below for further explanation), the gravitational energy of the star is not sufficient to cause further collapse nor to combine the electrons and protons into neutrons. Therefore, the collapse is halted by the electron-degeneracy pressure. See, e.g., Shapiro & Teukolsky (1986), Koester & Chanmugam (1990), and Kawaler (1997) for reviews of WD stars.

The chemical composition of the WD depends on the initial mass of the star. For intermediate-mass stars, the nuclear fusion of heavy elements in the core stops at O, resulting in a CO WD. However, for more massive stars ($8\,\mathrm{M}_{\odot} \lesssim M \lesssim 10\,\mathrm{M}_{\odot}$), the nuclear fusion can go beyond O to form heavier elements such as Ne (and sometimes Mg), resulting in an ONe WD. This implies that the mass of an ONe WD ($>1.1-1.3\ \mathrm{M}_{\odot}$) is typically greater than the mass of a CO WD ($\lesssim 1.2\ \mathrm{M}_{\odot}$; Iben & Tutukov 1989).

While the heavy elements move toward the centre of the WD, its atmosphere consists of a thin layer of light elements such as He and H. These elements are basically remnants of the outer layers of the progenitor star.

The radius of a WD depends on its gravitational energy and the kinetic energy of the electrons. Nauenberg (1972) derived a relationship between the mass (M_{WD}) and radius (R_{WD}) of a WD, where the radius decreases with increasing mass:

$$R_{\mathrm{WD}} = 0.78 \times 10^{9} \left((\frac{M_{\mathrm{Ch}}}{M_{\mathrm{WD}}})^{2/3} - (\frac{M_{\mathrm{WD}}}{M_{\mathrm{Ch}}})^{2/3} \right)^{1/2} \ [\mathrm{cm}], \tag{1.1}$$

as the mass increases the radius shrinks, to "hypothetically become" almost zero when the mass reaches an upper limit of $\sim 1.44\,\mathrm{M}_{\odot}$ (see Fig. 1.3), known as the Chandrasekhar mass limit (M_{Ch}; Chandrasekhar 1931).

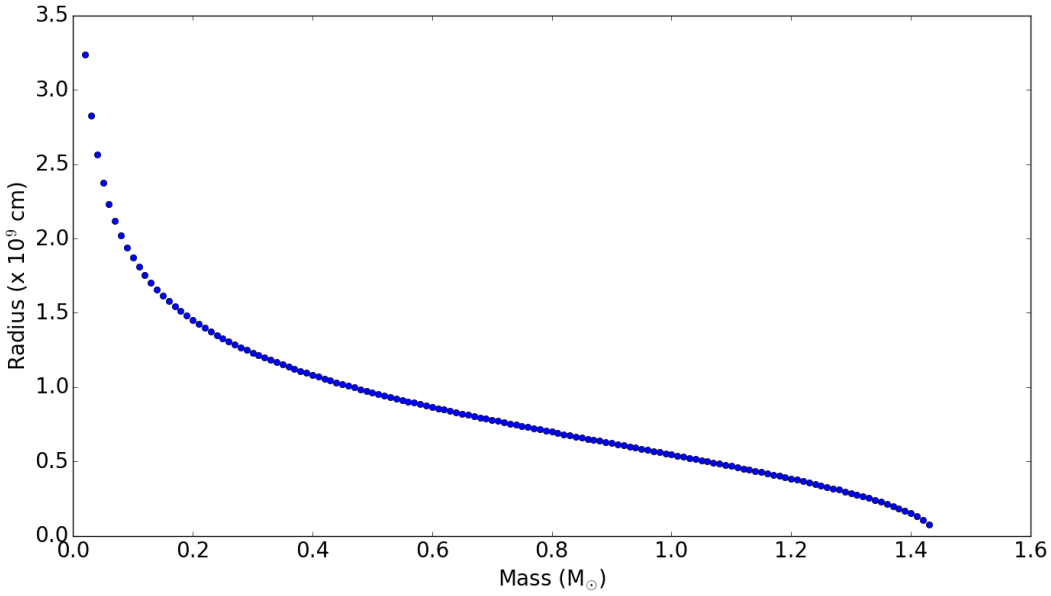

Figure 1.3: The white dwarf mass-radius relation of Nauenberg (1972).

In 1931, Chandrasekhar proved that the mass of a WD cannot exceed a limit of $\sim 1.44\,M_\odot$. If the WD mass increases with time, e.g., due to accretion from a companion, and it reaches the Chandrasekhar limit, the system cannot be supported by the electron-degeneracy pressure against gravitational collapse and one of two scenarios might take place, depending on the WD's chemical composition: (1) if the WD is a CO-type, the mass increase leads to a pressure and temperature increase. This will ignite carbon-oxygen burning and increase the temperature even more leading to thermonuclear runaway and further nuclear fusion reactions. Eventually the star explodes through a type Ia supernova (see, e.g., Hoyle & Fowler 1960; Hillebrandt et al. 2013 and references therein); (2) In contrast, ONe WDs collapse into a neutron star if they exceed the Chandrasekhar mass limit (see Section 1.4.4.3 for more details).

1.2.3 The secondary star

In CVs, the initially less massive secondary evolves more slowly than the more massive primary star, therefore the secondary is usually still on the main-sequence. Systems where the secondary star has evolved to become a RG or AGB star, characterized by a strong stellar wind, are known as symbiotic systems (for a review of symbiotic stars see, e.g., Mikolajewska et al. 1988). Although, these systems can exhibit different mass-transfer mechanisms when compared to CVs (see Section 1.2.5), they might still lead to nova eruptions (novae erupting within symbiotic binaries). A fraction of these novae have been known to be recurrent (see Section 1.3.3). This is attributed to the high mass of the WD and the high mass-transfer rate from the evolved secondary onto the WD. Based exclusively on the evolutionary state of the secondary star, Darnley et al. (2012) proposed a new classification system for novae (classical and recurrent novae): a main-sequence star secondary (MS-Nova), a sub-giant star secondary (SG-Nova), or a red giant star secondary (RG-Nova). These three classes

differ by the mass-transfer mechanisms (see Section 1.2.5) and rates, orbital separation/period, the amplitude of the eruption, the ejected mass during the eruption, and the ejecta velocity. They can also show different evolution of the light-curves and colours after the eruption (for further details see Darnley et al. 2012).

1.2.4 Progenitors of CVs

Not all stellar binaries evolve to become CVs - it depends on the combination of initial masses and orbital separations. More precisely, CVs originate from binary star systems with the following properties: (a) the primary star evolves into a WD on a timescale shorter than the Hubble time[3], hence, its initial mass is high enough to develop a H- or He-consumed core in less than this time; (b) the initial orbital separation between the two stars is large enough that the core of the primary star becomes a H- or He-consumed before the secondary star fills its Roche lobe (see Section 1.2.5); (c) the initial orbital separation is small enough for a common envelope to form when the primary fills its Roche lobe. This, along with the high initial mass ratio, will lead to an extensive reduction of the orbital separation to a state where mass transfer from the secondary to the WD remnant of the initial primary, is established. The mass-transfer rate should be high enough (larger than $\sim 10^{-11}\,M_{\odot}\,yr^{-1}$) to cause a nova eruption on the WD surface in less than a Hubble time (see, e.g., Iben, Fujimoto & MacDonald 1992; Iben & Fujimoto 2008).

1.2.5 Mass-transfer and -accretion mechanisms

In binary star systems, the Roche lobe is a part of the critical equipotential surface formed by the primary and secondary (see Fig. 1.4). It is a distinctively tear-drop-shaped region surrounding a star, within which any orbiting material is gravitationally bound to the star. Any material that is outside or on the surface of this tear-drop-shaped region, will either escape the system completely, orbit the system, or fall onto the binary companion, all depending on the initial location and momentum of the material. Therefore, once the the secondary star fills its Roche lobe, any material that leaks through the inner Lagrangian point (L1), falls onto the primary star (see, e.g., Warner 1995; Lamers & M. Levesque 2017).

For CVs, the main model that describes the mass-transfer mechanism from the secondary to the primary is the so-called Roche Lobe OverFlow (RLOF). An expansion of the secondary star through its evolution off the main-sequence and/or a size reduction of the Roche lobe, might both lead the secondary star to fill its Roche lobe. The reduction of the size of the Roche lobe takes place if the orbital separation decreases due to, e.g., angular momentum loss (see, e,g., Warner 1995; Kolb et al. 2001; Linial & Sari 2017). This is a consequence of either a magnetically coupled stellar wind, leading to magnetic braking (Verbunt & Zwaan, 1981) in case of a main-sequence secondary, or gravitational wave radiation (see, e.g., Faulkner 1971; Landau & Lifshitz 1975). For

[3]Hubble time: the time required for the Universe to expand to its present size, assuming that the Hubble constant has remained unchanged since the Big Bang.

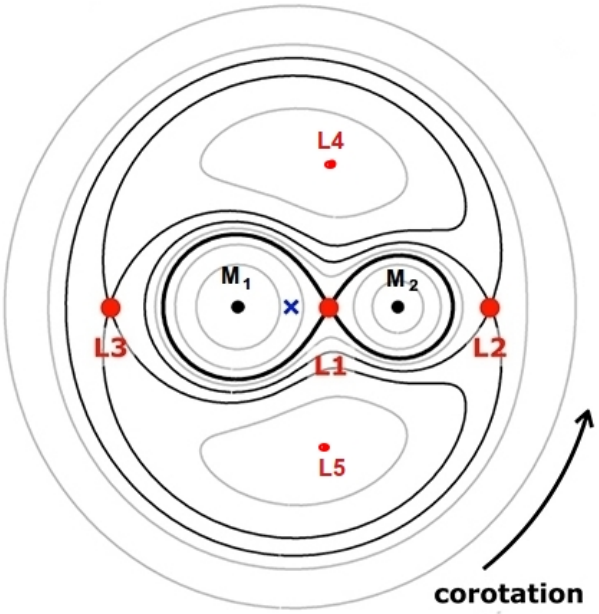

Figure 1.4: The Roche lobe (solid, black line) and sections of the equipotential surface of a binary system with a mass ratio of M_1:M_2 = 2:1. The plot is adopted from Lamers & M. Levesque (2017) and edited for the purposes of this work. The blue x-sign indicates the centre of mass of the system and the red dots indicate the Lagrangian points.

a further detailed description of the evolution of the system and the orbital separation see Iben & Fujimoto (2008).

Once the secondary star fills its Roche lobe, gas can escape from the atmosphere of the secondary into the Roche lobe of the primary (WD) through the L1 point. Warner (1995) describes this flow as: "The flow resembles the escape of gas through a nozzle into a vacuum; the flow velocity is approximately the thermal velocity of the atoms in the gas". The inflowing gas has angular momentum predominantly in the plane, hence, before falling onto the surface of the WD, it forms an accretion disk in the orbital plane around the primary. The gravitational potential of the secondary on the disk is almost negligible as the latter is mainly affected by that of the primary. Due to conservation of angular momentum, the angular velocity of the particles throughout the majority of the disk is almost Keplerian. Inside the disk, the material loses angular momentum through, e.g., viscous shear and magnetic stresses, so it moves in towards the primary where the material is accreted and accumulated on the surface of the WD (except at the edge of the disk where conservation of angular momentum may require an outward drift; see, e.g., Frank, King & Raine 1985; Bath & Pringle 1985; Warner 1995 and references therein). The intersection point of the stream trajectory coming from the secondary with the outer edge of the accretion disk is a shock-heated, hot, and bright area known as the bright spot. The energy radiated by the bright spot can equal or even exceed the energy radiated by the other components of the system (primary, secondary, and disk; see Fig. 1.5).

Another model for the mass-transfer mechanism, known as the wind-fed model, might also operate in the case of a secondary star exhibiting strong stellar winds, such as a RG or AGB

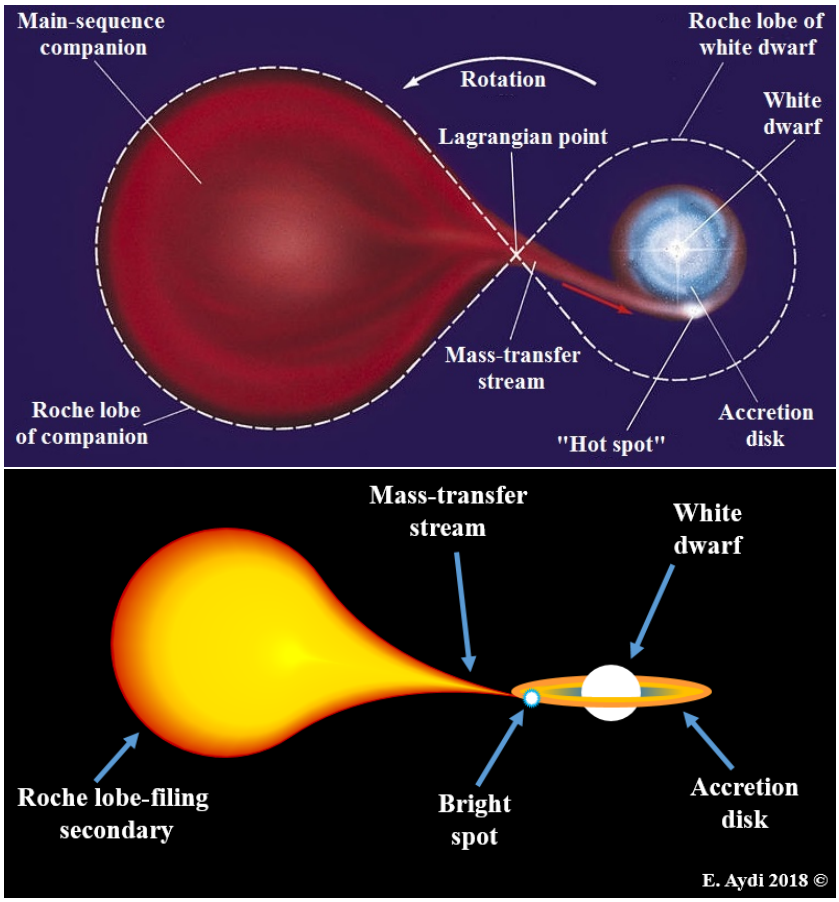

Figure 1.5: *Top:* an illustration of a pole-on view of a non-magnetic CV system (Credits: Pearson Prentic Hall, Inc. 2005). *Bottom:* an illustration of an edge-on view of a non-magnetic CV system.

star (symbiotic systems; see, e.g., Starrfield, Iliadis & Hix 2008). In such systems, the WD captures mass from the wind of the secondary star even when the latter does not fill its Roche lobe. Typically, these systems have larger orbital separation and the wind-fed model is the main mass-transfer mechanism that operates (Iben & Fujimoto, 2008). However, it is worth noting that both mass-transfer mechanisms, RLOF and wind-fed model, might operate in some symbiotic systems (Mikołajewska, 2012).

1.3 CNe: the theory of eruption

A classical nova eruption is the consequence of the accretion of H-rich material onto the WD: the H-rich matter from the secondary companion accumulates on the WD surface leading to an increase in pressure and density at the base of the surface layers. When these reach a critical level, a thermonuclear runaway (TNR) occurs on the surface of the WD (see e.g. Starrfield, Iliadis & Hix 2008), leading to a dramatic increase of the visual brightness of the system. The TNR is a nuclear chain-reaction on the surface of the WD and is the commonly accepted model for a classical nova eruption. It was first proposed by Kraft (1962), based on a work by Mestel (1952). The source of energy is the fusion of hydrogen nuclei to form heavier elements; a nuclear reaction that releases a

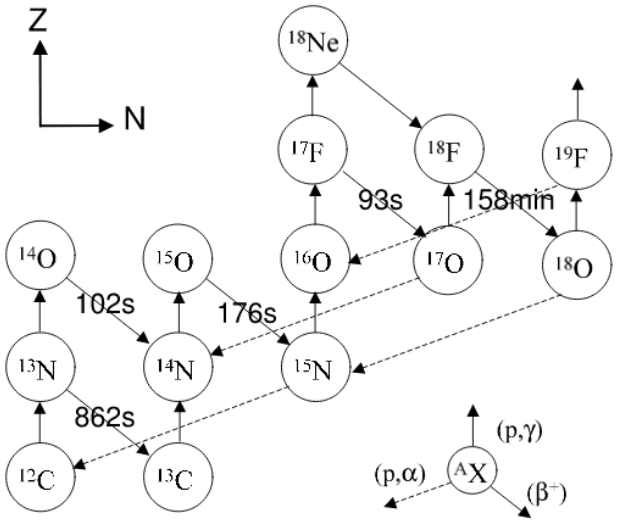

Figure 1.6: A schematic diagram of the CNO cycle from Hernanz (2005). The half-lives of the longest-lived β^+-unstable nuclei, which act as bottlenecks of the system, are shown.

tremendous amount of energy. In this Section I will elaborate on the thermonuclear processes, the nova evolution, and the recurrence of nova eruptions. For detailed reviews of the TNR theory and processes as well as the nova evolution see Starrfield (1989), Warner (1995), González-Riestra & Krautter (1998), and Starrfield, Iliadis & Hix (2008).

1.3.1 Thermonuclear processes

Although the WD is the remnant core of a star where most of the H has fused into heavier elements (such as He, C, O, Ne, and Mg), the accretion from the secondary onto the WD surface is a source of fresh H-rich material. While this material accumulates on the surface of the WD the pressure increases with time. Due to the extreme surface gravity of the WD, the weight of the H-rich layer crushes the material at the base of the layer so it becomes degenerate (see, e.g., Starrfield 1989; Hellier 2001).

The increase in temperature ignites nuclear reactions near the bottom of the accreted layers, where two mechanisms operate depending on the temperature: the proton-proton chain reaction (including the *pep* reaction: $p + e^- + p \longrightarrow d + \nu$, where p is a proton, e^- is an electron, d is a deuterium, ν is a neutrino; Schatzman 1958; Bahcall & May 1969) and the CNO cycles (see e.g Starrfield 1989; Hernanz 2005). Both nuclear reactions along with compressional heating raise the temperature of the accreted material until an eruption occurs.

The proton-proton chain reaction starts when the temperature of the accreted layers increases to $\sim 10^6$ K. It involves the fusion of two H nuclei (protons) into deuterium, releasing a positron and a neutrino as one of the protons changes into a neutron. The deuterium can then absorb another proton to form an isotope of helium (^{3}He). This is followed by one of three processes which eventually produce a $^4_2$He nucleus (Clayton, 1983; Adelberger et al., 2011). A total energy of $\sim$ 20 – 30 MeV per cycle is released and these reactions are dependent on temperature with a rate

$\propto T^4$. The energy generated by the proton-proton chain reactions increases the temperature, which can cause an increase in pressure in the case of normal matter, leading to an expansion of the material and eventually cooling. However, since the matter is degenerate, the pressure is only dependent on the density ($P \propto \rho^\gamma$; where P is the pressure, ρ is the density, and γ is the polytropic index) and any temperature increase does not increase the pressure and does not cause expansion, but it does increase the rate of nuclear reactions leading to a runaway effect. When the temperature reaches $\sim 10^7$ K the CNO cycles start and at $\sim 2{\times}10^7$ K they become the main source of energy release instead of the proton-proton chain reactions.

Although the proton-proton chain reactions are important during the accretion phase of the eruption, it is the CNO cycles that power the final stages of the TNR and the evolution to the peak of the eruption. These reactions consist of burning four H nuclei to form a He nucleus by using CNO nuclei as catalysts, while emitting energy of ~ 30 MeV per cycle. During the reactions, the heavy elements absorb protons, resulting in radioactive nuclei with half-lives on timescales of the order of ~ 100 s, which then decay (β^+-decay) and release a large amount of energy. Fig. 1.6 presents a schematic diagram of the CNO cycle reactions.

The energy generation rate is strongly dependent on temperature ($\propto T^{18}$) causing convection in the envelope, similar to that in the cores of massive stars. At $T \sim 10^8$ K the envelope becomes fully convective with the convective turn-over timescale ~ 100 s. This is comparable to the timescale of the half-lives of the longest lived unstable nuclei, which are transported by convection to the surface where they deposit large amounts of energy (the energy generation at the surface due to the decay of radioactive nuclei can exceed 10^{13} to 10^{15} erg s^{-1}, depending upon the enrichment). At the same time, convection transports fresh CNO nuclei towards the high temperature zone for burning.

The rate of nuclear energy generation at high temperatures ($T \geq 10^8$ K) is limited by the half-lives of the longest lived β^+-decay nuclei (^{13}N, ^{14}O, ^{15}O, ^{17}F with half-lives of 862 s, 102 s, 176 s, and 93 s, respectively) which act as bottlenecks of the cycle. These nuclei become the most abundant unstable nuclei in the envelope when $T \geq 10^8$ K. During these cycles, CNO isotopes such as ^{13}C, ^{15}N, and ^{17}O are formed (it is suggested that novae are one of the major sources of these isotopes in the Galaxy; Hernanz 2005; Starrfield, Iliadis & Hix 2008).

The runaway continues until the gas pressure exceeds the degeneracy pressure due to the temperature increase. This relieves the degeneracy and leads to expansion of the envelope (ejecta). The deposition of energy by the β^+-decay nuclei near the surface is the main contribution to the expansion of the envelope and to the total luminosity of the eruption. The energy released by the radioactive nuclei is sufficient to eject material with expansion velocities similar to those observed (~ 1000 km s^{-1}) and also reproduce the observed luminosities ($\sim 10^5$ L$_\odot$; see Starrfield 1989 and references therein).

1.3.2 The nova evolution

At the peak of the TNR, maximum bolometric luminosity is reached typically on timescale of hours, while the optical photosphere of the expanding envelope reaches its maximum radius later,

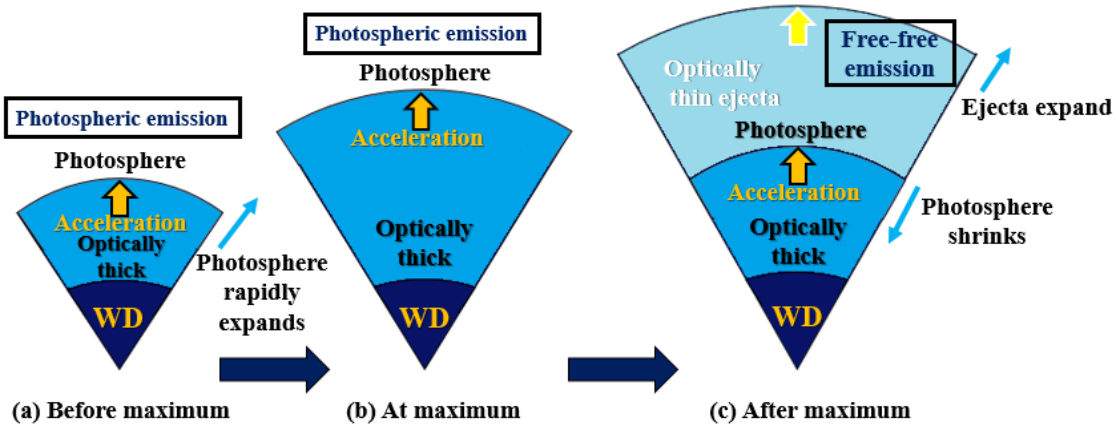

Figure 1.7: An illustration of the nova envelope evolution for fast and moderately fast evolving novae, adopted from Hachisu & Kato (2014a) and edited for clarity. Before optical maximum, the expanding envelope moves together with the optical photosphere. The maximum light is reached when the optical photosphere reaches its maximum radius. At this point the optical photosphere starts moving backwards into deeper layers and massive optically thin ejecta expands further while more ejecta are continuously supplied by optically thick winds.

manifesting as visual maximum. The time between the maximum bolometric luminosity and the visual maximum depends on the ejecta expansion rate (Warner, 1995). It was proposed that all novae at maximum light have an Eddington luminosity[4] of a $\sim 1-2\,M_{\odot}$ object (Bath & Shaviv, 1976). The maximum luminosities of some novae that show fast light-curve evolution after maximum (very fast novae; see Section 1.4.1.3) have even been super-Eddington (see e.g., Warner 1995; Orio et al. 2018 and references therein).

While rising to maximum the expanding envelope moves almost together with the optical photosphere; this is known as the "fireball stage". The ejecta accelerated below the photosphere are optically thick and they are described as an "optically thick wind" (see Fig. 1.7). The rapidly expanding optical photosphere reaches a maximum radius manifesting as maximum visual light. At this stage the optical photosphere detaches from the top of the ejecta and then its radius shrinks into progressively deeper layers, while optically thin ejecta outside of the optical photosphere continue expanding and they are described as "optically thin wind" (Hachisu & Kato, 2014a). Due to continuous H-burning on the WD surface, more ejecta are continuously supplied by optically thick winds. The hot expanding ejecta engulf both stars and the system enters a temporary short common-envelope phase, while the binary motion helps in ejecting the material. It is suggested that during the nova eruption, the mass accretion is temporarily disrupted. However, some have argued against this (see, e.g, Retter 2002; Walter & Battisti 2011).

The initial eruption is followed by a phase of constant bolometric luminosity (Sparks, Starrfield & Truran, 1976) powered by the remaining non-degenerate H-burning layer, since only a fraction

[4]The Eddington luminosity is the maximum luminosity a body can reach when there is a balance between the radiation pressure and the gravitational attraction: $L_{\rm Edd} = \frac{4\pi GcM}{\sigma_e N_e} \simeq 3.2\times10^4 \left(\frac{M}{M_{\odot}}\right) L_{\odot}$, where M is the mass of the object, G is the gravitational constant, c is the speed of light, σ_e is the electron scattering cross-section, and N_e is the electron number density.

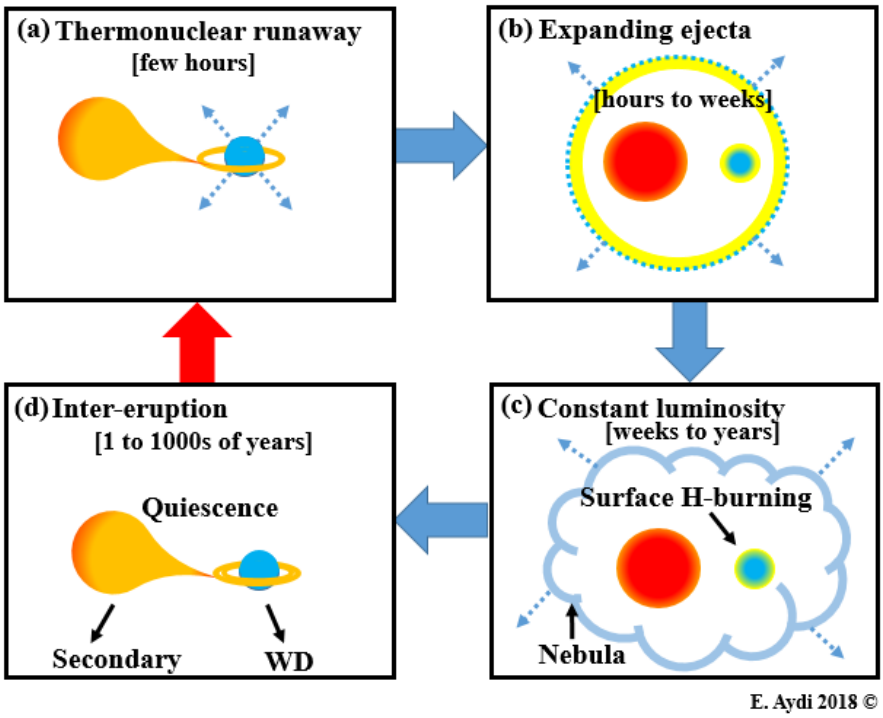

Figure 1.8: A simplified illustration scheme of the nova process from the (a) thermonuclear runaway followed by (b) the ejecta expansion, then (c) the phase of continuous bolometric luminosity, and finally (d) back to quiescence where the system evolves towards another eruption. The timescales of these phases are indicated between brackets.

of the envelope is ejected during the initial nova eruption. At constant bolometric luminosity the evolution of the eruption becomes slower during which continuous H-burning occurs on the surface of the WD, typically for a few years, while the nova evolves back to minimum (quiescence).

After $\sim$ 1000 days, the ejecta expand enough to become visible as a nebula surrounding the binary system. The nebula can be useful for deriving distances through the so-called expansion parallax (see, e.g., Mellema 2004), provided the ejection is uniform in space. The final turn-off phase of the nova eruption and the interruption of the nuclear burning on the WD surface is still poorly understood. At this stage, the mass accretion from the secondary onto the WD resumes, re-establishing the accretion disk around the WD and evolving the system towards a new eruption on a timescale ranging from a year (see, e.g., Darnley et al. 2014, 2016) up to hundreds of thousands of years (Warner, 1995).

Fig. 1.8 shows a simplified summary of the nova evolution, including a summary for the critical timescales: the development of the TNR (a few hours), the ejection of the envelope (from a few hours up to a few weeks), the constant luminosity phase (from a few months up to a few years), and the period between eruptions (from a few years up to thousands of years).

1.3.3 Accretion resumption, recurrence of nova eruptions, and supernova type Ia progenitors

Generally, when the nova eruption reaches an end, the accretion disk re-establishes itself so the mass accretion onto the surface of the WD resumes (several years after eruption), building-up the accreted layer for another eruption. However, it is argued that a few novae showed signatures of mass transfer and accretion resumption early after eruption or even a survival of the accretion disk during the eruption. This is either due to detection of narrow and moving He II lines and H I lines in the optical spectrum, a few days after eruption (Walter & Battisti, 2011; Mason et al., 2012; Munari, Mason & Valisa, 2014), possibly originating from the accretion disk or due to features in the X-ray data such as: dips and eclipses in the X-ray (or sometimes optical) light-curves caused by the reformed accretion disk (Schaefer, 2011; Ness et al., 2012; Orio et al., 2013); an obscuration of the central source by the supposedly re-formed accretion disk, manifesting as a relatively weak continuum in the X-ray spectra, during the continuous hydrogen-burning on the surface (Ness et al., 2013); modulation in the X-ray and UV light-curves early after eruption ($\sim$ 100 days post-eruption), attributed to "structured disc-rim occultation" (Beardmore et al., 2012); an extended surface hydrogen-burning attributed to freshly accreted material and manifesting as a long period of (soft) X-ray emission (see, e.g., Greiner, Orio & Schartel 2003); and a short recurrence period (order of few years; Darnley et al. 2016, 2017). Note that a description of nova emissions in X-ray and UV wavelengths is provided in Section 1.4.5.

The timescale for the recurrence of a nova eruption is controlled by several factors, mainly: the mass of the WD, its radius, and the accretion rate. The less massive the WD is and the larger its radius, the smaller is the gravity on its surface. This means that a large amount of matter is accreted by the WD from the secondary before the pressure at the bottom layers of the accreted envelope reaches the required levels to trigger the eruption, and vice versa.

The accretion rate also plays a major role in the time between two nova eruptions. When the accretion rate is higher it takes a shorter period for the matter on the surface of the WD to accumulate and reach the required pressure to trigger the TNR. Typically, the recurrence time of a classical nova is $\sim 10^4 - 10^5$ years. However, the recurrence times for some novae are short enough that our observational record spotted them more than once in the last $\sim$ 200 years. When a system is observed more than once in eruption it is classified as a recurrent nova (see, e.g., Schaefer 2010). Although some of the recurrent nova systems are indeed typical CVs (with a main-sequence secondary), the majority of them are in systems hosting an evolved companion, which are not typical CVs (Darnley et al., 2012). The high frequency of eruptions in systems with a giant companion is attributed to the high mass-transfer rate, caused by the giant's stellar wind, in addition to a massive primary (see, e.g., Warner 2008; Darnley et al. 2012). A very remarkable nova, M31N 2008-12a, has been recorded in eruption every year since 2008 (Darnley et al., 2014, 2016).

Since their recurrence time is short, these recurrent novae are suggested to host massive WDs ($\gtrsim$ 1.3 $M_\odot$) and therefore, are potential progenitors for type Ia supernovae (it is worth noting that this

is not restricted to recurrent novae). During a nova eruption, the majority of the accreted envelope is ejected, while a small fraction of the material might accumulate on the WD and increases its mass. In recurrent novae (or any CNe that host a massive CO WD), the increasing WD mass approaches the Chandrasekhar limit leading to a supernova type Ia eruption when the WD explodes in a thermonuclear eruption (Li & van den Heuvel, 1997; Hachisu, Kato & Nomoto, 1999; Hachisu, Kato & Luna, 2007; Nomoto et al., 2007; Osborne et al., 2011; Starrfield et al., 2011). This is known as the single-degenerate scenario. This scenario is still a matter of debate and some suggest that more mass is ejected/burned by the WD during the eruption and quiescence, than is accreted, therefore the WD mass might decrease with time (see, e.g., Kovetz & Prialnik 1994; Schaefer 2014).

PTF 11kx is a type Ia supernova which was discovered in 2011 and is one of the contenders that support the single-degenerate scenario. Dilday et al. (2012) have carried out a detailed study of absorption features of Ca II H&K and Na I, originating from an interaction between the ejecta and multiple shells of circumstellar material. Dilday et al. (2012) suggested that such dense circumstellar material originate from a recurrent nova and an extensive wind from a mass-losing giant secondary (see also Moore & Bildsten 2012), therefore the progenitor is likely a symbiotic, recurrent nova, similar to RS Ophiuchi. The latter is a symbiotic, recurrent nova hosting a giant secondary and that has been recorded in eruption several times (2006 was the latest eruption; see Narumi et al. 2006). This nova has been studied extensively and it has been demonstrated that it is surrounded by a dense circumstellar medium originating from recurrent eruptions and a mass-losing giant secondary. This is supported by imaging (Bode et al., 2007; Sokoloski, Rupen & Mioduszewski, 2008; Ribeiro et al., 2009), modelling of the eruption (Mohamed, Booth & Podsiadlowski, 2013; Booth, Mohamed & Podsiadlowski, 2016), and high-resolution spectroscopy (Patat et al., 2011; Somero, Hakala & Wynn, 2017). These studies demonstrate that RS Ophiuchi hosts a massive WD approaching the Chandrasekhar limit and therefore is a potential type Ia supernova progenitor.

1.4 Observational properties of classical novae

"No two novae show exactly the same observational properties or development during eruption" (Warner, 2008). However, there are general similarities in the evolution of the photometric and spectroscopic properties of the overall population of CNe. These similarities allow us to interpret the physics underlying their eruptions and help us understand the morphology, energetics, and emission from the eruption. In this section, I will give a general brief overview of the optical light-curve evolution, the spectral development, and the emission at different wavelengths of CNe during eruption.

1.4.1 Optical light-curve development during eruption

The majority of CNe are characterized by the typical light-curve evolution, from the pre-nova to the post-nova stages, shown in Fig. 1.9. The light-curve starts with a sudden rise to maximum by $\sim$ 8 up to 15 mag, followed by a post-maximum rapid decline in brightness which is shown by the

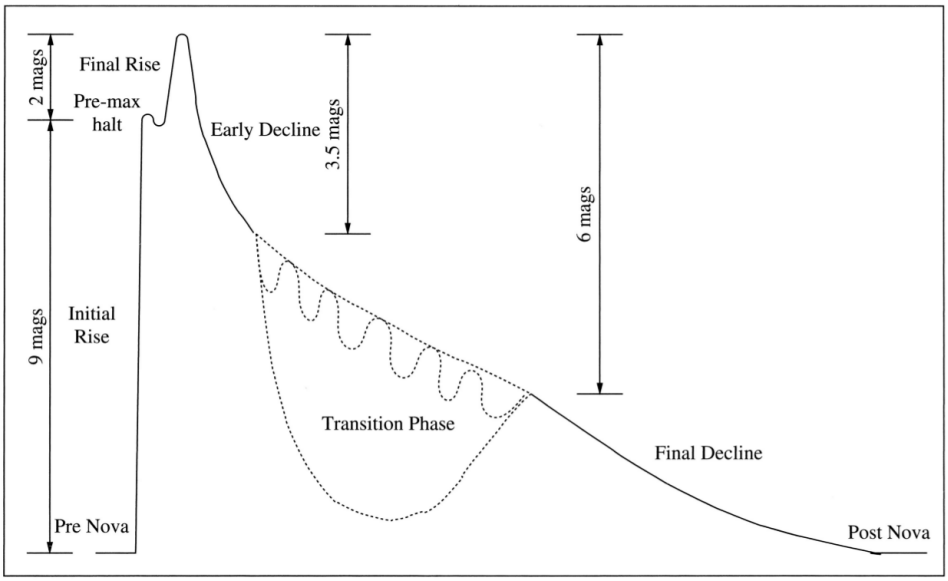

Figure 1.9: The typical morphology of a nova light-curve from Warner (2008) showing the different stages of the light-curve evolution.

majority of novae. This is then followed by a variety of individual light-curve developments during the transition phase. In the following sections, I will briefly summarize the different stages of the optical light-curve evolution. For a more detailed overview of the optical light-curve evolution of CNe see Warner (1995, 2008).

1.4.1.1 Early development

When the eruption starts the nova brightness climbs initially by around 10 mag in a matter of a few days (the initial rise can be as fast as < 1 d). Although only a few novae have been monitored during their initial rise to maximum (see, e.g., V1500 Cyg Liller et al. 1975; see also Cao et al. 2012 for more examples), the majority of novae show a pause in the rise for around 2 days or less (depending on the speed-class of the nova; see Section 1.4.1.3). This pause is known as the pre-maximum halt, which is then followed by the final rise to maximum by around 2 mag. The timescale of the visual maximum-light phase varies between a few hours to a few days depending on the speed-class of the nova (Section 1.4.1.3).

1.4.1.2 Early and late decline

Once at maximum, the light-curve of CNe usually show a smooth initial decline by ~ 3.5 mag, known as the early decline. This phase varies in timescale from one nova to another, ranging from a couple of days up to a few months. For slow novae, the early decline might show some brightness variations with amplitude up to ~ 2 mag on timescales of 1 to 20 days (see, e.g., Chapter 2).

Between the early decline and the final decline a transition phase in the light-curves of novae manifests with either a smooth, slow decline or a variety of behaviours, such as: (i) a sudden

Table 1.1: The classification scheme of nova light-curves based on t_2 and their rate of decline ($\dot{m}_V$) (Payne-Gaposchkin, 1964).

Speed class	t_2 (d)	$\dot{m}_V$ (mag d^{-1})
Very fast	$<$10	$>$0.2
Fast	11 – 25	0.18 – 0.08
Moderately fast	26 – 80	0.07 – 0.025
Slow	81 – 150	0.024 – 0.013
Very slow	151 – 250	0.012 – 0.008

decrease of brightness by 7 up to 10 mag, after which the nova brightness recovers to an extrapolated trend from the early decline. This decrease is usually attributed to the formation of dust around the system, which absorbs the optical radiation and emits at infrared (IR) wavelengths. In other words, the dust blocks the optical light from the system and an IR excess develops, which can be seen as an increase of brightness in the IR/mid-infrared (MIR) light-curves. However, the sum of the total of optical plus IR flux remains constant (see, e.g., Hyland & Neugebauer 1970; Evans & Rawlings 2008); (ii) periodic or quasi-periodic oscillations on timescales of the order of a few days and amplitudes up to 1.5 mag; (iii) substantial jittering above the base level of the light-curve. These jitters are isolated flickers with symmetrical sharp-topped shapes. Unlike the oscillations, the jitters can be prominent from the start of the decline, although, they occur below 3 mag from the peak for the majority of novae that show jittering in the light-curve. (iv) a plateau of constant magnitude at 3 – 6 mag for a few months, followed by a sharper decline (Warner, 2008; Strope, Schaefer & Henden, 2010). Hillman et al. (2014) carried out modelling of CN light-curves and they proposed explanations for some of the post-eruption light-curve behaviour. They attribute the oscillations to "the restructuring and rebalancing that the envelope undergoes as it begins to expand" and the jitters to multiple flashes due to the envelope contraction and re-expansion.

The final decline is very slow (timescale on the order of a few years) back to the pre-nova magnitude.

1.4.1.3 Properties and classification schemes of novae

Nova light-curves are characterized by several parameters such as: the rise rate, the rise time to maximum light, the rise behaviour, the maximum light, the decline rate, and decline behaviour (see, e.g., Hounsell et al. 2010; Cao et al. 2012). The main parameter that is used to classify nova light-curves is the decline rate. This classification is determined by the duration in days for the brightness to decrease by 2 or 3 mag from maximum optical light, known as t_2 and t_3, respectively. Based on the decline time t_2 and the decline rate, Payne-Gaposchkin (1964) classified nova light-curves into five speed-classes, which are listed in Table 1.1. More recently, Hachisu & Kato (2006) have carried out theoretical modelling of nova light-curves and introduced a universal decline law that describes their decline rate. They found that between 2 and 6 mag from optical

maximum, the typical universal decline law of the flux is proportional to the time t (since eruption) with a slope of index = -1.75 ($F \propto t^{-1.75}$). This index is = -3.5 at later stages (from 6 to 10 mag from optical maximum).

It is suggested that the speed-class of a nova light-curve depends mainly on the mass of the WD and the mass of the accreted envelope (see, e.g., Shara 1981; Livio 1992 and references therein). The large gravitational potential on the surface of high mass WDs (1.1 to $\lesssim$1.4 $M_\odot$) means that less hydrogen is accreted onto the WD surface before a TNR occurs. As low-mass envelopes can be ejected faster than high-mass envelopes, novae occurring on massive WDs will exhaust their thermonuclear-powered envelopes faster than low-mass WDs, manifesting in a fast light-curve decline from maximum-light. Based on that very fast novae usually occur on massive WDs and very slow novae usually occur on low-mass WDs.

Another scheme has been introduced by Strope, Schaefer & Henden (2010) which classifies novae based on the morphology of their light-curves during the decline from maximum and the transition phase. They defined seven classes: S (smooth) which are the stereotypical nova light-curves, P (plateau), D (dust dip), C (cusped secondary maximum), O (oscillations), F (flat-topped), and J (jitters; see Fig. 1.10 for a prototype of each class). A few novae show a combination of these different features in their light-curves and they can be classified as unusual (see, e.g., Chapter 2). It is worth noting that theoretical modelling by Hillman et al. (2014) resulted in a large variety of nova light-curves by changing the properties and parameters of the system.

1.4.2 Colours of novae

Since novae do not usually show strong line emission at maximum light, van den Bergh & Younger (1987) derived a mean intrinsic colour $(B-V)_0$ = + 0.23 $\pm$ 0.06 for novae at maximum light and $(B-V)_0 = -0.02 \pm 0.04$ for novae at t_2, after analyzing *UBV* photometry for 14 CNe. This provides a useful method to derive the reddening towards a nova, more precisely $E(B-V)$ and hence A_V.

Hachisu & Kato (2014a, 2016b) have carried out analyses and theoretical modelling of *UBV* photometry of several CNe, which show that the evolutionary track of novae in a colour-magnitude diagram (CMD) is different for those with giant secondaries compared to those with main-sequence secondaries (see also Darnley et al. 2016). Darnley et al. (2012) also showed that using the colours of the system during quiescence can provide a method to constrain the evolutionary state of the secondary star and the luminosity of the accretion disk by placing the quiescent nova on an optical or NIR CMD (see fig. 1 in Darnley et al. 2012).

1.4.3 Novae as standard candles

For several decades, CNe have been used as standard candles to measure Galactic and extragalactic distances. An "apparent" correlation between the decline rate of the nova optical light brightness with their absolute magnitude at maximum light, known as "Maximum Magnitude versus Rate of Decline" (MMRD) relations (see Fig. 1.11), allowed astronomers to derive distances to novae in

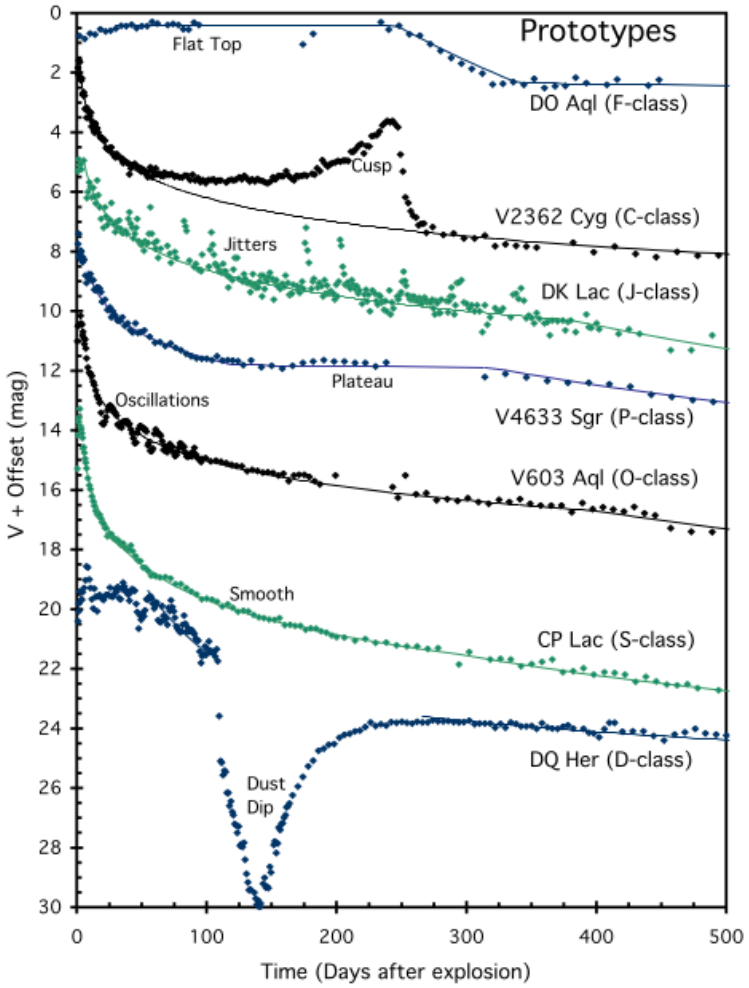

Figure 1.10: Prototypes of the seven light-curve classes from Strope, Schaefer & Henden (2010). The seven binned light-curves show the distinct features of each class.

the Galaxy and other neighbouring galaxies. These relations were first proposed by Zwicky (1936) and then improved by McLaughlin (1939b, 1945).

Half a century later, strong doubts about these relations started to emerge and their accuracy in estimating distances to novae was questioned. Starting with Ferrarese, Côté & Jordán (2003) after a survey of novae in M49, then the discovery of faint, fast novae in M31 by Kasliwal et al. (2011), to finally the Hubble Space Telescope survey for novae in M87 by Shara et al. (2017a) which showed that almost 40% of the novae population in M87 are faint, fast novae which do not follow the MMRD. The initial success of the MMRD and the apparent correlation between the maximum magnitude and rate of decline is attributed to the observational bias of early nova surveys which have missed the faint, fast novae due to the difficulty of detecting them (a combination of being both, faint and fast). That being said, it is worth noting that around 30% of classical novae do follow the MMRDs.

It is well known now that the mass of the WD is not the only parameter that controls a nova eruption and as mentioned above, several other parameters, such as the mass-accretion rate, the WD luminosity and its chemical composition, can play significant roles in controlling the behaviour

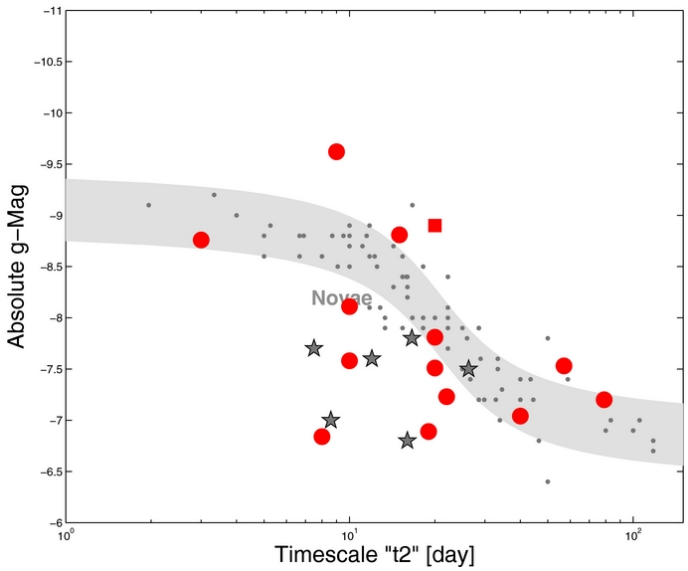

Figure 1.11: The maximum magnitude and the rate of decline (MMRD) empirical relation adopted from Cao et al. (2012): "The gray region denotes the MMRD from Della Valle & Livio (1995), while the small dark gray solid dots represent their nova sample. The six gray stars show the sample of faint, fast novae from Kasliwal et al. (2011). Red circles and a red rectangle are the M31 novae from Cao et al. (2012). The red square denotes the bright recurrent nova M31N 2010-12a."

of a nova eruption (see, e.g., Yaron et al. 2005; Hillman et al. 2014). With new high-cadence and deep-magnitude surveys, more faint, fast novae are expected to be discovered and a new class of ultra-fast novae ($t_2 \leq 1$ d; proposed via theoretical modelling; see Yaron et al. 2005) are predicted to be discovered (Shara et al., 2017a).

The absolute magnitude at t = 15 days

In the same spirit of the MMRD, a correlation between the rate of decline and the absolute magnitude of novae has been proposed by Buscombe & de Vaucouleurs (1955). These authors noted that all novae converge to the same magnitude at day 15 post-eruption. Cohen (1985) estimated this as $M_{V,15} = -5.60 \pm 0.45$ using 11 objects, while Downes & Duerbeck (2000) refined the value to $M_{V,15} = -6.05 \pm 0.44$ using 28 objects. Recently, Shara et al. (2018) showed that only novae with t_2 >10 d converge to a same absolute magnitude after two weeks of maximum and modified values of these relations might provide a distance estimate with $\sim \pm$ 20 percent accuracy.

1.4.4 Spectral analysis

Spectroscopy has always been a vital tool in astronomy to determine the chemical compositions, temperatures, velocities, and several other parameters of celestial objects. In the case of stellar transients, it is an essential technique for identifying the different groups of transients based on the spectral emission/absorption lines and their velocities. Spectral follow-up observations and analysis of CNe are very important for understanding the many processes and features associated with their eruptions, such as the nuclear reactions, the gas ejection mechanisms, the chemical composition of

the ejected matter, and the velocities of the expanding ejecta.

With new high-sensitivity instruments being commissioned, high-resolution spectroscopy is offering theorists and observers the ability to disentangle the origins of the ejected matter to constrain the morphology of the ejecta, particularly when coupled with line modelling.

1.4.4.1 Spectral development: from pre-maximum to nebular phase

Up until the second half of the $20^{\rm th}$ century, all the spectral evolution analyses of novae during eruption have been based on the general description of McLaughlin (1942, 1944) (emphasized later by Payne-Gaposchkin 1957), which divided the post-eruption spectra into four successive systems of absorption lines and five overlapping systems of emission lines, namely: (1) the pre-maximum spectrum, characterized by broad, blue-shifted absorption lines and P Cygni profiles. The line widths range between 100 and 1300 $\mathrm{km\,s^{-1}}$ and their profiles are characteristic of expanding optically thick ejecta. The pre-maximum spectrum is similar to that of B5 to F5 stars; (2) the principal spectrum, which appears at the visual maximum and is characterized by more blue-shifted absorption lines than the previous spectrum with enhancement in the C, N, O lines. The line widths vary between 150 and 1000 $\mathrm{km\,s^{-1}}$ depending on the nova speed-class. The principal spectrum is similar to that of A or F supergiants; (3) the diffuse enhanced spectrum, which appears shortly after visual maximum and is similar to the principal spectrum but the lines are broader; (4) the Orion spectrum, which appears at $\sim 2-4$ mag from maximum and is characterized by highly blue-shifted absorption lines (between -2700 and -1000 $\mathrm{km\,s^{-1}}$) and emission lines of O I, He I, N II, H I. The Orion spectrum is similar to that of luminous OB stars; (5) the nebular spectrum, which is dominated by emission lines and characterized by broad forbidden lines of [O I], [O III], [N II], and possibly [Ne III] and [Ne V], along with the lines from the principal spectrum. Coronal lines of highly ionized Fe lines up to [Fe XIV] might eventually emerge; (6) and the post-nova spectrum which appears after years to decades from the eruption. At this stage, emission from the inner binary can be distinguished without contamination from the ejecta. See, e.g., Warner (2008) for a more detailed review of the spectral development of CNe.

In the last decade of the $20^{\rm th}$ century, more physically based classification schemes have been introduced with the aim of providing more insight into the origin of the emission line spectra of CNe and their evolution.

1.4.4.2 Classification of emission spectra

Williams (1992) introduced a new classification of the post-eruption emission spectra of novae based on a better understanding of the evolution of the expanding ejecta and the changes of its photoionization, which reflects as a variety of ionization levels of the spectral emission lines. Williams' classification scheme divided the post-eruption spectra of CNe into two classes, namely "Fe II" and "He/N". This is based on the stronger of two groups of emission lines, either Fe II lines or He and N lines, apart from the Balmer lines, which are almost always the most intense emission

features in the post-eruption spectra [5] (Williams et al., 1991; Williams, 1992).

The "Fe II"-class novae have a spectrum which shows several low-excitation (collisionally excited) Fe II lines, along with CNO lines in the far red of the spectrum that are excited by recombination and fluorescence scattering. The lines have narrow and rounded profiles and they sometimes show P Cygni absorption features, which are an indication of optically thick expanding ejecta. The emission lines are characterized by low expansion velocities with a Full Width at Half Maximum (FWHM) $<2500\,\mathrm{km\,s^{-1}}$. These spectra point to their formation in a large circumbinary gas envelope originating from the secondary star (Williams, 2012).

The spectrum of "He/N"-class novae exhibits higher ionization, very broad lines of He and N. The emission line profiles are broad (FWHM $> 2500\,\mathrm{km\,s^{-1}}$) and usually characterized by rectangular profiles which are flat-topped, saddle shaped, or jagged. Such rectangular, broad line profiles are an indication of high-expansion-velocity gas consistent with their origin in the WD ejecta (Williams, 2012).

The "He/N" spectra show a relatively quick evolution on a timescale of the order of a few days up to a month. They are characterized by an evolution to a nebular spectrum, unlike the relatively slow evolving "Fe II" novae, which tend to show strong auroral transitions of N and O during the early forbidden phase. The intensity of the "Fe II" spectra decreases slowly on timescales of the order of a few months.

While evolving toward the nebular spectrum, "He/N" novae show one of three scenarios: (1) the emission lines in the spectrum fade to the continuum without producing forbidden features; (2) they develop relatively strong forbidden lines of Ne. These are classified as neon-novae (if they show Ne abundances greater than the solar ones); (3) they develop coronal, high-ionization forbidden lines such as [Fe X] and [Fe VII] (Williams, 1992, 2012).

After the abundant number of nova observations and surveys, it is suggested that around 70% of novae in the Galaxy belong to the "Fe II"-class (Williams, 2012). A close percentage ($\sim$80%) has been found in M31 (Shafter et al., 2011), while the rest are members of the "He/N"-class. A very small fraction of novae have shown a transition from one class to the other or even shown features from both classes simultaneously; these are classified as "hybrid" (Williams, 1992, 2012). In their survey, Shafter et al. (2011) have found that He/N-type novae generally fade faster and they are brighter than Fe II-type novae. This is strong evidence that He/N-type novae usually occur on massive WDs.

It is worth noting that Shore (2014) suggested that the Fe II and He/N-type spectra are strongly dependent on which stages of the eruption the observations were taken. He argued that an Fe II-type spectrum is a spectrum taken during the optically thick stage and an He/N spectrum is a spectrum taken during the optically thin stage, regarding the structure of the ejecta.

[5] Only one nova, V445 Puppis (Ashok & Banerjee, 2003; Kato & Hachisu, 2003), showed strong He lines and absence of Balmer lines in the post-eruption spectra. This nova is the first and only observed He-nova.

1.4.4.3 ONe novae

While solar-like stars evolve into a CO WD, more massive stars can result in WDs with high abundances of elements heavier than C and O, such as Ne and Mg. Novae occurring on ONe WDs exhibit a spectrum dominated by strong forbidden lines of Ne and O towards the nebular phase. These WDs originate from stars with initial mass ($M \sim 8$ to $10\,\mathrm{M}_{\odot}$), therefore they have high masses, possibly approaching the Chandrasekhar mass limit.

While massive CO WDs are candidate progenitors of supernova type Ia eruptions (see Section 1.3.3), ONe WDs were generally excluded. As despite the possibility of igniting Ne and Mg due to electron-captures, the pressure support is lost due to further electron-captures in the burning O remnants. This leads to the collapse of the WD into a neutron star instead of the complete disruption by a thermonuclear eruption (see, e.g., Miyaji et al. 1980; Nomoto 1984; Miyaji & Nomoto 1987; Nomoto & Kondo 1991). However, more recent studies have considered the possibility of ONe WDs being a candidate progenitor of supernova type Ia eruptions (see e.g. Marquardt et al. 2015; Willcox et al. 2016 and references therein).

1.4.4.4 Line modelling of CNe

With the multitude of high-resolution spectroscopic observations of CNe and with the exponential advancement in the field of theoretical modelling and computational astrophysics, line modelling has become a powerful tool to constrain the morphology of the ejecta and the physical processes associated with the eruption.

Starting with an assumption of the general morphology of the ejecta (usually constrained by imaging), it is possible to derive several parameters that characterize the late stages of the nova eruption, such as the inclination of the system, the expansion velocity of the gas, and the geometry of the ejecta. Ribeiro, Munari & Valisa (2013) carried out line modelling of the 2012 eruption of Nova Mon 2012. By modelling the nebular [O III] 4959 and 5007 Å lines they have concluded that the ejecta are characterized by a bipolar structure with an inclination of $\sim 82^{\circ}$ and a maximum expansion velocity of $\sim 2400\,\mathrm{km\,s^{-1}}$. The 2009 eruption of nova KT Eri was also modelled by Ribeiro et al. (2013). In this study they performed morpho-kinematical modelling of the evolution of the Hα line profile and found that a dumbbell structure is the best fitting morphology, characterized by a $\sim 58^{\circ}$ inclination and $2800\,\mathrm{km\,s^{-1}}$ maximum expansion velocity. For more examples of morpho-kinematical modelling studies of CNe see Ribeiro et al. (2009), Ribeiro et al. (2011), and Munari et al. (2011).

1.4.5 Emission of CNe in many wavelengths

One of the most interesting aspects of novae is the fact that their emission has been observed in all the bands of the electromagnetic spectrum, from radio to gamma-rays. With satellites in orbit, X-ray and UV observations became available and the first nova (GQ Mus) was detected in X-rays by EXOSAT in 1984. Nowadays, with space observatories like the Neil Gehrels *Swift* Observatory (hereafter, *Swift*; Gehrels et al. 2004), the *Chandra X-ray Observatory* (hereafter,

Chandra; Weisskopf et al. 2000), and the High Throughput X-ray Spectroscopy Mission and the X-ray Multi-Mirror Mission (hereafter, *XMM-Newton*; Jansen et al. 2001), monitoring the high-energy emission of novae throughout the eruption and obtaining high-resolution X-ray spectroscopy became possible and developed into a useful tool for the study of novae. More recently, novae have been observed to emit in GeV gamma-ray bands using the Fermi-Large Area Telescope (Fermi-LAT; Atwood et al. 2009). This has triggered new theoretical explanations for nova eruptions and emission processes and has led researchers to suggest that shocks in the ejecta can be responsible for part of the emission (see Chomiuk et al. 2014; Li et al. 2017).

Observations of CNe are not limited to optical and high energy bands, but they also extend to the opposite side of the electromagnetic spectrum where extensive radio studies have been carried out, particularly with the aim of better constraining the morphology of the ejecta. Infrared observations are also crucial in tracking the dust formation after the nova eruptions.

It is now widely acknowledged that multiwavelength observations of CNe are essential to provide a complete picture of the eruption and its characteristics, such as: the different physical parameters (e.g., temperatures and velocities), the gas ejection mechanisms, the radiative processes, the nuclear reactions, the shocks in the ejecta/wind, and the dust formation. In this section I will cover briefly nova emission at many wavelengths. I refer the reader to Bode & Evans (2008) for an overview of the nova emission processes in the different wavelength bands.

1.4.5.1 UV emission from novae

Immediately after the eruption, novae show strong emission over the UV range during the so-called "fireball" stage. However, this UV radiation is then blocked due to the recombination of the iron peak elements. This is known as the "Fe-curtain" stage, when all radiation shorter than 1700 Å is blocked due to absorption by many lines from heavy elements of the iron group, such as Fe I/Fe II, Ti I/Ti II, and Cr I/Cr II. The recombination of these iron peak elements is attributed to the decrease in temperature as the expansion progresses.

After a few weeks from the eruption and with the continuing expansion, the optical depth of the ejecta in the UV lines decreases and the flux starts to rise. Furthermore, due to the shrinking of the pseudo-photosphere its temperature increases, which in turn increases the ionization of the ejecta and eventually reduces its opacity further. At this stage, known as the "lifting of the Fe-curtain", numerous spectral features appear in the UV spectrum, such as Mg II, C II, and semi-forbidden lines of N II and N III. Ultimately the entire ejecta become transparent and completely ionized, so the nebular phase starts. Usually it is near the UV maximum when the nebular phase lines emerge. These lines are nebular and coronal forbidden lines from highly ionized species such as Ne VII and Fe VII to Fe XIV. In the UV all novae radiate at a maximum close to the Eddington limit for a $\sim$ 1 $M_{\odot}$ WD. For further detailed reviews of the evolution of the spectrum and continuum in the UV see Gonzales-Riestra (1995); Wamsteker, Gonzalez Riestra & Harris (1998), Cassatella, Altamore & González-Riestra (2002), and Shore (2008).

1.4.5.2 X-ray emission from novae

One of the main predictions of the TNR theory of nova eruptions is a supersoft source (SSS) phase as the radius of the optical photosphere shrinks at constant bolometric luminosity (MacDonald, Fujimoto & Truran, 1985): following the initial eruption, a fraction of the H-burning envelope can remain steadily burning on the surface of the WD. This nuclear-burning region is typically obscured by the optically thick ejected material. With continuous expansion, the ejecta become optically thin to the emission from the WD surface. During this period, the radius of the optical photosphere decreases and the energy distribution shifts towards shorter wavelengths, where the emission peaks in the soft X-ray band. This phase is known as the SSS state (see, e.g., Krautter 2008). The nuclear burning on the surface of the WD is expected to persist at constant bolometric luminosity consuming the remaining H-rich envelope. Eventually, the majority of the H-rich material is burned into heavier elements so the nuclear reactions can no longer be sustained. Therefore the emission in the soft X-rays disappears marking the end of the SSS phase, while the system returns back to quiescence.

The time since eruption for the SSS state to become visible to us is known as the SSS turn-on time ($t_{\rm on}$). Hence, the more massive the ejected material is and the slower it expands, the longer it takes to become optically thin and for the SSS state to become visible; the opposite is equally true. Therefore, the SSS turn-on time is proportional to the mass of the hydrogen ejected envelope and inversely proportional to the ejection velocity. Krautter et al. (1996) relate this timescale to the mass and velocity of the ejected hydrogen envelope by: $t_{\rm on} \propto M_H^{1/2} v_{\rm ej}^{-1}$.

The time since eruption for the SSS state to disappear is known as the SSS turn-off time ($t_{\rm off}$) and is strongly dependent on the WD mass. More precisely, the $t_{\rm off}$ is inversely proportional to the mass of the WD. For more massive WDs ($M_{\rm WD} > 1.0$ M$_\odot$) less accreted material is required to reach the TNR (compared to less massive WDs), hence, the fraction of the remaining H-rich envelope on their surfaces is relatively small and it takes only a short amount of time to completely deplete it, implying a quick end of the SSS state; MacDonald (1996) found $t_{\rm off} \propto {\rm M}_{\rm WD}^{-6.3}$.

These two timescales, $t_{\rm on}$ and $t_{\rm off}$, are very useful indicators of the masses of the WD and of the ejected H-envelope. Therefore, monitoring novae in X-rays from the start of the eruption is essential to constrain the physical properties of the system. Such monitoring has now become possible with space observatories such as *Swift*, *Chandra*, and *XMM-Newton*. For a recent review of X-ray observations of CNe see Osborne (2015).

Apart from the thermal emission from the remnant material on the hot WD during and after the eruption, there are several sources of X-ray emission in CNe such as: (1) emission originating in the circumstellar medium surrounding the nova due to shocks within the nova wind or due to shocks between the nova ejecta and pre-existing material from previous eruptions and/or an evolved companion wind; (2) re-establishment of accretion through accretion disk or magnetically confined accretion in the case of a highly magnetized WD (see Section 1.6); (3) hard X-ray emission possibly resulting from Compton downgrading of γ-rays or accretion shocked material on a highly magnetized WD (see Section 1.6).

With telescopes such as *Chandra* and *XMM-Newton*, high-resolution X-ray spectroscopy became possible. This has revealed X-ray spectra dominated by emission lines from elements such as Mg, Si, Ne, O, N, and C with very little continuum emission.

1.4.5.3 Infrared emission from novae

During the fireball and the expanding pseudo-photosphere phases, optical and IR free-free and line emission from the hot expanding ejecta dominate the flux. After the free-free emission phase, the IR flux temporal development can exhibit a sudden increase due to the formation of dust grains in the circumstellar environment. It is suggested that CO novae are more likely to form dust than ONe novae. After the free-free phase, ONe novae evolve into a prolonged coronal line emission phase where NIR and mid-IR forbidden line radiation from highly ionized coronal atomic states can continue for several years.

Many novae are observed to form dust on a timescale that typically ranges between 30 and 80 days after eruption. While the ejecta expand, the temperature of the gas drops below the condensation temperature of dust, leading to the formation of dust grains in the circumstellar environment. Dust is observed to condense at temperatures ranging between 1000 K and 1200 K. The formation of dust results in a sudden decrease in the optical/UV light accompanied with a simultaneous sudden increase in the IR light. This is attributed to the absorption of optical light by the dust grains which then re-emit at IR wavelengths. It has been demonstrated that the total flux (optical + IR) remains constant before and after the formation of dust. As examples of dust forming novae, see NQ Vul (Ney & Hatfield, 1978), LW Ser (Gehrz et al., 1980), and V705 Cas (Gehrz et al., 1995). See also Gehrz (2008) for an overview of IR studies of CNe.

1.4.5.4 Emission at other wavelengths

Hjellming & Wade (1970) detected the first CNe (HR Del and FH Ser) at radio wavelengths. Since then many novae have been observed in the radio (see, e.g., Bode, Seaquist & Evans 1987; Roy et al. 2012 and references therein). The main radio emission process is thermal bremsstrahlung, which is attributed to the ionized ejected gas. Non-thermal emission (synchrotron emission) has been also observed in a few novae. For an overview of radio emission from novae see, e.g., Seaquist & Bode (2008). Radio observations of CNe are a useful tool to study the structure and morphology of the expanding ejected material and to constrain their temperatures. Tracking the radio evolution of the thermal ejecta, from the optically thick to the optically thin phase, enables us to infer the density profile of the ejecta and estimate the total mass ejected, particularly when coupled with observations in other bands (see, e.g., Krauss et al. 2011; Chomiuk et al. 2012; Nelson et al. 2014; Ribeiro et al. 2014 and references therein). This became possible with the advent of large radio telescopes that can provide high quality data, such as the Westerbork Synthesis Radio Telescope (WSRT; Baars & Hooghoudt 1974), the Very Large Array (VLA; Thompson et al. 1980) telescope, the e-Multi-Element Radio-Linked Interferometer Network (e-MERLIN)[6], Low Frequency Array

[6] http://www.e-merlin.ac.uk/

(LOFAR)[7], and eventually MeerKAT and the Square Kilometer Array (SKA)[8] which are expected to play a key role in future radio studies of CNe.

It was only very recently (2010) that the first nova eruption (V407 Cyg 2010) was detected in gamma-rays with Fermi-LAT. However, it was not a classical nova eruption. V407 Cyg (see Abdo et al. 2010) is a symbiotic system consisting of a pulsating, Mira-type, giant secondary and a WD primary. A couple of years later, Fermi-LAT detected 3 nova eruptions, V959 Mon, V1324 Sco, and V339 Del (Ackermann et al., 2014). These were all CNe systems, as their secondaries are thought to be main-sequence stars. Currently, a handful of novae have been observed by Fermi-LAT to emit in gamma-rays, more precisely at GeV energies (see, e.g., Hays, Cheung & Ciprini 2013; Cheung et al. 2015, 2016; Finzell et al. 2018), but the mechanisms involved in the production of gamma-ray emission are still not well understood.

Such high energy emission in novae can only be due to relativistic particles generated during the eruption and emitting in gamma-rays after being accelerated by strong shocks. These shocks can accelerate particles to relativistic speeds via the diffusive shock acceleration mechanism (see, e.g., Metzger et al. 2016). As described by Finzell et al. (2018) the two main models proposed for gamma-ray emission from relativistic particles are the leptonic and hadronic models. In the leptonic model: accelerated electrons reach relativistic speeds and emit at gamma-ray wavelengths via inverse Compton and/or relativistic bremsstrahlung processes (see, e.g., Metzger et al. 2016 and references therein). In the hadronic model: accelerated ions reach relativistic speeds and collide with dense material producing π^0 mesons, which then decay and emit at gamma-ray wavelengths (Drury, Aharonian & Voelk, 1994).

As the symbiotic system V407 Cyg hosts a Mira variable that is losing mass extensively via stellar wind, it is suggested that the shocks between the nova ejecta and the pre-existing, dense circumstellar material are the generators of particle accelerations and producers of gamma-ray emission. This model successfully reproduced the observational features of V407 Cyg (Abdo et al., 2010).

What is adopted for the symbiotic system V407 Cyg cannot be extrapolated to the gamma-ray emitting CNe. This is due to the presence of a main-sequence companion in typical CNe systems and hence, a low-density circumstellar environment. Therefore, it is suggested that the shocks occur between the nova ejecta internally. To explain these internal shocks, Chomiuk et al. (2014) proposed a model, supported by high-resolution radio imaging, where ejecta with different speeds collide with one another, producing strong shocks that power the emission at high energies. Using hydrodynamics modelling and multiwavelength observations of the gamma-ray emitting nova V5856 Sgr, Li et al. (2017) have argued that the majority of the optical flux is reprocessed emission from these shocks rather than the nuclear burning on the WD. This is supported by a remarkable correlation between the optical and gamma-ray light-curves of V5856 Sgr. Such studies demonstrate the usefulness of multiwavelength observations of novae.

[7] http://www.lofar.org/

[8] https://www.skatelescope.org/

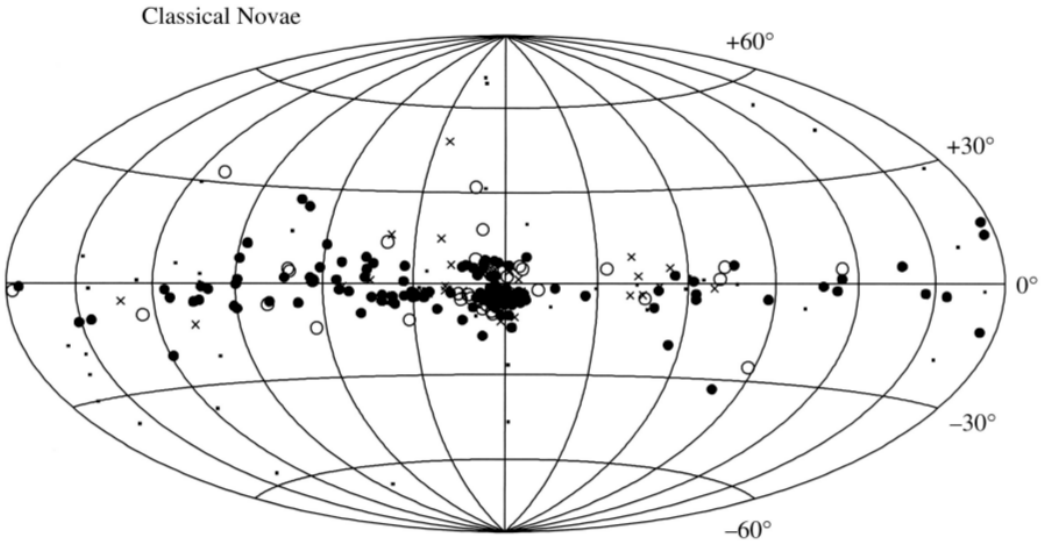

Figure 1.12: The distribution in Galactic coordinates of CNe from Warner (2008). The Galactic centre is located at the centre of the diagram, with increasing Galactic longitude towards the left. Filled circles correspond to fast novae, open circles to slow novae, crosses to uncategorized novae, and small dots to uncertain novae.

1.5 Nova populations

1.5.1 Galactic novae

Novae are one of the most frequent stellar eruptions in the local Universe with an occurrence rate of 35 to 70 per year in galaxies like the Milky Way and M31 (Liller & Mayer, 1987; Ciardullo et al., 1990; Shafter, 2002). The detection rate of novae in the Galaxy is affected by many factors such as: selection effects, sky coverage, interstellar extinction, weather conditions, cadence and sensitivity (non-detection of very fast novae). Nevertheless, over the past 10 years, the detection rate of Galactic novae has improved tremendously with the new all-sky surveys such as the MASTER Global Robotic Net[9], the Optical Gravitational Lensing Experiment (OGLE)[10], the All-Sky Automated Survey for Supernovae (ASAS-SN)[11], and The Zwicky transient facility[12], as well as, the significant contribution of amateur astronomers (e.g. the American Association of Variable Star Observers[13]) in detecting and following-up on transient events such as novae.

Taking into consideration the different observational biases, Darnley et al. (2006) estimated a Galactic bulge rate of $14^{+6}_{-5}\,\mathrm{yr}^{-1}$, a Galactic disk rate of $20^{+14}_{-11}\,\mathrm{yr}^{-1}$, and a global Galactic rate of $34^{+15}_{-12}\,\mathrm{yr}^{-1}$, compared to global nova rate of $65^{+16}_{-15}\,\mathrm{yr}^{-1}$ in M31. It is worth noting that extragalactic nova rates are much easier to measure than those in the Milky Way (for a review of extragalactic novae see Shafter 2008). Fig. 1.12 illustrates the Galactic distribution of novae. More recently,

[9] http://observ.pereplet.ru/
[10] http://ogle.astrouw.edu.pl/
[11] http://www.astronomy.ohio-state.edu/asassn/index.shtml
[12] https://www.ptf.caltech.edu/ztf
[13] https://www.aavso.org/

Mróz et al. (2015) derived a Galactic bulge rate of $13.8 \pm 2.6\,\mathrm{yr}^{-1}$, based on OGLE monitoring of the Galactic bulge, in good agreement with Darnley's (2006) estimates. Duerbeck (1990); Della Valle & Livio (1998) classified novae into two classes: "disk" novae and "bulge" novae, based on their parent stellar population and location within the Galaxy.

Novae are expected to reach an absolute magnitude at maximum in the V-band ($M_{V,\mathrm{max}}$) between -6 and -10. Some novae are extremely luminous, showing maximum magnitude below -10 (see, e.g., Shafter et al. 2009). The eruption of V1500 Cyg in 1975 is one of them, as well as CP Pup, which erupted in 1945 (e.g. Warner 1985). These two novae hold the record as the most luminous Galactic novae ever observed so far, with $M_{V,\mathrm{max}}$ estimated between -10 and -10.7 depending on the distance and extinction adopted (see Stockman, Schmidt & Lamb 1988; Warner 1985; Shafter et al. 2009 and references therein). More luminous novae generally fade faster (very fast novae) and hence, despite their brightness, are easy to miss. With more extremely luminous novae being discovered (see Chapter 3) a new class of "hyper-luminous" novae might emerge.

1.5.2 Novae in the Magellanic Clouds

The Magellanic Clouds are two irregular dwarf galaxies, namely the Large Magellanic Cloud (LMC) and the Small Magellanic Cloud (SMC), visible in the southern celestial hemisphere and are members of the Local Group. At a known distance from us (albeit with a finite spread), the Magellanic Clouds serve as laboratories for studying variable stars, particularly novae. In addition to the known distance, the low foreground reddening make these two galaxies ideal to derive the properties of the eruption and its energetics to a better accuracy than within our Galaxy.

In the Magellanic Clouds, the occurrence of nova eruptions is not as frequent as in the Galaxy or M31. On average, almost 1 nova is detected per year in the LMC and half of that in the SMC. After 10 years of monitoring the Magellanic Clouds with OGLE and taking into consideration the observational biases, Mróz et al. (2016) estimated an absolute nova rate of $2.4 \pm 0.8\,\mathrm{yr}^{-1}$ in the LMC and $0.9 \pm 0.4\,\mathrm{yr}^{-1}$ in the SMC. Although the absolute nova rate per year is much smaller in these two galaxies compared to, e.g., the Milky Way and M31, however, the nova rate per unit mass in the Magellanic Clouds is larger. This is attributed to the star formation histories of the galaxies, when a re-ignition of the star formation occurred 3 – 5 Gyr ago (see, e.g., Yungelson, Livio & Tutukov 1997).

Throughout the observational record and prior to nova SMCN 2016-10a (see Chapter 3), only 22 novae have been detected in the SMC[14]. The last nova to be observed in the SMC was in 2012 (Wyrzykowski, Udalski & Kozlowski, 2012). Among the past 22 novae, only a few have been observed/monitored at different wavelengths. Therefore, with such a low nova rate and lack of pan-chromatic observations, a multiwavelength study of a nova in the SMC is of great interest, particularly for providing more insights into nova properties in a parent galaxy that has a different metallicity, luminosity class, Hubble type, and star formation history from the Galaxy or M31.

[14] http://www.mpe.mpg.de/∼m31novae/opt/smc/SMC_table.html

1.6 Novae occurring in magnetic CVs

While the vast majority of novae have been observed in non-magnetic CVs (i.e., magnetic field of the WD $<10^6$ G), very few novae have been observed or suggested to occur in magnetic cataclysmic variables (mCVs). These systems consist of a highly magnetized WD and they are divided into two main groups: polars (also known as AM Her stars after the prototype AM Herculis system) which have the strongest magnetic fields ($\gtrsim 10^7$ G) and intermediate-polars (IPs; DQ Her stars are a subset of these) which have a weaker magnetic field ($10^6 - 10^7$ G). While both systems have rapidly rotating WDs (compared to WDs in the field), in polars the WD rotational period (spin period) is locked (synchronized or even nearly so) to the binary orbital period. However, for IPs or DQ Her stars the WD is a rapid rotator characterized by a spin period (timescales on the order of a few minutes) that is shorter compared to the orbital period (timescales on the order of a few hours). For a detailed review of mCVs see Warner (1995).

1.6.1 Polars

1.6.1.1 Mass-accretion mechanism in Polars

One question that is always asked when studying stellar objects is: "But have you considered the effect of the magnetic field?". When it comes to CVs, this question has been tackled extensively, particularly for systems that host a strongly magnetized WD (mCVs), where the role of the magnetic field cannot be ignored because it has a strong effect on the accretion mechanism and the mass-transfer from the secondary to the primary. In most systems where the magnetic field of the WD exceeds 10^7 G (polars), the stream of material from the secondary to the primary is fully dominated by the strong magnetic field, which usually prevents the formation of an accretion disk around the WD. Instead, the material flows from the secondary through the $L1$ Lagrangian point following the ballistic accretion stream, to be then captured by the magnetic field. At this point, the magnetic field controls the flow and the material follows the magnetic field lines creating an accretion funnel (accretion columns) that feeds the material onto the WD surface where it is accreted near the magnetic poles, creating strong shocks (see Fig. 1.13). The high temperatures of the gas at the shock formation regions ($\sim 10^8$ K) lead to emissions at high energies, particularly X-ray bands (both soft and hard). It is the, approximately, vertical accretion that leads to this high energy emission.

One of the most important consequences of the strong magnetic field that characterizes the WD in polars is that it synchronizes the spin period of the WD with the orbital period of the system through magnetic torques. This is a defining feature of polars and it means that the same side of the WD always faces the secondary. The strong magnetic fields also produce beamed optical and IR cyclotron emission, which is strongly polarized (Potter, Hakala & Cropper, 1998; Buckley et al., 2000; Potter, 2000; Potter et al., 2002). The spectral lines of polars are complex, showing multiple emission components attributed to emission from different parts of the system, such as the irradiated side of the secondary, the accretion stream, and the accretion columns. A strong, high

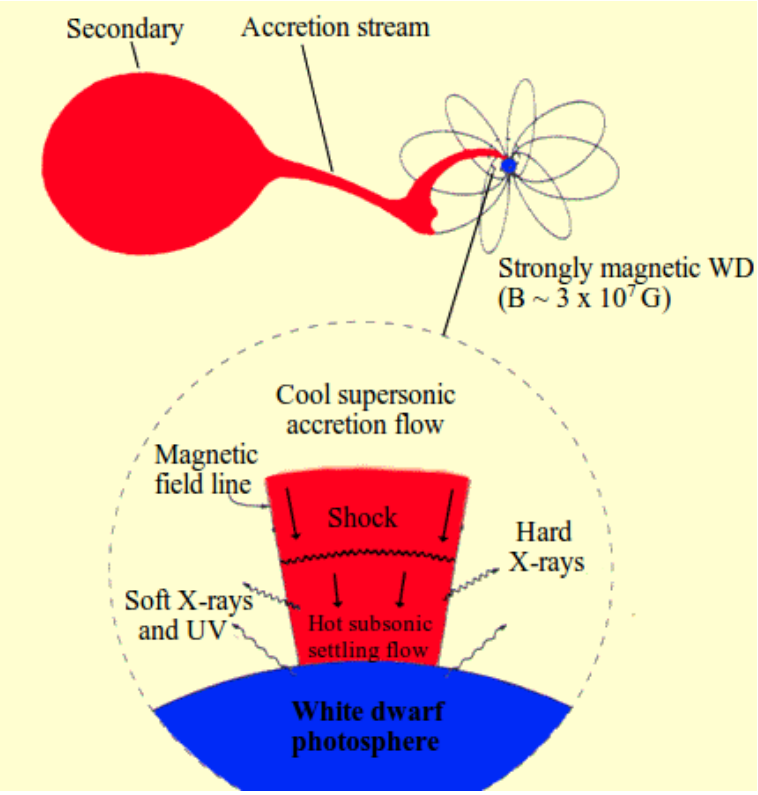

Figure 1.13: A schematic illustration of a polar system. Matter flows from the companion star through the accretion stream where it is captured by the magnetic field of the WD and funneled onto its magnetic poles following the magnetic lines. Credits: NASA - http://heasarc.gsfc.nasa.gov/docs/objects/cvs/cvstext.html.

excitation He II 4686 Å line is usually a characteristic of the spectrum. Most of the He II 4686 Å emission is attributed to the irradiated accretion stream (Potter et al., 2004).

1.6.1.2 Novae occurring in polars and their properties

V1500 Cyg is the only known nova to erupt in a polar system. The eruption which occurred in 1975 was one of the most intrinsically luminous eruptions on record, along with CP Pup (Warner, 1985) and nova SMCN 2016-10a (see Chapter 3). It was also a very fast nova, with $t_2 < 2$ d. Many studies have been done on this object, but the first to suggest that it is a polar system were Kaluzny & Semeniuk (1987), which has since been confirmed after detecting substantial optical polarization from the system, modulated on a period slightly different from its orbital cycle. This asynchronism is believed to be due to the eruption (see, e.g., Kaluzny & Chlebowski 1988; Schmidt & Stockman 1991).

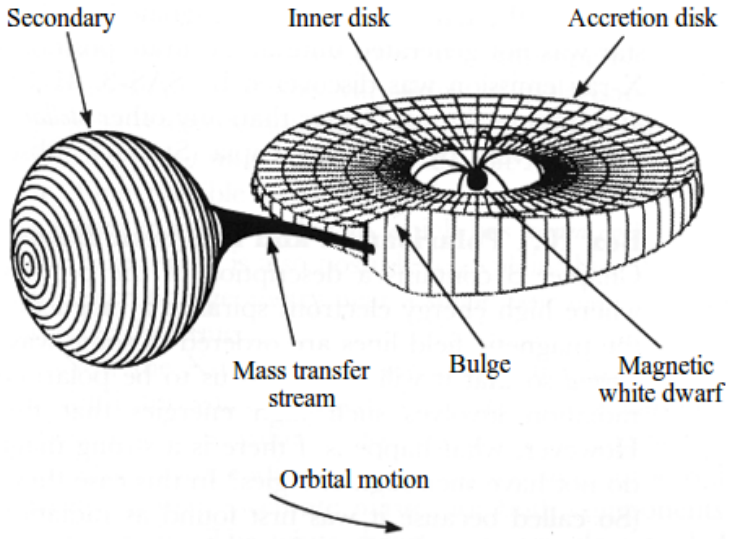

Figure 1.14: A schematic diagram of an intermediate-polar system. Matter flows from the companion star into an accretion disk which is truncated by the magnetic field of the WD. The matter is then funneled onto one of the magnetic poles of the WD through accretion curtain. Credits: NASA - http://heasarc.gsfc.nasa.gov/docs/objects/cvs/cvstext.html

1.6.2 Intermediate-polars

1.6.2.1 Mass-accretion mechanism in intermediate-polars

In IPs, the magnetic field is typically not as strong as it is in polars. This can allow an accretion disk to form around the WD as in non-magnetic CVs. However, close to the WD, where the magnetic field is stronger, the accretion disk is truncated near to the Alfvén radius[15] and the material is accreted along the magnetic field lines through the so-called accretion curtain (Patterson, 1994a). The material passes through the curtain and then accretes onto the WD near its magnetic poles. Bright hard X-ray emission is a common signature for these systems, which is caused by shocks from the accretion on the WD surface (see Fig. 1.14). It is worth noting that at least one IP (V2400 Oph) is suggested to be diskless (Buckley et al., 1995; Buckley, 1997; Hellier & Beardmore, 2002). This happens when the gas stream becomes attached to the field lines much further out. In this case, the gas follows the magnetic lines to near one of the magnetic poles and alternates between them over the beat period between the orbital and spin periods (where $1/P_{\rm beat} = 1/P_{\rm spin} - 1/P_{\rm orb}$).

The observational features that characterize an IP are also a strong He II 4686 Å line, possibly circular polarization, and most significantly, a spin period that is shorter than the orbital period of the system. The physical cause of optical-spin-period oscillations is usually attributed to changing the viewing aspect of the accretion curtain as it converges near the WD.

[15]The Alfvén radius is the radius where the magnetic and ram pressures are equal. It is at this radius where the disk is truncated and the material is accreted along the magnetic field lines.

1.6.2.2 Novae occurring in IPs

Several novae have been suggested to occur in IPs, including V533 Her, GK Per, DD Cir, V1425 Aql, V4743 Sgr, Nova Sco 1437 (see, e.g., Warner & Woudt 2002; Bianchini et al. 2003; Woudt & Warner 2003, 2004; Zemko et al. 2016; Potter & Buckley 2018 and references therein). For these systems, the magnetic nature of the WD has only been revealed (indirectly) from observations made after the eruption. When the system returns back to quiescence, it is more straightforward to detect the IP characteristic features, such as the spin and orbital periods, the hard X-ray emission, the circular polarization, and the strong He II 4686 Å line, which can all be hidden by the eruption itself during the nova event.

1.7 Structure of this thesis

In this Chapter I have presented a general review of novae covering: the theory of their eruptions, their observational properties in optical and other bands, their classification schemes, their rates in the Galaxy and the Magellanic Clouds, the importance of studying novae at many wavelengths, and their occurrence in magnetic CVs. The rest of the thesis is structured as follows: in Chapter 2, I present an optical and infrared study of the unusual nova V5852 Sgr, which is possibly a member of the Sagittarius dwarf galaxy. In Chapter 3, I present a multiwavelength study of the very fast nova SMCN 2016-10a, which is one of the most intrinsically luminous novae on record. Chapter 4 presents a multiwavelength study of nova V407 Lup which has possibly occurred in an IP system (each of these three chapters contains all the information to be read independently). Finally, a general summary and future prospects are given in Chapter 5.

Chapter 2

V5852 Sgr: an unusual nova possibly associated with the Sagittarius stream

Abstract

We report spectroscopic and photometric follow-up of the peculiar nova V5852 Sgr (discovered as OGLE-2015-NOVA-01), which exhibits a combination of features from different nova classes. The photometry shows a flat-topped light curve with quasi-periodic oscillations, then a smooth decline followed by two fainter recoveries in brightness. Spectroscopy with the Southern African Large Telescope shows first a classical nova with an Fe II or Fe II b spectral type. In the later spectrum, broad emissions from helium, nitrogen and oxygen are prominent and the iron has faded which could be an indication to the start of the nebular phase. The line widths suggest ejection velocities around $1000\,\mathrm{km\,s^{-1}}$. The nova is in the direction of the Galactic bulge and is heavily reddened by an uncertain amount. The V magnitude 16 days after maximum enables a distance to be estimated and this suggests that the nova may be in the extreme trailing stream of the Sagittarius dwarf spheroidal galaxy. If so it is the first nova to be detected from that, or from any dwarf spheroidal galaxy. Given the uncertainty of the method and the unusual light curve we cannot rule out the possibility that it is in the bulge or even the Galactic disk behind the bulge.

Keywords: stars: binaries: close – novae, cataclysmic variables – white dwarfs.

2.1 Introduction

Classical novae (CNe) form a subclass of the cataclysmic variable stars. They are "close binary systems consisting of a white dwarf (WD) and a Roche-lobe filling companion" (Bode & Evans, 2008). Matter accreted by the WD from the secondary accumulates and is compressed on the WD surface. When the critical temperature and density are reached a thermonuclear runaway (TNR)

is triggered, causing a nova eruption (Prialnik, 1986). Typical ejecta velocities and masses are $\sim$ 1000 $\mathrm{km\,s^{-1}}$ and between 10^{-5} and $10^{-4}\,\mathrm{M_{\odot}}$, respectively (Payne-Gaposchkin, 1957; Gallagher & Starrfield, 1978).

Nova light curves are classified on the basis of their decline rate in various ways, but often in terms of time in days (t_2) for the decline by 2 mag from maximum light (Payne-Gaposchkin, 1964). More recently, Strope, Schaefer & Henden (2010) published an Atlas of light curves of 93 novae based on visual estimates collected by AAVSO and they proposed a classification scheme based on the light curve shape and rate of decline. They defined seven classes: S (smooth), P (plateau), D (dust dip), C (cusped secondary maximum), O (oscillations), F (flat-topped), and J (jitters). It is important to recognize that this classification is based on visual light curves and given that the colours of novae typically change during their evolution we should not expect other bands to track the visual curves with any degree of precision. Nevertheless, this nomenclature has been used by others for I-band light curves of novae (e.g. Mróz et al. (2015) where they classified OGLE I-band light curves of 39 novae in the Galactic bulge using the same scheme) and we therefore refer to it here.

In addition to the photometric classification various approaches have been taken to classify the spectral evolution of novae (McLaughlin, 1944; Payne-Gaposchkin, 1957; Williams, 2012). Post-eruption spectra are divided into two spectroscopic classes: the Fe II type novae which show numerous narrow Fe II emission lines with P Cygni profiles and He/N type novae which show broad He, N and H emission lines. A third class was also introduced, known as hybrid novae. These show a transition between the two types (Fe II and He/N) or simultaneous emission lines of both types (Williams, 1992). From a study of 22 Galactic novae, Della Valle & Livio (1998) established that novae showing He/N spectroscopic features are faster, and have brighter maxima, compared to those from the Fe II class. The precise mechanism responsible for the formation of the different spectral features after the explosion is poorly understood, but it is thought that the WD mass and the circumstellar environment play a crucial role in this matter (Shafter et al., 2011).

In this chapter, we report the discovery of an unusual nova, V5852 Sgr, that may be a member of the trailing stream of the Sagittarius Dwarf Spheroidal Galaxy (henceforth the Sagittarius stream). At about 20 kpc the Sagittarius Dwarf is our nearest neighbour and is being tidally disrupted by its interaction with the Milky Way. It was discovered by Ibata, Gilmore & Irwin (1995) via the distinctive velocities of its stars. It has since been shown to be stretched into a stream that loops around the Milky Way, with an estimated total mass of about $5 \times 10^8\ M_{\odot}$ (Majewski et al., 2003), making it the largest dwarf spheroidal galaxy in the Local Group.

The nova shows combined features from different novae spectro-photometric classes and presents an interesting case to study. In Section 2.2 we present the discovery and the photometric (optical and IR) follow-up of the object. Southern African Large Telescope (SALT) spectroscopic optical data (between 4500 Å and 7800 Å) are detailed in Section 2.3. We present in Section 2.4. a discussion aiming to classify the nova, and establish its location and our conclusions.

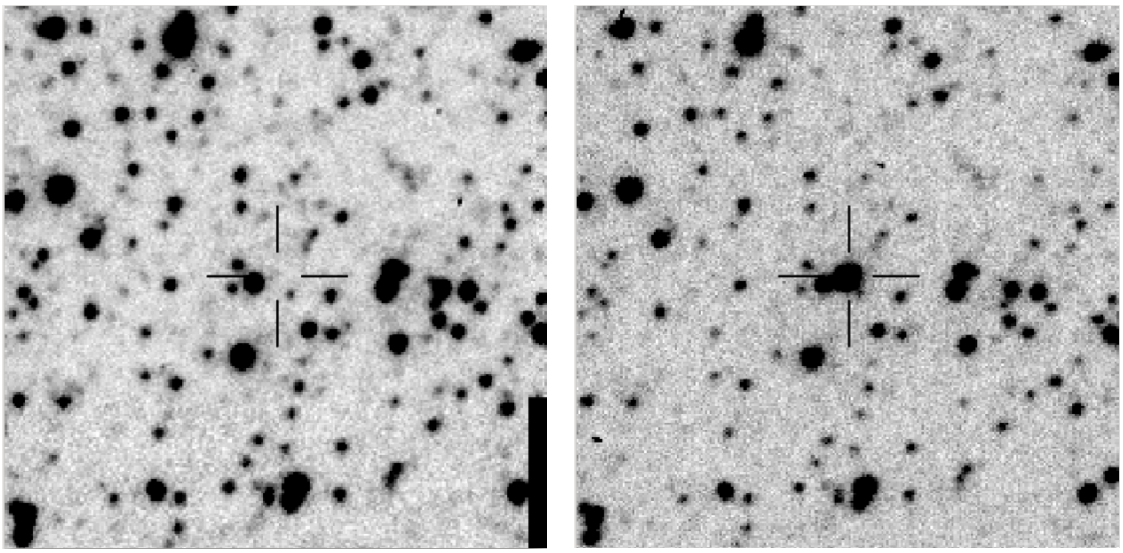

(a) Finding chart before the eruption. (b) Finding chart during the eruption (March 5, 2015).

Figure 2.1: Finding charts for V5852 Sgr before and during the eruption in the I band. (North is up and East is to the left, image size $1' \times 1'$).

2.2 Discovery and Photometric data

2.2.1 Discovery

V5852 Sgr was announced as a classical nova candidate and given the name OGLE-2015-NOVA-01, on 2015 March 5 by Mróz & Udalski (2015) based on observations from the Optical Gravitational Lensing Experiment (OGLE) survey. The transient was detected by the Early Warning System (EWS), which has been designed for the detection of microlensing events. Fig. 2.1 presents charts of the nova before and during the eruption. From the time of the discovery, however, it was clear that the light curve (Fig. 2.2) does not resemble that of a microlensing event. The star is located in the direction of the Galactic bulge at equatorial coordinates of $(\alpha, \delta)_{\rm J2000.0}$ = ($17^{\rm h}$:$48^{\rm m}$:$12\overset{\rm s}{.}78$, –32°:35′:13.″44) and Galactic coordinates of (l, b) = (357.°16, –2.°36).

2.2.2 Observation and data reduction

The source has been observed by the OGLE variability survey since 2010 with a typical cadence of 1–2 d. This survey uses the 1.3-m Warsaw Telescope located at Las Campanas Observatory, Chile, operated by the Carnegie Institution for Science. Observations were taken through V- and I-band filters, closely resembling those of the standard Johnson-Cousins system. The photometry was carried out with the Difference Image Analysis (DIA) algorithm (Alard & Lupton, 1998; Wonźiak, 2000). Details of reductions and calibrations can be found in Udalski, Szymański & Szymański (2015). The light curve of the 2015 eruption data is shown in Fig. 2.2. In Tables 2.1 and 2.2 we present OGLE V- and I-band photometry, respectively.

Multicolour gri photometry was obtained using the LCOGT 1-m robotic telescope at the South African Astronomical Observatory (SAAO), Sutherland, South Africa on 2015 March 19 and April

22-23. The data are presented in Table 2.3 and included in Fig. 2.2. The photometry was carried out with DoPHOT (Schechter, Mateo & Saha, 1993) and calibrated with the aid of the AAVSO Photometric All-Sky Survey (APASS[1]) (Henden et al., 2009).

The source was observed by the *Swift* satellite (Gehrels et al., 2004) on 2015 April 11, 15, and 20 with a total exposure time of 2.61 ks. No X-ray source was detected with the XRT (X-Ray Telescope; Burrows et al. 2005) at the position of the nova, which gives 3σ upper limits of 0.022, 0.024, and 0.008 cts/s, respectively, in the 0.3-10 keV energy range. Upper limits were estimated with the SOSTA tool, which is a part of the XIMAGE package (version 4.5.1).

We also analyzed images taken with the UVOT (Ultraviolet/Optical Telescope; Roming et al. 2005) on-board *Swift* and estimated the brightness of the source with the UVOTSOURCE tool, which performs aperture photometry. We detected a faint counterpart in the U-band (21.03 ± 0.58 mag), while the source was invisible in the $UVW1$ filter (which peaks at 260 nm) images. The UVOT observations are summarized in Table 2.3.

We obtained infrared photometry with the SIRIUS camera (Nagayama et al., 2003) on the 1.4-m Japanese-South African InfraRed Survey Facility (IRSF) at SAAO Sutherland. This has a $7' \times 7'$ field of view, $0''.45$ pixels and provides simultaneous JHK_S photometry. Exposures of 125 s were achieved by combining 25 dithered 5 s exposures. Photometry on the 2MASS system was performed relative to the nearby stars 2MASS17481467–3235040 and 2MASS17481308–3235223. The rms of the instrumental magnitudes of these reference stars was only $\sigma_J = 0.010,\ \sigma_H = 0.008,\ \sigma_K = 0.007$ mag, demonstrating that they do not vary.

As can be seen in Fig. 2.1, the field is crowded, in particular the nova is only $2''.8$ from 2MASS17481299–3235142 ($J = 12.9\ H = 11.4\ K_S = 10.8$). So to do aperture photometry the stars in the immediate vicinity of the nova, and of the two reference stars, were subtracted using DAOPHOT in the Image Reduction and Analysis Facility (IRAF) software (Tody, 1986) before the photometry was performed. The 2MASS magnitudes of the reference stars were then used to derive the zero points and an average taken. Photometry was done using apertures with radii of 5, 7 and 10 pixels. For measurements of $J, H < 14$ and $K_S < 13.5$ the choice of aperture makes no significant difference to the result. For much fainter magnitudes the results from the 5 and 10 pixel apertures can differ by up to 0.2 mag. The measurements listed in Table 2.4 were made with a 7 pixel aperture.

2.2.3 Light curve

The eruption started between 2015 February 25 (HJD 2457078.88) and 27 (HJD2457080.90), when the source brightened by 2 mag from $I = 19.7$ to $I = 17.6$; by March 3 (HJD 2457084.8) it had reached $I = 14.4$. This was followed by a short pre-maximum halt and then a nearly linear rise by 1.5 mag in 14 days. The source peaked on 2015 April 3 (HJD=2457115.87) at $I = 12.7$ (although the maximum could have taken place ten days earlier, when no observations were collected because of heavy storms over Las Campanas). Between 2015 March 20 and May 1, the source showed

[1] https://www.aavso.org/apass

a long, flat peak, similar to F class light curves, with additional semi-regular oscillations on a time-scale of 12 d and amplitude of 0.8 mag, reminiscent of the early stages of D class (e.g. V992 Sco) or J class light curves (Strope, Schaefer & Henden, 2010). At this phase the light curve also resembled the early stages of the eruption of the red nova V838 Mon (Munari et al. 2002 fig. 5) and the 2011 eruption of the recurrent nova T Pyx (Surina et al. 2014 fig. 1).

Infrared JHK_S (Table 2.4) measurements were only initiated when it was clear that the I light curve development was unusual and, as can be seen in Fig. 2.2, the JHK_S-curves, more or less follow the fall of the I curve. Fig. 2.3 shows the development of the infrared colours. The reddening vector indicates that $(J-H)_0$ is close to zero or slightly negative and that it is remarkably constant, while $(H-K_S)_0$ gets slightly redder with time. A negative value for $(J-H)_0$ has been seen in other novae (Whitelock et al., 1984) and is attributed to very strong emission lines in the J band (the SAAO J filter used by Whitelock et al. is more sensitive to the HeI 1.083 μm line than is the IRSF J filter and therefore their $J-H$ is very negative when this line is strong). Given that novae spectra are dominated by emission lines it is not possible to properly transform photometry taken through different filters, so detailed comparisons of nova colours are difficult.

It is obvious that the overall development of the light curve (Fig. 2.2) is quite unlike any of the standard nova classes as can be seen by comparing it with the OGLE light curves of bulge novae (Mróz et al., 2015). The decline at around HJD2457150 and the recovery around HJD2457230 could possibly have been the consequence of dust forming and gradually dispersing. However, Fig. 2.3 shows no indication of the very red colours associated with significant quantities of dust. The colours of dust-forming novae are illustrated in fig. 4 of Whitelock et al. (1984) for several other novae.

We measured decline times in the I band over 2 and 3 mags of $t_2 = 34 \pm 2$ days and $t_3 = 45 \pm 2$ days, respectively. So this nova was moderately fast to average according to the criteria in Warner (2008) or Bode & Evans (2008), although given the unusual characteristics of the light curve and the fact that we only have decay rates at I, and not V, it is not entirely clear how this should be interpreted.

In the pre-eruption images we detected a possible very faint progenitor $I_{\rm pre} = 20.77$, which is invisible in the V-frames (as expected given the reddening discussed in section 2.2.4). We did not find any significant periodic variability before the eruption.

In summary, our photometric data show a moderately fast eruption, followed by a flat-topped light curve with oscillations and a smooth decline followed by two faint recoveries in the brightness (between HJD 2457220 and 2457270 and between 2457280 and 2457300). A comparison with the light curve classes presented by Strope, Schaefer & Henden (2010) shows that the flat-topped light curve of V5852 Sgr is similar to the F class light curves. In addition, the quasi-periodic oscillations during the peak in the intensity are similar to both J class and O class light curves. This combination of features indicate the unusual light curve development of V5852 Sgr. Note that a flat-topped light curve with oscillations is also seen for the 2011 light curve of the recurrent nova T Pyx. A detailed spectro-photometric study by Surina et al. (2014) of the T Pyx 2011 eruption shows a pre-maximum halt followed by a slow flat-topped eruption with quasi-periodic oscillations

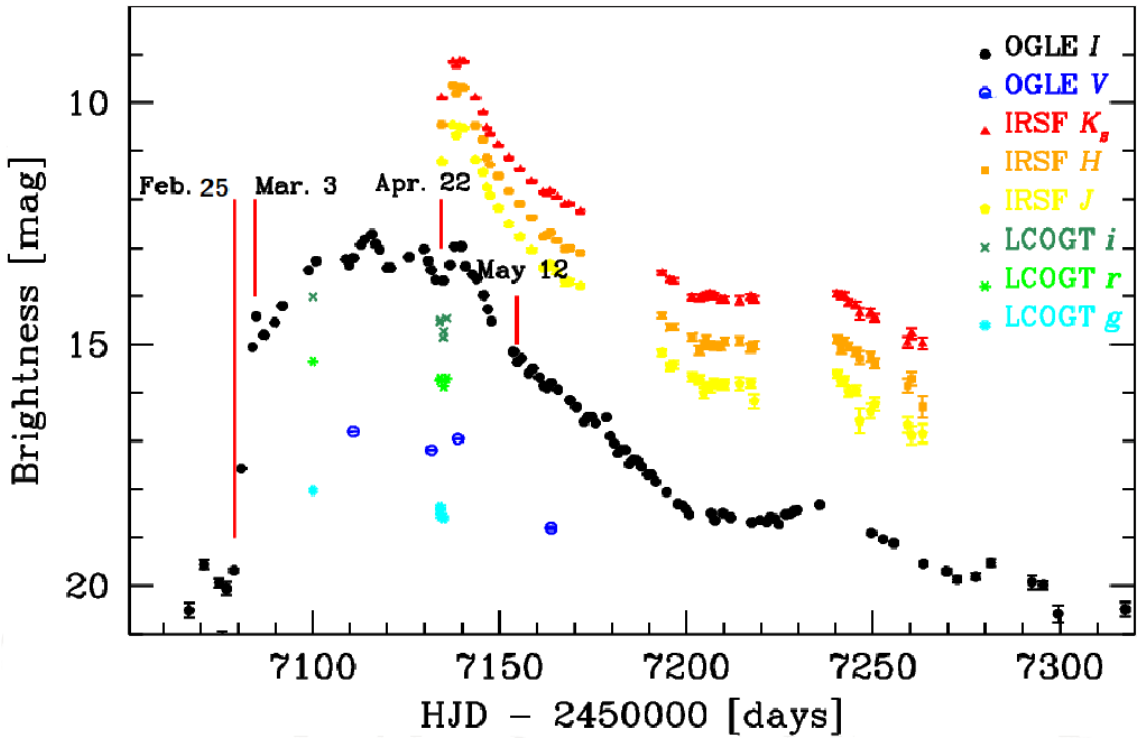

Figure 2.2: The photometric data from OGLE, LCOGT, and IRSF as a function of Heliocentric Julian Date (HJD), colour coded as indicated. The first two red bars indicate the dates when the eruption starts. The SALT spectra were obtained on April 22 and May 12.

HJD	V	ΔV
-2457000	(mag)	
110.84656	16.799	0.005
131.79511	17.184	0.006
138.84101	16.924	0.005
163.78319	18.945	0.017

Table 2.1: OGLE V-band photometry. The time-series photometry is available from the OGLE Internet Archive[2].

of a period ~ 2 days.

The remarkable features in the light curve justified our request for SALT spectra to establish if the spectral development was also unusual.

2.2.4 Reddening and Distance

Given its position towards the bulge, we expect the nova to be heavily reddened; determining exact values poses a challenge. At $l = -2^{\circ}.8$ and $b = -2^{\circ}.4$ it is very close, but just outside the region around the Galactic centre ($|l| < 3^{\circ}$, $|b| < 1^{\circ}$) for which Nishiyama et al. (2009) determined an interstellar extinction law that is significantly different from that generally assumed (Cardelli, Clayton & Mathis, 1989). Recently, Nataf et al. (2015) have shown that large variations in the

[2] ftp://ftp.astrouw.edu.pl/ogle/ogle4/NOVAE/BLG

HJD -2457000	I (mag)	ΔI
66.86475	20.507	0.153
70.89930	19.559	0.092
74.85976	19.941	0.089
75.83561	21.281	0.335
76.90152	20.055	0.135
78.87609	19.678	0.043
80.89831	17.569	0.010
83.80943	15.059	0.002

Table 2.2: A sample of OGLE I photometry. The rest of the data are available from the OGLE Internet Archive[3].

HJD -2457000	Filter	Exp. time (s)	Magnitude
LCOGT			
100.60483	g	450	18.026 +/- 0.011
100.61375	r	180	15.366 +/- 0.006
100.61103	i	180	13.982 +/- 0.004
134.54530	g	200	18.552 +/- 0.054
134.54815	i	100	14.545 +/- 0.017
134.55012	r	100	15.751 +/- 0.022
134.57024	g	200	18.405 +/- 0.033
134.60703	g	200	18.468 +/- 0.043
134.60988	i	100	14.513 +/- 0.029
134.61164	r	100	15.749 +/- 0.028
134.64962	g	200	18.365 +/- 0.065
134.65258	i	100	14.499 +/- 0.028
134.65433	r	100	15.712 +/- 0.033
135.49551	i	100	14.858 +/- 0.035
135.52847	g	200	18.598 +/- 0.040
135.53115	i	100	14.739 +/- 0.049
135.53302	r	100	15.870 +/- 0.024
136.41910	i	100	14.462 +/- 0.053
136.42073	r	100	15.712 +/- 0.056
Swift			
124.36	$UVW1$	720	> 20.07[a]
127.52	$UVW1$	479	> 19.85[a]
133.41	U	1345	21.03 +/- 0.58

[a] 3σ limit

Table 2.3: LCOGT and *Swift* photometry of V5852 Sgr.

Table 2.4: Near-infrared photometry from IRSF at JHK_S bands.

HJD -2457000	J	ΔJ	H	ΔH	K_S	ΔK_S
			(mag)			
134.52332	11.21	0.02	10.45	0.01	9.91	0.01
137.49937	10.45	0.02	9.64	0.01	9.15	0.01
138.46439	10.67	0.03	9.81	0.02	9.25	0.01
139.55240	10.49	0.02	9.67	0.01	9.14	0.01
140.40741	10.52	0.02	9.69	0.01	9.15	0.01
143.61646	11.19	0.02	10.47	0.01	9.91	0.01
145.55649	11.43	0.03	10.76	0.01	10.20	0.01
146.50150	11.75	0.03	11.14	0.02	10.52	0.01
147.43051	11.91	0.03	11.28	0.02	10.65	0.01
149.66654	12.18	0.03	11.51	0.02	10.87	0.01
152.49157	12.51	0.03	11.82	0.02	11.15	0.01
155.45161	12.77	0.03	12.10	0.02	11.38	0.02
158.57664	13.05	0.04	12.37	0.02	11.62	0.02
161.62666	13.41	0.04	12.77	0.03	11.85	0.02
162.64767	13.40	0.04	12.74	0.03	11.88	0.02
163.60868	13.34	0.04	12.68	0.02	11.82	0.02
165.41369	13.50	0.04	12.85	0.03	11.95	0.02
167.57171	13.72	0.06	13.03	0.04	12.12	0.03
168.65172	13.70	0.04	13.01	0.03	12.10	0.02
171.65273	13.79	0.05	13.11	0.03	12.25	0.02
193.51274	15.17	0.07	14.40	0.05	13.52	0.04
195.61862	15.46	0.08	14.64	0.07	13.65	0.05
196.61061	15.43	0.08	14.64	0.07	13.69	0.05
201.53558	15.68	0.09	14.86	0.08	14.03	0.06
203.59956	15.74	0.09	15.12	0.09	14.04	0.06
204.60055	16.00	0.11	15.01	0.09	14.02	0.06
205.31855	15.89	0.10	14.89	0.07	13.99	0.06
206.37154	15.90	0.10	15.01	0.08	13.96	0.06
207.34053	15.81	0.09	15.03	0.08	14.01	0.06
209.26551	15.83	0.09	15.04	0.09	14.07	0.06
210.41849	15.82	0.10	14.94	0.08	14.07	0.06
214.23445	15.81	0.13	14.93	0.09	14.09	0.09
217.27441	15.81	0.10	15.07	0.08	14.01	0.06
218.19040	16.17	0.14	15.02	0.08	14.06	0.06
240.39200	15.62	0.08	14.89	0.08	13.96	0.06
241.47998	15.78	0.10	15.09	0.09	13.99	0.06
242.31996	15.75	0.09	14.94	0.08	13.99	0.06
243.40194	15.98	0.10	15.05	0.08	14.13	0.06
245.38289	15.95	0.10	15.16	0.08	14.18	0.07
246.43287	16.58	0.27	15.28	0.14	14.37	0.13
249.44780	16.38	0.15	15.26	0.10	14.34	0.08
250.45178	16.23	0.13	15.39	0.10	14.45	0.08
259.29456	16.66	0.16	15.86	0.15	14.96	0.12
260.31153	16.88	0.19	15.71	0.14	14.78	0.10
263.28446	16.85	0.19	16.29	0.22	14.97	0.12

extinction ratios are common around the Galactic centre.

The VISTA Variables in the Via Lactea (VVV) extinction calculator (Saito et al., 2012), which is based on Gonzalez et al. (2012), indicates $E(J-K_S) = 1.03$ corresponding to $A_K = 0.71 \pm 0.12$ and $A_V = 6.44$ mag on the Cardelli, Clayton & Mathis (1989) law (using R_V = 3.1) or $A_K = 0.54 \pm 0.12$ and $A_V = 8.88$ mag on the Nishiyama law. As an alternative approach we measured the centroid of the red giant clump $(V-I)_{\rm clump} = 3.99 \pm 0.03$ on the colour-magnitude diagram, using the OGLE data for stars in an area of $2' \times 2'$ around the nova. The intrinsic colour of the Galactic bulge red clump stars is 1.06 (e.g., Nataf et al. 2013), so the colour excess is $E(V-I) = 2.93 \pm 0.03$ in this direction. Using the extinction relations for the Galactic bulge from Nataf et al. (2013), we find $A_I = 3.60 \pm 0.17$ mag and $A_V = 6.53 \pm 0.18$ mag. Although this method estimates the extinction foreground of the bulge red clump stars, we can reasonably assume that most of the extinction is in the foreground disc and therefore included. This method should provide the best possible measure for the line-of-site to the nova and therefore in the following analysis we assume: $A_V = 6.53$ and $A_I = 3.60$. It is important to recognize that many of the conclusions of this chapter are critically dependent on this assumption.

The distances to novae are often estimated from their decline rates, noting that fast novae are more luminous than slow ones. However, the individual measurements have considerable uncertainties and the validity of the so-called "maximum magnitude versus rate of decline" (MMRD) relations was recently questioned by Kasliwal et al. (2011), Cao et al. (2012), and Shara et al. (2016). Furthermore, these relations have not been defined in the I-band and no empirical relation between the rate of decline in I and V has been derived (Munari private communication).

A relationship sometimes used to derive distances is based on the understanding that all novae have a similar M_V mag 15 days after maximum: $M_V = -6 \pm 0.44$ (Downes & Duerbeck, 2000). Coincidentally V5852 Sgr was measured at V about 16 days after maximum (Table 2.1) with $V = 17.18$ (making the reasonable assumption that maximum at V and I are close together in time), corresponding to $V_0 = 10.65$ and a distance ($(m-M)_0 = 16.65$ mag) in the range 17 to 27 kpc. Because of the unusual light curve (section 2.2.3) and the extension in the peak of brightness with quasi-periodic oscillations, this distance must be regarded as very uncertain.

There are several possible explanations of the large distance estimate. Most obviously it suggests the nova is behind the bulge, rather than in it. At about 22 kpc it would be about the right distance to be associated with the Sagittarius stream (Ibata, Gilmore & Irwin, 1995). Although it is a few degrees away from where the Sagittarius stream crosses the Galactic plane, it is within the area where the OGLE group found RR Lyr variables that are members of the Sagittarius stream (see fig. 3 in Soszyński et al. (2014)). The nova is not coincident with the main density of OGLE variables (with distances from Pietrukowicz et al. 2015), but it is plausibly within the volume occupied by the trailing stream from the Sagittarius dwarf which can be seen from Torrealba et al. (2015) when their fig. 16 is interpolated through the Galactic plane. Furthermore, the radial velocity (see Section 2.3.3) although uncertain is consistent with membership of the Sagittarius stream.

We need to consider other possible explanations as alternatives to membership of the Sagittarius stream. First it could be in the Galactic disk behind the bulge; at 22 kpc it is less than 1 kpc above

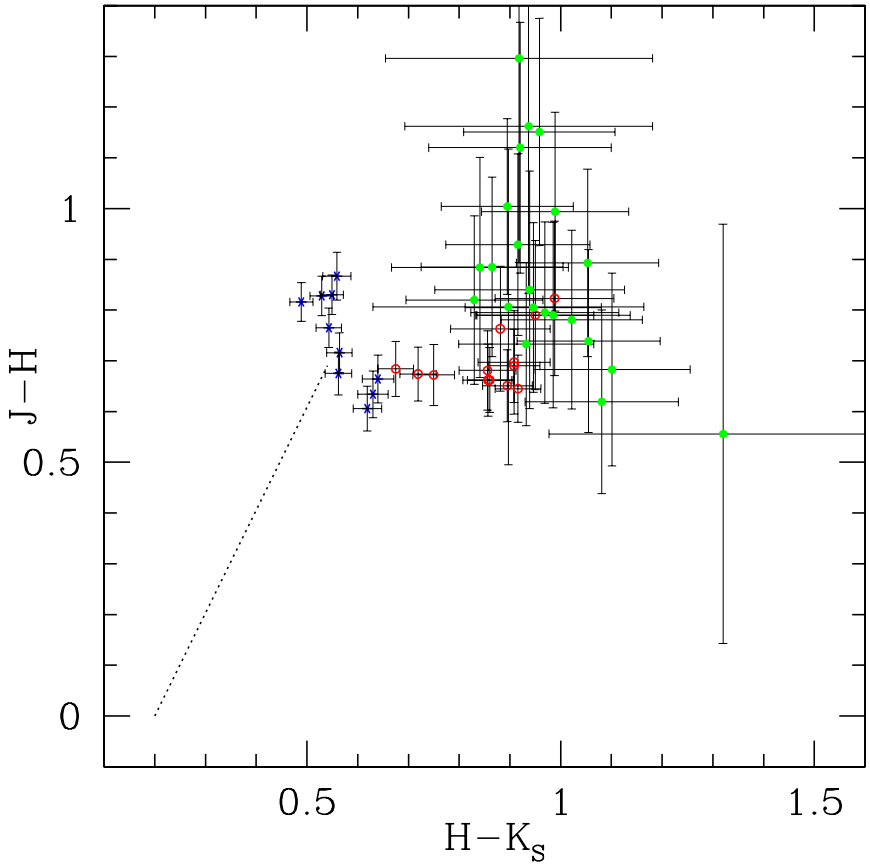

Figure 2.3: Evolution of the JHK_S colours; asterisks, open circles and closed circles represent observations before HJD 2457150, between HJD 2457150 and 2457200 and after HJD 2457200, respectively. The dotted vector shows the effect of correcting for reddening assuming $E(J-H) = 0.69$ and $E(H-K_S) = 0.34$ (see section 2.2.4).

the plane. This is discussed further in Section 2.3.3 in the context of the nova's radial velocity. Secondly, given its peculiar light curve this nova may not follow the usual decay-rate luminosity relations and therefore could be in the bulge. Thirdly, because of the peculiarity of the reddening law discussed above it is possible that the interstellar extinction at V is higher than the $A_V = 6.53$ used here and therefore that the nova is in the bulge and not sub-luminous. Although values as high as the $A_V = 8.88$ mag derived from the Nishiyama law can be ruled out, because in that case the red clump stars would not have been observable.

Some combination of greater reddening and slightly sub-luminous nova could also explain the observations. It has been suggested that novae in the bulge, which originate from low mass white dwarfs, are somewhat fainter than those in the disk (e.g. Della Valle & Livio (1998) and Della Valle (2002)). There is also some evidence that relatively slow novae are more common in the bulge and fast novae in the disk (Shafter et al., 2011).

2.3 Spectroscopic Data

2.3.1 Observation and Data Reduction

The nova was observed on 2015 April 22 and May 12, using the Robert Stobie Spectrograph (RSS; Burgh et al. 2003; Kobulnicky et al. 2003), mounted on the SALT situated at the SAAO, Sutherland, South Africa. The observation on 2015 April 22 consists of two spectral ranges; [4500 – 5850 Å] and [5800 – 7000 Å]. The RSS long-slit mode was used with a 0.6 arcsec slit at a resolution of $R \sim 5000$ for both spectral ranges with exposure times of (4×100 s) and (2×150 s), respectively. The poor weather conditions and seeing resulted in a limited signal to noise (S/N).

The May 12 observation was carried out, under good seeing ($\sim$1.0 arcsec). The data cover three spectral ranges, [4500 – 5450 Å], [5400 – 6750 Å], and [6700 – 7850 Å]. The RSS long-slit mode was used with the same narrow slit as above resulting in a resolution of $R \sim 7000$ for the first spectral range while a different grating was used for the second and third spectral ranges at a resolution of $R \sim 5000$, with exposure times of (5×200 s), (4×100 s), and (4×100 s), respectively. The spectra are reduced and calibrated using the PySALT pipeline (Crawford et al., 2010). The images are combined, the background is subtracted, and the spectra are extracted using the IRAF.

2.3.2 Spectral Changes

In Figs 2.4 to 2.8, we show the smoothed spectra, where the top spectrum represents the April 22 observation and the bottom spectrum represents the May 12 observation. The spectral lines were identified mostly using the list from Williams (2012). The only clear absorption features in either spectrum are telluric. The April 22 spectra show several broad flat-topped Fe II, H I, and N II emission lines. However, in the May 12 spectra, the Fe II lines become weaker and almost disappear, in contrast to the He and N lines that become stronger. Hβ (Fig. 2.4) and to some extent Hα (Fig. 2.7), show a double peak. These could be the consequence of bipolar ejection or an optically thin shell of gas (see, e.g., models of Nova Eri 2009 by Ribeiro et al. (2013)). Further in the red, between 6750 Å and 7850 Å, the May 12 spectrum shows strong He, O and possibly C emission lines.

2.3.3 Radial and Expansion Velocities

The Balmer lines have asymmetric profiles, similar to other novae in the transition stage. In the May spectrum Hα and Hβ have double peaks with the red peak stronger than the blue one; [N II] 5755 Å, O I 7773 Å and possibly C II 7236 Å are also double peaked. We derived, using Lorentzian fitting (applied to the whole profile), the FWHM of Hα, Hβ, and [N II] 5755 Å lines. We found that for Hα the FWHM $\sim 2300 \pm 200$ km s^{-1}, for Hβ the FWHM $\sim 2400 \pm 200$ km s^{-1}, and for [N II] 5755 Å the FWHM $\sim 2700 \pm 200$ km s^{-1}.

In order to derive the radial velocity of the nova, we measured the Hα, Hβ, Fe II 5018 Å, Fe II 5317 Å, N II 5679 Å, and [N II] 5755 Å emission lines for the April 22 observation. We also

measured the Hα, Hβ, N II 5679 Å, [N II] 5755 Å, C II 7326 Å and O I 7773 Å emission lines from the second spectrum (May 12). For the radial velocity calculations, the rest wavelengths of the emission lines are derived from the multiplet table of astrophysical interest (Moore, 1945) and the results listed in Table 2.5. In view of the change in the mean velocities of the lines we checked the wavelengths of the overlapping night sky lines with care. We used the European Southern Observatory UVES sky emission spectrum (Hanuschik, 2003) for this purpose. The lines at 4861.5 Å, 5577.5 Å, 5890 Å, 5896 Å, 6300 Å, 6562 Å, 6864 Å, 7276.3 Å, 7316.1 Å, 7341 Å, ... all agree well with the UVES sky emission lines.

Measurements of permitted lines are potentially shifted to the red by optical depth effects and must be regarded as unreliable. The most reliable measures of a nova radial velocity come from the CNO recombination lines and forbidden lines, which are almost always optically thin. The [O II] 7319,7330 Å is a blend, so we use only N II 5679 Å, [N II] 5755 Å, and C II 7236 Å from the May spectrum to derive the radial velocity. These lines give a mean heliocentric radial velocity of $\sim 110 \pm 50\,\mathrm{km\,s^{-1}}$.

The determination of novae radial velocities is not straight forward since many factors can affect it, including the WD orbital motion, optical depth effects, and most importantly the asymmetry of the ejecta (Williams, 1994). In both observations, the lines are shifted towards the red which would not be expected from optically thick ejecta.

It is not entirely clear why the radial velocity changes between the two epochs. Although both spectra appear to lack P Cygni absorptions it is possible that the first one was not optically thin and that absorption influences the blue side of the lines shifting them to the red, although the size of the shift makes this unlikely. It is also possible to speculate that the eruption was very asymmetric and that what we see in the first spectrum is a red-shifted clump of material, that later slows, although such an explanation seems contrived.

The velocity of the Sagittarius stream has not been measured in the direction of the nova, but the central part of the Sagittarius Dwarf Spheroidal galaxy has a mean velocity of $140\,\mathrm{km\,s^{-1}}$ with a velocity dispersion of only $10\,\mathrm{km\,s^{-1}}$ (Ibata, Gilmore & Irwin, 1995). The mean measurement from the more reliable lines in the second spectrum is consistent with this value. On the other hand the Galactic bulge has a high velocity dispersion and it is certainly not possible to use the velocity to rule out membership of the bulge.

Williams (1994) discusses the radial velocities of Galactic novae that are mostly within the solar circle and in the direction of the bulge. These have systematically large negative velocities and, as Williams points out, this indicates that either high internal absorption skews their emission lines to bluer velocities or most of the novae are moving out from the Galactic centre. It is much more difficult to skew the lines of a nova to the red, so if our nova is in the plane, behind the bulge, it would be moving away from the Galactic centre. That possibility cannot be ruled out, but it seems more likely that it is in the bulge, or the Sagittarius stream.

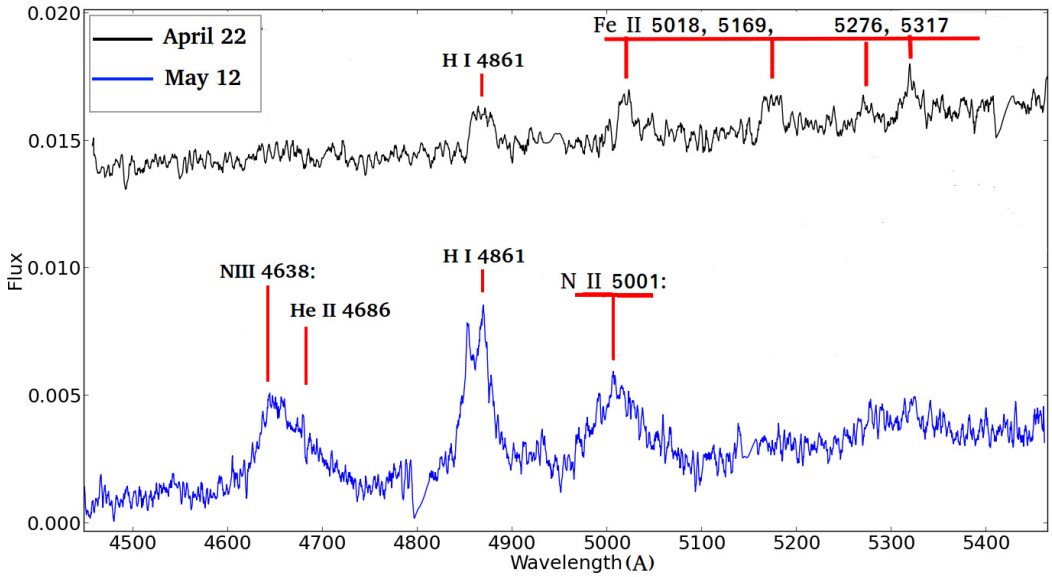

Figure 2.4: The flux plotted to arbitrary units between 4440 Å and 5450 Å. The 2015 April 22 spectrum (upper) shows several broad Fe II emission lines and Hβ line. However, in the 2015 May 12 spectrum (lower), the Fe II lines become weaker and almost disappear in contrast to the He and N that start to appear. The Hβ line shows a double-peak. For clarity, the April 22 spectrum is vertically shifted. In the April 22 spectrum, chip gaps are between: 4927.2 Å and 4953.4 Å and between: 5409.0 Å and 5433.9 Å. In the May 12 spectrum, the chip gaps are between: 4790.9 Å and 4810.0 Å and between: 5140.5 Å and 5158.4 Å.

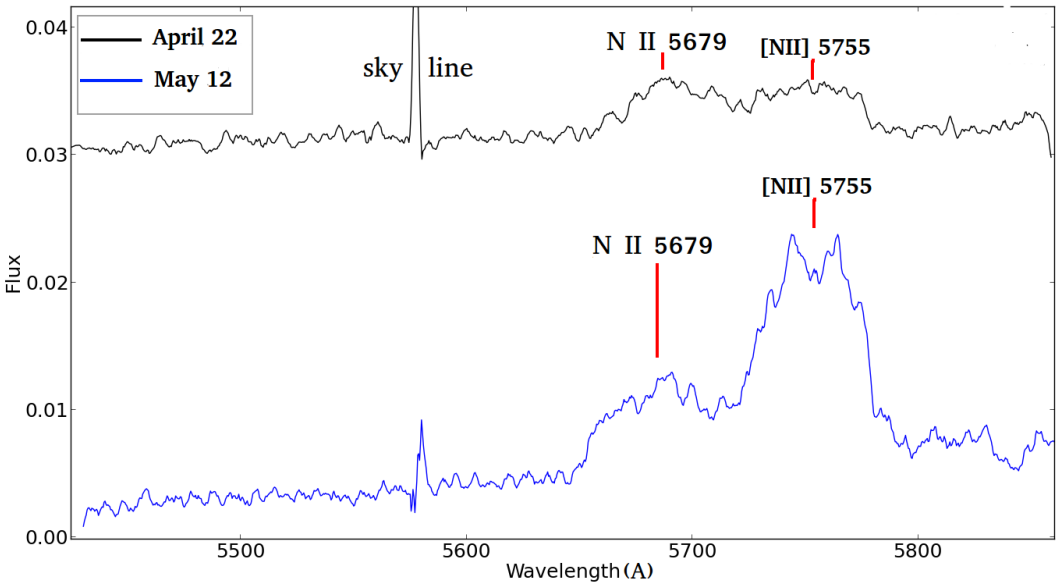

Figure 2.5: As in Fig. 2.4, but between 5400 Å and 5850 Å. The April 22 spectrum (upper) shows broad and relatively weak N II 5679 Å line and [N II] 5755 Å line. In the May 12 spectrum (lower), the [N II] line becomes stronger compared to the N II line. For clarity, the April 22 spectrum is vertically shifted.

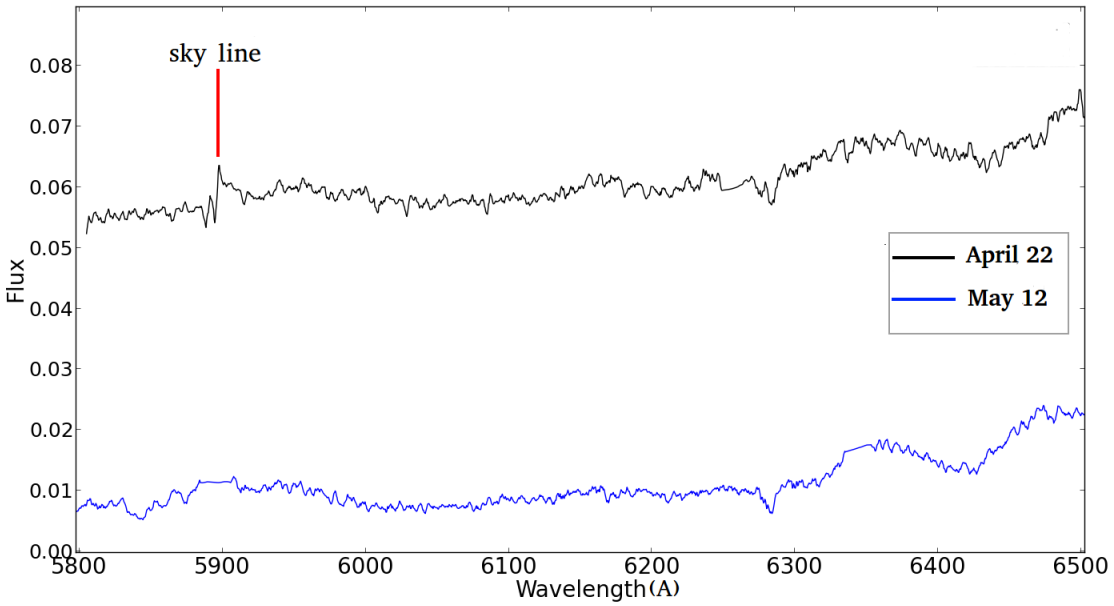

Figure 2.6: As in Fig. 2.4, but between 5850 Å and 6500 Å. No strong emission lines are present in this spectral range. For clarity, the April 22 spectrum is vertically shifted. In the April 22 spectrum, the chip gap is between: 6242.8 Å and 6267.1 Å. In the May 12 spectrum, the chip gaps are between: 5877.9 Å and 5902.7 Å and between: 6332.6 Å and 6355.9 Å.

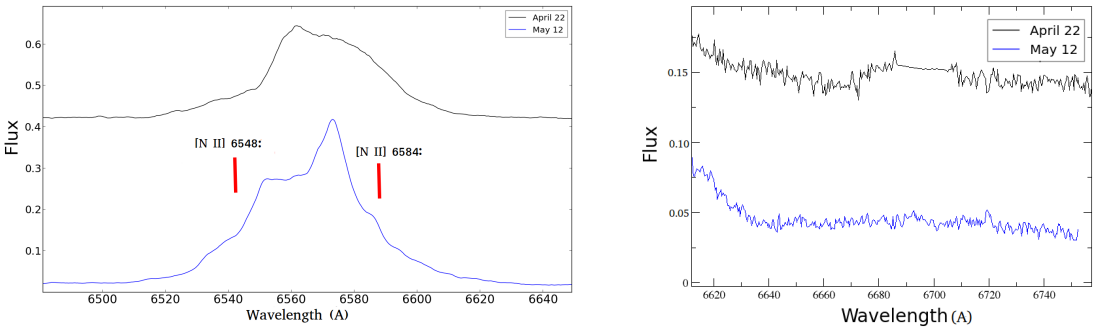

Figure 2.7: As in Fig. 2.4, but between (a) 6480 Å and 6640 Å, (b) 6620 Å and 6750 Å. The April 22 spectrum (upper) shows broad Hα emission line (FWHM $\sim$ 2300 km s^{-1} $\pm$ 200 km s^{-1}). In the May 12 spectrum (lower), the Hα line shows a double-peak similar to the one of Hβ. Both [N II] 6548 Å and [N II] 6584 Å are expected to be present but merged with the broad Hα. For clarity, the April 22 spectrum is vertically shifted. In the April 22 spectrum, the chip gap is between: 6685.5 Å and 6708.1 Å.

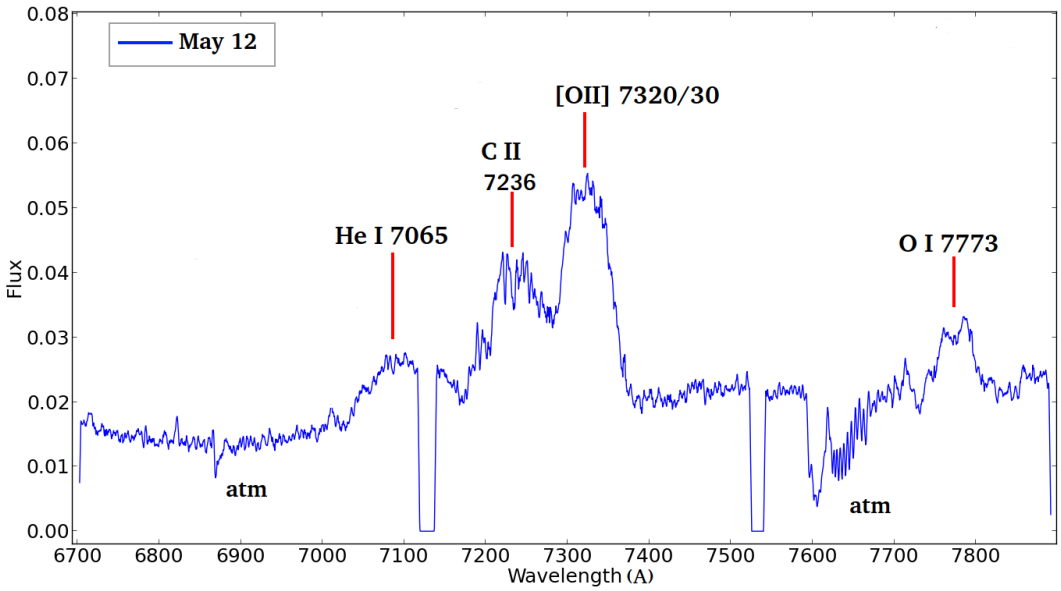

Figure 2.8: As in Fig. 2.4, but between 6750 Å and 7850 Å. The May 12 spectrum shows strong C, He and O emission lines. In the May 12 spectrum, the chip gaps are between: 7111.8 Å and 7134.4 Å and between: 7521.4 Å and 7542.1 Å.

Table 2.5: Heliocentric radial velocities of the emission lines for the April 22 and May 12 observations. The uncertainty for all the values is $\pm$ 50 km s^{-1}.

Line	V_{rad} (April 22)	V_{rad} (May 12)
	(km s^{-1})	
Hα	300	155
Hβ	320	140
Fe II 5018 Å	260	–
Fe II 5317 Å	180	–
N II 5679 Å	380	140
[N II] 5755 Å	150	45
C II 7236 Å	–	140
O I 7773 Å	–	160

2.3.4 Spectroscopic Classification

The spectra of V5852 Sgr leave no doubt that this is a CN. CNe are divided into two spectroscopic classes (Fe II and He/N). The two novae spectral classes have distinctly different properties. He/N novae exhibit broad, high ionization lines, rectangular profiles, few absorption features if any, and a rapidly decreasing visible luminosity. The line broadening is due to high expansion velocities. The spectra are dominated by He, N, and H emission lines. The prominent He and N transitions, the line widths and the rectangular line profiles, are all attributed to emission from high velocity gas (WD ejecta) (Williams, 2012).

Fe II novae have spectra characterized by low excitation narrow Fe II, Na I lines, and CNO lines in the far red. They also show prominent P Cygni absorption features characteristic of an optically thick expanding gas. The class of Fe II can be divided into two sub-classes Fe II n (narrow) and Fe II

b (broad) where respectively narrow or broad emission lines are present in the spectrum. Although no P Cygni absorption features are seen in either spectra, the April 22 spectrum presents features and lines that characterize the Fe II spectroscopic class. A moderate FWHM of $\sim 2500\,\mathrm{km\,s^{-1}}$ and the flat-topped broad lines favours the possibility of a Fe II b (broad) spectroscopic class. The May 12 spectrum shows several N lines which might indicate a transition into He/N class. However the absence of some helium lines, (He I 5876 Å and 6678 Å) that are expected to be present for the He/N class suggests that at this stage the nova was actually in transition to the nebular phase.

2.4 Discussion & Conclusions

V5852 Sgr was reported as a possible classical nova by the OGLE sky survey on 2015 March 5. Putting together the nova distance, luminosity, and radial velocity with their uncertainties, leaves the membership of the nova open to three possibilities. The first puts the nova in the Sagittarius stream and the second puts it in the plane behind the bulge moving away from the Galactic centre and the third puts it in the Galactic bulge (see Section 2.3.3). It is worth noting that the mass of the Sagittarius dwarf is $10^8 - 10^9\,\mathrm{M_\odot}$ so the expected nova rate in that galaxy will only be one per 10 to 100 years. The nova rate in the bulge is ~ 2 orders of magnitude higher, so the bulge is a more probable site (Mróz et al., 2015). So the location will have to remain open, at least until we gain a better understanding of the characteristics of novae with this type of light curve. The membership to the Sagittarius dwarf galaxy would make it the first nova to be discovered in a dwarf spheroidal galaxy.

The photometric follow up (OGLE, IRSF, LCOGT) revealed a peculiar nova light curve. The spectroscopic and photometric data revealed combined features rarely observed in CNe. The nature of V5852 Sgr is best described as an unusual one. Based on our spectra and the classification criteria of Williams (1992) V5852 Sgr shows a Fe II or Fe II b spectroscopic class in a transition to the nebular phase. Tracking the spectroscopic and photometric evolution of the object is essential for a definitive classification. If the object is a classical, moderately fast nova, the same spectroscopic features should remain until the nebular phase develops. A detailed study of the elemental abundances is also essential. Hence, further observations are needed to definitively identify the object and understand the physical mechanism responsible for this explosion.

Chapter 3

Multiwavelength observations of nova SMCN 2016-10a — one of the brightest novae ever observed

Abstract

We report on multiwavelength observations of nova SMCN 2016-10a. The present observational set is one of the most comprehensive for any nova in the Small Magellanic Cloud, including: low, medium, and high resolution optical spectroscopy and spectropolarimetry from SALT, FLOYDS, and SOAR; long-term OGLE V- and I- bands photometry dating back to six years before eruption; SMARTS optical and near-IR photometry from ~ 11 days until over 280 days post-eruption; *Swift* satellite X-ray and ultraviolet observations from ~ 6 days until 319 days post-eruption. The progenitor system contains a bright disk and a main sequence or a sub-giant secondary. The nova is very fast with $t_2 \simeq 4.0 \pm 1.0$ d and $t_3 \simeq 7.8 \pm 2.0$ d in the V-band. If the nova is in the SMC, at a distance of $\sim 61 \pm 10$ kpc, we derive $M_{V,\max} \simeq -10.5 \pm 0.5$, making it the brightest nova ever discovered in the SMC and one of the brightest on record. At day 5 post-eruption the spectral lines show a He/N spectroscopic class and a FWHM of $\sim 3500\,\mathrm{km\,s^{-1}}$ indicating moderately high ejection velocities. The nova entered the nebular phase ~ 20 days post-eruption, predicting the imminent super-soft source turn-on in the X-rays, which started ~ 28 days post-eruption. The super-soft source properties indicate a white dwarf mass between $1.2\,\mathrm{M}_\odot$ and $1.3\,\mathrm{M}_\odot$ in good agreement with the optical conclusions.

Keywords: stars: individual (SMCN 2016-10a) – novae, cataclysmic variables – white dwarfs – ultraviolet: stars – X-rays: binaries

3.1 Introduction

A classical nova (CN) is a result of an eruption on the surface of a white dwarf (WD) in an interacting binary, namely "cataclysmic variable". Classical novae (CNe) consist of an accreting WD and a companion that typically fills its Roche lobe (Warner, 1995). The accreted matter builds up on the surface of the WD and when the pressure and density reach critical levels, a thermonuclear runaway occurs (Starrfield, Iliadis & Hix, 2008). Within a few days, the eruption increases the visual brightness of the star between 8 and 15 mag. After the peak, the brightness of the star decreases gradually over a timescale of a few weeks up to months. Typically, the ejecta from the eruption can reach a velocity of $\sim 1000\,\mathrm{km\,s^{-1}}$ and contains a mass between $10^{-6}\,\mathrm{M_{\odot}}$ and $10^{-4}\,\mathrm{M_{\odot}}$ (Payne-Gaposchkin, 1957; Gallagher & Starrfield, 1978), although more recently, faster, lower ejecta mass systems have been found (Kasliwal et al., 2011; Shara et al., 2017a).

Immediately following the thermonuclear runaway, the surface of the WD is obscured by material thrown out during the eruption. Over time these ejecta expand, becoming optically thin to X-rays, allowing the atmosphere of the nuclear burning region on the WD to become visible. This emission typically peaks in the soft X-ray band, when the nova then enters what is known as the super-soft source (SSS) state (Krautter et al., 1996) (for a review of X-ray observations of CNe see, e.g., Osborne 2015 and references therein).

Novae are also observed in ultraviolet (UV) light. In some cases, such as V2491 Cyg (Page et al., 2010) and V745 Sco (Page et al., 2015), the UV light-curve is completely uncorrelated with the X-ray emission, indicating the emission regions are unrelated. HV Cet (Beardmore et al., 2012) is an example where the X-ray and UV emission varies in phase throughout the orbit; in this case, we may be observing a high-inclination (edge-on disk) system, where the X-ray- and UV-emitting region is periodically occulted, perhaps by the lip of an accretion disc. The final situation is one in which the X-rays and UV are anti-correlated – for example, V458 Vul (Ness et al., 2009; Schwarz et al., 2011). This could be explained by temperature variations (Schwarz et al., 2011), with the spectral energy distribution shifting between the extreme-UV (EUV) and X-ray bands as the photosphere expands and contracts (see also Schwarz et al. 2015).

Novae are classified based on their optical light-curves and spectra. This classification is determined by the duration in days for the brightness to decrease by 2 or 3 mag from the intensity peak, known as t_2 and t_3, respectively (Payne-Gaposchkin, 1964; Shafter, 1997). Strope, Schaefer & Henden (2010) classified a sample of 93 nova light-curves based on visual estimates and V band photometry from the AAVSO Photometric All-Sky Survey (APASS[1] - Henden et al. 2009).

From a spectroscopic point of view novae are classified according to the early decline spectra, before they enter the nebular phase (McLaughlin, 1944; Payne-Gaposchkin, 1957; Williams, 2012). Based on the post-eruption spectral features, Williams (1992) divided novae into two spectroscopic classes "Fe II" and "He/N". Aside from the Balmer lines that dominate the spectrum in all classes, the first class exhibits narrow Fe II emission lines with P Cygni profiles and the second one exhibits broad He and N emission lines. Some novae show features from both classes simultaneously or

[1] https://www.aavso.org/apass

a transition from one class to the other and they are classified as hybrids (Williams, 1992, 1994, 2012). The spectra of the Fe II class may be formed in the circumbinary envelope which originated from mass loss from the secondary. The intensity of Fe II spectra fades slowly and lasts for weeks and sometimes months after the eruption due to the low expansion velocities. The spectra of the He/N class are thought to originate from the gas on the WD due to the prominence of He and N transitions, the rectangular line profiles, and the large line widths (Williams, 2012).

Novae in the Milky Way and M31 have been extensively studied with global nova rates of $\sim 34^{+15}_{-12}$ yr^{-1} and $\sim 65^{+16}_{-15}$ yr^{-1}, respectively (Darnley et al., 2006). In contrast, novae in the Small Magellanic Cloud (SMC) occur less frequently. Since 1897 only 22 novae have been discovered in the SMC (Pietsch 2010[2]), and most of these novae have been poorly investigated with multiwavelength observations. Little effort has been made to constrain the nova rate for the SMC (see, e.g., Graham 1979; Della Valle 2002). Recently Mróz et al. (2016) published an atlas of classical novae in the Magellanic Clouds, offering a systematic study of novae in the SMC where they derived an observed rate of $0.5 \pm 0.2\,\mathrm{yr}^{-1}$ and an absolute rate of $0.9 \pm 0.4\,\mathrm{yr}^{-1}$. With such a low nova rate, multiwavelength studies of nova events in the SMC are of interest for: (1) understanding better the nova event itself, (2) providing more insights into nova properties in parent galaxies that have different metallicity content, luminosity classes, Hubble types, and star formation histories from the Milky Way or M31 (Mason et al., 2005; Mróz et al., 2016), and (3) the distance modulus to novae belonging to the SMC is known more accurately than is typical for Galactic novae, so that physical properties can also be derived more accurately.

Tracking the evolution of the post-eruption spectral lines and relating this to the multiwavelength light-curve evolution is an important tool to understand the physical mechanism of nova eruptions, hence the importance of extensive low and high resolution spectroscopic monitoring of novae. High resolution spectroscopy allows us to study the evolution of line profiles which provides details about the morphology and velocities of the ejecta, and also offers us the opportunity for modelling the system (Ribeiro, Munari & Valisa, 2013; Ribeiro et al., 2013; De Gennaro Aquino et al., 2015; Jack et al., 2017).

One of the advantages of studying novae in the Magellanic Clouds (MCs) is the known distance (albeit with a finite spread). Deriving distances to novae is a challenge. High ejecta velocities and different light-curve decline rates (e.g. Strope, Schaefer & Henden 2010) make it difficult to derive an accurate estimate. Nevertheless, many methods have been suggested for this purpose. Most of these methods are based on the decline rate of the nova optical light brightness which is correlated with their absolute magnitude at maximum light and are known as "Maximum Magnitude versus Rate of Decline" (MMRD) relations (e.g. McLaughlin 1939b; Livio 1992; Della Valle & Livio 1995; Downes & Duerbeck 2000). Recently, these methods have been questioned (e.g. Kasliwal et al. 2011; Cao et al. 2012; Shara et al. 2017a). Alternative methods have been proposed to derive distances to novae (see, e.g., Downes & Duerbeck 2000; Shara et al. 2017b) and we will refer to these methods in Section 3.6.1.

[2] `https://mpe.mpg.de/~m31novae/opt/smc/index.php`

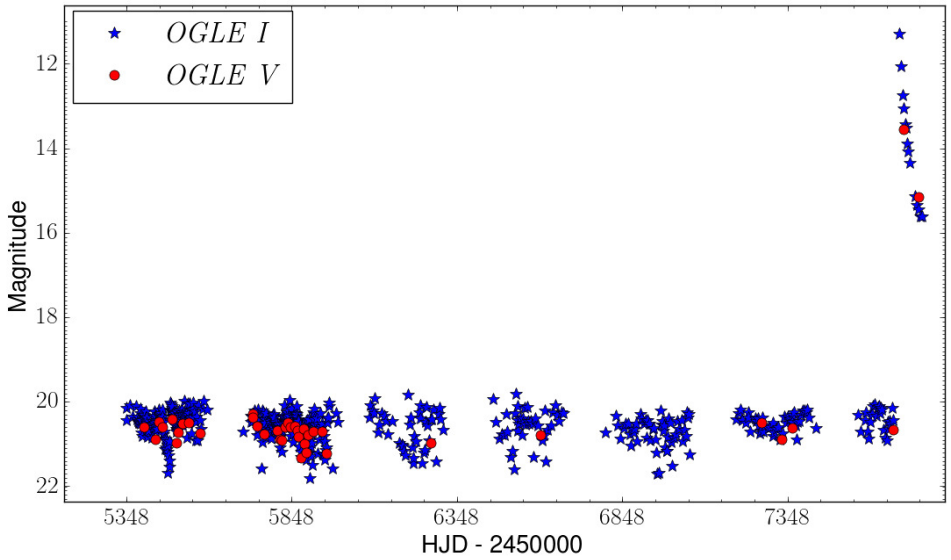

Figure 3.1: The photometric VI data, from the OGLE-IV Survey (Udalski, Szymański & Szymański, 2015), as a function of Heliocentric Julian Date (HJD), colour and symbol coded as indicated in the legend. The standard error on individual observations in quiescence is less than 0.2 mag, so much of the apparent variability is real.

In this chapter we report on multiwavelength spectroscopic and photometric observations of nova SMCN 2016-10a that was discovered by MASTER (OT J010603.18-744715.8) on HJD 2457675.6 (2016-10-14.2 UT;Shumkov et al. 2016). The eruption started on HJD 2457670.7 (2016-10-09.2 UT; Jablonski & Oliveira 2016), this date is considered as t_0 throughout the chapter. The nova is located in the direction of the SMC at equatorial coordinates, $(\alpha, \delta)_{J2000.0}$ = ($01^{\rm h}06^{\rm m}03\overset{\rm s}{.}27$, $-74^\circ47'15\overset{''}{.}8$) (Mroz & Udalski, 2016). It might be the brightest nova ever discovered in the SMC and one of the brightest on record. Multiwavelength follow-up has been carried out to study in detail the post-eruption behaviour of the nova at optical, near-infrared (NIR), X-ray, and UV wavelengths.

The chapter is outlined as follows: in Sections 3.2 and 3.3 we present and analyze the optical photometric and spectroscopic observations, respectively. We present the X-ray data in Sections 3.4 and the UV data in Section 3.5, followed by our discussion in Section 3.6. We present a summary and the conclusions in Section 3.7. The observation log is presented in Appendix A.1.

3.2 Optical photometric observations and data reduction

3.2.1 OGLE observations and data reduction

The nova has been monitored since 2010 in the I- and V-bands by the OGLE-IV Survey (Udalski, Szymański & Szymański, 2015), as part of the Magellanic System survey. These long-term observations provide information on the progenitor system. All data were reduced and calibrated following the standard OGLE pipeline (Udalski, Szymański & Szymański, 2015). Owing to saturation, the data poorly cover the eruption period and the early decline. The last observations

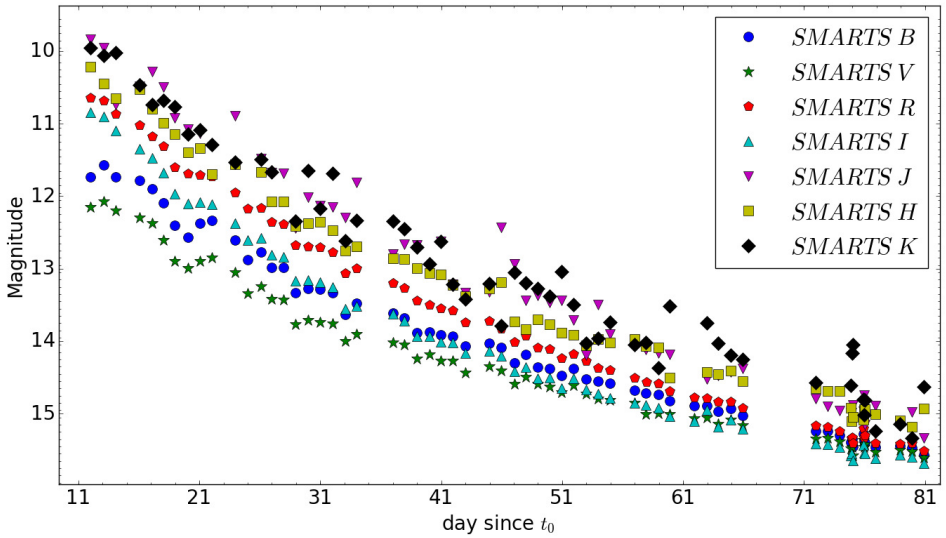

Figure 3.2: The photometric $BVRIJHK$ data from SMARTS as a function of days since eruption, colour and symbol coded as indicated in the legend. The scatter at K is due to observational uncertainty. Data after day $\sim$ 80 suffer from moderate uncertainties (especially in the JHK bands) and thus are not presented in the plot.

before the eruption were made on HJD 2457667.6 (2016 October 6) and the first unsaturated image was obtained on HJD 2457686.6 (2016 October 25). The OGLE V- and I- band data are presented in Fig. 3.1. See Tables A.1 and A.2 for a log of the observations.

3.2.2 SMARTS observations and data reduction

The Small and Moderate Aperture Research Telescope System (SMARTS) obtained optical *BVRI* and near-infrared (NIR) *JHK* photometric observations. The observations started on HJD 2457682.6 (2016 October 21). The integration times at *JHK* were 15 s (three 5 s dithered images) before 2016 December 03, and 30 s thereafter. Optical observations are single images of 30, 25, 20, and 20 s integrations respectively in *BVRI* prior to 2016 December 03, and uniformly 50 s after 2016 December 03. The details of the data reduction are presented in Walter et al. (2012). The *BVRI* and *JHK* data are plotted in Fig. 3.2. See Table A.3 for a log of the observations.

3.2.3 Optical light-curve parameters

CNe light-curves are characterized by several parameters: the rise rate, the rise time to maximum light, the maximum light, the decline rate, and the decline behaviour (morphology) (e.g. Hounsell et al. 2010; Cao et al. 2012). The light-curves of nova SMCN 2016-10a show a smooth decline with weak oscillations. In comparison to the Strope, Schaefer & Henden (2010) classification, the light-curves of nova SMCN 2016-10a look like an S-class event. The S-class is considered as the stereotypical nova light-curve and it is characterized by a rapid rise, a relatively sharp peak, followed by a smooth decline that starts off steep and then becomes more gradual with time (Strope,

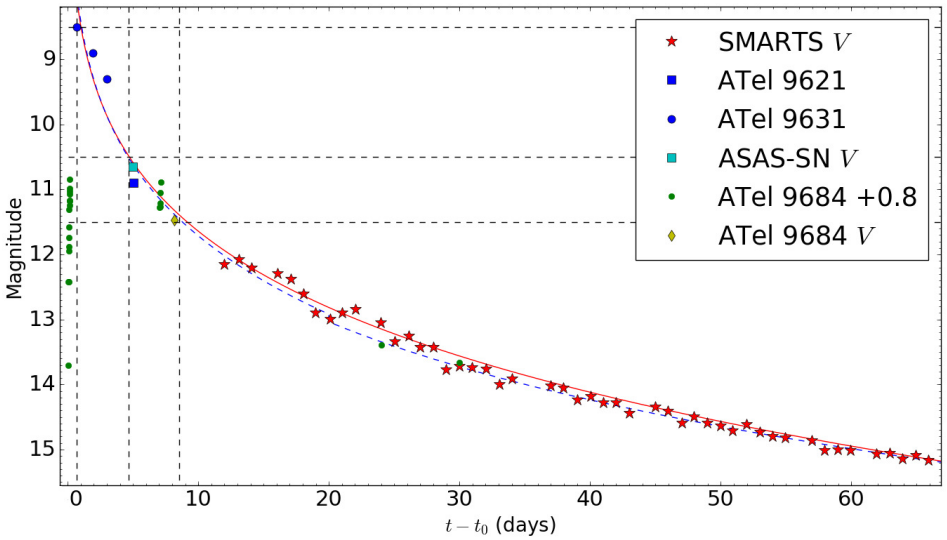

Figure 3.3: V-band photometry from SMARTS and ASAS-SN along with data from Shumkov et al. (2016); Lipunov et al. (2016); Jablonski & Oliveira (2016). An offset of + 0.8 is added to the data from (Jablonski & Oliveira 2016; see main body of text). The blue dashed line represents a broken power law fit to the data and the red solid line represents a power law fit to the data. The black horizontal dashed lines represent from top to bottom ($V_{\rm max}$), ($V_{\rm max}$ + 2), and ($V_{\rm max}$ + 3) respectively. The black vertical dashed lines represent from left to right $t_{\rm max}$, t_2, and t_3 respectively.

Schaefer & Henden, 2010). Note that the SMARTS optical photometry show a plateau starting about day $\sim$ 100 and ending after day $\sim$ 130, during solar conjunction (see Fig. A.1).

On HJD 2457667.67 the nova was observed with OGLE V-band at a magnitude of 20.65. Pre-discovery observations by a robotic DSLR camera at Sao Jose dos Campos, Brazil (Jablonski & Oliveira, 2016) showed that on HJD 2457670.7 (2016-10-09.2 UT) the nova was at a magnitude of 12.9. We assume this date as t_0.

The magnitude then reached 9.9, after 0.1 days. The nova subsequently brightened to a maximum on HJD 2457671.3 at a magnitude of 8.5. After 1.2 days the magnitude dropped to 8.9, then to 9.3 two days later, indicating the start of the decline. These measurements were obtained using the MASTER Very Wide Field (VWF) camera. According to Gorbovskoy et al. (2010), the instrumental photometric band of the MASTER VWF camera can be described fairly well by the $V_{\rm TYCHO2}$ filter and it corresponds to V-band photometry (private communication with E. Gorbovskoy). We will consider these measurements as an approximation of V-band photometry.

We consider HJD 2457671.3 (2016-10-9.8 UT) as the day of maximum light and $V_{\rm max} \approx 8.5$. This means that the magnitude decreased from $>$ 13 to 8.5 in less than 1 day which is relatively fast compared to other classical novae (see, e.g., Hounsell et al. 2010; Cao et al. 2012).

In order to get an estimate of the rate of decline, we carried out broken power law and power law fitting to the MASTER and SMARTS magnitudes. We also make use of the All-Sky Automated Survey for Supernovae (ASAS-SN, Shappee et al. 2014) V-band measurement 1.7 h before the discovery. A broken power law is best fitting an S-class light-curve (see, e.g., Hachisu & Kato

2006; Strope, Schaefer & Henden 2010). The fitting resulted in $t_2 \simeq 4.0 \pm 1.0$ d, $t_3 \simeq 7.8 \pm 2.0$ d, and a decline rate of $\simeq 0.55 \pm 0.1$ mag d^{-1} over t_2. A power law index of ~ 1.76 was derived from the early slope, in good agreement with the theoretical power law of Hachisu & Kato (2006) and the empirical values of Strope, Schaefer & Henden (2010). We also derive t_2 and t_3 from a linear interpolation between points and we get very similar results.

We increased the uncertainty on t_2 and t_3 to take into consideration the usage of different measurements from different telescopes and detectors. It is important to recognize that several of our conclusions are dependent on these assumptions. By comparing to the empirical relation from Hachisu & Kato (2006) which relates t_3 to t_2 as: $t_3 = 1.69t_2 + 0.69\Delta t_0$ days, with the rise time $\Delta t_0 \sim 0.6$, we obtain $t_3 = 7.1 \pm 1.0$, in agreement with the values estimated above.

In Fig. 3.3 we present the first 70 days of the SMARTS V-band photometry along with data from Shumkov et al. (2016); Lipunov et al. (2016); Jablonski & Oliveira (2016) and the V-band measurement from ASAS-SN. The DSLR cameras used to obtain the data from Jablonski & Oliveira (2016) are very red sensitive and the data require colour correction to be compared with V-band photometry. Because of the colour correction required, we exclude these data from the fitting and we just plot them for comparing their agreement with the fit. We adopt an offset of + 0.8 mag from Munari, Hambsch & Frigo (2017) to correct for the colour difference. As can be seen in Fig. 3.3, the broad DSLR measurement after maximum agree with the simultaneous SMARTS V-band data.

Munari, Hambsch & Frigo (2017) derived different values of t_2 and t_3. This is because of the offset they added to the MASTER VWF data (Lipunov et al., 2016). They considered that the VWF is very red sensitive and they added an offset of +1 mag to correct for the colour difference, leading them to larger values of t_2, t_3, and $V_{\rm max}$. Since the MASTER VWF measurements correspond to V-band photometry (Gorbovskoy, private communication), such an offset is too large.

Payne-Gaposchkin (1964) classified the light-curves of novae into 5 speed classes. Novae with $t_2 < 10$ d and $\dot{m}_v > 0.20$ mag d^{-1}, which is the case for this nova, are classified as “very fast".

3.3 Optical spectroscopic observations and data reduction

3.3.1 SALT medium resolution spectroscopy

We observed the nova on 2016 October 17 (day 8) and November 1 (day 23) using the Robert Stobie Spectrograph (RSS; Burgh et al. 2003; Kobulnicky et al. 2003), in Long Slit (LS) mode, mounted on the Southern African Large Telescope (SALT; Buckley, Swart & Meiring 2006; O'Donoghue et al. 2006) situated at the SAAO, Sutherland, South Africa. Both observations consist of two spectral ranges; [3500 Å – 6300 Å] and [6000 Å – 9000 Å]. For the October 17 observations the RSS long-slit mode was used, with a 1.5 arcsec slit and the PG900 grating, resulting in a resolution of $R \sim 850$ for the first range and $R \sim 1400$ for the second one. For the November 1 observations we used a 1.0 arcsec slit and the PG900 grating, resulting in a resolution of $R \sim 1250$ for the first range and $R \sim 2000$ for the second one. For both observations, ThAr and Ne lamp arc spectra were taken immediately after the science frames for the first and second range respectively. See

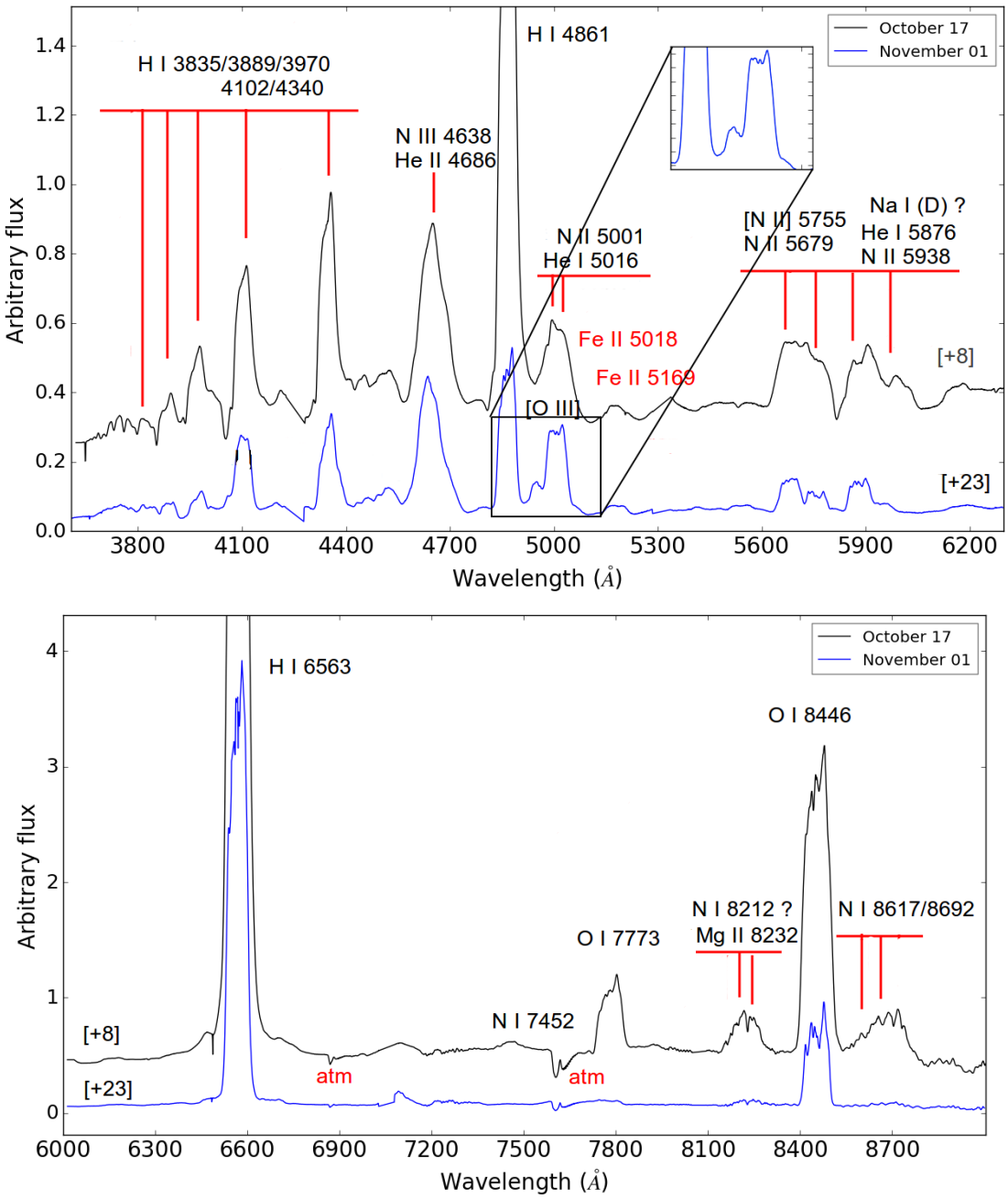

Figure 3.4: The LS medium resolution spectra plotted between 3600 – 6300 Å and 6000 – 9000 Å with the flux in arbitrary units. For clarity, the spectra are shifted vertically. The numbers between brackets are days since t_0.

Table A.4 for a log of the observations.

The spectra were first reduced using the PySALT pipeline (Crawford et al., 2010), which involves bias subtraction, cross-talk correction, scattered light removal, bad pixel masking, and flat-fielding. The wavelength calibration, background subtraction, and spectral extraction are done using IRAF (Tody, 1986). The spectra are presented in Fig. 3.4.

3.3.2 SALT high resolution echelle spectroscopy

The SALT High Resolution Spectrograph (HRS; Barnes et al. 2008; Bramall et al. 2010; Bramall et al. 2012; Crause et al. 2014), a dual-beam, fibre-fed echelle spectrograph, was used to obtain high resolution observations on the nights of 2016 October 17, November 5, November 10, November 23, and December 10 (respectively day 8, 27, 32, 45, and 65). The observations were taken in the low-resolution (LR) mode of HRS to provide a spectrum covering a spectral range of 3800 Å – 9000 Å at a resolution of $R \sim 15000$. A weekly set of HRS calibrations, including four ThAr + Ar arc spectra and four spectral flats, was obtained in all the modes (low, medium, and high resolution). See Table A.4 for a log of the observations.

Primary reduction of the HRS data was done using the SALT science pipeline (Crawford et al., 2010), which includes over-scan correction, bias subtraction, and gain correction. The rest of the reduction was done using the standard MIDAS FEROS (Stahl, Kaufer & Tubbesing, 1999) and $echelle$ (Ballester, 1992) packages. The reduction procedure is described in detail in Kniazev, Gvaramadze & Berdnikov (2016). The spectra are presented in Fig. 3.5.

3.3.3 FLOYDS spectroscopy

A series of eleven epochs of spectroscopy of nova SMCN 2016-10a were obtained on the nights of 2016 October 14, 17, 18, 19, 20, 22, 23, 29, 31, November 02, and 10 (respectively day 5, 8, 9, 10, 11, 13, 14, 20, 22, 24, 32) using the FLOYDS spectrograph[3] on the Las Cumbres Observatory (LCO; Brown et al., 2013) 2.0m telescope at Siding Springs, Australia[4]. FLOYDS is a cross-dispersed low resolution ($R \sim 550$) spectrograph using an Andor Newton DU940P-BU detector and with a wavelength coverage of 3200 Å–10000 Å. Data reduction was carried out using the FLOYDS data pipeline (v2.2.1). See Table A.5 for a log of the observations. The flux calibrated spectra are presented in Fig. 3.6. Due to poor photometric conditions during the observations as well as slit losses, the absolute flux calibration is uncertain.

3.3.4 SOAR spectroscopy

We also performed spectroscopy of the nova on 2017 July 11, using the Goodman spectrograph (Clemens, Crain & Anderson, 2004) on the Southern Astrophysical Research (SOAR) telescope. One single 1200 s spectrum was obtained, using a 400 l mm^{-1} grating and a 1.07 arcsec slit, giving resolution of ~ 7 Å over the wavelength range 3810 Å – 7860 Å. The spectrum was reduced in the standard manner, with a relative flux calibration applied, and including an approximate correction for slit losses. The spectrum is presented in Fig. 4.5.

3.3.5 Line identification

The strongest features in the spectra of day 5 and 8 (Figs 3.4, 3.5, and 3.6) are the broad Balmer lines (Hα, Hβ, Hγ, Hδ, Hϵ, Hζ, and Hη). The hydrogen Balmer lines are accompanied by weak

[3] `https://lco.global/observatory/instruments/floyds`

[4] Formally known as Faulkes Telescope South.

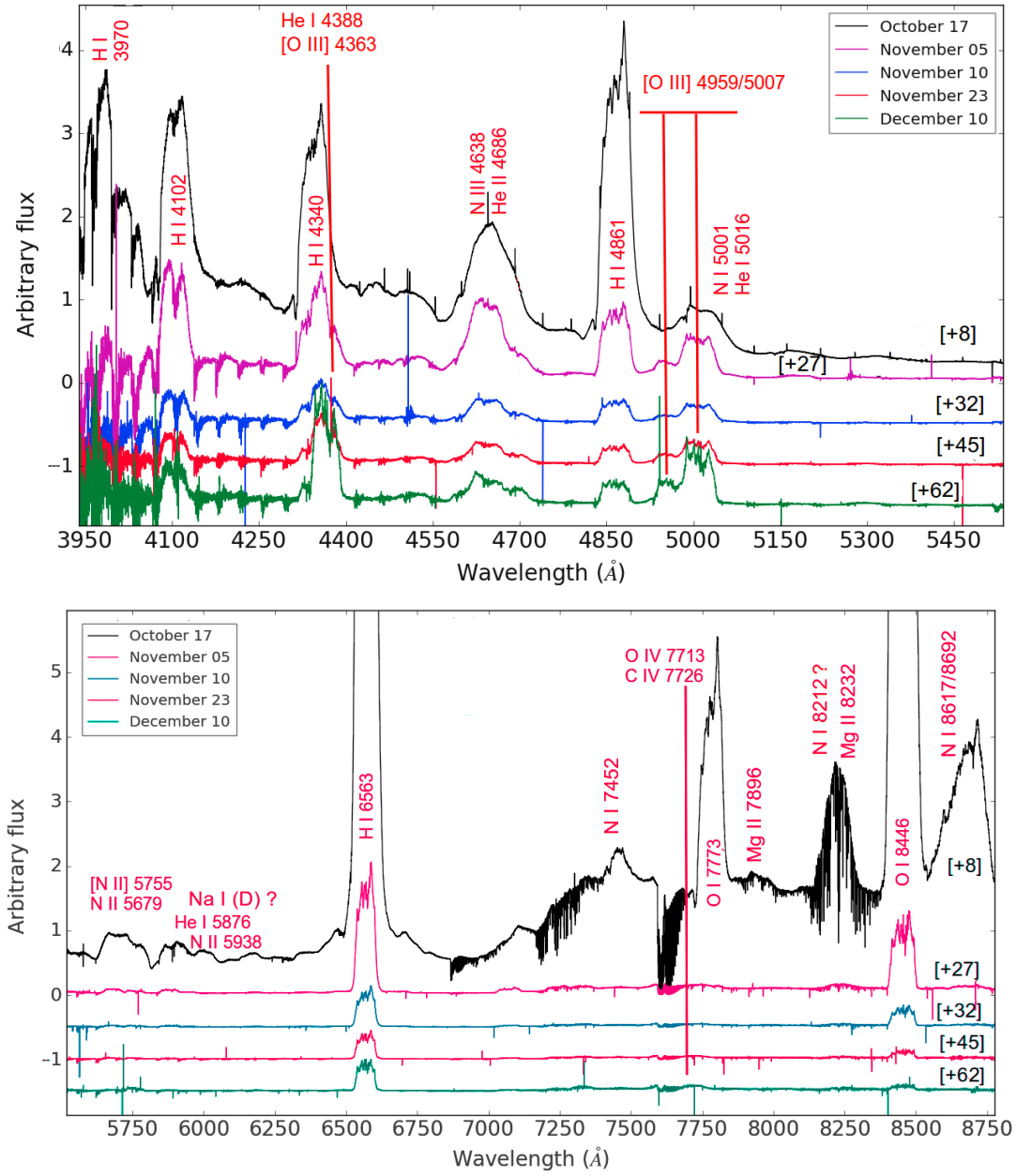

Figure 3.5: The HRS high resolution spectra plotted between 3900 – 5500 Å and 5700 – 8750 Å with the flux in arbitrary units. For clarity, the spectra are shifted vertically. The numbers between brackets are days since t_0.

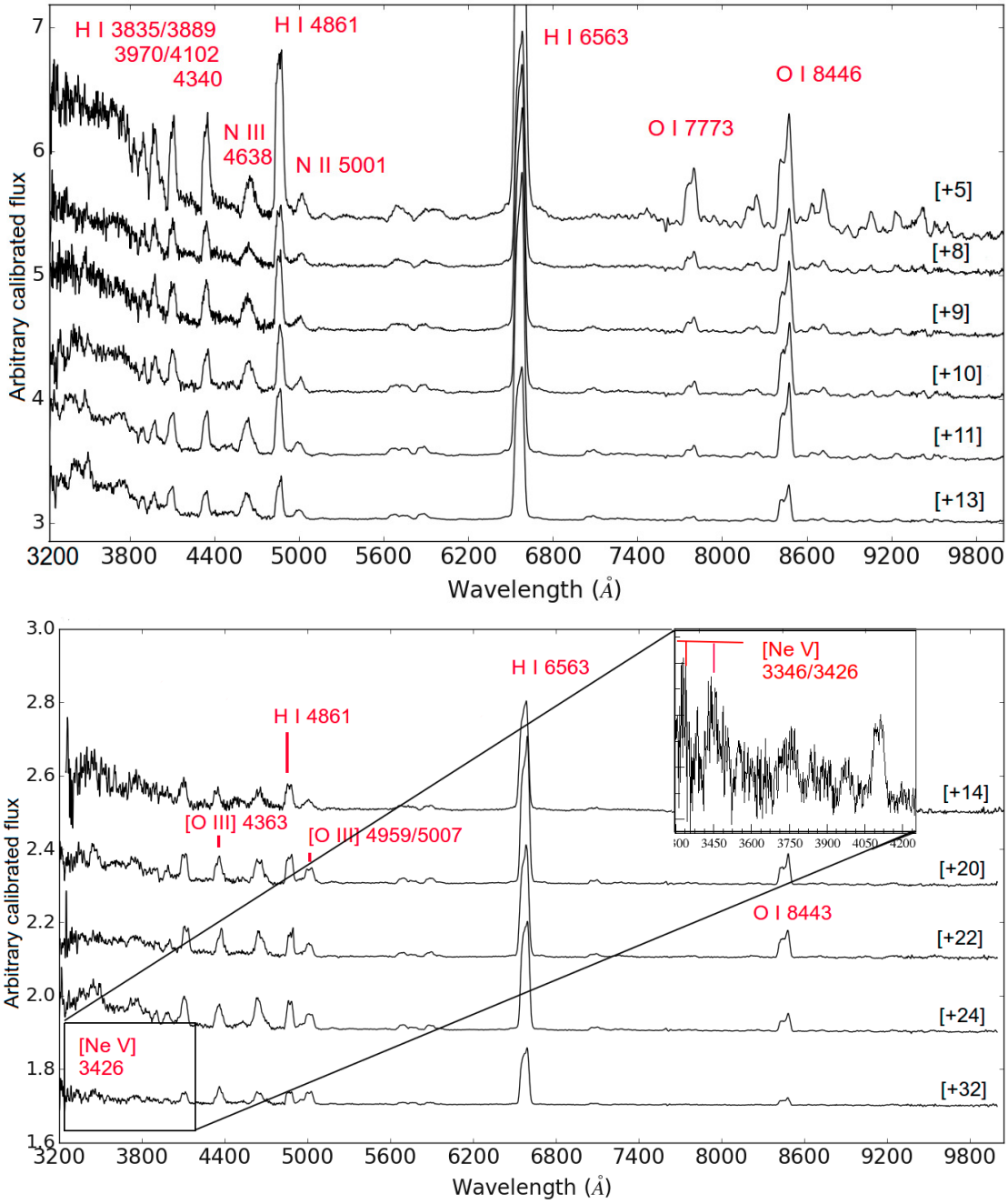

Figure 3.6: The FLOYDS spectra plotted between 3200 – 10000 Å, with the flux in arbitrary units. For clarity, the spectra are shifted vertically. From top to bottom: Oct 14, 17, 18, 19, 20, 22, 23, 29, and 31, Nov 02, and 10. The numbers between brackets are days since t_0.

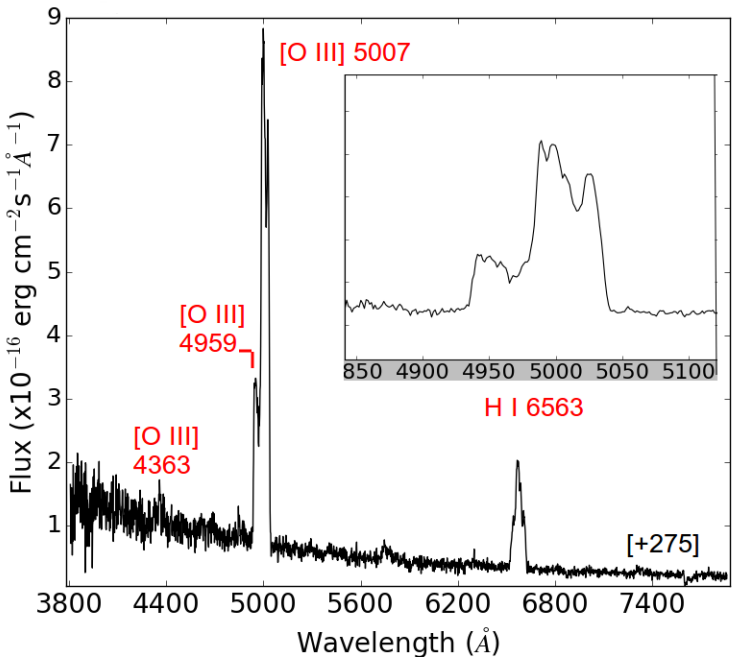

Figure 3.7: The SOAR spectrum of day 275 plotted between 3800 Å – 7860 Å. The number between brackets is days since t_0. We added a zoom-in plot on the [O III] 4959 Å and 5007 Å lines for clarity.

absorption features. The radial velocities (RVs) derived from the P Cygni absorption on day 8, by measuring the wavelengths at the minimum flux, are as follows: H$\gamma \sim -2300 \pm 200\,\mathrm{km\,s^{-1}}$, H$\delta \sim -2700 \pm 200\,\mathrm{km\,s^{-1}}$, H$\epsilon \sim -2700 \pm 200\,\mathrm{km\,s^{-1}}$, and H$\zeta \sim -2500 \pm 200\,\mathrm{km\,s^{-1}}$. Another set of prominent features are the Oxygen lines (O I 7773 and 8446 Å). Nitrogen emission lines are also present (N III 4638 Å, N II 5001 Å, 5679 Å, 5938 Å, [N II] 5755 Å, N I 7452 Å, 8212 Å, 8617 Å, and 8692 Å), noting that the N III 4638 Å might be accompanied by a weak P Cygni absorption. There is a possible weak detection of He I 7065 Å. He II 4686 Å and He I 5016 Å might be blended with their neighbouring nitrogen lines. He I 5876 Å might also be affected by Na I D and the nitrogen line at 5938 Å. Mg II 7896 Å and 8232 Å are also present. The line at 5169 Å is possibly Fe II while the other multiplet (42) lines at 4924 Å and 5018 Å might be blended with other lines.

The spectra from day 9 to 14 show the same emission features with the O I 7773 Å and N II 5001 Å lines fading gradually. The spectra of day 20 to 23 (Figs 3.4, and 3.6) show similar lines, with the appearance of [O III] 4959 Å and 5007 Å nebular lines. The weak absorption features had faded. The O I 7773 Å line weakened compared to the 8446 Å line. The [N II] 6548 Å, 6583 Å might be blended with the broad Hα line (see section 3.6.6.1).

In the spectra of day 32 (Fig. 3.6) forbidden Ne lines emerge at 3346 Å and 3426 Å (see Section 4.4.2), while the Balmer features start to fade compared to the [O III] emission lines (4363 Å, 4959 Å, 5007 Å). The O I lines at 7773 Å and 8446 Å further in the red also faded noticeably. The spectra of day 45 and 65 show strong emission lines of [O III] and He I 4388 Å in the blue while the O IV 7713 Å and C IV 7726 Å nebular lines emerge.

The late spectra of day 275 (Fig. 4.5) were dominated by the [O III] 4363 Å, 4959 Å, and 5007 Å lines, along with Hα. The spectral line identification was primarily done using the list from Williams (2012) and the Multiplet Table of Astrophysical Interest (Moore, 1945). In Table A.6 we list the line IDs along with the FWHM, Equivalent Widths (EWs), and fluxes for those emission lines for which an estimate was possible.

3.3.6 SALT spectropolarimetry

Spectropolarimetry observations were obtained on the nights of 2016 October 24 and November 21 (days 15 and 43) using the RSS spectrograph. The RSS is capable of imaging polarimetry and spectropolarimetry (for more details on the optics see Nordsieck et al. 2003). Both observations consist of two spectral ranges; [3500 Å – 6300 Å] and [6000 Å – 9000 Å]. The RSS LS mode was used, with a 1.5 arcsec slit and the PG900 grating, resulting in a resolution of $R \sim 850$ for the first range and $R \sim 1400$ for the second one. ThAr and Ne lamp arc spectra were taken immediately before the science frames for the first and second range, respectively.

The spectropolarimetry data reduction was carried out using the PolSALT pipeline (Crawford et al. in preparation). This pipeline performs basic reductions (e.g. bias subtraction, cross-talk correction, over-scan correction, and cosmic-ray rejections), wavelength calibration and spectrum extraction, whereafter the Stokes parameters are determined.

The linear polarization, and the position angle are plotted as a function of wavelength in Fig. 3.8. We show the observations from day 15 as a sample for both observations. The enhancement at the blue and red ends of the spectra might be due to low signal to noise ratio and hence we consider only the range between 4000 Å and 8000 Å in our analysis. The linear polarization is on average $\sim$ 0.3%. This may be due to the interstellar medium or intrinsic to the nova, or both. Rodrigues et al. (1997) studied the interstellar polarization toward the SMC. Nova SMCN 2016-10a is situated just south of their region III which has the smallest foreground polarization (P = 0.17%).

In order to estimate the contribution of the interstellar medium, we derive the linear polarization at different wavelengths using the Serkowski empirical relation (Serkowski, Mathewson & Ford, 1975; Wilking et al., 1980), and assuming $p_{\max}$ = 0.4% at λ = 4450 Å. The values are plotted in Fig. 3.8. The polarization is below the values derived for the interstellar medium.

Although, the interstellar polarization is low, it is nevertheless likely to be the primary source of polarization in our observations. There is no sign of de-polarization effect due to emission lines that is usually observed in case of polarization originating from novae (see, e.g., Ikeda, Kawabata & Akitaya 2000). The polarization in novae can originate either from scattering on dust or from a magnetic field, so if the observed polarization is indeed from the interstellar medium, the lack of intrinsic polarization can indicate the following: first, that there is no dust in the ejecta, consistent with the behaviour of the optical and infrared light-curves; secondly, there might be only a weak magnetic field, or none at all. Polarization is sometimes produced when electrons are accelerated in a magnetic field and emit cyclotron radiation, which is highly polarized. This is observed from magnetic CVs where the magnetic field of the WD confines the accretion stream from the red dwarf

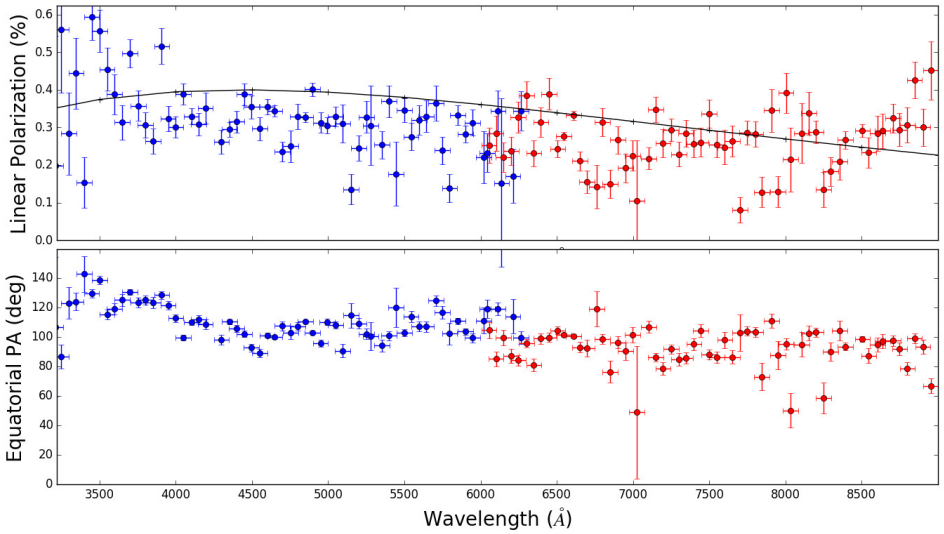

Figure 3.8: The linear polarization (top) and position angle (bottom) plotted against the wavelength from day 15. The blue and red points correspond to observations from the first and second spectral range respectively. The black solid line represents the values derived from the Serkowski relation, assuming $p_{\max} = 0.4\%$ at $\lambda = 4450$ Å, for the polarization due to the interstellar medium.

(see e.g. Warner 1995; Potter, Hakala & Cropper 1998; Rodrigues et al. 2005; Butters et al. 2009 and references therein).

3.4 X-ray observations

Swift (Gehrels et al., 2004) observations of nova SMCN 2016-10a started on 2016 October 15 (6.1 days after t_0). At this time, no X-rays were detected, but a 500 s grism spectrum showed a bright UV source with strong lines (Kuin et al., 2016). Additional observations were performed on the following two days, after which the cadence was lowered to once every few days. On 2016 November 07 (day 28.2), a bright, soft X-ray source was detected, at a count rate of 1.57 ± 0.06 count s^{-1}. In order to parameterize the onset of the SSS phase, multiple short snapshots of data were collected on 2016 November 11-12 (days 33-34), revealing the high amplitude flux variability seen in a number of other novae (e.g. Ness et al. 2009; Osborne et al. 2011; Bode et al. 2016). Observations then continued approximately every two to four days until 2017 May 12, with further observations following an eight day cadence running until 2017 June 25. Five further observations were obtained between 2017 July 8 and August 24. We note that the location of the SMC is not observable by *Swift* for up to 10 days each month because of the so-called “pole constraint”; this arises from the requirement that *Swift* not point too close to the Earth limb.

The *Swift* data were processed with HEASoft 6.19, and analyzed with the most up-to-date calibration files. The X-ray Telescope (XRT; Burrows et al. 2005) was operated in “Auto" state, so that the most appropriate mode (Windowed Timing - WT - when the source was above about 5 count s^{-1}; Photon Counting - PC - when the source was fainter) would be automatically chosen.

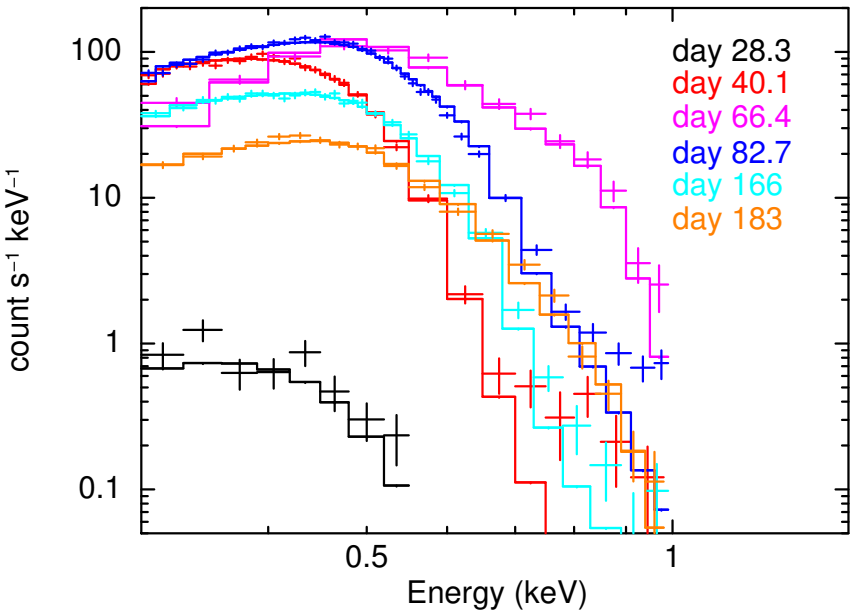

Figure 3.9: A sample of *Swift* X-ray spectra from days 28.3, 40.1, 66.4, 82.7, 166 and 183 since eruption (t_0), fitted in each case with the best-fit TMAP atmosphere model (see Fig. 3.10).

Reaching a peak count rate of $\sim 50\,\mathrm{count\,s^{-1}}$, the WT data did not suffer from pile-up[5], so a circular extraction region was used for these data. PC mode data above around $0.5\,\mathrm{count\,s^{-1}}$ were considered to be affected by pile-up, so, at these times, the core of the Point Spread Function was excluded, and corrected for, as required, using annular extraction regions. Background counts were estimated from nearby, source-free regions. In order to facilitate Cash statistic (Cash, 1979) fitting within XSPEC (Arnaud, 1996), the X-ray spectra were binned to ensure a minimum of 1 count bin^{-1}. Fitting using the Cash-statistic (C-stat; modified by XSPEC to work in the case of a background spectrum) provides less biased parameter estimates, even in the high-count regime (Humphrey, Liu & Buote, 2009).

The first X-ray detection of nova SMCN 2016-10a showed the emission already to be super-soft. At the distance of the SMC, any underlying shock emission would be likely to be faint and difficult to detect (cf. Nova LMC 2009a; Bode et al. 2016). Assuming optically thin emission at a temperature of 5 keV, and combining all the X-ray data collected, a 90% upper limit of $\sim 2 \times 10^{34}\,\mathrm{erg\,s^{-1}}$ can be placed on the unabsorbed 0.3-10 keV luminosity for any hard spectral component. The X-ray spectra were therefore fitted below 1 keV with an absorbed plane-parallel, static, non-local-thermal-equilibrium stellar atmosphere model (grid 003)[6]; samples of the spectra are shown in Fig. 3.9, and the parameter results from the fitting are shown in Fig. 3.10 while Fig. 3.11 focuses in on the early variability phase. This highlights the order of magnitude or more variability seen in the X ray count rate over an interval of two days as the SSS became established. The atmosphere grids typically provide good fits, with the reduced Cash statistic values mainly

[5] pile-up occurs when there is a high probability that several photons registering within a given CCD frame will have overlapping charge distributions.

[6] TMAP: Tübingen NLTE Model Atmosphere Package: http://astro.uni-tuebingen.de/~rauch/TMAF/flux_HHeCNONeMgSiS_gen.html

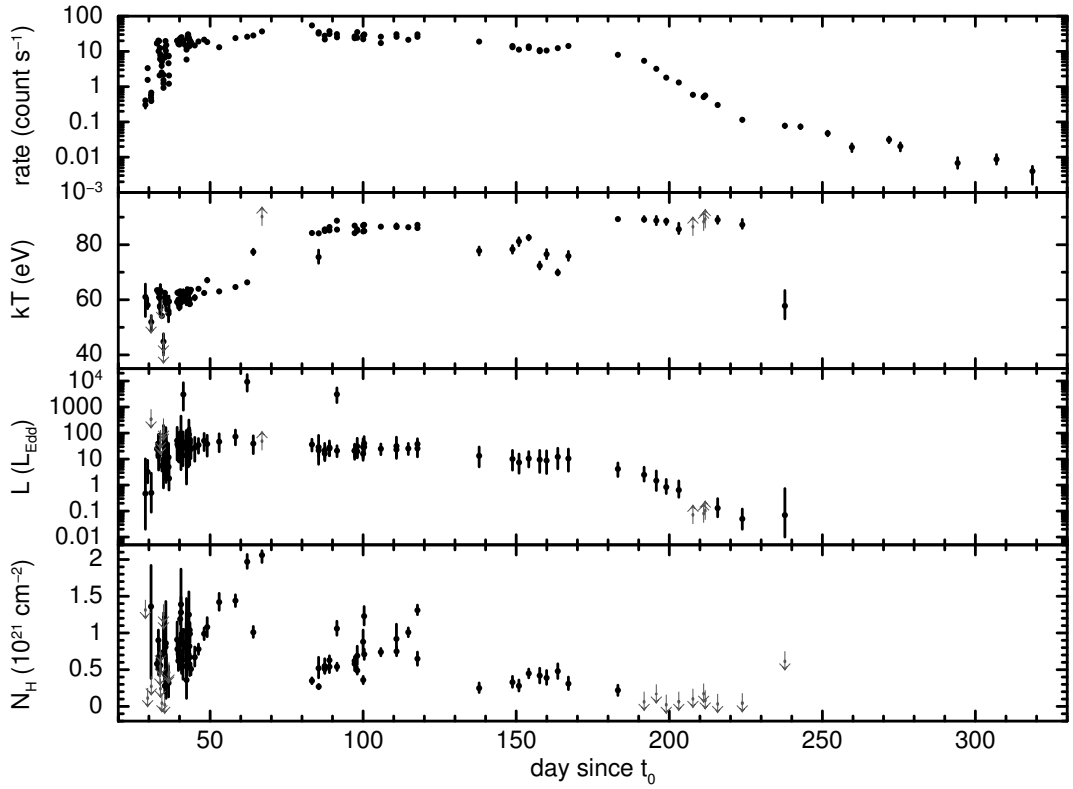

Figure 3.10: From top to bottom: the count rate, the temperature of the SSS emission, the bolometric luminosity in units of the Eddington value for a 1.2 $M_\odot$ WD, and the absorbing column density plotted against the days since t_0 (HJD 2457670.70). All parameters were determined from the TMAP model atmosphere fits as described in the text. Grey arrows indicate upper or lower limits (90 %) as necessary. For the luminosity calculation, a distance = 61 kpc is used.

lying in the range 0.8-1.2. The model atmosphere is limited to temperatures of between $\sim$ 38 eV and 91 eV, and a small number of the spectra for this nova had temperatures which hit the upper or lower limits of these bounds, suggesting the actual values are outside the range covered by the grids; these are shown by upper or lower limits in the second panel of Fig. 3.10 and Fig. 3.11 as necessary. The third panel of Figs 3.10 and 3.11 show the bolometric luminosity of the soft emission component, in terms of the Eddington luminosity for a 1.2 $M_\odot$ WD, assuming a distance of 61 kpc. The absorbing column was allowed to vary in the fits, and is shown in the bottom panel of Figs 3.10 and 3.11.

The temperature of the SSS was lower at earlier times, increasing suddenly after day 60, and reaching an apparent peak (as shown by the magenta spectrum in Fig. 3.9) at a time the source location unfortunately became non-observable by *Swift*. Following the emergence from the observing constraint (day 82.7), the temperature of the SSS emission was consistently high, $\sim$ 90 eV. We note that there are occasional fast changes in the X-ray count rate, for example around day 36.5, without corresponding variations in the spectral shape (i.e. the temperature remains approximately constant). This implies that there must be partial obscuration by clumps of high optical depth material at these times.

Even as the X-ray emission started to fade sharply, after day 180, the temperature remained

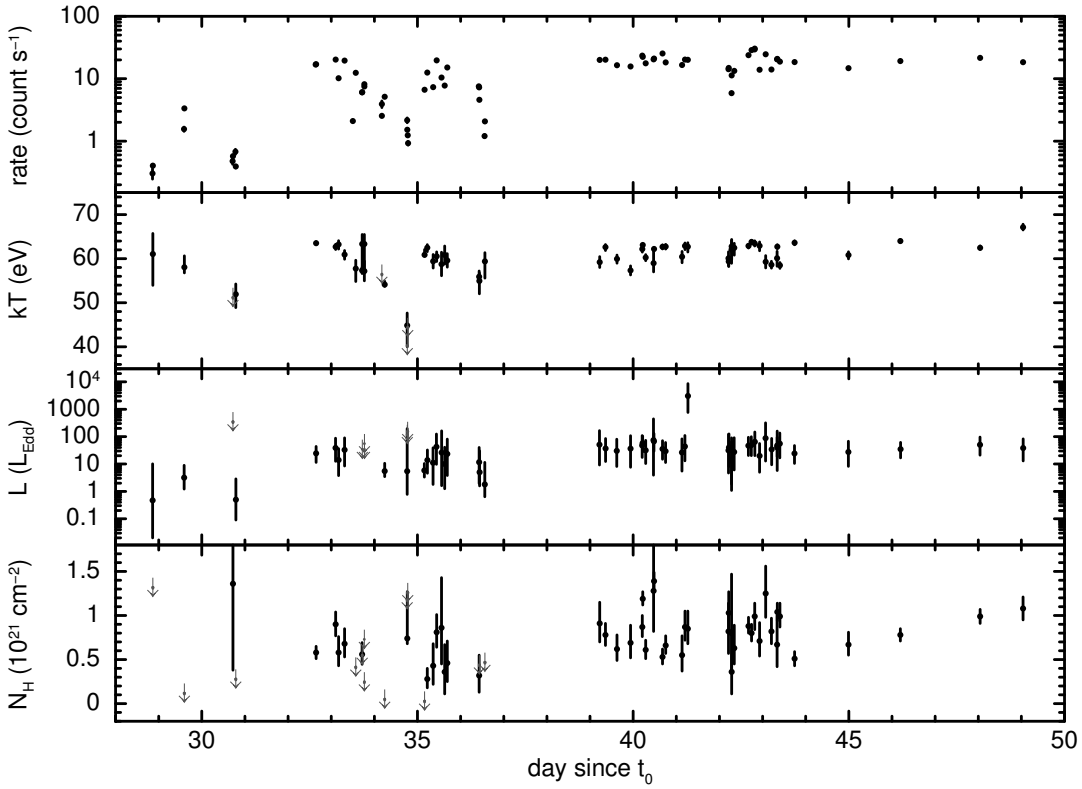

Figure 3.11: As for Fig. 3.10, but a zoomed-in version for the observations up to day 50 showing the early variability more clearly.

high, actually increasing slightly compared to earlier spectra. However, on day 237 a significant drop in temperature was observed. A final cooling of the X-ray emission is expected (Soraisam et al., 2016), and has been seen in other novae well-monitored by *Swift* (Page & Osborne, 2014). From day 242 onwards, the X-ray spectrum was not well fitted by the atmosphere model, with the shape better parametrized by an optically thin component with kT $\sim$ 80 eV. These data-sets have therefore not been included in panels 2-4 in Fig. 3.10. This adds to the evidence that the eruption has ended. As the X-rays faded, there was no longer any evidence for excess absorption above the interstellar value in the direction of the SMC (6×10^{20} cm^{-2}; Coe et al. 2011); in fact, some of the late-time upper limits suggest that the total absorbing column is below this value suggesting either an uncertainty in the absorption in the direction of the SMC, or a limitation of the emission model applied to the X-ray spectra.

Krautter et al. (1996) first showed that the X-ray emission from a fading post-eruption nova remains soft. The residual material is hot and extended and, even as the nuclear fusion comes to an end, the evolving WD decreases in radius (towards the quiescent radius of the star) at nearly the same luminosity for a while, leading to an increase in temperature.

A number of novae with bright X-ray emission have shown short period ($<$ 100 s) oscillations (e.g. Osborne et al. 2011; Beardmore et al. 2010; Ness et al. 2015). We have therefore searched for the presence of such oscillations in the soft X-ray light-curves of nova SMCN 2016-10a, following

the procedure outlined in Beardmore et. al. (in prep.).

WT light-curves were extracted with a time bin size of 17.8 ms over the energy range 0.3-1.0 keV (i.e. where the SSS emission is dominant). Periodograms were then computed from continuous light-curve sections up to 512 s duration – given the short nature of some of the XRT snapshots, those with exposures less than 256 s were rejected while those between 256–512 s were padded to a duration of 512 s using the mean rate for the interval. The average periodogram constructed from 80 individual ones spanning days 32.03 to 157.07 reveals no evidence for any oscillations with a timescale ranging from 1 - 256 s, with a 3 sigma fractional rms upper limit of 1.4 per cent.

3.5 UV observations

3.5.1 *Swift* UVOT photometry

UV/Optical Telescope (UVOT; Roming et al. 2005) photometric observations started on day 12 (2016 October 21) and continued until day 319 (2017 August 24). The initial photometry was obtained using the readout streak method (Page et al., 2013c), as the nova was too bright for normal aperture photometry, described in Poole et al. (2008). Each image was inspected and those where the spacecraft failed to achieve a lock-on were discarded. The observations were mainly in the *uvw2* band, with additional observations in the UVOT *uvm2* and *uvw1* bands, with central wavelengths: $uvw2$ = 1928 Å; $uvm2$ = 2246 Å; $uvw1$ = 2600 Å. See Tables A.7 and A.8 for a log of the observations. Fig. 3.12 illustrates the UVOT light-curve. There is a plateau in the UV emission between at least days 90 and 170, approximately coinciding with the main interval of bright, high-temperature, super-soft X-rays (Fig. 3.10). While it is hard to be definitive, due both to data gaps and small scale variability, the plateau in the *uvw2* filter may start slightly later and end slightly earlier than the soft X-ray plateau. Such a plateau phase has been seen in other novae (e.g. Kato, Hachisu & Luna 2008; Page 2013). Note that the SMARTS optical photometry shows a plateau as well, starting about day $\sim$ 100 (consistent with $uvw1$), and ending after day $\sim$ 130, during solar conjunction (see Fig. A.1).

Temporal structure was looked for in the *uvw2* photometry by computing the n = 2, 3, and 4 structure functions using the method described in Saxton et al. (2012). No evidence of a preferred timescale in the range of 0.01-10 d was found.

3.5.2 *Swift* UVOT spectroscopy

The initial *Swift* UVOT observations, which were obtained on 2016 October 15, 6.1 days after the eruption, used the UV grism. On the next two days, two further UV spectra were obtained (Kuin et al., 2016). The nova brightness was just below the limit where the flux calibration is possible (Kuin et al., 2015). The initial *Swift* Target of Opportunity observations were taken with no offset, slew in place, or photometry, to allow for quick scheduling of the observation.

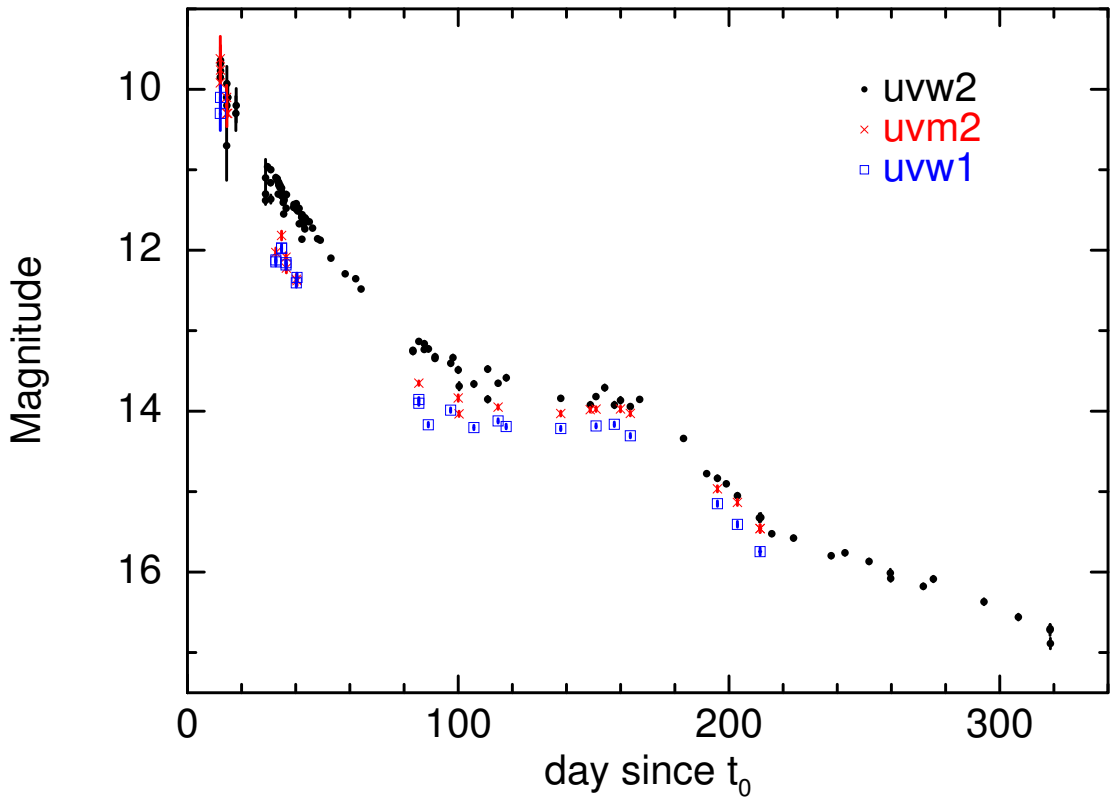

Figure 3.12: The UVOT light-curve of nova SMCN 2016-10a plotted against time in days since t_0.

Starting on 2016 October 21, we continued with UV grism clocked-mode (Kuin et al., 2015) observations every two days as scheduling allowed. These were typically taken at an offset of 5.6arcmin vertically in the detector plane so that the overlap of zeroth orders of field stars is limited to wavelengths shorter than about 2100 Å. For the periods 2016 November 7-14 and 2016 December 31 to 2017 January 6, the observations were made at no offset, and during the period of 2016 November 23 to December 12, the offset varied with the roll angle. The main effect is that in the spectra with no offset there are clear signatures of second order emission lines present, namely those at 1750 Å, 1909 Å, and 2143 Å in second order appear around 2880 Å, 3310 Å, and 3910 Å in the first order. These emission lines have also been found in other CO novae, like nova V339 Del (Page et al., 2014; Shore et al., 2016). The line at 3130 Å is likely the O III 3133.7 Å resonance line (Young, Feldman & Lobel, 2011) and is being fluoresced by the He II 304 EUV line. For that reason it is not affected by optical thickness effects as the other resonance lines are. The O II 2471 Å line is probably present, but weak and blended with other weak features.

The spectra were extracted from each image using the `UVOTPY` software (Kuin, 2014) with the calibration of Kuin et al. (2015). The grism images were inspected to identify contamination from zeroth and first orders of other sources. The spectra were summed in groups of 3 to 5 exposures to improve the continuum which retains a noise contribution from irreducible MOD-8 noise (Kuin et al., 2015). Prior to summing, the individual spectra were lined up by shifting them in pixel/bin space, re-computing the wavelengths after the shift. This is needed as the dispersion changes from the short to long wavelengths. The dates of the summed spectra are provided in Table A.1. The

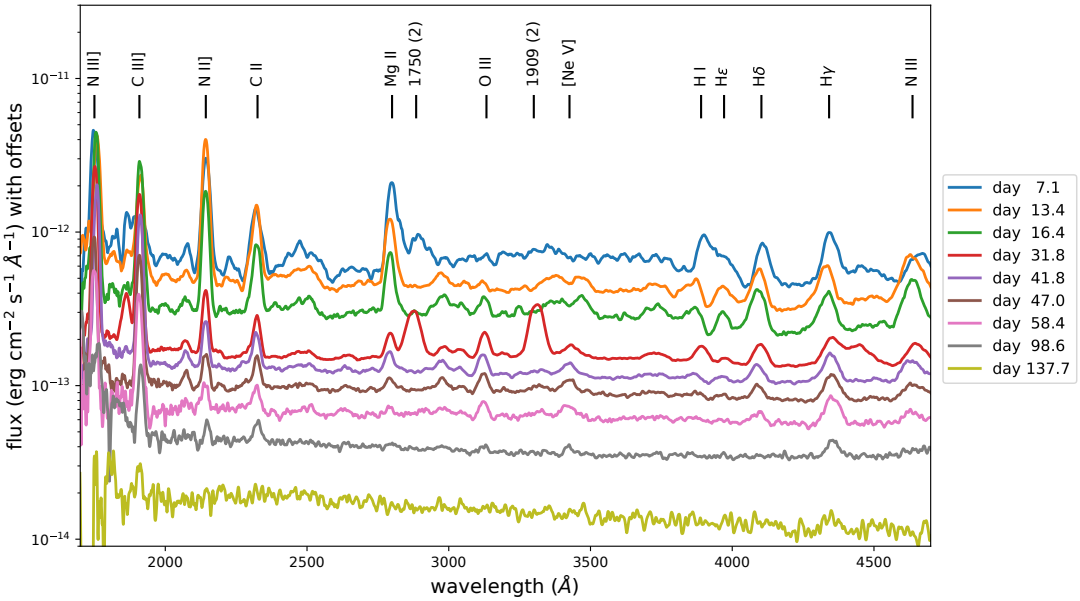

Figure 3.13: The UV grism summed spectra. For clarity the spectra are all shifted vertically, starting with an offset of 1e-14 then incrementally by 2e-14 in flux. The numbers to the right are days since eruption (t_0).

spectra are illustrated in Fig. 3.13. Up to day 9 there is unresolved absorption in the 2550-2650 Å range consistent with the Fe-curtain (optically thick) still being weakly present. The UV spectra show strong emission from N III] 1750 Å, C III] 1909 Å, N II 2143 Å, C II 2324 Å, Mg II 2800 Å, and [Ne III] 3868 Å, 3967 Å. Up to day 43 we see the Al III 1860 Å resonance line, while the lines from O III 3130 Å and [Ne V] 3346 Å, 3426 Å become prominent after day 28, suggesting a gradual increase in ionization. After day 117 post-eruption, the UV grism data (4 ks summed exposure) become too noisy showing only evidence of the continued presence of the N III] 1750 Å and C III] 1909 Å lines.

The line flux was determined by integrating the flux above the nearby continuum. Some lines were difficult to measure. The [Ne V] 3346 Å line suffers from the nearby C III] 1909 Å line in the second order which is offset from the first order, but presents such a large coincidence loss pattern that it causes a re-distribution of the line flux (e.g. Kuin et al. 2015). We measured the flux across the pattern. Fig. 3.14 illustrates the evolution of the line fluxes with time.

The Mg II 2800 Å and C III] 1909 Å were compared to establish that no coincidence loss affects the C III] 1909 Å line fluxes. The reason we believe that coincidence loss is corrected appropriately is that the Mg II 2800 Å line flux is comparable and lies in the much more sensitive range of the grism where it would be affected more.

Having established this, the initial rise in the C III] 1909 Å flux prior to day 16 is real and different from the flux changes seen in the Mg II 2800 Å resonance line. Other resonance transitions are present, N II 2143 Å, C II 2324 Å, and Al III 1860 Å, and they all show a similar behaviour, where the line flux shows a decrease from the first spectrum observed at day 6.

In the O III 3130 Å line, which is probably optically thin because it is caused by fluorescence

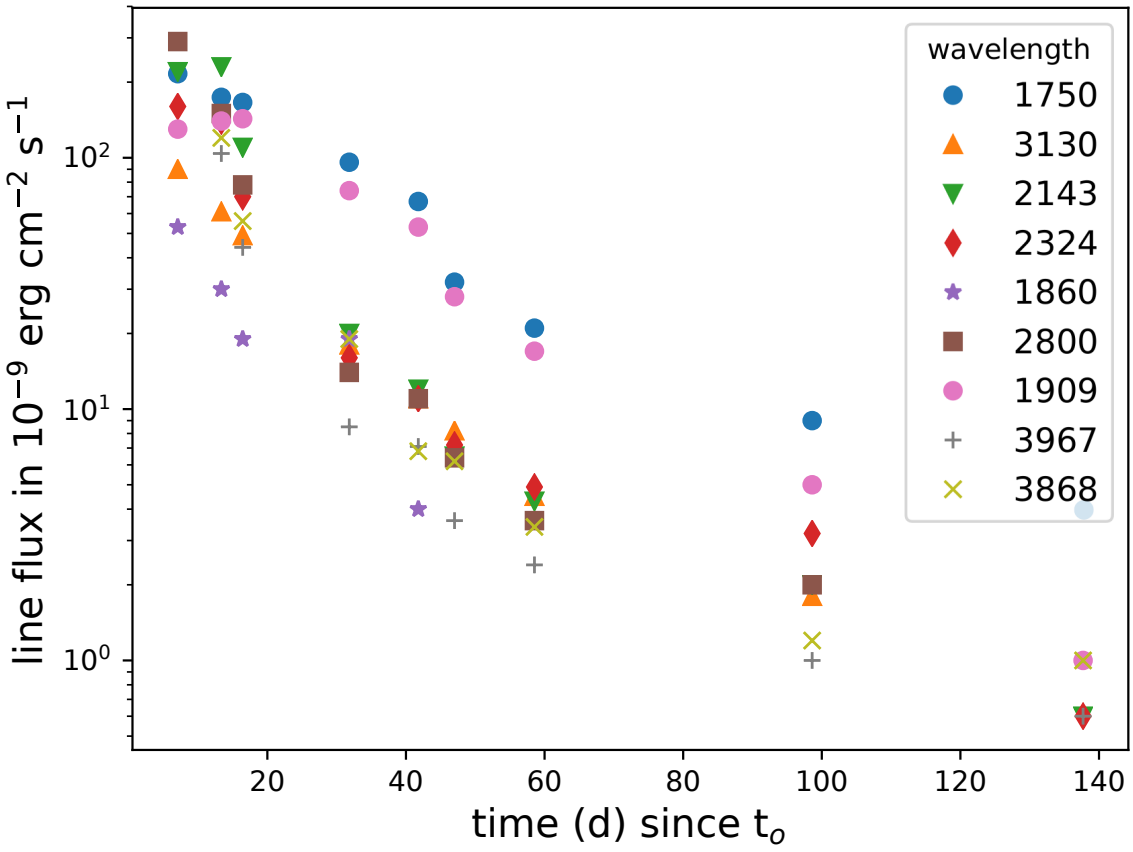

Figure 3.14: The evolution with time post-eruption of the line fluxes in the UVOT spectra, colour and symbol coded based on the lines rest-wavelength.

from the He II 304 EUV line, we observe a nearly straight slope, whereas in the permitted lines the flux decrease is initially steeper to join in the same rate of decrease as all lines some time after day 20. As in the photometric data, after day 60 the slope changes, and the line flux evolution is seen to be consistent with the photometric light-curve (see Fig. 3.12) taking into consideration the large uncertainties due to the large S/N in the late time spectra. The steady decrease in of the O III 3130 Å line flux is probably due to the source function of the He II 304 EUV line emission decreasing.

The different temporal development of the line fluxes is possibly due to opacity and density effects. In the resonance lines we can approximate the emission originating from an optical depth of one. Comparison of the temporal development of the optically thick lines to the optically thin line might be interpreted that the initial flux in the optically thick lines is higher. This can be explained if the flux source of the optically thick lines is dependent on the earlier and higher flux. Assuming that the ejecta are moving at a nearly constant speed, so that there are no frequency shifts, the optically thick line may trap some of the earlier high flux radiation. A likely mechanism would be the back-scatter of the WD radiation by the ejecta. By that means the radiation density in the line is enhanced within the confines of the ejecta and the flux in the line is partly from the earlier radiation density. When the line becomes effectively optically thin (i.e., photons will escape through the

shell, even when the optical depth is still larger than one), the temporal development of the line flux in the optically thick lines will start to match the optically thin line.

What this tells us is that the ejecta up to at least day 20 are not transparent, consistent with the SSS flux not being observed until day 28. It also suggests that the central source is still mostly covered by optically thick ejecta in all directions in these lines, i.e, there is no large hole in the ejecta letting the back-scattered radiation field escape before that time. In the context of asymmetric ejecta (Shore et al., 2011), this means that at least some matter is ejected in all directions, though the mass in certain directions may be much larger.

Another explanation for the initial rise in the line fluxes of C III] 1909 Å and N III] 1750 Å might be due to the decreasing density as the ejecta expands, which leads to a reduction of the opacity for UV radiation and therefore increasing the flux temporarily. In this case, the following decrease in the line flux of these two lines would be just due to the decrease of the emission from the WD at the end of the eruption, which is consistent with the evolution of the UV light-curve.

3.6 Discussion

3.6.1 Distance Modulus

While the mean distance to the SMC is around 61 kpc this galaxy is very extended in the line-of-sight (Caldwell & Coulson, 1986; Jacyszyn-Dobrzeniecka et al., 2016), with Cepheid variables distributed from <54 kpc to >76 kpc. In this Section we will try to derive an estimate of the distance to the nova using the available methods and test at the same time the usefulness of these methods.

Buscombe & de Vaucouleurs (1955) suggested that all novae have a similar absolute magnitude 15 days after eruption. Cohen (1985) estimated this as $M_{V,15} = -5.60 \pm 0.45$ using 11 objects, while Downes & Duerbeck (2000) refined the value to $M_{V,15} = -6.05 \pm 0.44$ using 28 objects. Interstellar reddening towards the SMC is small and for our analysis we assume $A_V = 0.11 \pm 0.06$ and $A_I = 0.07 \pm 0.06$, using relations (4) and (5) in Haschke, Grebel & Duffau (2012) and the average value of $E(V-I)$ for the SMC from Haschke, Grebel & Duffau (2011). Using the EWs of the Na I D absorption lines (Fig. 3.15 - EW_{D1} = 0.13±0.02 and EW_{D2}= 0.17±0.02), and their relationship to the interstellar extinction (as specified by Munari & Zwitter 1997 and Poznanski, Prochaska & Bloom 2012) we obtain values of A_V consistent with our assumptions. Most likely the reddening contribution from the SMC is very low (see Section 3.6.3.1 and the discussion about the radial velocities of the Na I D absorption lines).

At day 15 from the eruption this SMC nova was at an apparent magnitude $V = 12.30 \pm 0.01$ or $V_0 = V - A_V = 12.19 \pm 0.07$. Using the Downes & Duerbeck (2000) relation this gives $(m-M)_0 = 18.23 \pm 0.51$ and a distance $d \sim 44^{+11}_{-9}$ kpc.

After a survey of 24 novae in M87, Shara et al. (2017b) recently found that the minimum scatter of novae absolute magnitude occurs at day 17 in the V-band and day 20 in the I-band. Using the Hubble Space Telescope F606W and F814W filters for the V and I bands respectively, they found

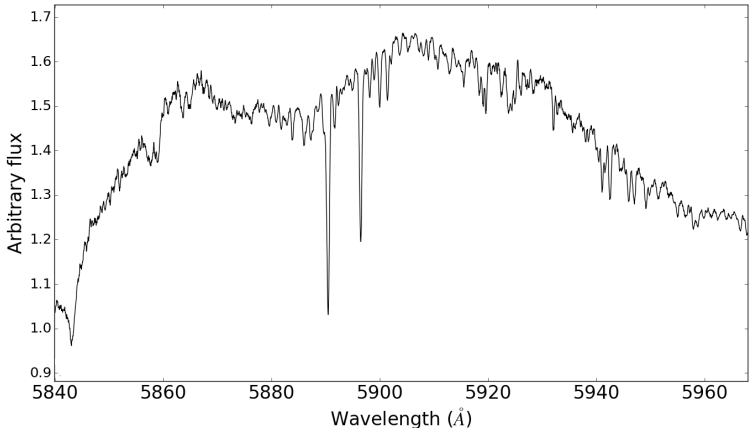

Figure 3.15: The Na I D doublet absorption lines D1 (5896.6 Å) and D2 (5890.6 Å) from the high resolution spectrum of day 8.

$M_{V,17} = -6.06 \pm 0.23$ and $M_{I,20} = -6.11 \pm 0.34$. At day 17 from maximum light, nova SMCN 2016-10a was at V = 12.60 ± 0.01 or V_0 = 12.49 ± 0.07. Using the absolute magnitude at day 17 from Shara et al. (2017b) gives $(m - M)_0$ = 18.55 ± 0.30 and a distance $d \sim 51^{+7}_{-6}$ kpc. At day 20 from maximum light, nova SMCN 2016-10a was at $I = 12.08 \pm 0.01$ or $I_0 = I - A_I = 12.01 \pm 0.07$. Using the absolute magnitude at day 20 from Shara et al. (2017b) gives $(m - M)_0 = 18.12 \pm 0.41$ and a distance $d \sim 42^{+8}_{-7}$ kpc.

The nova is located about two degrees south of the central body of the SMC and outside of the region examined by Subramanian et al. (2017). Nevertheless, it is worth noting that these authors identify a red clump population at $\sim 12 \pm 2$ kpc in front of the main body of the SMC, that may have been the result of tidal stripping. Other explanations for the discrepancies in the distance: (1) the validity of using $M_{V,15}$ as a distance indicator which was questioned by several authors (see, e.g., Jacoby et al. 1992; Ferrarese, Côté & Jordán 2003; Darnley et al. 2006); (2) These relations are supposed to give a rough estimate of the distance and not accurate values; (3) underestimating the absolute magnitude derived using the relations of Downes & Duerbeck (2000) and Shara et al. (2017b). The latter derived their relations using a sample of novae in M87, hence, a parent galaxy with different metallicity than the SMC; (4) Although, the extinction is not expected to play a major role relative to the direction of the nova, an overestimation in the extinction values adopted can lead to a slight underestimation in the distance (~ 2 kpc). We conclude that the nova is within the SMC and possibly foreground of the bulk of the stars in the field. A less likely possibility that the nova belongs to the Galaxy is discussed in Section 3.6.3.1. On the assumption that it is associated with the SMC we will adopt a distance of 61 ± 10 kpc throughout the rest of the chapter. The assumed distance puts the nova within the extended SMC.

3.6.2 The progenitor system

During quiescence, the emission from a CN system is mainly from the secondary star and the accretion disk (depending on its inclination relative to the line of sight). The emission from the WD is almost negligible during quiescence. The OGLE survey has been monitoring the target since

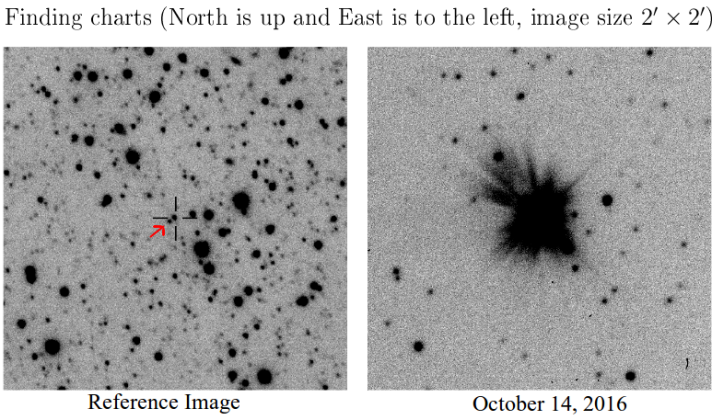

Figure 3.16: Left: OGLE finding chart of the progenitor system before the eruption. Right: image of the field 5 days after the eruption.

2010. Fig. 3.16 shows a finding chart of the object during quiescence (left) and an image of the object during the eruption (right). The star South-East of the nova (indicated with the red arrow) is $\sim$ 2.1 arcsec away.

In quiescence, the target shows irregular variability that might be due to variations in the mass-transfer rate (see Fig. 3.1). No periodic variability appears in the light-curve of the progenitor that can lead us to constrain the orbital period of the system. This means that the orbital plane of the system may be oriented face-on to the observer, so that the contribution of the disk to the total emission from the system might be large. During quiescence, the progenitor is observed at $\langle V \rangle \sim 20.70$ and $\langle I \rangle \sim 20.55$. The changes in V and I during quiescence (Fig. 3.1) might reflect the contribution of a bright disk that is showing temporal variability.

We found several sources less than $\sim$ 1.0 arcsec from the nova in archival data from: USNO-B1 catalogue (Monet et al., 2003) ($B = 20.17$ and $R = 20.0$); the Magellanic Cloud Photometric Survey (MCPS; Zaritsky et al. 2002) (U = 19.71 $\pm$0.14, B = 20.44 $\pm$0.07, and V = 20.58 $\pm$0.04); GALEX catalogues (Bianchi et al., 2011) (NUV = 20.57 $\pm$ 0.20 and FUV = 20.53$\pm$0.33). After checking several charts and images of the field from OGLE, MASTER and Simbad (Wenger et al., 2000), it seems likely that all these observations refer to the nova progenitor. These data along with the OGLE data, allow us to place the progenitor on B versus $B - R$, V versus $B - V$, I versus $B - I$ and I versus $V - I$ colour-magnitude diagrams (CMDs, Fig. 3.17). The B versus $B - R$ indicates a system which may have a sub-giant companion (SG-novae). However, the three other CMDs indicate a system with a main sequence companion (MS-novae). The inconsistency of the B versus $B - R$ with the other plots could be understood if the progenitor had strong Hα emission. It is worth noting that B, V, R, and I bands are very sensitive to the emission from the disk. The optical colours depend sensitively on the ratio of the disk to stellar photospheric emission.

Darnley et al. (2012) show that, ideally, placing the system on a CMD using NIR colours can give us an insight into the secondary star type. The NIR colours are more sensitive to the emission from the secondary than that from the disk. With lack of observations in NIR for the progenitor in the archival data, it is difficult to say much about the secondary star.

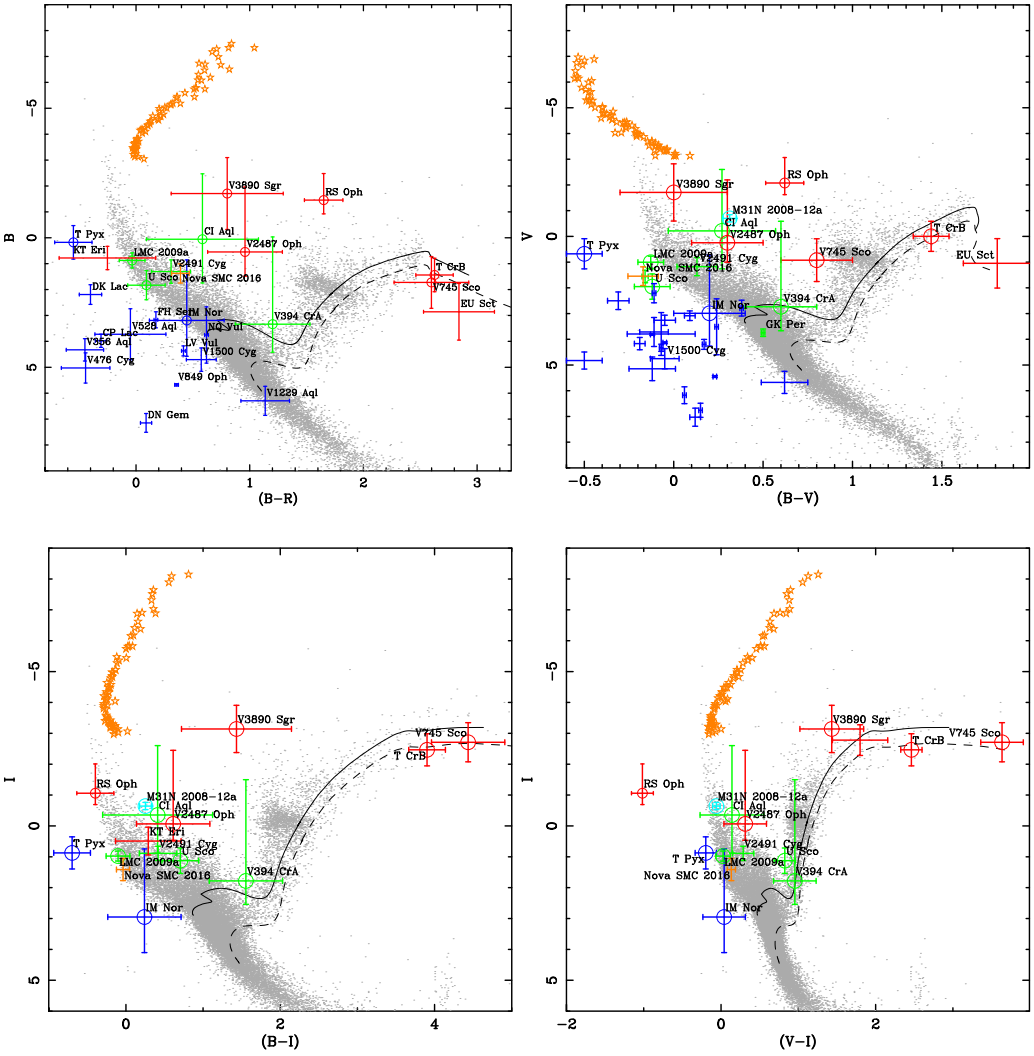

Figure 3.17: Colour-magnitude diagrams showing stars (grey dots) from *Hipparcos* data set (Perryman, 1997) with parallax errors $< 10\%$. These stars have been transformed to the distance and extinction of the SMC. *BVI* photometry is taken directly from the *Hipparcos* catalogue, R photometry is taken from the USNO-B1 catalogue (Monet et al. 2003; via the VizieR database, Ochsenbein, Bauer & Marcout 2000). The blue points represent Galactic MS-novae, the green points represent Galactic SG-novae and red points represent Galactic red giant novae (RG-novae) (see Schaefer 2010; Darnley et al. 2012, and references therein). The known recurrent novae in this sample have been identified with an additional circle. Orange points represent nova SMCN 2016-10a during quiescence. The orange stars indicates the track of nova SMCN 2016-10a from day 11 till day 108 post-eruption. M31N 2008-12a is shown in light blue due to its uncertain donor.

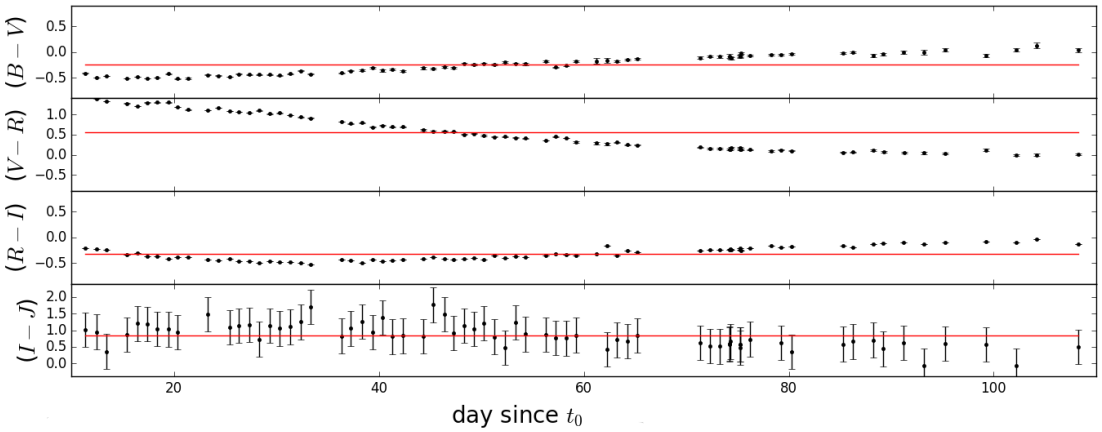

Figure 3.18: Optical and NIR broadband colour evolution of nova SMCN 2016-10a between day ∼11 and day ∼100 post-eruption. The red line is the average of the values between the two dates.

3.6.3 Eruption and early decline

The system was last observed by OGLE before the eruption on 2457667.67 at $V = 20.65 \pm 0.03$. Adopting a distance of 61 ± 10 kpc and $A_V = 0.11 \pm 0.06$ will result in $M_V = +1.61 \pm 0.45$ three days before the eruption. Although the MASTER VWF camera measurements are not precise V-band photometry, the measurements can be considered as an approximation of V-band photometry (see Section 3.2.3). Hence, we consider $V_{\max} \approx 8.5 \pm 0.1$ which results in $M_{V,\max} \approx -10.5 \pm 0.5$. We can thus constrain an approximation for the eruption amplitude as $A \approx 12.1 \pm 1.0$. The amplitude of the eruption is not only related to the eruption itself, but also to the luminosity of the donor during quiescence. Hence, such a high eruption amplitude might also indicate a sub-luminous donor, such as a main sequence one. The eruption amplitude agrees well with the amplitudes given in the A versus t_2 relationship for CNe in Warner (1995), where CNe of similar speed class to SMCN 2016-10a, with a main sequence donor, are characterized by $A \geq 12$.

3.6.3.1 The brightest nova discovered in the SMC?

If nova SMCN 2016-10a is indeed in the SMC, $M_{V,\max} \approx -10.5 \pm 0.5$ will make it the brightest nova discovered in the SMC, and probably one of the brightest ever discovered. At $M_{V,\max} \approx -10.5 \pm 0.5$ it is at least as bright as V1500 Cyg and CP Pup. These two novae are considered the brightest nova events ever recorded (see, e.g., Warner 1985; Stockman, Schmidt & Lamb 1988; Hachisu & Kato 2006; Shafter et al. 2009). If the nova is in the foreground of the SMC at $\sim 46 \pm 10$ kpc (the mean value of the three distances derived in Section 3.6.1), we derive $M_{V\max} \approx -9.9 \pm 0.6$ meaning it is still a very luminous nova ($M_{V\max} \leq -9.0$; Shafter et al. 2009). If the nova belongs to our Galaxy, which is very much less likely, then $M_{V\max}$ is greater than -6.0. In this case the nova may be under-luminous and possibly classified as a faint fast nova (see, e.g., Kasliwal et al. 2011; Shara et al. 2017a).

The first value is in good agreement with the SMARTS V-band photometry. The nova mag-

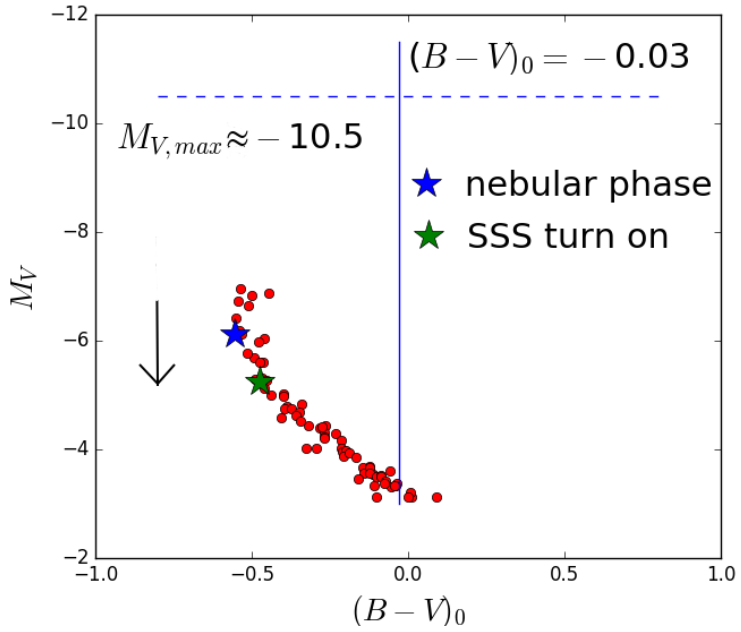

Figure 3.19: Colour-magnitude diagram of SMCN 2016-10a showing M_V against $(B-V)_0$ (red dots) at a distances $d = 61$ kpc. The evolution spans from day 12 to day ∼100 post-eruption. The black arrow indicates the evolution of M_V with time. The blue horizontal dashed line indicates the maximum absolute magnitude. The blue vertical line indicates the intrinsic colours for an optically thick wind free-free emission (see Hachisu & Kato 2014b and Darnley et al. 2016 for further details). The green and blue stars represent the start of the SSS phase (day 28) and the nebular phase (day 20) respectively.

nitude in the V-band has been measured as 12.14 (V_0 = 12.03 ± 0.06) at $t = 11.3$ d. We estimate $t_3 = 7.8 \pm 2.0$ d which is < 11.3 d, meaning that the nova reached a maximum brightness in the V-band smaller than 12.03 ± 0.06 − 3.0 = 9.03 ± 0.06. This value leads us to constrain a maximum on $M_{V,\max} < -9.9 \pm 0.5$ (at d = 61 ± 10 kpc).

In order to constrain the distance to the nova, we derived radial velocities from the Na I D doublet absorption lines at 5890 Å and 5896 Å. The lines are detected at ∼ 5890.6 Å and ∼ 5896.6 Å, showing a red-shift of $\sim 16 \pm 2\,\mathrm{km\,s^{-1}}$ in all five HRS spectra. The origin of these lines is either circumstellar or interstellar material. The line widths are too narrow to be produced in an outflow and hence they come from a static region (see Fig. 3.15). Since the average radial velocity of the SMC is $\sim 160\,\mathrm{km\,s^{-1}}$ (Neugent et al., 2010), these absorption lines are due to Galactic interstellar medium absorption. Note that if these absorption lines originate from the SMC, they should be at ∼ 5893 Å and ∼ 5899 Å. In conclusion, none of the three possibilities of the distance to the nova can be ruled out. But it is still very likely that the nova is in the SMC or foreground of the SMC, and the interstellar absorption is from the Milky Way.

3.6.3.2 Post-eruption colour evolution

In Fig. 3.18 we present the evolution of different broadband colours during the early decline until ∼ 100 days post-eruption. We only include the days when the magnitudes of different broadband colours are measured quasi-simultaneously.

For objects that show emission lines in their spectra, the emission lines can be a significant contributor to the flux. Hence, the evolution of the colours is an indication of the evolution of both the lines and the continuum (Bode et al., 2016). In the optical, the emission lines contribute strongly to the B-band flux, especially the Balmer lines (Hβ, Hγ, Hδ, and Hϵ) during the early days after the eruption. In the R-band, Hα is a strong contributor to the flux. The O I lines are also an important contributor to the I-band flux during the early decline. The $B-V$ broadband colour evolution starts bluer at $\sim$ 11 days after eruption, showing a monotonic evolution toward redder colours until 100 days post-eruption. This evolution of $B-V$ can be explained by the dimming of the Balmer emission lines during the decline from maximum light which affect the flux in the B-band, followed by the emergence of the nebular [O III] lines, at the blue edge of the V band, after the start of the nebular phase (see section 3.6.5).

The evolution of $V-R$ starts redder and becomes bluer monotonically with time, which in turn can also be attributed to the dimming of Hα. The $R-I$ evolution shows slight variation around the mean, probably due to the relative variation of the O I lines compared to Hα. In the NIR, the evolution of the broadband colours show no trend with time. They show slight random changes around the mean, but the uncertainty on the data is very high and hence it is difficult to say anything about the variation of these colours.

Hachisu & Kato (2016b) have demonstrated that the evolution of the colours, during and after the eruption, is different for systems hosting a red giant companion (RG-novae) than for SG-novae or MS-novae. They showed that for the RG-novae, the colour evolution follows a vertical track, on the CMD, along the two lines of optically thick wind and optically thin wind free-free emission intrinsic colours, respectively $(B-V)_0 = -0.03$ and $(B-V)_0$ = 0.13 (see also Hachisu & Kato 2014b; Darnley et al. 2016). For SG- and MS-novae, the colour-magnitude tracks show an evolution towards bluer colour to reach a turning point, close to the start of the nebular phase, from where the colours evolve backward and become redder.

In Fig. 3.19 we present a CMD, illustrating the evolution of M_V against $(B-V)_0$, for nova SMCN 2016-10a. The track shows an evolution similar to novae with a sub-giant or a main sequence secondary (see fig. 7 in Darnley et al. 2016). Although we lack broadband observations during the first 10 days after maximum optical light, the available data show a blue-ward evolution before the turning point into a red-ward evolution near the start of the nebular phase. The evolution of the CMD can be interpreted as follows: at the very early phase after maximum optical peak, the colours show a gradual change towards the blue, corresponding to the free-free emission phase of the nova spectrum. Later, after maximum, the colours becomes bluer due to the strong emission lines within the B-band. Then, these lines start to fade and the turning point starts. Close to the start of the nebular phase, the colours turn red-ward due to the emergence of nebular lines such as [O III] 4959 Å and 5007 Å (see Section 3.6.5) at the blue edge of the V-band (Hachisu & Kato, 2016b).

Fig. 3.20 illustrates distance- and extinction- corrected spectral energy distribution (SED) plots, showing the evolution of the post-eruption SED of nova SMCN-2016-10a. SMARTS and *Swift* UVOT data are combined to form the SED across the NIR, optical, and UV spectral range.

We only plot the data that have corresponding observations in all the bands. In the optical, the evolution of the SED plots is affected by the line emission as discussed for the CMD and colour evolution plots. Hα contributes strongly in the, initially bright, R band. Since nova behaviour during and after peak is similar to blackbody emission (see, e.g., Gallagher & Ney 1976; Bode & Evans 2008), we can conclude from Fig. 3.20 that the peak of emission is beyond the *uvw2* of *Swift* UVOT (shorter than 2000 Å) throughout the 12-100 day interval. At optical maximum the spectra of CNe show a blackbody emission peaking in the optical with temperatures around 10,000 K (see, e.g., Bode & Evans 2008 and references therein). A simplified model of an evolving pseudo-photosphere, in the optically thick ejecta, has been adopted to re-produce the evolution of the post-eruption emission from novae (see, e.g., Bath & Harkness 1989). The temperature of the photosphere reaches its lowest at the optical peak, and then increases with time while the radius of the photosphere shrinks. This increase in the temperature shifts the blackbody temperature towards the UV. Since nova SMCN 2016-10a is a very fast nova and since the first SED plot is around 12 days post-optical-maximum, it is expected that the SED peaks toward the UV. This peak is beyond the *uvw2* of the *Swift* UVOT, which indicates temperatures above 15,000 K.

3.6.4 Mass of the WD and the ejected envelope

It is now well understood that several parameters other than the WD mass affect nova eruptions, including the accretion rate on the WD surface, the WD temperature (and thus luminosity), the WD chemical composition, and the chemical composition of the accreted matter (see, e.g., Yaron et al. 2005; Hillman et al. 2014; Shara et al. 2017a, and references therein). However, it is widely accepted that the WD mass is the critical factor in nova eruptions, and it has a great effect on the light-curve morphology and decline rate. Novae with high mass WDs ($M_{\rm WD} > 1.0\,{\rm M}_{\odot}$) are expected to show fast declines in the optical light, while novae with low mass WDs are expected to show slow optical decline rates. The Hillman et al. (2016) models predicted that any novae with $t_2 < 10$ days must contain a WD with a mass ≥ 1.25 M$_{\odot}$.

The mass of the accreted envelope is also related to the decline rate and the WD mass. We use the empirical relation from Shara et al. (2017a) to estimate the accreted envelope mass:

$$\log M_{\rm env} = 0.825 \log(t_2) - 6.18\,,$$

resulting in $M_{\rm env} = (0.20 \pm 0.05) \times 10^{-5}\,{\rm M}_{\odot}$, which is in good agreement with Hachisu & Kato (2016b) models for fast novae. One should note that the empirical relation presented in Shara et al. (2017a) was derived by fitting novae from M87, M31, LMC, and the Milky Way.

3.6.4.1 SSS and $M_{\rm WD}$

The timescale of the SSS phase and uncovering the X-ray source is proportional to the hydrogen ejected envelope mass and inversely proportional to the ejection velocity. Krautter et al. (1996) relate the SSS phase turn-on to the mass of the ejected H envelope and the ejecta velocity by: $t_{\rm on} \propto M_{\rm H}^{1/2} v_{\rm ej}^{-1}$. With relatively low envelope mass and high ejecta velocity, the time since eruption

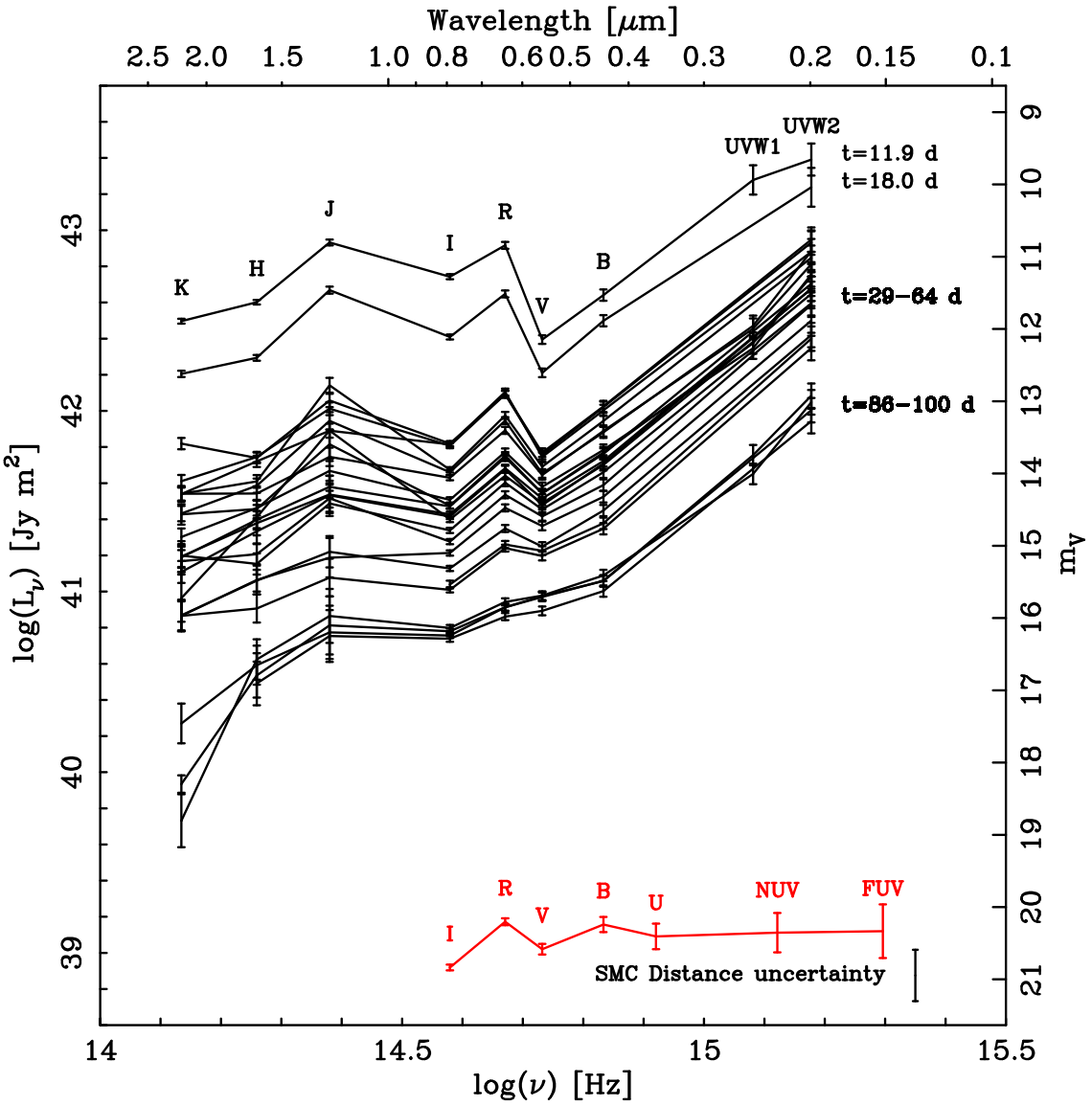

Figure 3.20: Distance- and extinction-corrected SED plots showing the evolution of the SED of nova SMCN 2016-10a eruption. The error bars include contributions from the photometric and distance uncertainties. Red data at the bottom present the quiescence SED, using the MCPS UBV, USNO-B1 R, OGLE I and GALEX NUV/FUV.

to observe the SSS phase should be relatively short, which is the case for nova SMCN 2016-10a with $t_{\rm on} = 28$ days. This value is comparable to other novae of the same speed class (see, e.g., Bode et al. 2016 and references therein). $t_{\rm on}$ is dependent on the mass of the WD, hence for systems with high $M_{\rm WD}$, $t_{\rm on}$ is expected to be shorter than for systems with low $M_{\rm WD}$. The SSS phase of RS Oph (Osborne et al., 2011), the first nova monitored in detail by *Swift*, was first detected on day 26 after eruption, very similar to nova SMCN 2016-10a, while V745 Sco (Page et al., 2015) provided an extreme example, where t_{on} was only 4 d. An extra-galactic perspective is given by nova LMC 2012 (Schwarz et al., 2015), with $t_{\rm on} = 13 \pm 5$ d. All of these novae are likely examples of high WD mass systems. In comparison, nova SMC 2012 (OGLE-2012-NOVA-002) was a much slower system, not seen as a supersoft source until around nine months after the first optical detection (Page et al., 2013b).

The turn-off time, since eruption, for nuclear burning ($t_{\rm off}$) is also strongly dependent on $M_{\rm WD}$, more precisely it is inversely proportional to the WD mass. MacDonald (1996) found $t_{\rm off} \propto M_{\rm WD}^{-6.3}$. Novae with similar $t_{\rm off}$ to that of the nova SMCN 2016-10a are expected to have a WD mass between 1.1 $M_\odot$ and 1.3 $M_\odot$ (see, e.g., Krautter et al. 1996; Balman, Krautter & Ögelman 1998; Osborne et al. 2011 and references therein). Despite RS Oph having a similar $t_{\rm on}$ to SMCN 2016-10a, its $t_{\rm off}$ is noticeably shorter, at ~ 58 d (Osborne et al., 2011), implying the WD in the RS Oph system is more massive (see also Brandi et al. 2009; Booth, Mohamed & Podsiadlowski 2016).

Henze et al. (2014) monitored novae in M31 presenting a series of correlations relating SSS parameters. The values of $t_{\rm on} = 28$ d and $t_{\rm off} = 180$ d lie within the scatter of their results. The luminosity-temperature models in Wolf et al. (2013) (see also Sala & Hernanz 2005) suggest a high (~ 1.25–1.3 $M_\odot$) WD mass for the ~ 90 eV SSS temperatures measured for nova SMCN 2016-10a. Thus, the X-ray data agree with the conclusion from the optical that the WD is likely of high mass.

3.6.5 Spectroscopic classification

The spectroscopic and photometric data leave no doubt that the object is a CN eruption. The spectral evolution of nova SMCN 2016-10a shows initially a He/N spectrum dominated by broad prominent Balmer, He, N, and O emission lines (Williams & Darnley, 2016). A FWHM of ~ 3500 km s^{-1} was measured for Hα and Hβ suggesting expansion velocity of around 1800 km s^{-1}. This moderately high expansion velocity, as well as the broad, jagged profiles of the Balmer emission lines (see section 3.6.6.1), are features of the He/N class that is characterized by a HWZI larger than 2500 km s^{-1} (Williams, 1992). The large HWZI values for the He/N novae are due to high ejecta velocities, these arise from the initial explosion on the WD. Before the nebular phase of nova SMCN 2016-10a, we note similarity with the spectrum of KT Eri, also a very fast He/N nova. However, when KT Eri enters the nebular phase the blended lines of N III 4638 and He II 4686 split and a narrow He II emerges and grows becoming stronger than Hβ (see fig. 2 in Imamura & Tanabe 2012) which is not the case for nova SMCN 2016-10a.

In the spectra of day 20 to 23, the forbidden nebular [O III] transitions at 4363 Å, 4959 Å and 5007 Å emerge while the nitrogen lines start to fade. The blending of the [O III] 5007 Å with the

N II 5001 Å gives an artificially high [O III] 5007/4959 flux ratio at this stage. This flux ratio and the present emission lines indicate that the nova is in transition and had started to enter the optically thin nebular phase by the end of October leading to a correct prediction of the imminent SSS turn-on (Darnley & Williams, 2016). These forbidden lines are expected to initially emerge from low density gas due to the expansion of the nova (Williams, 1992).

The spectra of day 27 and 32 show that the nova had entered the nebular phase with the He II 4686 Å line becoming stronger than Hβ. According to Williams (1992), He/N novae are expected to evolve in three distinct ways in the nebular stage: either showing no forbidden lines while the emission spectra fade into the continuum; coronal lines emerge (e.g. [Fe X] 6375 Å); or the third scenario, where strong forbidden Ne lines emerge resulting in a Ne nova. The spectra of day 32 (Fig. 3.6) show relatively strong [Ne V] lines compared to the Balmer and [O III], where the strength of [Ne V] 3426 Å is comparable to [O III] 5007 Å. Some novae show very strong Ne emission, and these novae are considered Ne novae. For these novae, the Ne abundance exceeds solar abundance. Without a detailed calculation of element abundances, it is difficult to determine if the progenitor of nova SMCN 2016-10 contains a Ne WD. According to stellar evolution theory, Ne novae are expected to originate on a high mass WD (close to Chandrasekhar mass, $M_{\rm WD} \geq 1.08$ M$_{\odot}$; see e.g. Nomoto 1984; Truran & Livio 1986; Hurley, Pols & Tout 2000 and references therein). It is worth noting that Shara & Prialnik (1994), showed that it is possible to form a moderate-mass Ne–Mg rich WD, due to a high accretion rate of hydrogen onto the surface of a C–O WD prior to the nova eruption, resulting in a massive Ne-Mg rich layer on the surface of the WD (see also Hachisu & Kato 2016a). It is worth noting that the evolution of Hγ is strongly affected by the [O III] 4363 Å line from day 27 and that the evolution of Hδ is affected by instrumental noise. The late spectrum of day 275 shows [O III] lines and Hα with the absence of forbidden Ne lines.

3.6.6 Line profile evolution

3.6.6.1 Balmer lines

The Balmer lines in the SALT high resolution spectra showed asymmetric profiles soon after maximum light (Fig. 3.21). On day 8, all the Balmer lines showed a red-shifted - relative to the rest wavelength - single-emission peak at around +1200 km s^{-1}. This single emission peak might be due to an inclined (relative to the observer) asymmetric ejecta. Aspherical ejecta might also explain the difference between the positive (red) and negative (blue) sides of the line profiles. The relative strength of this emission feature decreases passing from Hα to Hδ. Faint absorption features are observed for Hβ, Hγ, and Hδ. Such absorption features were also observed in the same lines of nova V339 Delphini, also a fast nova (Burlak et al., 2015) that formed dust at some point. For V339 Del, the hydrogen Balmer lines were initially flat-topped and later developed a more “peaked" profile, which is opposite to the evolution of nova SMCN 2016-10a. In the latter case, the peak at $\sim$ + 1200 km s^{-1} faded and the lines show jagged, flat-topped profiles. These jagged, flat-topped profiles are probably an indication of clumpiness in the ejecta, which might lead to a disordered magnetic field and therefore reduce the intrinsic polarization (see Section 3.3.6). They might also

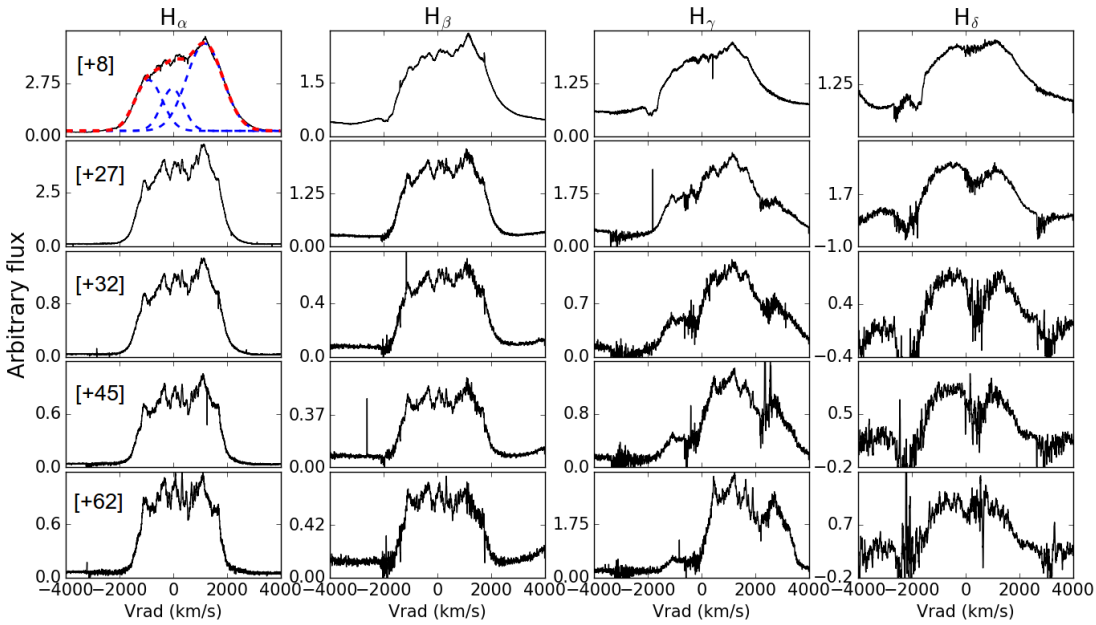

Figure 3.21: The evolution of Balmer lines from SALT high resolution spectra. From left to right: Hα, Hβ, Hγ, and Hδ. The numbers between brackets are days after t_0. Heliocentric correction is applied to the radial velocities. The top-left panel shows a sample of multiple Gaussian fitting to the Hα line used to derive the FWHM.

be associated with the complete envelope ejection at the end of the wind phase after the eruption (Della Valle et al., 2002). The evolution of the lines also resemble that of nova V959 Mon (nova Mon 2012) in Shore et al. (2013). Nova V959 Mon is a slow ONe nova and it was discovered in the γ-rays prior to optical detection because the system was close to the Sun during the eruption and therefore the optical detection was not possible. The Balmer lines of Nova V959 Mon show a red-shifted single emission peak with jagged profiles that evolved into more flat-topped profiles with time (see fig. 2 in Shore et al. 2013).

The FWHM of Hα and Hβ were derived by applying multiple component Gaussian fitting in the IRAF and python environments separately (see Fig. 3.21). The results are shown in Table 3.1. The FWHM of both lines shows a decreasing trend and a systematic narrowing of the lines, which might be due to the deceleration of the ejecta after the eruption. This deceleration is possibly due to the interaction of the ejecta with low density circumstellar/interstellar material (from previous eruptions or low mass loss from the system) while the density of the ejecta decreases. The evolution of the FWHM is presented in Fig. 3.22. This evolution follows a decreasing trend of a power law in time (Δt^n) with an exponent $n \sim -0.14$ and where Δt is equal to the time since maximum light. Other novae have shown similar line narrowing after the eruption (see, e.g., Della Valle et al. 2002; Hatzidimitriou et al. 2007; Shore et al. 2013; Darnley et al. 2016).

Bode & Kahn (1985) carried out modelling for the 1985 eruption of RS Ophiuchi and they suggested a three-phase shock model, where the high-velocity ejecta interact with the low-velocity stellar wind from the companion, which is a red giant in the case of RS Ophiuchi. The interaction between the ejecta and the wind generates shocks that are responsible for the ejecta deceleration,

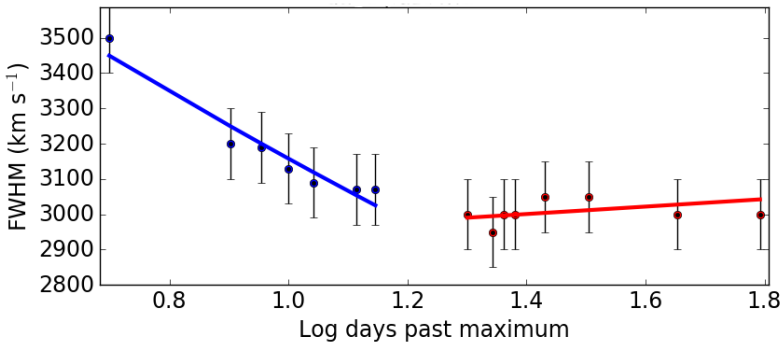

Figure 3.22: The FWHM of Hα plotted against the log time in days since maximum light. The blue circles represent the FWHM before day 14 and the red circles represent the FWHM from day 20 onward. A power law was fitted to the evolution of the FWHM of Hα from day 5 to day 14 resulting in an exponent of $\sim$ -0.14.

Table 3.1: The FWHM of Hα and Hβ at each observation. The values are in km s^{-1}.

$\Delta t = t - t_0$ (days)	FWHM (Hα) $\pm$ 100 (km s^{-1})	FWHM (Hβ)
5	3500	3450
8	3200	3050
9	3190	3050
10	3130	3000
11	3090	2850
13	3070	2950
14	3070	–
20	3000	3150
22	2950	2900
23	3000	2850
24	3000	2900
27	3050	3000
32	3050	2950
45	3000	2850
62	3000	2800

and hence the line narrowing.

Another explanation for this line narrowing was proposed by Shore et al. (1996), who suggested that it is due to the distribution of the matter velocity at the ejection moment. The emissivity of the fastest moving gas decreases with time at a higher rate than the slower moving gas, due to the decrease of its density, leading to the line narrowing. While this is true for the recurrent nova RS Oph which has a mass-losing giant secondary, this might not be the case of nova SMCN2016-10a. In the case of the latter the mass transfer from the main-sequence/sub-giant secondary to the WD is likely to be more conservative compared to systems such as RS Oph where the system loses material to the circumstellar environment due to the wind from the giant secondary.

McLaughlin (1960) has derived a relation between the FWHM of Hα and the light-curve

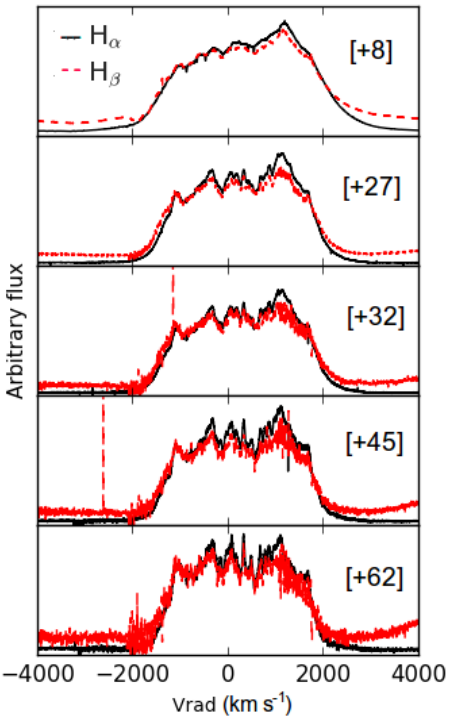

Figure 3.23: The evolution of Hα (solid black) and Hβ (dashed red) line profiles. The numbers between brackets are days since t_0.

parameter t_2, based on a Galactic novae sample. More recently, after a survey of novae in M31, Shafter et al. (2011) carried out spectroscopic and photometric analysis of 91 novae and derived a comparable relation which shows a clear trend of faster novae exhibiting higher expansion velocities. Although, the study of Shafter et al. is conducted in a different galaxy than the SMC, which means different metallicity and Hubble type, we applied their relation to this nova:

$$\log t_2(d) = 6.84 \pm 0.1 - (1.68 \pm 0.02) \times \log[\mathrm{FWHM}_{\mathrm{H}\alpha}(\mathrm{km\,s^{-1}})],$$

with a FWHM of $\sim 3500 \pm 100\,\mathrm{km\,s^{-1}}$, leading to $t_2 = 7.6 \pm 2$ days which is slightly larger than the values derived from our photometric data (see section 3.2.3).

In order to check for the blending of the [N II] 6548 Å and 6583 Å lines with Hα in terms of an apparent extra emission component in radial velocity, we directly compared the evolution of Hα and Hβ (Fig. 3.23). Although the lines are very broad, no evidence of blending is present in any of the observations. If present, the [N II] 6548 Å is at $\sim$ - 600 $\mathrm{km\,s^{-1}}$ to the blue side of Hα and [N II] 6583 Å is at $\sim$ + 1000 $\mathrm{km\,s^{-1}}$ to the red side of Hα. The line profile structure and evolution of Hα and Hβ is almost identical in the five high resolution observations. Hα does not show any extra emission at these two velocities in comparison to Hβ. The peak at $\sim$ + 1200 $\mathrm{km\,s^{-1}}$ is present in both lines, as well in Hδ and Hγ as discussed previously.

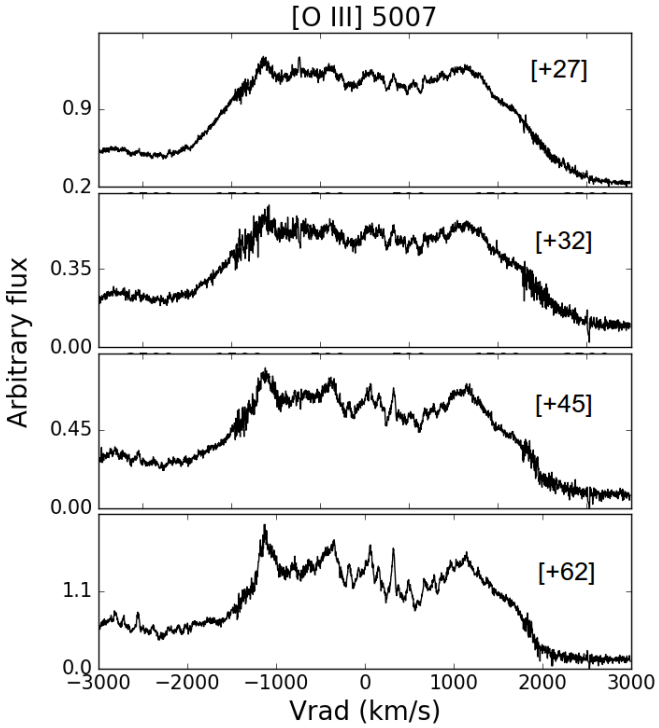

Figure 3.24: The evolution of [O III] 5007 Å line profiles. The rise to the blue side of the line is due to the [O III] 4959 Å line. The numbers between brackets are days after t_0. Heliocentric correction is applied to the radial velocities.

3.6.6.2 Oxygen lines

The nebular [O III] 4363 Å, 4959 Å, and 5007 Å lines were observed in all the spectra from day 20 onwards. The lines were absent in the first two spectra (day 5 and 8) since the nova was still close to maximum light and only entered the nebular stage in late October. The [O III] 4363 Å is blended with Hγ. We show the evolution of the [O III] 5007 Å line in Fig. 3.24.

Williams (2012) showed that the O I 8446/7773 intensity ratio is a good indicator of the density of gas that forms the spectrum during early decline. Fe II spectra are expected to have a high intensity 7773 Å line, which is thought to originate from high density gas that persists for months after the eruption. Hence, the O I 8446/7773 ratio is low for the Fe II spectra (sometimes lower than 2), and sometimes showing small changes over months time. For the He/N class, the lines are expected to originate from low density gas where the line at 7773 Å is sometimes not even detected. Hence, the ratio of the two oxygen lines should be high, followed by a fast decrease. We derived the flux ratio of O I 8446/7773 for all our observations and the results are shown in Table 3.2. They show a high increasing ratio followed by a fast decrease, as expected for a He/N nova.

3.7 Summary and conclusions

Nova SMCN 2016-10a was discovered on 2016-10-14.19 UT by MASTER-OAFA auto-detection system (Shumkov et al., 2016). Pre-discovery observations from MASTER (Lipunov et al., 2016)

Table 3.2: The flux ratio of O I 8446/7773 from the HRS and RSS observations. The flux is not corrected for reddening.

$\Delta t = t - t_0$ (days)	F(O I 8446/7773)
5	2.3
8	3.6
23	5.5
27	5.4
32	4.5
45	2.3
62	1.2

and a DSLR camera from Sao Jose dos Campos, Brazil (Jablonski & Oliveira, 2016), allowed us to estimate t_0 as 2016-10-09.2 UT and the date of maximum optical light as 2016-10-09.8 UT. Nova SMCN 2016-10a is the best studied nova in the SMC so far. The optical, NIR, X-ray, and UV data, led us to the following conclusions:

1. Nova SMCN 2016-10a is a very fast nova with $t_2 \simeq 4.0 \pm 1.0$ d. This is an indication of an eruption that occurred on a high mass WD ($M_{\rm WD} \geq 1.25\,{\rm M}_{\odot}$).

2. The light-curve is consistent with a nova at the distance of the SMC, although its magnitudes at 15 and 17 days indicate it may be to the fore of the bulk of the SMC. However, these distances derived from the MMRD relations must be considered uncertain.

3. Assuming a distance of 61 ± 10 kpc, it is the brightest nova discovered in the cloud with $M_{V,\rm max} \approx -10.5 \pm 0.5$ and probably one of the brightest on record.

4. Based on the photometric data from the quiescence phase and the early decline phase, we suggest that the progenitor system is likely to contain a main sequence secondary, or a sub-giant secondary.

5. Based on the optical spectra, we classified nova SMCN 2016-10a as a He/N nova indicating a system with a high mass WD.

6. After 5 days from optical peak, we measured FWHM of $\sim 3500 \pm 100\,{\rm km\,s^{-1}}$ from the Hα and Hβ lines, indicating moderately high expansion velocities.

7. The light-curve during quiescence, the Balmer line profiles, as well as the negligible polarization, suggest the system might be at a low inclination and that there are clumps in the ejecta. Line modelling is definitely needed to give us a better insight into the structure and morphology of the system and the ejecta.

8. The high temperature ($\sim$90 eV) of the super-soft X-ray emission, together with the relatively rapid turn-on and -off times (28 d and 180 d, respectively), suggest a high mass WD ($\sim$1.25-1.3 ${\rm M}_{\odot}$), in agreement with the results from the optical data. We note that, at a distance of 61 kpc, the bolometric luminosity is a factor of 1.76 higher than at 46 kpc.

9. The plateaux in the UV light-curves extend at least from day $\sim$90 to 170, approximately corresponding to the interval of bright, high temperature soft X-rays.

10. The UV line fluxes show different light-curves before day 20 suggesting optical thickness is the cause. The line fluxes have the same light-curves in the later data, suggesting the ejecta are effectively optically thin by then, and that is also when we see the rise of the X-ray flux.

Once the system returns to quiescence, more observations are essential to constrain the type of the secondary star. If it becomes possible to measure the expansion parallax of this nova then the question of its brightness and location could be settled. Such measurements are not easy and often raise questions about the symmetry of the eruption. With the available spectroscopic data, line modelling is encouraged to follow-up this work, which can help to constrain the structure and morphology of the system.

Chapter 4

Multiwavelength observations of V407 Lupi (ASASSN-16kt) — a very fast nova erupting in an intermediate-polar

Abstract

We present a detailed study of the 2016 eruption of nova V407 Lupi (ASASSN-16kt), including optical, near-infrared, X-ray, and ultraviolet data from SALT, SMARTS, SOAR, *Chandra*, *Swift*, and *XMM-Newton*. Timing analysis of the multiwavelength light-curves shows that, from 168 days post-eruption and for the duration of the X-ray supersoft source phase, two periods at 565 s and 3.57 h are detected. We suggest that these are the rotational period of the white dwarf and the orbital period of the binary, respectively, and that the system is likely to be an intermediate-polar. The optical light-curve decline was very fast ($t_2 \leq 2.9$ d), suggesting that the white dwarf is likely massive ($\gtrsim 1.25\,\mathrm{M}_\odot$). The optical spectra obtained during the X-ray supersoft source phase exhibit narrow, complex, and moving emission lines of He II, also characteristics of magnetic cataclysmic variables. The optical and X-ray data show evidence for accretion resumption while the X-ray supersoft source is still on, possibly extending its duration.

Keywords: stars: individual (V407 Lup) – novae, cataclysmic variables – white dwarfs.

4.1 Introduction

Classical novae (CNe) are stellar eruptions that take place within the surface layers of accreting white dwarfs (WDs) in cataclysmic variable (CV) systems. These are interacting binaries consisting of a WD primary accreting from a secondary that typically fills its Roche lobe (see, e.g., Warner

1995). The hydrogen-rich material accreted by the WD accumulates on its surface causing an increase in pressure and density to a level where a thermonuclear runaway (TNR) is triggered (Starrfield, 1989; Starrfield, Iliadis & Hix, 2008; José & Shore, 2008; Starrfield, Iliadis & Hix, 2016). Due to this, a part of the accreted envelope is ejected. The fast expanding envelope moves together with the optical photosphere (Hachisu & Kato, 2006, 2014a), in what is known as the "fireball stage". During this the brightness of the star increases (magnitude decreases by 8 up to 15 mag; Payne-Gaposchkin 1964) and reaches its maximum visual brightness when the optical photosphere attains its maximum radius (Warner, 1995; Hachisu & Kato, 2014a). Following the TNR, the remaining hydrogen-rich, accreted envelope continuously burns on the WD surface and may become visible when the expanding ejecta become optically thin.

After maximum the optical depth of the expanding ejecta decreases progressively as its density decreases and therefore the optical photosphere starts shrinking. This shifts the emission to higher energies, and would peak in the soft X-ray band and a SuperSoft Source (SSS) emerges, unless the ejecta become optically thin before that happens. In this case the SSS emergence is due to the visibility of the WD photosphere, which is at that time extended due to the ongoing nuclear burning (Krautter, 2008; Osborne, 2015). As the hydrogen in the surface layers is consumed, the SSS "turns off" and the system eventually evolves back to quiescence (for a series of reviews of CNe see Bode & Evans 2008).

Observing CNe across many wavelengths is essential to provide a full picture of the eruption and its characteristics, such as: the different physical parameters (e.g., temperatures and velocities), the gas ejection mechanisms, the radiative processes, the nuclear reactions, the shocks in the ejecta/wind, the dust formation, and the properties of the progenitor. However, despite their importance systematic multiwavelength studies are still lacking and only a few CNe have been followed panchromatically and in detail (see, e.g., Shore et al. 2013; Schwarz et al. 2015; Bode et al. 2016; Shore et al. 2016; Darnley et al. 2016; Li et al. 2017; Mason et al. 2018; Aydi et al. 2018). Therefore, observing these events in multiple frequency bands is essential for a better understanding of these individual events and ultimately adding to the wealth of knowledge in the field.

While most nova eruptions occur in non-magnetic CVs, where the WD is usually weakly magnetized (magnetic field of the WD is $\lesssim 10^6$ G), a few novae have been seen to occur in magnetic CVs (mCVs). These systems form a sub-group of CVs in which the WD is highly magnetized, and they include two main sub-types: polars which have the strongest magnetic fields ($\gtrsim 10^7$ G) and intermediate-polars (IPs) with weaker fields ($10^6 - 10^7$ G). The strong magnetic field of polars causes the spin (rotational) period of the WD and the orbital period of the binary to synchronize. This is not the case for IPs where the optical, X-ray, and ultraviolet (UV) light-curves might show multiple periodicities, modulated on the orbital period of the binary (with typical values of 3 to 6 h), the spin period of the WD (with values ranging between ~ 0.5 up to ~ 70 min), and the sideband periods (typically dominated by the beat period). Although in such systems the mass-accretion mechanism is dominated at some point by the magnetic field of the WD, the accretion onto the surface of WD can still result in a nova eruption. For a comprehensive review of mCVs and their mass-transfer/ -accretion mechanisms see Warner (1995) and Hellier (2001).

The only nova known to have erupted in a polar system is V1500 Cyg (Kaluzny & Semeniuk, 1987; Stockman, Schmidt & Lamb, 1988). The eruption occurred in 1975 was one of the most luminous on record, along with CP Pup (Warner, 1985) and nova SMCN 2016-10a (Aydi et al., 2018). On the other hand, a few novae have been either confirmed (GK Per, DQ Her, V4743 Sgr, and Nova Scorpii 1437 AD) or suggested (V533 Her, DD Cir, V1425 Aql, M31N 2007-12b, and V2491 Cyg) to occur in IPs (see, e.g., Osborne et al. 2001; King, Osborne & Schenker 2002; Warner & Woudt 2002; Bianchini et al. 2003; Woudt & Warner 2003, 2004; Leibowitz et al. 2006; Dobrotka & Ness 2010; Pietsch et al. 2011; Zemko et al. 2016; Potter & Buckley 2018 and references therein). The effect of the magnetic field on the nova eruption and progress is not well understood.

In this chapter we present a multiwavelength study of nova V407 Lupi which was discovered by the All-Sky Automated Survey for Supernovae (ASAS-SN)[1] on HJD 2457655.5 (2016 September 24.0 UT; Stanek et al. 2016) at V = 9.1. It is located at equatorial coordinates of $(\alpha, \delta)_{\rm J2000.0}$ = ($15^{\rm h}29^{\rm m}01\overset{\rm s}{.}82$, –44°49′40.″89) and Galactic coordinates of (l, b) = (330.°91, –9.°569). The last ASAS-SN pre-discovery observation reported the source at $V > 15.5$ on HJD 2457651.5. Therefore, in the following we assume HJD 2457655.5 (2016 September 24.0 UT) is t_0 (eruption start). Our study consists of a set of comprehensive, multiwavelength observations obtained with the aim of studying in detail the post-eruption behaviour of the nova at optical, near-infrared (NIR), ultraviolet (UV), and X-ray wavelengths. Note that this object has not been seen in eruption before. This chapter is structured as follows: in Section 4.2 we present the observations and data reduction. The analysis of the photometric and spectroscopic results are given in Sections 4.3 and 4.4, respectively. We present the discussion in Section 4.5, while Section 4.6 contains a summary and the conclusions.

4.2 Observations and data reduction

4.2.1 SMARTS observations and data reduction

Since 2016 September 26 (day 2) the eruption has been monitored using the Small and Moderate Aperture Research Telescope System (SMARTS) to obtain optical *BVRI* and near-infrared (NIR) *JHK* photometric observations. The integration times at *JHK* were 15 s (three 5 s dithered images) before 2016 October 6 (day 12) and 30 s thereafter. Optical observations are single images of 30 s, 25 s, 20 s, and 20 s integrations, respectively, in *BVRI* prior to 2016 October 6 (day 12), and uniformly 50 s thereafter. The procedure followed for reducing the SMARTS photometry is detailed in Walter et al. (2012). Fig. 4.1 represents the SMARTS *BVRI* and *JHK* observations. See Table B.3 for a log of the observations.

4.2.2 SALT high-resolution Echelle spectroscopy

We used the SALT High Resolution Spectrograph (HRS; Barnes et al. 2008; Bramall et al. 2010; Bramall et al. 2012; Crause et al. 2014) to obtain observations on the nights of 2017 March 6; April 20; May 31; June 13, 24, 29; July 05, 24, 29; and August 06 (respectively, days 164, 209,

[1] http://www.astronomy.ohio-state.edu/asassn/index.shtml

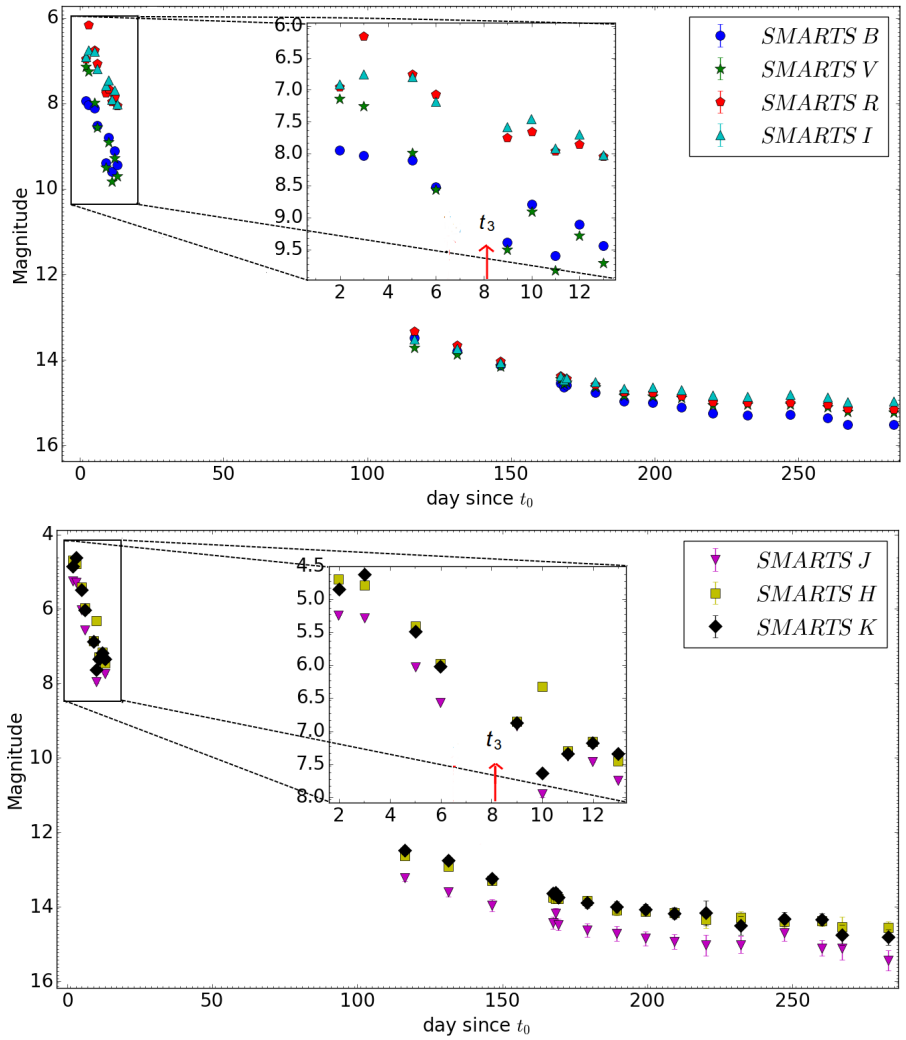

Figure 4.1: The *BVRI* (top) and *JHK* (bottom) photometry from SMARTS as a function of days since eruption, colour and symbol coded as indicated in the legend. We present a zoomed sub-plot to show in more detail the evolution of the light-curve during the early decline. Day to day variability appear in the light-curve after t_3 (marked by a red arrow).

250, 263, 274, 279, 285, 304, 309, and 317). HRS, a dual beam, fibre-fed Echelle spectrograph housed in a temperature stabilized vacuum tank, was used in the low-resolution (LR) mode to obtain all the observations. This mode provides two spectral ranges: blue (3800 – 5550 Å) and red (5450 – 9000 Å) at a resolution of $R \sim 15000$. A weekly set of HRS calibrations, including four ThAr + Ar arc spectra and four spectral flats, is obtained in all the modes (low, medium, and high-resolution). All the HRS observations are 1800 s exposures. See Table B.4 for a log of the observations.

The primary reduction was conducted using the SALT science pipeline (Crawford et al., 2010) which includes over-scan correction, bias subtraction, and gain correction. The rest of the reduction and relative flux calibration was done using the standard MIDAS FEROS (Stahl, Kaufer & Tubbesing, 1999) and *echelle* (Ballester, 1992) packages. The reduction procedure is described in detail in Kniazev, Gvaramadze & Berdnikov (2016). Note that absolute flux calibration is not feasible with SALT data. As part of the SALT design, the effective area of the telescope constantly

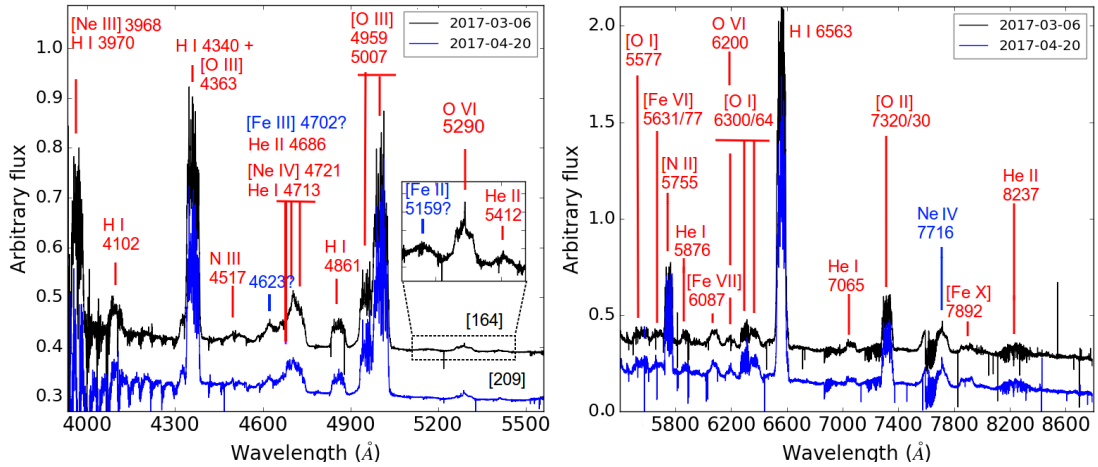

Figure 4.2: The SALT HRS high-resolution spectra of days 164 and 209, plotted between 3900 – 5500 Å (left) and 5450 – 8800 Å (right) with the flux in arbitrary units. For clarity, the spectra are shifted vertically. The numbers in square brackets are days since t_0. We present a zoomed in plot on the range between 5100 Å and 5450 Å to show the possible presence of weak emission lines in this range. Below 4200 Å instrumental noise dominates the spectra.

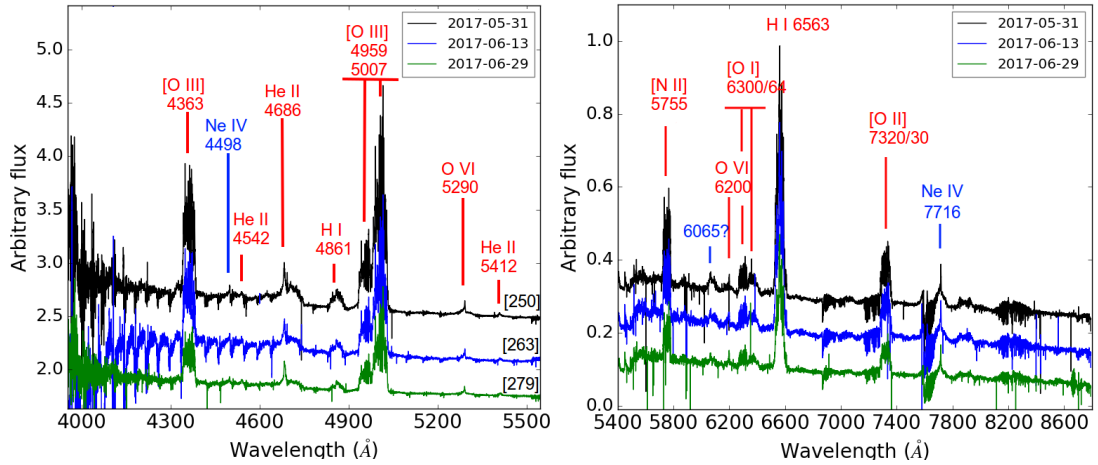

Figure 4.3: The SALT HRS high-resolution spectra of days 250, 263, 274, and 279, plotted between 3900 – 5500 Å (left) and 5450 – 8800 Å (right) with the flux in arbitrary units. For clarity, the spectra are shifted vertically. The numbers in square brackets are days since t_0. Below 4200 Å, instrumental noise dominates the spectra.

changes with the moving pupil during the track and exposures. Figs 4.2, 4.3, and 4.4 show the SALT HRS spectra.

4.2.3 SOAR medium-resolution spectroscopy

We performed optical spectroscopy of the nova on 2017 June 20 (day 270) using the Goodman spectrograph (Clemens, Crain & Anderson, 2004) on the 4.1 m Southern Astrophysical Research (SOAR) telescope. We obtained a single exposure of 600 s, using a 600 l mm^{-1} grating and a 1.07 arcsec slit to provide a resolution of $\sim$ 1.3 Å over the range of 3200 – 6800 Å. The spectrum

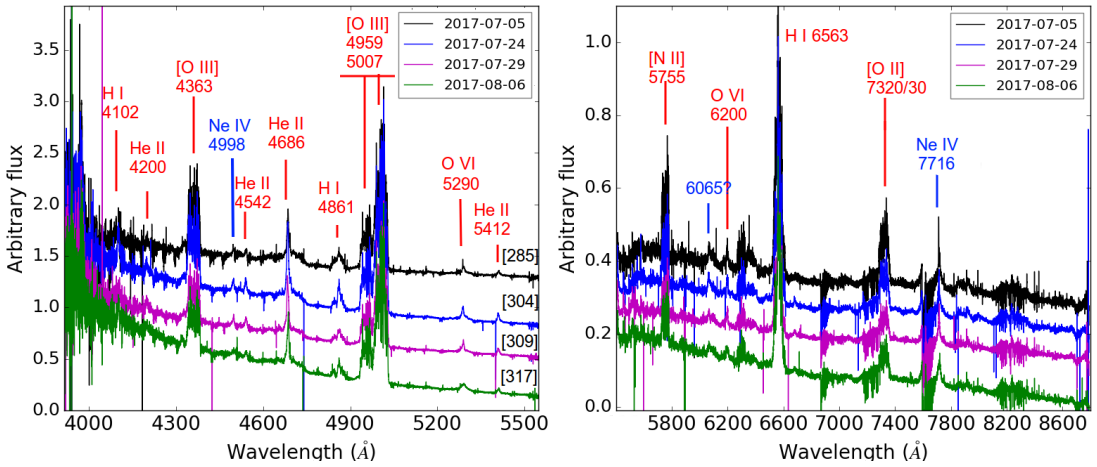

Figure 4.4: The SALT HRS high-resolution spectra of days 285, 304, 309, and 317, plotted between 3900 – 5500 Å (left) and 5450 – 8800 Å (right) with the flux in arbitrary units. For clarity, the spectra are shifted vertically. The numbers in square brackets are days since t_0. Below 4200 Å, instrumental noise dominates the spectra.

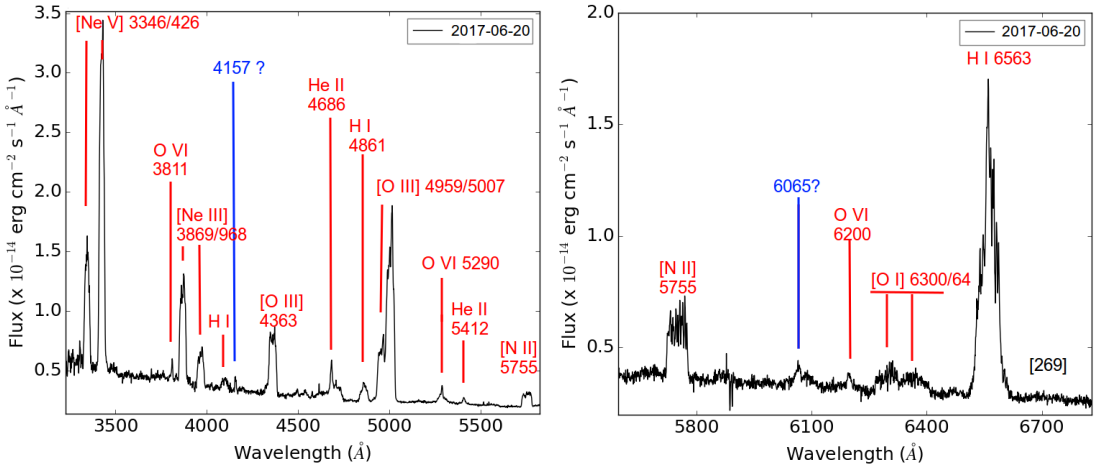

Figure 4.5: The SOAR medium-resolution spectrum of day 270, plotted between 3200 – 5800 Å (left) and 5600 – 6800 Å (right) with the flux in erg cm^{-2} s^{-1} Å^1.

(Fig. 4.5) was reduced using the standard routine and a relative flux calibration has been applied.

We also obtained two spectra using the Goodman spectrograph on the nights of 2018 January 20 and 21 (days 484 and 485), each of 20 min exposure. For these two observations we used a setup with a 2100 l mm^{-1} grating and a 0.95 arcsec slit, yielding a resolution of about 0.88 Å full width at half maximum (FWHM) (56 km s^{-1}) over a wavelength range of 4280 – 4950 ÅÅ. The spectra (Fig. 4.6) were reduced and optimally extracted in the usual manner.

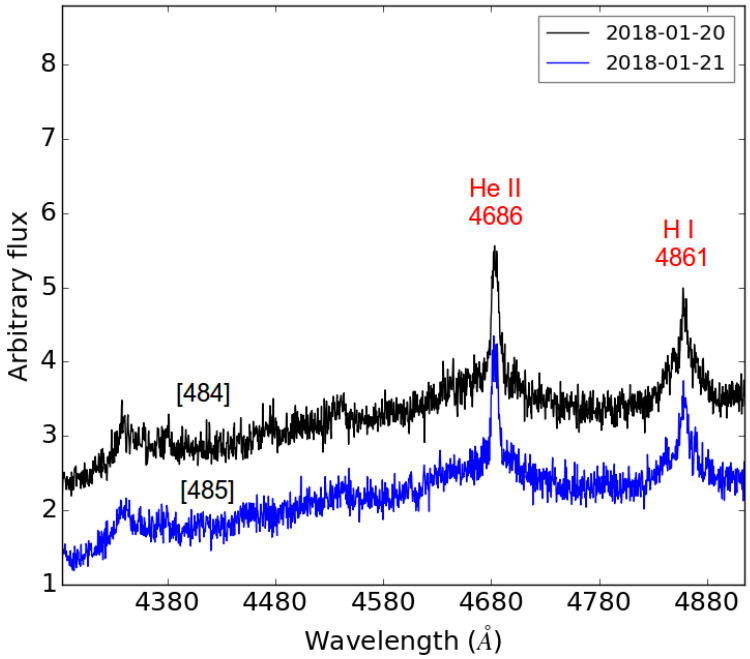

Figure 4.6: The SOAR medium-resolution spectra taken on day 484 and day 485, plotted between 4300 and 5000 Å with the flux in arbitrary units.

4.2.4 *Swift* X-ray and UV observations

4.2.4.1 *Swift* XRT observations

The Neil Gehrels *Swift* Observatory (hereafter, *Swift*; Gehrels et al. 2004) first observed V407 Lup on 2016 September 26, two days after the discovery. The high optical brightness of the nova at this time meant that the UV/Optical Telescope (UVOT; Roming et al. 2005) could not be used, and the X-ray Telescope (XRT; Burrows et al. 2005) needed to be operated in Windowed Timing (WT) mode for the initial observation, in order to minimize the effects of optical loading, whereby a large number of optical photons can pile-up to appear as a false X-ray signature[2]. No X-ray source was detected at this time (< 0.02 count s^{-1}; grade 0 – single pixel events), or in the individual subsequent daily observations taken in Photon Counting (PC) mode between 2016 October 2 and 9 (days 8 – 15). Coadding these PC data, there is a source detected at the 99 per cent confidence level, with a count rate of $(1.4^{+0.5}_{-0.4}) \times 10^{-3}$ count s^{-1} (grade 0). There was also a suggestion of a detection in the October 10 (day 16) data alone. These detections could not be confirmed at a higher significance before V407 Lup became too close to the Sun for *Swift* to observe on 2016 October 13 (day 19).

Observations recommenced on 2017 February 21 (day 150), finding a bright, supersoft X-ray source (Beardmore et al., 2017), with a count rate of 56.1 ± 0.3 count s^{-1}. By this time the UVOT could also be safely operated, and a UV source with *uvw2* = 13.49 ± 0.02 mag was measured. Daily observations were performed between 2017 February 22 and 28 (days 151 – 157), followed by observations approximately every two to three days until 2017 April 24 (day 212). Observations

[2] http://www.swift.ac.uk/analysis/xrt/optical_loading.php

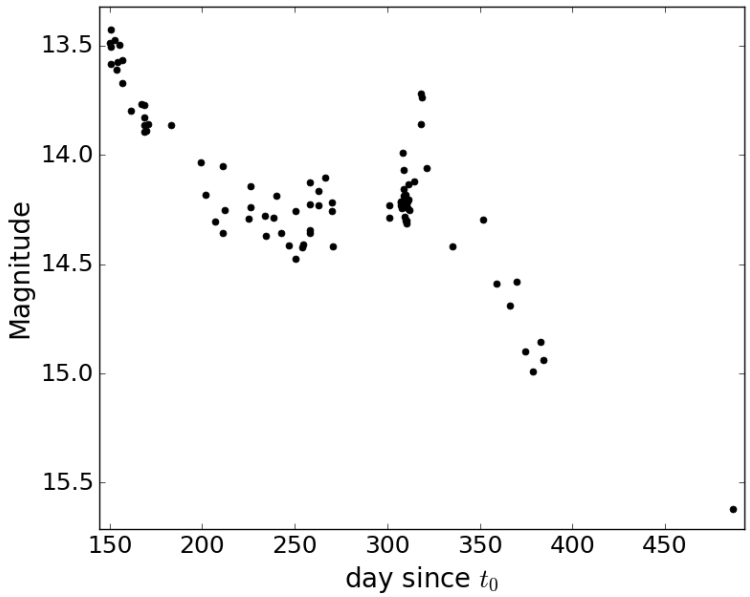

Figure 4.7: The UVOT *uvw2* ($\lambda_{\rm central}$ = 1928 Å) light-curve plotted against day since t_0.

were continued, though with a slightly lower cadence of every four days, until 2017 September 10 (day 351), with the cadence then decreasing to every eight days until 2017 October 13 (day 384), when the Sun constraint began again. A final dataset was obtained once the source again emerged from the Sun constraint, on 2018 January 23 (day 486). All observations were typically 0.5-1 ks in duration, with the exception of the final observation which was 3 ks. In addition to this regular monitoring a high cadence campaign was performed between 2017 July 4 – 8 (days 283 – 287), aimed at pinning down the periodicity seen in the UVOT light-curve (see Section 4.3.4). In this case, $\sim$ 500 s snapshots were taken approximately every 6 h. Because of complications caused by a nearby bright star, no UVOT data were actually collected, and so the campaign was repeated from 2017 July 28 – August 1 (days 307 – 311) using an offset pointing to avoid this problem. The *Swift* XRT observations log is given in Table B.5.

The *Swift* data were processed with the standard HEASoft tools (version 6.20)[3], and analysed using the most up-to-date calibration files. All observations between 2017 February 21 and August 11 (days 150 and 321 post-eruption), inclusive, were obtained using WT mode, because of the high brightness of the X-ray source. These data were extracted using a circular region of a radius of 20 pixels (1 pixel = 2.36 arcsec) for the source, and a background annulus as described at http://www.swift.ac.uk/analysis/xrt/backscal.php. Observations from 2017 August 15 (day 325) onwards were taken with the XRT in PC mode; the first three of these suffered from pile-up, so an annulus (outer radius 30 pixels; inner exclusion radius decreasing from seven to three pixels) was used when extracting the source counts. The later data were analysed using circular regions, decreasing in radius from 20 to 10 pixels as the source further faded. Background counts were estimated from near-by, source-free circular regions of 60 pixels radius.

[3] `https://heasarc.gsfc.nasa.gov/FTP/software/ftools/release/archive/Release_Notes_6.20`

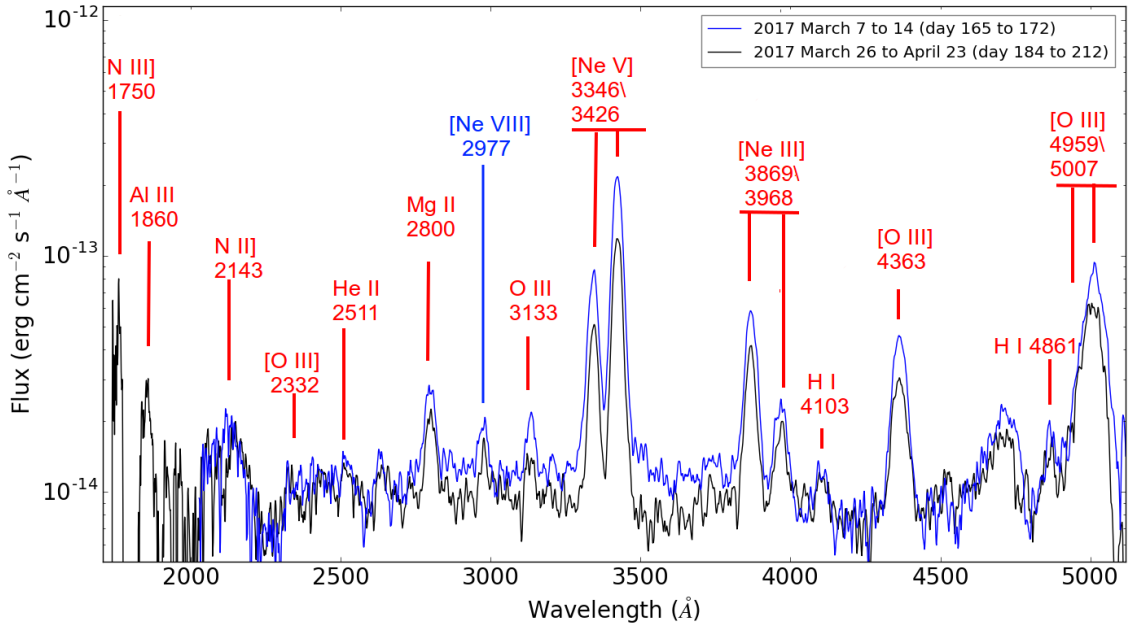

Figure 4.8: The *Swift* UV-optical grism spectra plotted between 1700 and 5100 Å. The blue spectrum represents the first four spectra combined (from 2017 March 7 to 14) and the black spectrum represents the second four spectra combined (from 2017 March 26 to April 23).

The X-ray spectra were binned to provide a minimum of 1 count bin^{-1} to facilitate Cash statistic (Cash, 1979) fitting within XSPEC (Arnaud, 1996).

4.2.4.2 *Swift* UVOT observations

Observations with the $Swift$ UVOT instrument started once the nova could be observed again after its passage behind the Sun. On 2017 February 26 (day 156), the nova was observed in the *uvw2* ($\lambda_{\rm central}$ = 1928 Å) filter; the next day in the *uvm2* ($\lambda_{\rm central}$ = 2246 Å) filter. Photometric observations continued until 2017 October 13 (day 385). The UVOT *uvw2* light-curve is shown in Fig. 4.7 and a log of the observations is given in Table B.5.

Weekly observations with the UV grism started on 2017 March 7, until April 23 (day 165 until day 212) when they were discontinued as the brightness was too low. The UV grism provides a spectral range of $\sim$ 1700 – 5100 Å. The log of the observations are given in Table B.6. The eight grism observations were reduced using the UVOTPY software (Kuin, 2014) using the calibration described in Kuin et al. (2015) with a recent update to the sensitivity affecting the response of the UV grism mainly below 2000 Å [4]. The net continuum counts in the UV part of the individual spectra are very low, so the first four and last four spectra were summed, which also improved the signal to noise (S/N) of the weaker lines significantly. The UV grism spectra are presented in Fig. 4.8 with no reddening correction.

[4] see:`http://mssl.ucl.ac.uk/npmk/Grism/`

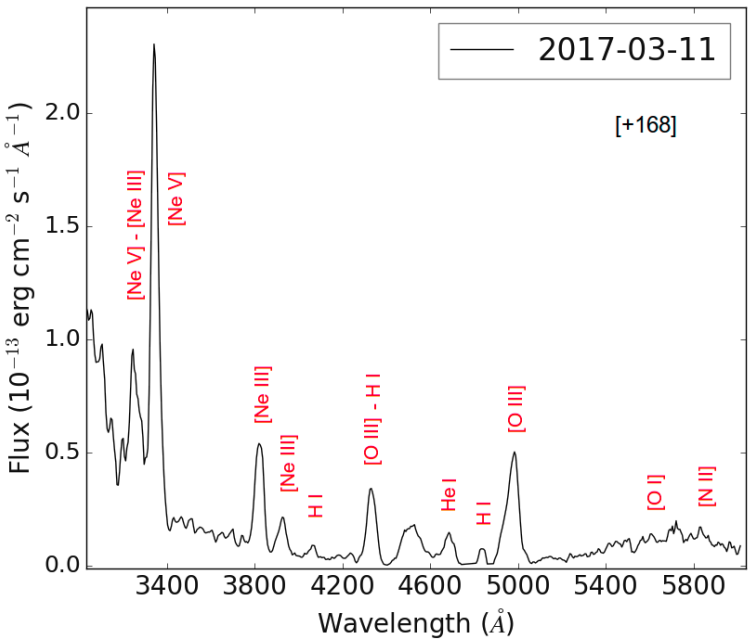

Figure 4.9: The OM (Optical Monitor on board *XMM-Newton*) grism spectrum plotted between 3000 and 6000 Å. The numbers in square brackets are days since t_0.

4.2.5 *XMM-Newton* X-ray and UV observations

V407 Lup was observed by *XMM-Newton* from 2017 March 11, 11:45 to 17:08 UT, 168.5 days post-eruption with an exposure duration of 23 ks (Ness et al., 2017). The *XMM-Newton* observatory consists of five different X-ray instruments behind three mirrors plus an optical monitor (OM;Mason et al. 2001; Talavera 2009), which all observe simultaneously. For a full description of the X-ray instruments onboard of *XMM-Newton* see Jansen et al. (2001), den Herder et al. (2001), Strüder et al. (2001), Turner et al. (2001), and Aschenbach (2002).

In this work, we only used the spectra and light-curves from the Reflection Grating Spectrometer (RGS;den Herder et al. 2001), the light-curves from the European Photon Imaging Camera (EPIC)/pn (Strüder et al., 2001), and the OM light-curves/grism spectra (see Table B.7 for a log of the observations).

The OM took five exposures, one of which with the visible grism provided a spectrum between 3000 and 6000 Å (*XMM-Newton* could not take a U-grism spectrum because of a contaminating nearby star, so we only obtained a V-grism spectrum); and four with Science User Defined imaging plus fast mode, which provided a UV light-curve with the *uvw1* ($\lambda \sim 2910 \pm 830$ Å) filter. The OM UV and imaging mode light-curves and the V-grism spectrum are given in Figs 4.11 and 4.9, respectively.

The RGS provides a spectral range of 6 – 38 Å, fully covering the Wien tail of SSS spectra (30 – 80 eV) while the Rayleigh Jeans tail is not visible (owing to interstellar absorption). It also provides X-ray light-curves in the same energy range. RGS consists of two instruments RGS1 and RGS2. One of the nine CCDs in RGS2 is suffering from some technical problems. Therefore, we will avoid the use of the light-curve provided by RGS2. Fig. 4.10 shows the RGS spectrum

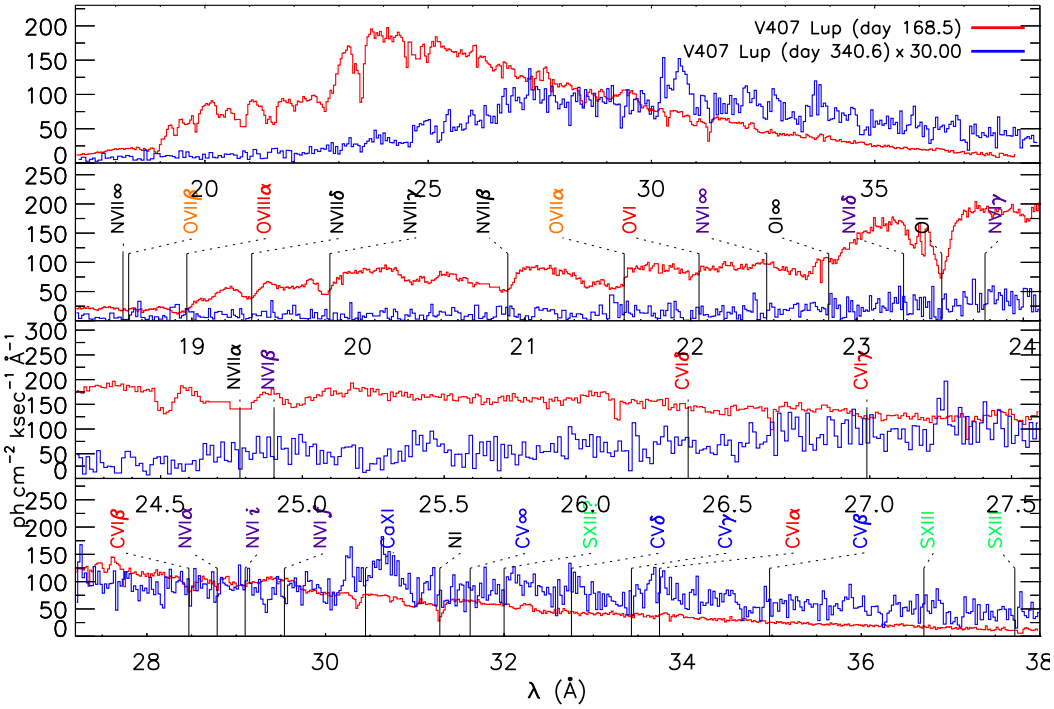

Figure 4.10: The *XMM-Newton* RGS spectrum (red) taken on day 168.5. The spectrum is combined from RGS1 and RGS2 using the SAS tool RGSFLUXER. The *Chandra* spectrum (blue) taken on day 340.6 is also plotted for comparison and has been multiplied by a factor of 30. It is worth noting that the *Chandra* LETG spectral range is much larger (see text for more details).

(combined RGS1 and RGS2 spectra) taken on day 168.5. Combining the RGS1 and RGS2 spectra allow us to overcome the problem of the broken CCD in the RGS2 instrument.

The EPIC/pn instrument was operated in Timing Mode with medium filter providing another X-ray light-curve. Fig. 4.11 shows the RGS (RGS1) and EPIC/pn light-curves.

4.2.6 *Chandra* X-ray observations

V407 Lup was observed with the *Chandra X-ray Observatory* (hereafter, *Chandra*; Weisskopf et al. 2000), using the High Resolution Camera (HRC; Murray et al. 1997) and the Low Energy Transmission Grating (LETG; Brinkman et al. 2000a,b) on 2018 August 30 (day 340.6), with an exposure time of 34 ks. The LETG instrument provides a spectrum over a range of $\sim$ 1.2 – 175 Å (0.07 – 10.33 keV), however most of the flux from nova V407 Lup is in the range 15 – 50 Å (0.24 – 0.82 keV). The LETG spectrum and the HRC light-curve (0.06 – 10 keV) are plotted in Figs 4.10 and 4.12, respectively.

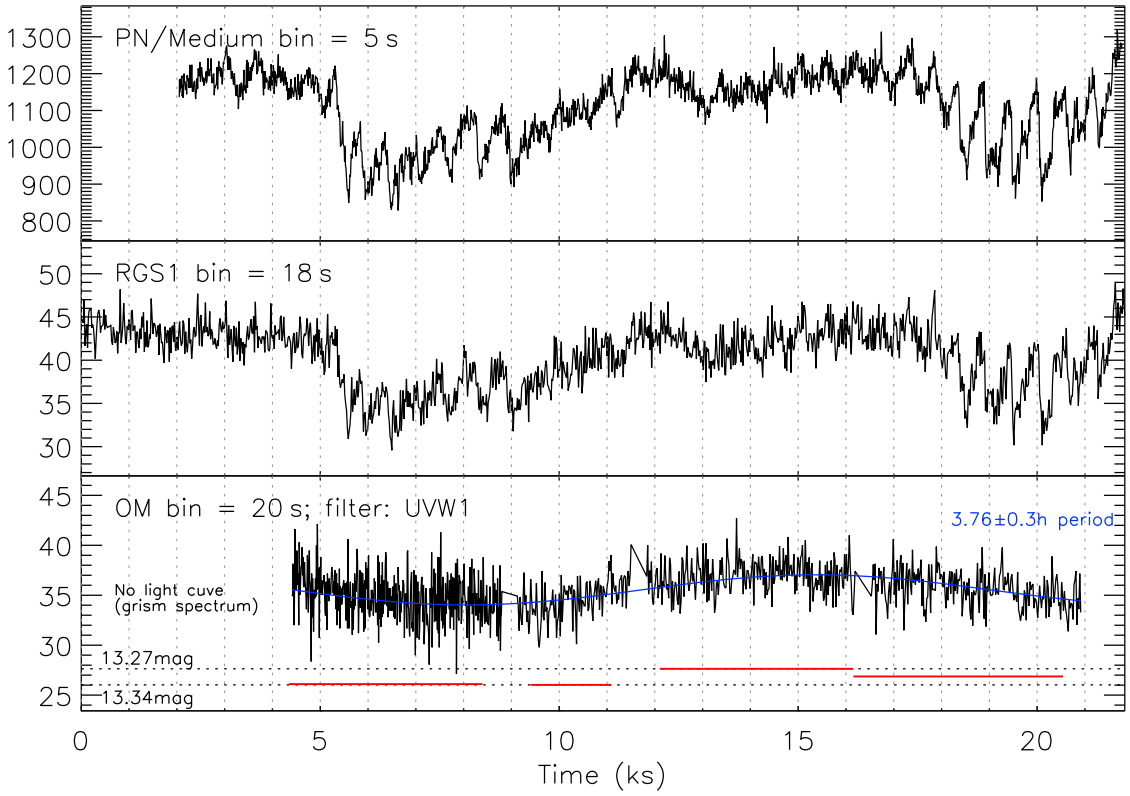

Figure 4.11: *First panel:* the *XMM-Newton* EPIC/pn X-ray light-curve. *Second panel:* the RGS1 X-ray light-curve. The X-ray light-curves show two broad ($\sim 2-3$ ks wide) dips separated by 12.6 ks, consistent with the 3.57 h modulation seen in the *Swift*-UVOT data (see Section 4.3.4). *Third panel:* the *uvw1* OM fast mode (black) and imaging mode (red) light-curves. The first OM exposure is a grism spectrum, hence the light-curves only start at ~ 5 ks. The blue line represents a best fit sine curve to the OM data with a period of 3.76 ± 0.3 h. This period is consistent, within uncertainty, with the period seen in the *Swift*-UVOT data (see Section 4.3.4 for further discussion on the timing analysis). The y-axis in all the panels are counts per second.

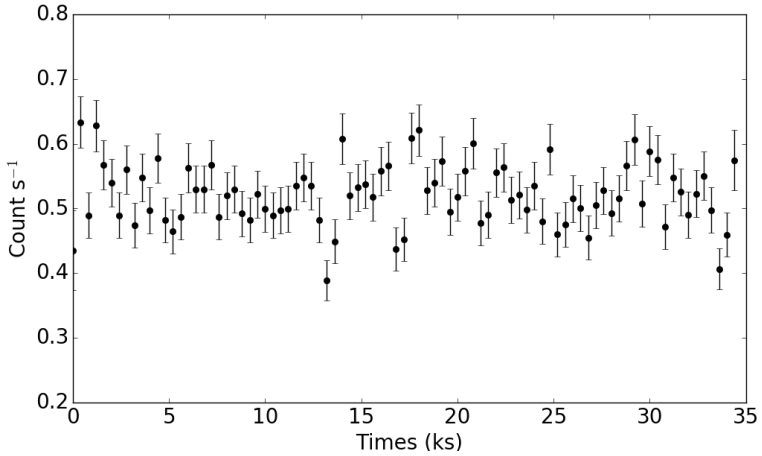

Figure 4.12: The *Chandra* High Resolution Camera (HRC) X-ray light-curve. The HRC energy range is 0.06 – 10 keV. There is a clear short-term variability in the light-curve and it is discussed in Section 4.3.4.

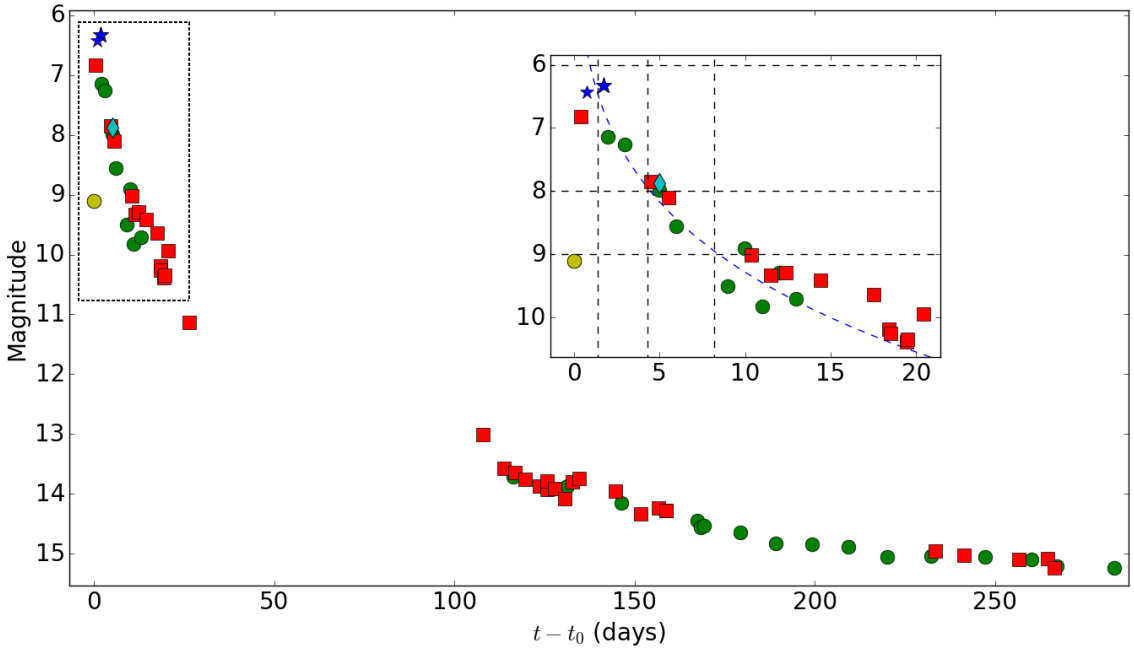

Figure 4.13: V-band light-curve using data from SMARTS (green circles), AAVSO (red squares), and ATels from Stanek et al. (2016) (yellow circle), Chen et al. (2016) (blue stars), and Prieto (2016) (cyan diamond). A zoom-in plot around the first $\sim$ 25 days is added for clarity. Within this plot: the blue dashed line represents a power-law fit to the data (before day 25), excluding the discovery measurement; the black horizontal dashed lines represent from top to bottom $V_{\rm max}$, $V_{\rm max}$ + 2, and $V_{\rm max}$ + 3, respectively; the black vertical dashed lines represent from left to right, $t_{\rm max}$, t_2, and t_3, respectively.

4.3 Photometric results and analysis

4.3.1 Optical light-curve parameters

Several parameters characterize nova light-curves including the rise rate, the rise time to maximum light, the maximum light, the decline rate, and the decline behaviour (see e.g. Hounsell et al. 2010; Cao et al. 2012). Nova V407 Lup was not extensively observed during its rise to maximum.

Based on V-band and visual (*Vis*) measurements from SMARTS and the American Association of Variable Star Observers (AAVSO)[5], we see that the nova reached V = 6.8, 0.4 d after t_0. Then it was reported at $V = 6.4$ on HJD 2457656.24 (Prieto, 2016) and *Vis* = 6.3 on HJD 2457656.57, reaching *Vis* = 5.6 on HJD 2457656.90 (see Table 4.1). Half a day later, the nova was at $V = 6.33$ and *Vis* = 6.5, then dropped to $V = 7.85$ in around two days, indicating that the decline had started. Hence, we assume HJD 2457656.90 as $t_{\rm max}$ (day 1.4).

Caution is required in interpreting magnitudes of novae. This is particularly so for *Vis* where Hα may contribute to the flux detected by eye, but not to CCD V-magnitudes. Furthermore, normal transformation relations for CCD magnitudes cannot be used for objects with strong emission lines. Unfortunately, no spectra were taken around maximum light, so the contribution and development of line emission is unknown until later times (day 5; Izzo et al. 2018). In the following, we assume

[5] https://www.aavso.org/

Table 4.1: V and *Vis* measurements around maximum from different detectors.

HJD	$(t - t_0)$ (days)	Magnitude	Uncertainty	Band	Source
2457655.50	0.0	9.10	0.010	V	ATel 9538
2457655.93	0.43	6.82	0.075	V	AAVSO
2457656.24	0.74	6.43	0.050	V	ATel 9550
2457656.57	1.02	6.32	—	*Vis*	AAVSO
2457656.90	1.10	5.60	—	*Vis*	AAVSO
2457657.22	1.72	6.33	0.060	V	ATel 9550
2457657.45	1.95	6.50	—	*Vis*	AAVSO
2457657.46	1.96	6.84	—	*Vis*	AAVSO
2457657.48	1.97	6.80	—	*Vis*	AAVSO
2457657.48	1.97	7.14	0.001	V	SMARTS
2457657.51	2.01	6.70	—	*Vis*	AAVSO
2457657.89	2.39	6.62	0.050	*Vis*	AAVSO
2457657.92	2.42	6.70	—	*Vis*	AAVSO
2457658.41	2.91	7.10	—	*Vis*	AAVSO
2457658.46	2.96	6.92	—	*Vis*	AAVSO
2457658.48	2.98	6.90	—	*Vis*	AAVSO
2457658.48	2.98	7.26	0.001	V	SMARTS
2457658.99	3.49	7.20	—	*Vis*	AAVSO
2457659.41	3.91	7.50	—	*Vis*	AAVSO
2457659.42	3.92	7.50	—	*Vis*	AAVSO
2457659.44	3.94	7.60	—	*Vis*	AAVSO
2457659.46	3.96	7.54	—	*Vis*	AAVSO
2457659.46	3.96	7.40	—	*Vis*	AAVSO
2457659.98	4.48	7.85	—	*Vis*	AAVSO
2457660.23	4.73	7.70	—	*Vis*	AAVSO
2457660.41	4.91	8.20	—	*Vis*	AAVSO
2457660.42	4.92	8.00	—	*Vis*	AAVSO
2457660.43	4.93	8.10	—	*Vis*	AAVSO
2457660.46	4.96	8.00	—	*Vis*	AAVSO
2457660.46	4.96	7.70	—	*Vis*	AAVSO
2457660.48	4.98	7.88	0.080	V	ATel 9564
2457660.50	5.00	7.98	0.001	V	SMARTS
2457660.92	5.42	8.70	—	*Vis*	AAVSO
2457661.02	5.52	8.10	0.012	V	AAVSO
2457661.20	5.70	8.30	—	*Vis*	AAVSO
2457661.40	2.90	8.60	—	*Vis*	AAVSO
2457661.41	5.91	8.50	—	*Vis*	AAVSO
2457661.48	5.98	8.56	0.001	V	SMARTS

that maximum light was $V_{\rm max} \leq 6.0$ on HJD 2457656.90. Since novae do not usually have strong line emission at maximum light (van den Bergh & Younger, 1987) and given that simultaneous V and *Vis* measurements show very similar magnitudes, before and after maximum light, it may be that $V \sim$ *Vis* =5.6, on HJD 2457656.90, is a reasonable estimate. However, we use $V_{\rm max} \leq 6.0$ for the rest of the analysis to avoid overestimating the maximum brightness.

We construct a V-band light-curve by combining the published photometry from different telescopes and instruments and the SMARTS data (see Fig. 4.13), noting the above caveat. This shows a rapid rise and a sharp peak followed by a fast decline. Such behaviour is characteristic of the S-class nova light-curves (Strope, Schaefer & Henden, 2010), which is considered stereotypical for a nova. However, the broadband light-curves show day-to day variability after t_3 similar to that of an O-class light-curves (see Fig. 4.1). It is worth noting that there is no plateau in the tail of the light-curve (after $\sim 3-6$ mag from maximum) similar to that seen in recurrent novae (see Schaefer 2010).

Although there is a gap in the light-curve between day 26 and day 107 (due to solar constraints), we fit a power-law to the light-curve (only early decline - before day 25) and derive $t_2 \leq 2.9 \pm 0.5$ d, $t_3 \leq 6.8 \pm 1.0$ d and a power index of ~ 0.16 (Note, Izzo et al. 2018 derived longer values of t_2 and t_3. This was due to misinterpretation of their light-curve – Izzo, private communication). We took into account the use of measurements from different instruments by increasing ($\times$ 2) the uncertainty on t_2 and t_3.

With $t_2 \leq 2.9$ d and a decline rate of ~ 0.69 mag d^{-1} over t_2, nova V407 Lup is a "very-fast" nova in the classification of Payne-Gaposchkin (1964) and is one of the fastest known examples. Only a few other novae have shown a decline time $t_2 \lesssim 3.0$ days, including M31N 2008-12a, U Sco, V1500 Cyg, V838 Her, V394 CrA, and V4160 Sgr (see, e.g.,Young et al. 1976; Schaefer 2010; Munari et al. 2011; and table 5 in Darnley et al. 2016).

4.3.2 The *Swift* UVOT light-curve

The UVOT *uvw2* light-curve (Fig. 4.7) declined slowly after day 150 before flattening off at around a *uvw2* magnitude of 14.2 by around day 200, with signs of a 0.1 mag variability superimposed on the overall decline. We find periodicities in the light-curve, which we discuss in Section 4.3.4. The UV data rebrightened after day 300, to reach a *uvw2* magnitude of 13.7 around day 320. Then the brightness started to decline again, reaching a *uvw2* magnitude of 14.9 at day ~ 385. Fig. B.2 shows a direct comparison between the *Swift* X-ray, *Swift* UV, and SMARTS optical light-curves.

4.3.3 The *XMM-Newton* and *Chandra* UV and X-ray light-curves

The *XMM-Newton* RGS1 light-curve (Fig. 4.11) shows evidence of variability on different timescales. This includes two broad ($\sim 2-3$ ks wide) dips separated by ~ 12.6 ks ~ 3.5 h. The *Chandra* HRC light-curve (Fig. 4.12) also shows evidence for short-term variability, which we discuss in Section 4.3.4. The OM fast mode UV light-curve (Fig. 4.11) shows a variation characterized by a 3.76 ± 0.3 h period, which is also consistent (within uncertainty) with the duration between the dips in the RGS1 light-curve. However, no other periodicity is found in the OM light-curve.

4.3.4 Timing analysis

Since the *Swift*/UVOT *uvw2* light-curve (Fig. 4.7) shows evidence for intrinsic variability superimposed on the long term decline, we searched for periodicities in the data. Fig. 4.14 shows a

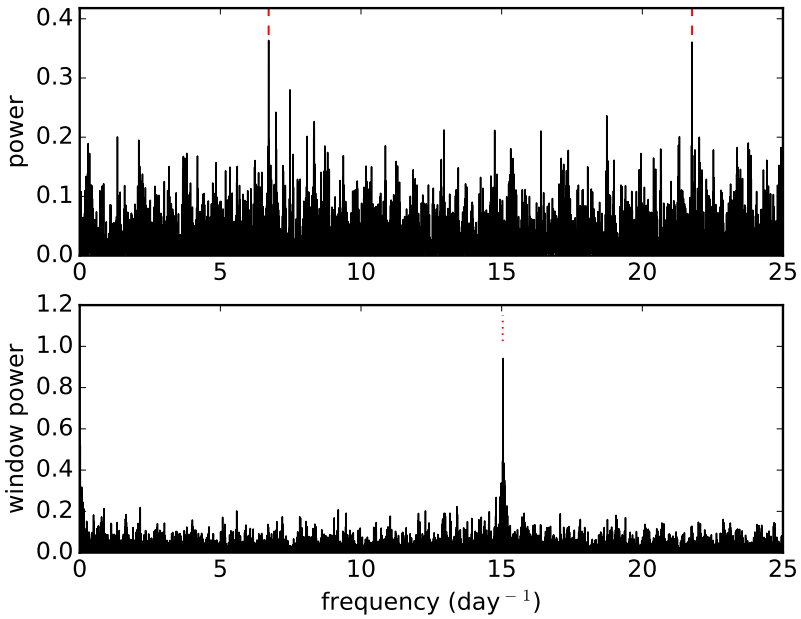

Figure 4.14: Upper panel: the Lomb Scargle periodogram of the detrended *uvw2* light-curve, revealing significant modulation at frequencies of 6.7168 d^{-1} (7.77×10^{-5} s^{-1}; $P = 3.573$ h) and 21.7696 d^{-1} (2.52×10^{-4} s^{-1}; $P = 1.102$ h; with estimated uncertainties of 0.0003 d^{-1}), marked with red dashed lines. Lower panel: periodogram of the observing window, showing *Swift*'s orbital frequency (dotted line).

Lomb-Scargle periodogram (LSP) of the barycentric corrected *uvw2* light-curve after subtracting a third order polynomial to remove the long term trend. The most significant peaks occur at periods of 3.5731 ± 0.0014 h and 1.1024 ± 0.0002 h, which are aliases of each other caused by *Swift*'s 1.6 h orbit. One of these periods might represent the orbital period of the binary ($P_{\rm orb}$). The low cadence of the UVOT data means we cannot break the degeneracy between the periods (the high-cadence observation interval between days 307 and 311 failed to resolve this issue). The amplitude of the modulation is approximately 0.1 mag.

We performed a similar Lomb-Scargle analysis of the *XMM-Newton* RGS1 and *Chandra* HRC data (see Fig. 4.15). The light-curve of the former shows considerable flux variations, while the flux in the latter is approximately constant over the duration of the observation. The *XMM-Newton* periodogram is dominated by a low frequency of $\Omega = 7.77\times10^{-5}$ s^{-1} (3.57 h). This signal only covers $\sim$ two cycles of the 3.57 h period and cannot be believed in isolation. However, as this signal is consistent with the long period seen in the UVOT data, we identify it as the same 3.57 h modulation.

The long-timescale modulation and variability seen in the *XMM-Newton* light-curves, the time between the dips, and the weak modulation observed in the OM light-curve (see Figs 4.11 and 4.15) are all consistent with the 3.57 h signal seen in the *Swift* UV light-curve. In addition, the absence of any variability in the *XMM-Newton* RGS and OM light-curves related to the 1.6 h signal (seen in the *Swift* UV light-curve) has the potential to rule out the modulation at this short period. Therefore

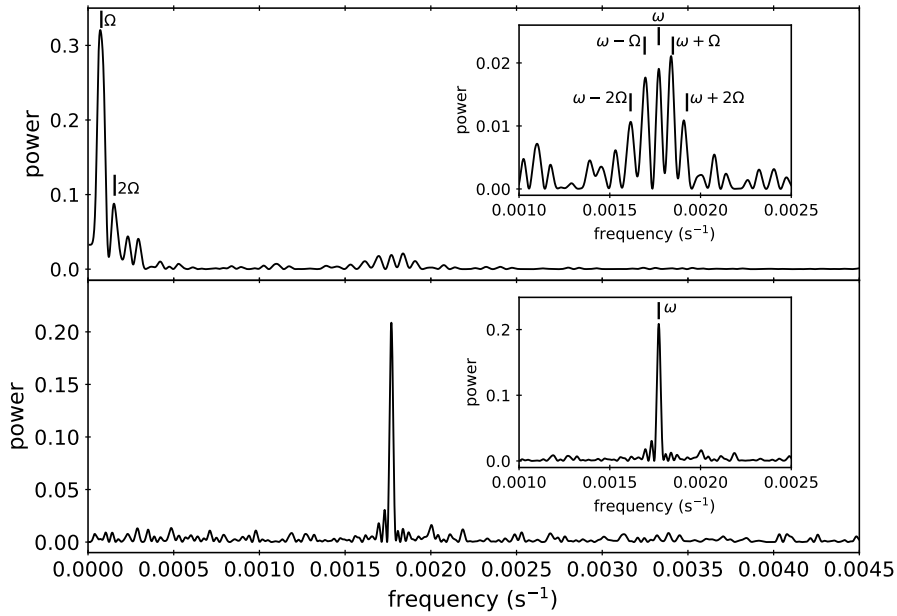

Figure 4.15: Lomb Scargle periodograms of the *XMM-Newton* RGS1 (top) and the *Chandra* HRC (bottom) light-curves. Various frequencies are indicated where $\Omega = 1/P_{\rm orb}$ and $\omega = 1/P_{\rm spin}$ (see text for more details). We present zoom-in plots around the 1.77×10^{-3} s^{-1} in each periodogram.

we assume that the 3.57 h is most likely the $P_{\rm orb}$ of the binary.

Ignoring this long-term variability seen in the low frequency part of *XMM-Newton* periodogram, we find significant signals at $\omega \simeq 1.77\times10^{-3}$ s^{-1} in both (*XMM-Newton* and *Chandra*) light-curves. More precisely, the periodicities we found are at 565.04 ± 0.68 s for the *Chandra* HRC light-curve and 564.96 ± 0.50 s for the *XMM-Newton* RGS light-curve. The *Swift*/XRT observations are almost all too short to usefully constrain the modulation at this short period.

The 565 s X-ray period and the longer 3.57 h UV/X-ray period are clearly reminiscent of the typical spin period ($P_{\rm spin}$) and $P_{\rm orb}$ seen in IP CVs (Warner, 1995). This implies that the system may host a magnetized WD. The ratio of $P_{\rm spin}/P_{\rm orb}$ is ~ 0.44, typical for IPs (Warner, 1995; Norton, Wynn & Somerscales, 2004). Therefore, we suggest that the ~ 565 s period is the $P_{\rm spin}$ of the WD.

While the *Chandra* HRC power spectrum (Fig. 4.15) is relatively easy to read with a single dominant peak (at 1.77×10^{-3} s^{-1}; $P_{\rm spin}$ = 565 s), the *XMM-Newton* data shows a more complicated periodogram with some asymmetry in peak amplitudes. This suggests rather complicated signal behaviour. The different peaks around the central one ($\omega \simeq 1.77\times10^{-3}$ s^{-1}) coincide with $\omega \pm \Omega$ and $\omega \pm 2\Omega$ sidebands. Such signals are commonly seen in IPs (see e.g. Norton, Beardmore & Taylor 1996; Ferrario & Wickramasinghe 1999).

Fig. 4.16 represents the *XMM-Newton* RGS1 soft and hard light-curves and the hardness ratio. When folded at the $P_{\rm spin}$ = 565 s, the light-curves show near sinusoidal variation. Such variation is expected from an IP (see, e.g., Osborne 1988; Norton & Watson 1989; Norton et al. 1992b,a;

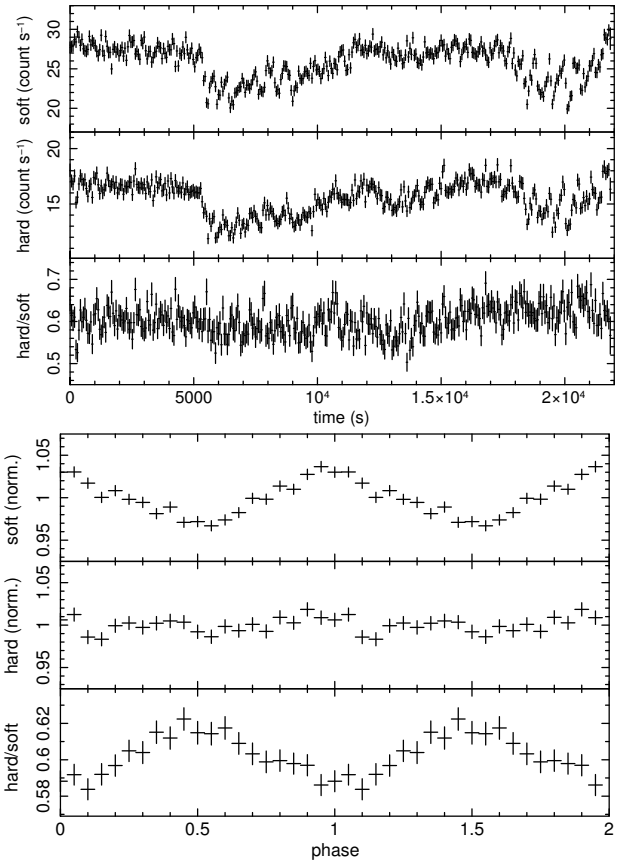

Figure 4.16: *Top:* from top to bottom, soft RGS1 light-curve, hard RGS1 light-curve, and the hardness ratio. The energy bands for the soft and hard light-curves are 23.5 – 37.0 Å (0.3325 – 0.528 keV) and 15.0 – 23.5 Å (0.528 – 0.827 keV), respectively. *Bottom:* same as top but all folded at the 565 s spin period and normalized to their respective mean rates. Therefore, the y-axis represents the relative amplitude of the modulation in both the soft and hard bands.

Norton 1993; Warner 1995), however the RGS data were taken during the post-nova SSS phase and therefore the mechanism responsible for such modulation might be different from that seen usually in IPs (see Section 4.5.4 for further discussion).

Fig. 4.17 represents the folded *Chandra* HRC soft and hard light-curves over the $P_{\rm spin}$, as well as the hardness ratio. The HRC light-curve (taken 340 days after the eruption) shows stronger modulation in the harder bands while the hardness ratio is slightly modulated. This might also suggest that the variation over the $P_{\rm spin}$ is not simply due to absorption by an accretion curtain as it is usually the case for IPs (Warner, 1995).

Typically, the physical reason behind an optical/X-ray modulation over the $P_{\rm spin}$ of the WD seen in IPs is attributed to the variation of the viewing aspect of the accretion curtain as it converges towards the WD surface near the magnetic poles or due to the absorption caused by the accretion curtains. Therefore, such a modulation is usually a sign of accretion impacting the WD surface near the magnetic poles and possibly in this case a sign of accretion restoration. However, the *XMM-Newton* observations were taken during the SSS phase and therefore the soft X-ray is dominated by emission from the H burning on the surface of the WD. Thus, there must be another explanation for

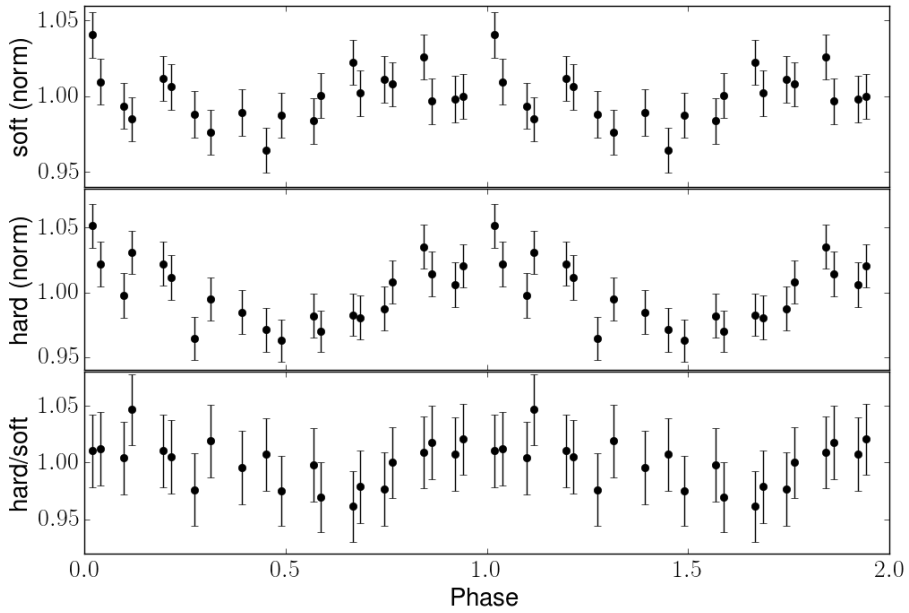

Figure 4.17: From top to bottom, soft *Chandra* HRC light-curve, hard *Chandra* HRC light-curve, and the hardness ratio, all folded over the spin period and normalized to their respective mean rates. Therefore, the y-axis represents the relative amplitude of the modulation in both the soft and hard bands. The energy bands for the soft and hard light-curves are 30 – 50.0 Å (0.248 – 0.413 keV) and 15.0 – 30.0 Å (0.413 – 0.827 keV), respectively.

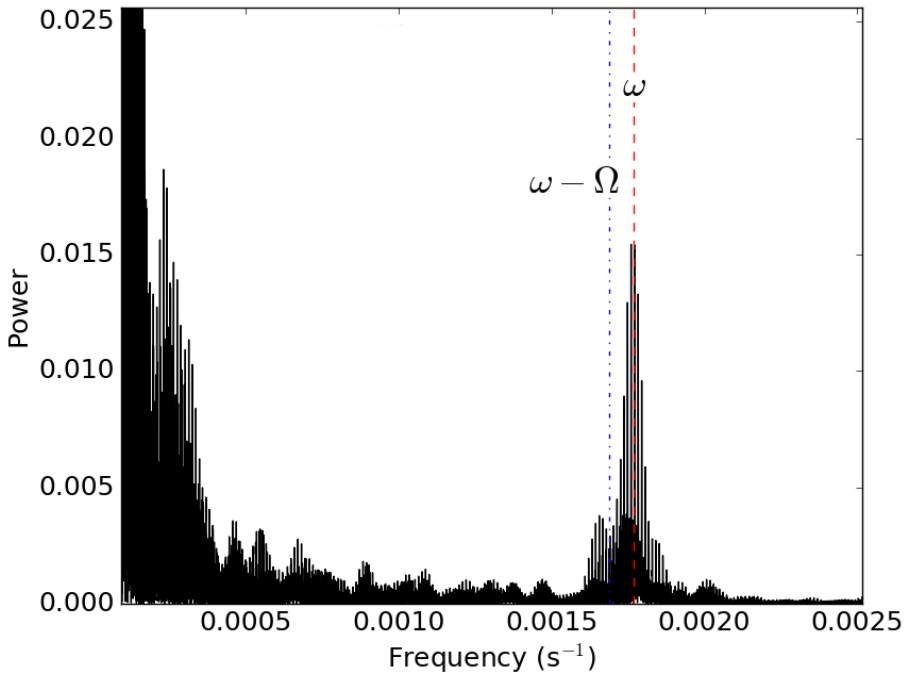

Figure 4.18: Lomb Scargle periodograms of the AAVSO data taken between days 327 and 350 post-eruption. The red dashed line represents the frequency $\omega = 1.77 \times 10^{-3}\,\mathrm{s}^{-1}$ ($1/P_{\mathrm{spin}}$) and the blue dotted line represents the sideband frequency ($\omega - \Omega$).

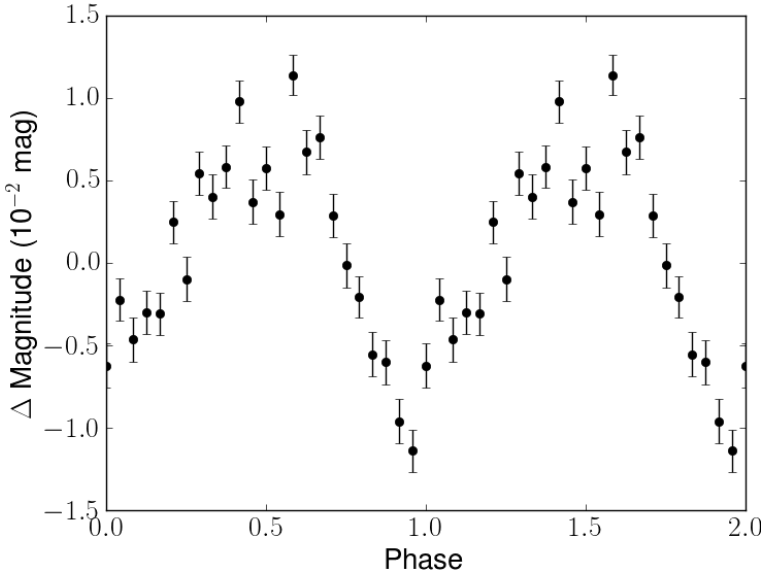

Figure 4.19: The AAVSO optical light-curve folded over the WD spin period of 565 s, using the same ephemeris used to fold the *XMM-Newton* RGS1 light-curves (Fig. 4.16). The y axis represents the change in magnitude relative to the mean brightness level (positive values mean brighter and negative values mean fainter).

the $P_{\rm spin}$ modulation seen in the X-ray light-curves (see Section 4.5.4 for further discussion about the accretion resumption and the origin of the X-ray modulation).

We also performed Lomb-Scargle analysis of the optical AAVSO data (unfiltered reduced to V band) obtained between 327 and 350 days post-eruption. The observations were performed almost every other night and they consist of multiple exposures separated by ∼40 s and spanning for ∼ 4 h. The power spectrum shows a peak at $\sim 1.77\times10^{-3}$ s^{-1} the same as that seen in the *Chandra* power spectrum and which is an indication of the $P_{\rm spin}$ of the WD (Fig. 4.18). The signals seen in the periodogram (Fig. 4.18) at small frequencies are not consistent with either the 3.57 h or the 1.1 h signals seen in the UVOT light-curve and are most likely due to red noise. The spin phase-folded AAVSO optical light-curve is shown in Fig. 4.19. We folded the light-curve using the same ephemeris used to fold the RGS1 light-curves. While the AAVSO optical and *XMM-Newton* X-ray light-curves are out of phase, caution is required when comparing these two light-curves as the *XMM-Newton* observations were done more than 150 days prior to the AAVSO ones (see Section 4.5.4 for further discussion).

4.4 Spectroscopic results and analysis

4.4.1 Optical spectroscopy

4.4.1.1 Line identification

The strongest emission features in the first two SALT HRS spectra, on days 164 and 209 (Fig. 4.2), are the forbidden oxygen lines, [O III] 4363 Å, 4959 Å, 5007 Å, and [O II] 7320/30 Å, along with

the Balmer lines. The lines are very broad with flat-topped, jagged profiles. Forbidden neon lines are also present ([Ne III] 3698 Å blended with Hϵ and [Ne IV] 4721 Å, which might be blended with other neighbouring lines). Other forbidden neon lines, such as [Ne III] 3343 Å, 3869 Å, [Ne V] 3346 Å and 3426 Å, are also present in the SOAR spectrum of day 269 (Fig. 4.5) and in the *Swift* UVOT spectra (Section 4.4.2). Also present are weak permitted lines of helium (He I 4713 Å, 5876 Å, He II 4686 Å, 5412 Å, and 8237 Å - the lines of the Pickering series at 4860 Å and 6560 Å might be blended with Hβ and Hα, respectively), high excitation oxygen lines (O VI 5290 Å), and weak [O I] lines at 6300 Å and 6364 Å. The forbidden [N II] line at 5755 Å is strong and broad, while the permitted N III line at 4517 Å is relatively weak and the one at 4638 Å is possibly blended with other lines. The [N II] doublet at 6548 and 6584 Å might be blended with broad Hα. Relatively weak high ionization, coronal lines of iron might also be present ([Fe VII] 6087 Å, [Fe XI] 7892 Å, and possibly [Fe II] 5159 Å and [Fe III] 4702Å). The spectra also show lines with a FWHM of $\sim$ 100 km s^{-1} at $\sim$ 4498 Å, 5290 Å, and 7716 Å (see Section 4.4.1.3).

The optical spectra show three different types of lines characterized by significantly different widths, therefore, in the remainder of the chapter we will use the following terms:

- "Very narrow lines" to denote those lines with a FWHM $\sim$ 100 km s^{-1} (see Section 4.4.1.3).
- "Moderately narrow lines" to denote those lines with a FWHM $\sim$ 450 km s^{-1}, such as He II 4686 Å (see Sections 4.4.1.3 and 4.4.1.3).
- Broad lines to denote those lines with a FWHM $\sim$ 3000 km s^{-1}, that originate from the ejecta, such as the Balmer and [O III] lines (see Sections 4.4.1.3 and 4.4.1.3).

From day 250 to day 317, the SALT HRS spectra are still dominated by the broad forbidden oxygen lines (see Figs 4.3 and 4.4). The Balmer lines are fading gradually, while other lines such as forbidden Ne and Fe start to disappear. At day 250, a moderately narrow and sharp He II line at 4686 Å emerges and is accompanied by less prominent He II lines at 4200 Å, 4542 Å, and 5412 Å. Similar features of O VI 5290 Å and 6200 Å emerge simultaneously and become more prominent $\sim$ 30 days later. On top of these two O VI lines, the aforementioned very narrow lines are still present. We also detect similar emission features at $\sim$ 4498 and 6050 Å that we could not identify.

All the very narrow and moderately narrow lines show changes in radial velocity and structure, unlike the broad lines. At day 285 He II 4686 Å becomes as strong as [O III] 4363 Å and surpasses it after $\sim$ 300 days. At this stage, moderately narrow Balmer features emerge, superimposed on the pre-existing broad features.

Further to the blue (below 4200 Å) the SOAR medium-resolution spectrum of day 269 shows very narrow emissions of O VI at 3811 Å and $\sim$ 4157 Å. Relatively strong and broad lines of [Ne V] at 3426 Å and 3346 Å and [Ne III] at 3869 Å and 3968 Å are also present (Fig. 4.5).

The late SOAR medium-resolution spectra of days 484 and 485 were of limited-range, centred near to He II at 4686 Å, which appears stronger than Hβ. The latter has a significant broad base (Fig. 4.6). In Table 4.2 we list the line identifications along with the FWHM, Equivalent Widths (EWs), and fluxes of those lines for which an estimate was possible.

Table 4.2: Spectral line identification of the optical SALT and SOAR spectra. We list the EW, FWHM and integrated flux of the lines for which an estimate was possible.

Line	λ_0	EW (λ) (Å)	FWHM (km s^{-1})	Flux 10^{-13}erg cm^{-2}s^{-1}	$(t - t_0)$
[Ne V]	3346	-55 ± 5	2400±100	3.0 ±0.2	269
[Ne V]	3426	-160 ± 10	2400±100	8.0 ±0.5	269
O VI	3811	-1.8 ± 0.2	400± 50	0.08 ±0.02	269
[Ne III]	3869	-75 ± 10	2400±100	2.7 ±0.2	269
[Ne III]	3968	-35 ± 5	2400±100	1.2 ±0.2	269
Hδ	4102	-10 ± 2	2600±100	0.34 ±0.05	269
[O III]	4363	-450 ± 50	2400±100	–	164
Hγ	4341	–	–	–	164
He II	4542	-0.8 ± 0.2	270 ± 50	–	263
He II	4686	-8.7 ± 1.0	435 ± 50	–	250
He I	4713	–	–	–	164
[Ne VI]	4721	–	–	–	164
Hβ	4861	−100±20	2850±100	–	164
[O III]	4959	–	–	–	164
[O III]	5007	–	–	–	164
O VI	5290	0.7 ± 0.2	120±30	–	164
He II	5412	-3.8 ± 0.5	460 ± 50	–	250
[O I]	5577	–	–	–	164
[Fe VI]	5631	–	–	–	164
[Fe VI]	5677	–	–	–	164
[N II]	5755	-80 ± 10	2800±100	–	164
He I	5876	-20 ± 5	2400±100	–	164
[Fe VII]	6087	-35 ± 5	3100±100	–	164
O VI	6200	–	–	–	164
[O I]	6300	-30 ± 5	–	–	164
[O I]	6364	-25 ± 5	–	–	164
Hα	6563	−575 ±2 0	2900±100	–	164
He I	7065	-25 ± 5	2800±100	–	164
[O II]	7320/30	–	–	–	164
Ne IV	7716	-1.1 ± 0.2	150 ± 30	–	164
[Fe X]	7892	-30 ± 5	2800±100	–	164
He II	8237	–	–	–	164

4.4.1.2 Spectral classification and evolution

Izzo et al. (2018) obtained spectra as early as day 5 post-eruption. These spectra show characteristics of the optically thin He/N spectral class with ejecta velocity $\sim 2000\,\mathrm{km\,s^{-1}}$. They also point out the presence of Fe II lines which they attribute to a very rapid iron-curtain phase.

The HRS spectra taken on days 164 and 209 were entirely emission lines and dominated by broad nebular forbidden oxygen lines, along with Balmer and forbidden neon and iron lines. The spectra show that the nova is well into the nebular phase by then. We expect that this phase started around a month from the eruption, based on the fast light-curve evolution, consistent with the spectra of Izzo et al. (2018). The presence of forbidden neon lines in the spectrum also suggests that V407 Lup might be a "neon nova", showing that the eruption occurred on a ONe WD. This has since been confirmed by Izzo et al. (2018) after deriving a Ne abundance $\sim$ 14 times Solar. The highlight of that study was the detection of the ^{7}Be II 3130 Å doublet and that V407 Lup, an ONe nova, has produced a considerable amount of ^{7}Be, which decays later into Li. They concluded that not only CO but also ONe novae produce Li, confirming that CNe are the main producers of Li in the Galaxy.

The optical spectra show the presence of high ionization coronal lines (e.g. [Fe VII] 6087 Å and [Fe XI] 7892 Å). Such lines can be attributed to photoionization from the central hot source during the post-eruption phase, to a hot coronal-line-region, physically separated from the ejecta responsible for the low ionization nebular lines, or possibly to shocks within the ejecta (see e.g. Shields & Ferland 1978; Williams et al. 1991; Wagner & Depoy 1996 and references therein).

In the spectra of day 250 onwards, moderately narrow lines of He II and O VI emerge, the strongest being He II 4686 Å. These lines show changes in their radial velocity between $\sim -210\,\mathrm{km\,s^{-1}}$ and $0\,\mathrm{km\,s^{-1}}$. Similar narrow and moving lines have been observed in a few other novae (e.g. novae KT Eri, U Sco, LMC 2004a and 2009) and their origins have been debated (see e.g. Mason et al. 2012; Munari, Mason & Valisa 2014; Mason & Munari 2014 and references therein; see Sections 4.4.1.3 and 4.4.1.3 for further discussion).

4.4.1.3 Line profiles

Balmer lines: in the early spectra of nova V407 Lup (days 5, 8, and 11), the Balmer lines showed a FWHM of $\sim 3700\,\mathrm{km\,s^{-1}}$ (Izzo et al., 2016, 2018). This FWHM had decreased to $\sim 3000\,\mathrm{km\,s^{-1}}$ by the first HRS spectra at day 164. The lines then show a systematic narrowing with time (Fig. 4.20). We measure the FWHM of these lines by applying multiple component Gaussian fitting in IRAF Tody 1986 and Python (SCIPY packages[6]) environments separately. The values are given in Table 4.3.

This line narrowing has been observed in many other novae (see, e.g., Della Valle et al. 2002; Hatzidimitriou et al. 2007; Shore et al. 2013; Darnley et al. 2016) and can be attributed to the distribution of the velocity of the matter at the moment of ejection. The density of the fastest moving

[6] https://www.scipy.org/

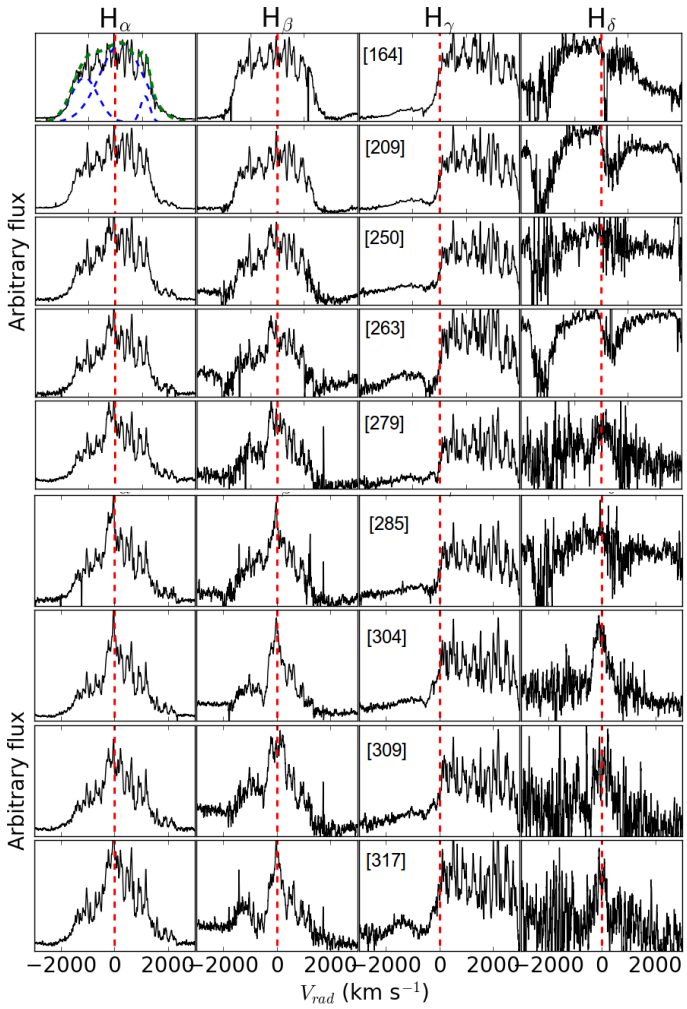

Figure 4.20: The evolution of the line profiles of the Balmer emission. From left to right: Hα, Hβ, Hγ, and Hδ. From top to bottom: days 164, 209, 250, 263, 279, 285, 304, 309, and 317. A heliocentric correction has been applied to the radial velocities. The flux is in arbitrary units. The red dashed lines represent the rest-wavelength of each line ($V_{\rm rad}$ = 0 km s^{-1}). The top-left panel shows an example of multiple Gaussian fitting that was used to derive the FWHM.

Table 4.3: The FWHM of the broad Hα and Hβ. In the last three spectra, the narrow features dominate the broad nebular emission, hence we exclude them from the fitting.

HJD	$t - t_0$ (days)	FWHM (Hα) ± 100 (km s^{-1})	FWHM (Hβ)
2457819.49	164	2900	2850
2457864.38	209	2800	2800
2457905.52	250	2700	2600
2457918.47	263	2650	2400
2457934.43	279	2650	2300
2457940.41	285	2200	2400
2457959.36	304	–	–
2457964.35	309	–	–
2457972.32	317	–	–

Table 4.4: The radial velocity of the "moderately narrow" Hβ and Hα features. These measurements were done by cursor position, when possible.

HJD	$t - t_0$ (days)	$V_{\rm rad}$(Hβ) $\pm$ 50 (km s^{-1})	$V_{\rm rad}$ (Hα)
2457905.52	250	-210	-230
2457918.47	263	-215	-235
2457934.43	279	–	-220
2457940.41	285	-20	-100
2457959.36	304	-20	-20
2457964.35	309	–	–
2457972.32	317	10	-20

gas decreases faster than that of the slower moving gas, leading to a decrease in its emissivity and in turn to the line narrowing (Shore et al., 1996).

While most novae occur in systems hosting a main-sequence secondary, some nova systems have a giant secondary. For such systems, an alternative explanation for the line narrowing has been presented by Bode & Kahn (1985) after efforts to model the 1985 eruption of RS Oph. These authors suggested that shocks and interaction between the high velocity ejecta and low-velocity stellar wind from the companion (red giant in case of RS Oph) are responsible for decelerating the ejecta, which manifests as line narrowing. Of course this might not be the case of V407 Lup where the secondary is very likely a main-sequence star and therefore the mass transfer is more conservative compared to that of systems hosting a giant secondary such as RS Oph.

The Balmer lines have flat-topped, jagged profiles (probably due to clumpiness in the ejecta) with no changes in radial velocity, indicating an origin associated with the expanding ejecta. At day 250 moderately narrow Balmer emission features (FWHM$\sim$ 500 km s^{-1}), superimposed on the broad emission profiles, start to emerge. They become prominent in later spectra (day 304 onwards; see Fig. 4.20). These emission features show variability in structures and radial velocity (see Table 4.4), which is difficult to measure accurately due to the contamination by the broad emission component. However, due to their width and the change in radial velocity, it is very likely that these features originate from the inner binary system, possibly associated with an accretion region (as it is unreasonable to associate such moderately narrow features, which show such a change in radial velocity, with emission from the expanding ejecta).

At this stage, Hγ is still completely dominated by the [O III] line at 4363 Å. However, moderately narrow Hδ emission became prominent while its broad base has completely faded. We also note a dip or absorption feature to the blue of Hβ, Hγ, and Hδ. This dip becomes very prominent in the last spectrum at ~ -650 km s^{-1} (Fig. 4.20).

These moderately narrow Balmer features became prominent $\sim$ 30 days after the emergence of the narrow He II lines (see Section 4.4.1.3). This is expected because such features, which may originate from the inner binary system, can only be seen clearly once the broad Balmer emission has weakened significantly. They also show single-peak emission in most of the spectra, indicating

Table 4.5: The FWHM of [O III] 4363 Å.

HJD	$t - t_0$ (days)	FWHM $\pm$ 100 (km s^{-1})
2457819.49	164	2950
2457864.38	209	2700
2457905.52	250	2400
2457918.47	263	2200
2457934.43	279	2300
2457940.41	285	2200
2457959.36	304	2100
2457964.35	309	1800
2457972.32	317	1600

that if they are originating from the accretion disk, the system may have a low inclination (e.g. close to face-on; between 0° and 15°; see fig. 2.39 in Warner 1995).

Forbidden oxygen lines: broad, nebular emission features of forbidden oxygen dominated the late spectra of nova V407 Lup (day 164 onwards). The [O III] 4363 Å is superimposed over Hγ, hence the blue-shifted pedestal feature. The forbidden oxygen emission features are broad (FWHM $\sim$ 3000 km s^{-1}) and show jagged profiles, possibly an indication of clumpiness in the ejecta.

We measured the FWHM of the [O III] 4363 Å by applying multiple component Gaussian fitting in the IRAF and Python environments separately. The values are listed in Table 4.5. The other [O III] lines are blended with other lines or with each other. Similar to the Balmer lines, the [O III] lines show a systematic narrowing with time (Section 4.4.1.3), but no changes in radial velocity.

The He II moderately narrow lines: several novae have shown relatively narrow He components superimposed on a broad pedestal during the early nebular stages. While the spectra evolve, the narrow components become narrower and stronger (e.g. novae KT Eri, U Sco, LMC 2004a and 2009). For these novae it has been suggested that during the early nebular stage, when the ejecta are still optically thick, the relatively narrow components originate from an equatorial ring while the broad pedestal components originate from polar caps (see, e.g., Munari et al. 2011; Munari, Mason & Valisa 2014 and references therein). Then, when the ejecta become optically thin, these components become narrower by a factor of around 2 (FWHM changing from $\sim$ 1000 km s^{-1} to $\sim$ 400 km s^{-1}) and show cyclic changes in radial velocity. Such cyclic changes in radial velocity can only be associated with the binary system, most likely the accretion disk (Munari, Mason & Valisa, 2014).

This is not the case for V407 Lup as only at day 250 the moderately narrow lines of He II start to emerge (it is possible that early in the nebular stage, these lines have been blended and dominated by the broad and prominent lines coming from the ejecta). We detect He II 4686 Å, 4542 Å, 5412 Å, and 4200 Å. The latter is heavily affected by the increased noise at the edge of the blue arm of HRS. The profiles of the three higher S/N He II lines are presented in Fig. 4.21. We measure the radial

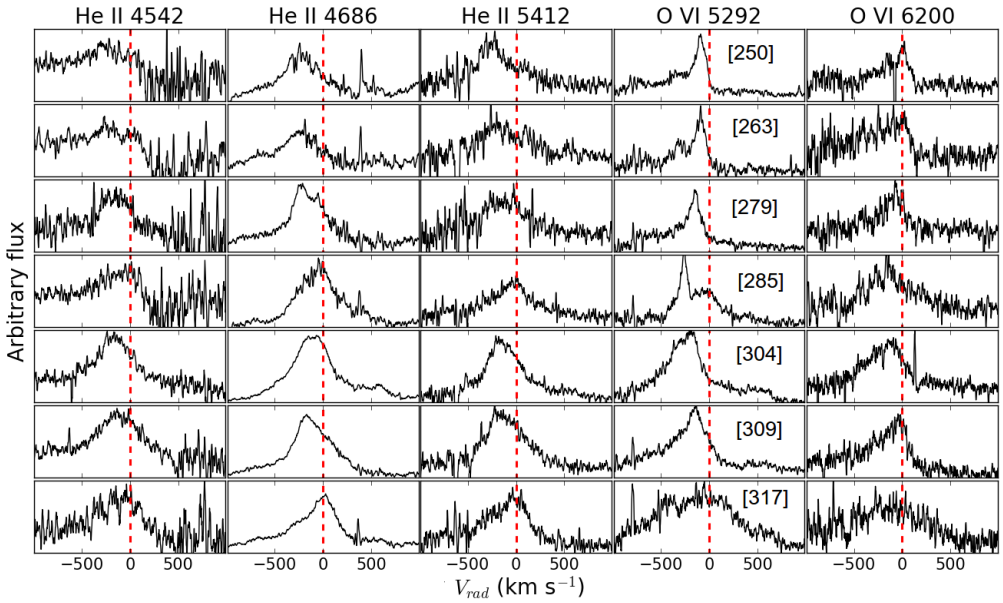

Figure 4.21: The evolution of the profiles of the "moderately narrow" emission lines. From left to right: He II 4542 Å, He II 4686 Å, He II 5412 Å, O VI 5290 Å, and O VI 6200 Å. From top to bottom: days 250, 263, 279, 285, 304, 309, and 317. A heliocentric correction is applied to the radial velocities. The flux is in arbitrary units. The red dashed lines represent the rest-wavelength of each line ($V_{\rm rad}$ = 0 km s^{-1}).

velocity and FWHM of the He II lines by fitting a single Gaussian component. The measurements are illustrated in Table 4.6. The orbital phase is derived using:

$$\text{Phase} = \text{frac}(\frac{[T_{\text{obs.}} - T_0]}{P}) \tag{4.1}$$

where P = 3.57 h is the orbital period, frac() is the fractional part of the value between the parentheses, and T_0 = 2458172.437 is adopted from the ephemeris available on the AAVSO database[7]. The radial velocities of the He II lines range between ~ -210 km s^{-1} and 0 km s^{-1} and they have an average FWHM of $\sim$ 450 km s^{-1}. This range of velocities indicates that the system might have a negative systemic velocity of around -100 km s^{-1}. The three lines show consistent velocity and structure changes across the different spectra, suggesting that they are originating from the same regions.

The He II moderately narrow lines are complex and can be subdivided into at least three components: (1) a medium width component (MWC) with FWHM $\sim$ 300 km s^{-1}; (2) a small width component (SWC) with FWHM $\sim$ 100 km s^{-1}, blended with the MWC in most of the spectra; (3) and a broad base component (BBC; Fig. 4.22). Such complex structures of He II lines are characteristic of mCVs, and they are variously associated with emission from the accretion stream, the flow through the magnetosphere, and the secondary star (Rosen, Mason & Cordova, 1987; Warner, 1995; Schwope, Mantel & Horne, 1997). We also note the presence of a very weak

[7] https://www.aavso.org/vsx/index.php?view=detail.ephemeris&nolayout=1&oid=474105

Table 4.6: The radial velocity ($V_{\rm rad}$), FWHM, and EW derived from a single component fitting of the He II lines. The orbital phase is derived from equation 4.1.

HJD	$t = t - t_0$ (days)	Orbital Phase	$V_{\rm rad}$(He II 4686)	$V_{\rm rad}$(He II 5412) $\pm$ 30 (km s^{-1})	$V_{\rm rad}$(He II 4542)
2457905.52	250	0.088	−210	−205	−240
2457918.47	263	0.072	−210	−177	−210
2457924.51	270	0.583	−175	–	–
2457934.43	279	0.269	−155	−140	−135
2457940.41	285	0.464	−25	−20	−40
2457959.36	304	0.766	−70	−100	−100
2457964.35	309	0.229	−90	−100	−105
2457972.32	317	0.762	0	−20	−60
2458139.84	484	0.033	−90	–	–
2458140.85	485	0.806	−95	–	–
HJD	$t - t_0$ (days)	Orbital Phase	FWHM (He II 4686)	FWHM (He II 5412) $\pm$ 50 (km s^{-1})	FWHM (He II 4542)
2457905.52	250	0.088	435	460	–
2457918.47	263	0.072	470	550	270
2457924.51	270	0.583	550	–	–
2457934.43	279	0.269	470	530	260
2457940.41	285	0.464	400	420	360
2457959.36	304	0.766	510	420	380
2457964.35	309	0.229	430	500	380
2457972.32	317	0.762	410	420	380
2458139.84	484	0.033	570	–	–
2458140.85	485	0.806	465	–	–
HJD	$t - t_0$ (days)	Orbital Phase	EW (He II 4686) $\pm$ 1 (Å)	EW (He II 5412) $\pm$ 0.5 (Å)	EW (He II 4542) $\pm$ 0.2 (Å)
2457905.52	250	0.088	−8.7	−3.8	−0.8
2457918.47	263	0.072	−8.8	−4.2	−0.8
2457924.51	270	0.583	−9.0	–	–
2457934.43	279	0.269	−11.5	−3.0	−1.1
2457940.41	285	0.464	−19.0	−4.6	−1.5
2457959.36	304	0.766	−18.0	−5.3	−2.0
2457964.35	309	0.229	−14.1	−5.0	−1.9
2457972.32	317	0.762	−9.6	−3.0	−1.6
2458139.84	484	0.033	−90	–	–
2458140.85	485	0.806	−95	–	–

red-shifted emission at $\sim$ +600 km s^{-1} from He II 4686 Å that strengthens and weakens from one spectrum to another (Fig. 4.21).

We measure the velocity of the different components of the He II 4686 Å line, by applying multiple Gaussian component fitting (Fig. 4.22). The radial velocity and FWHM of the MWC and SWC of the He II 4686 Å line are listed in Tables 4.7 and 4.8, respectively. Although the two components are clearly out of phase, their velocity measurements should be regarded as uncertain and caution is required when interpreting them, since it is not straightforward to deconvolve the

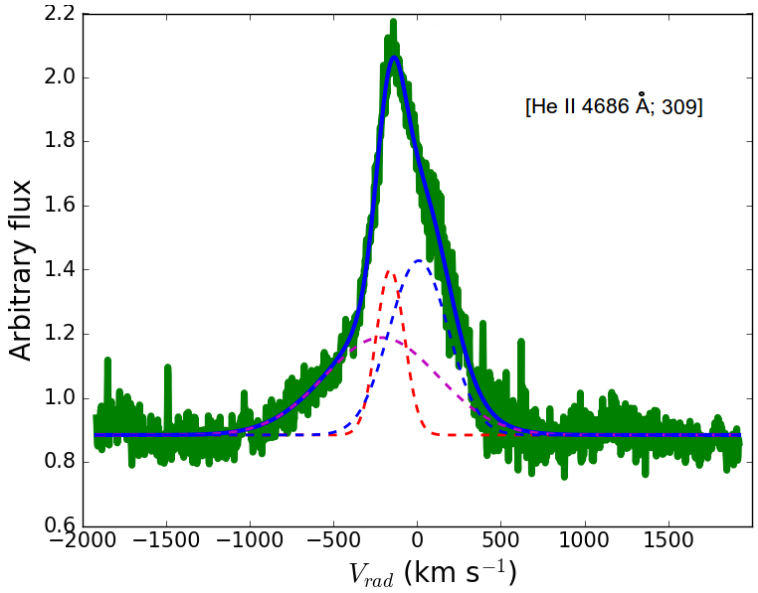

Figure 4.22: A sample of the complex He II 4686 Å "moderately narrow" line from day 309. The line is possibly a complex of 3 components; the green line represents the observation, while the blue solid line is the total fit of the 3 Gaussian components (dashed lines).

Table 4.7: The radial velocity ($V_{\rm rad}$) and FWHM of the medium width component (MWC) of the He II 4686 Å line. The orbital phase is derived from equation 4.1.

HJD	$t - t_0$ (days)	Orbital Phase	$V_{\rm rad}$ $\pm$ 30 (km s^{-1})	FWHM (km s^{-1})
2457819.49	164	0.151	–	–
2457864.38	209	0.753	–	–
2457905.52	250	0.088	-200	240
2457918.47	263	0.072	-215	260
2457934.43	279	0.269	-30	340
2457940.41	285	0.464	-125	230
2457959.36	304	0.766	-170	265
2457964.35	309	0.229	+15	415
2457972.32	317	0.762	-165	300

different components. We also measure the full width of the BBC (see Table 4.9).

Although the complexity of the He II line profiles makes it difficult to draw conclusions about the origins of the different components, we suggest that the SWC, characterized by a FWHM $\sim$ 100 km s^{-1}, must originate from an area of low velocity (possibly the heated surface of the secondary). However, the other two components are possibly associated with emission from an accretion region. It is possible that a fourth component is also present in the He II lines, which adds to the complexity.

The O VI moderately narrow lines: from day 250 we detect relatively weak, moderately narrow lines of O VI 5290 Å and 6200 Å. These two lines are initially dominated by very narrow lines (see Fig. 4.21 and Section 4.4.1.3) possibly associated with a different element and certainly originating

Table 4.8: The radial velocity ($V_{\rm rad}$) and FWHM of the small width component (SWC) of the He II 4686 Å line. The orbital phase is derived from equation 4.1.

HJD	$t - t_0$ (days)	Orbital phase	$V_{\rm rad}$ $\pm$ 30 (km s^{-1})	FWHM
2457819.49	164	0.151	–	–
2457864.38	209	0.753	–	–
2457905.52	250	0.088	-35	70
2457918.47	263	0.072	-5	65
2457934.43	279	0.269	-205	120
2457940.41	285	0.464	-25	–
2457959.36	304	0.766	-10	106
2457964.35	309	0.229	-165	196
2457972.32	317	0.762	+40	200

Table 4.9: The full base width of the broad base component (BBC) of the He II 4686 Å line. The orbital phase is derived from equation 4.1.

HJD	$t - t_0$ (days)	Orbital phase	$[\lambda_i - \lambda_f]$ $\pm$ 1.0 (Å)	$\Delta\lambda$
2457819.49	164	0.151	–	–
2457864.38	209	0.753	–	–
2457905.52	250	0.088	[4671– 4691]	20
2457918.47	263	0.072	[4671– 4691]	20
2457934.43	279	0.269	[4671– 4691]	20
2457940.41	285	0.464	[4677– 4697]	20
2457959.36	304	0.766	[4671– 4693]	22
2457964.35	309	0.229	[4670– 4692]	22
2457972.32	317	0.762	[4670– 4693]	23

Table 4.10: The radial velocity ($V_{\rm rad}$) of the "moderately narrow" O VI 5290 Å and 6200 Å lines. The orbital phase is derived from equation 4.1.

HJD	$t - t_0$ (days)	Orbital Phase	$V_{\rm rad}$(5290) $\pm$ 30 (km s^{-1})	$V_{\rm rad}$(6200)
2457819.49	164	0.151	–	–
2457864.38	209	0.753	5	–
2457905.52	250	0.088	-260	-165
2457918.47	263	0.072	-265	–
2457934.43	279	0.269	-115	-100
2457940.41	285	0.464	-75	-65
2457959.36	304	0.766	-255	-185
2457964.35	309	0.229	-80	-80
2457972.32	317	0.762	–	–

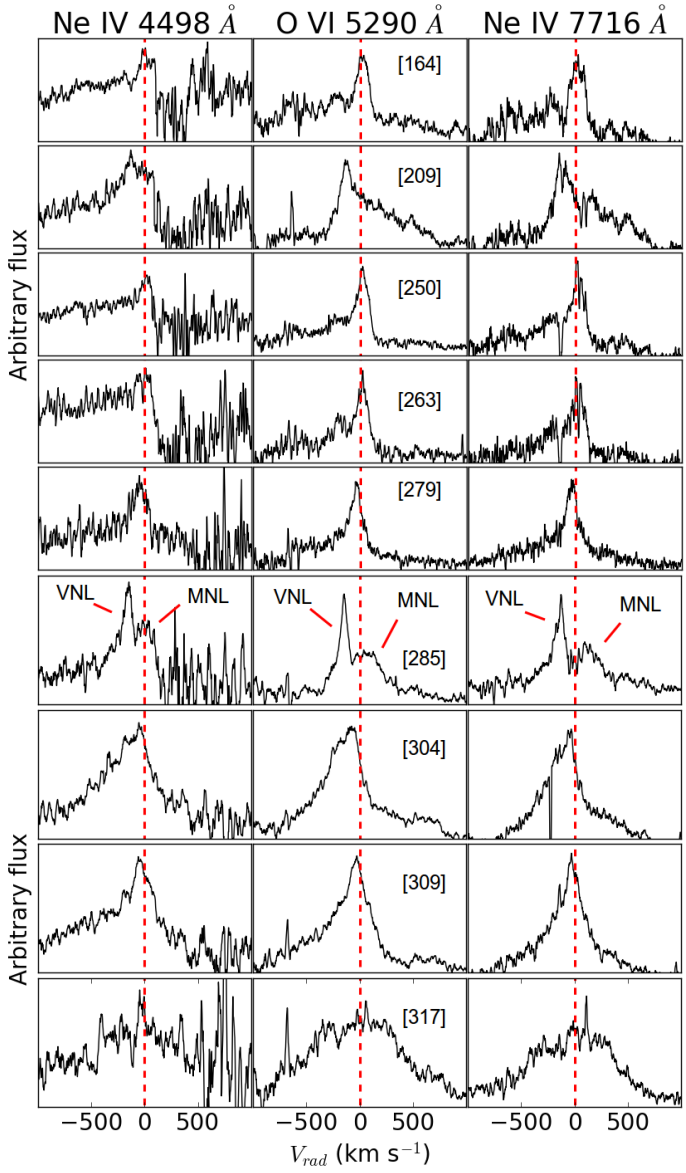

Figure 4.23: The evolution of the profiles of the three "very narrow lines" (VNL) plotted against wavelength. From left to right: Ne IV 4498 Å, O VI 5290 Å, and Ne IV 7716 Å. From top to bottom: days 164, 209, 250, 263, 279, 285, 304, 309, and 317. At day 285, the "very narrow lines" stand out very clearly from the neighbouring "moderately narrow lines" (MNL) as indicated on the plot. A heliocentric correction is applied to the radial velocities.

from a different region. At day 304 the intensity of the O VI lines becomes comparable to the neighbouring very narrow lines and they form a blend. In addition we detect a similar line at 6065 Å (possibly N II). We derive the radial velocity of the moderately narrow O VI lines by fitting a single Gaussian. The values are listed in Table 4.10.

There is no clear correlation between the velocity and the structure of the moderately narrow O VI lines with those of their He II counterparts. It is worth noting that the ionization potential of He II is ~ 54 eV while that of O VI is ~ 138 eV.

Table 4.11: The radial velocity, FWHM and EW of the "very narrow lines": Ne IV 4498.4 Å (top), O VI 5290 Å (middle), and Ne IV 7715.9 Å (bottom). In the last two measurements (days 304 and 309) the lines merge with neighbouring "moderately narrow lines" and therefore the FWHM increases considerably. The orbital phase is derived from equation 4.1.

HJD	$t - t_0$ (days)	Orbital Phase	$V_{\rm rad}$ $\pm$ 30 (km s^{-1})	FWHM (km s^{-1})	EW $\pm$ 0.2 (Å)
2457819.49	164	0.151	−5	120	−0.4
2457864.38	209	0.753	−130	–	–
2457905.52	250	0.088	15	90	−0.4
2457918.47	263	0.072	10	–	–
2457934.43	279	0.269	−50	140	−0.8
2457940.41	285	0.464	−150	85	−0.3
2457959.36	304	0.766	−90	230	−0.3
2457964.35	309	0.229	−50	265	−0.7
2457972.32	317	0.762	–	–	–
2457819.49	164	0.151	20	120	−0.7
2457864.38	209	0.753	−125	–	–
2457905.52	250	0.088	25	110	−0.9
2457918.47	263	0.072	25	110	−0.7
2457934.43	279	0.269	−35	110	−0.9
2457940.41	285	0.464	−145	60	−0.4
2457959.36	304	0.766	−75	340	−2.5
2457964.35	309	0.229	−30	280	−1.5
2457972.32	317	0.762	–	–	–
2457819.49	164	0.151	20	150	−1.1
2457864.38	209	0.753	−120	150	−1.0
2457905.52	250	0.088	20	105	−1.0
2457918.47	263	0.072	20	110	−0.9
2457934.43	279	0.269	−35	110	−1.5
2457940.41	285	0.464	−145	75	−1.1
2457959.36	304	0.766	−80	250	−2.3
2457964.35	309	0.229	−40	310	−3.5
2457972.32	317	0.762	–	–	–

Very narrow lines: a remarkable aspect of the optical HRS spectra is the presence of very narrow, moving lines. These very narrow lines have an average FWHM of $\sim 100\,{\rm km\,s^{-1}}$ and show variation in their velocity (ranging between -150 and +20 km s^{-1}), width, and intensity. The most prominent lines are at $\sim$ 5290 Å (possibly O VI 5290 Å) and $\sim$ 7716 Å (possibly Ne IV 7715.9 Å). A less prominent line is at $\sim$ 4998 Å (possibly Ne IV 4498.4 Å). The line identification is done using the CMFGEN atomic data[8]. These lines stand out in the first few spectra, while a broader neighbouring component emerges later so they form a blend. In Fig. 4.23 we present the evolution of the lines.

We measured the radial velocity and width of these lines by applying single Gaussian fitting. The values are listed in Table 4.11. Their width associates them with a region of low expansion velocity. If these are indeed high ionization O VI and Ne IV lines, they must originate from a very

[8] http://kookaburra.phyast.pitt.edu/hillier/web/CMFGEN.htm

hot region. Belle et al. (2003) found similar lines of N V in the spectra of the IP EX Hydrae and they have attributed these to an emission region close to the surface of the WD. Wind from the accretion disk might also be responsible for the formation of such lines (see, e.g., Matthews et al. 2015; Darnley et al. 2017).

4.4.1.4 Radial velocities

Despite detecting changes in radial velocity of the He II and O VI lines, we failed to derive any periodicity from their radial velocities. This is expected as the SALT spectra are taken on different nights, separated by a few days, up to a month. With such a cadence we would not expect to find modulation in the radial velocity curves. Phase-resolved spectroscopy is needed to do this and to investigate the structure of the system via Doppler tomography (see, e.g., Kotze, Potter & McBride 2016). In addition, the emission from different components (such as the accretion stream, disk, and curtain and the secondary) adds to the complexity of the line profiles.

The absence of any spin-period-related modulation in the velocity curves is also expected, due to the long exposure time and cadence of the spectra. The exposure time of the SALT HRS spectra is more than three times that of the $P_{\rm spin}$, thus, any possible WD spin-dependent effects will be smeared out in the spectra.

Fig. 4.24 shows the phase-folded (over the $P_{\rm orb}$) radial velocities of the MWC and SWC of the He II 4686 Å emission line. The velocities of these two components are anti-correlated. The SWC and MWC are out of phase and they show opposite radial velocity curves, neither of which is consistent with the 3.57 h period. The opposite phase is probably an indication for the origin of these components where the SWC might be associated with emission from the surface of the secondary and the MWC is originating from an accretion region around the WD (accretion disk; see, e.g., Rosen, Mason & Cordova 1987; Schwope, Mantel & Horne 1997). However, the lack of periodicity in the velocity curves, related to the orbital period, makes it difficult to confirm this claim.

The radial velocity amplitude of the emission lines from CVs is strongly dependent on the inclination of the system, as well as the $P_{\rm orb}$ and the mass ratio. Ferrario, Wickramasinghe & King (1993) have modelled IPs with a truncated accretion disk and a dipolar magnetic field, resulting in two accretion curtains above and below the orbital plane, which are responsible for most of the line emission. For such systems, the amplitude of the radial velocities can range from $\sim 200\,{\rm km\,s^{-1}}$ up to $\lesssim 1000\,{\rm km\,s^{-1}}$ depending mainly on the inclination of the system. They also showed that velocity cancellation can occur if both curtains are visible, leading to velocity amplitudes in the range of $\sim 200-300\,{\rm km\,s^{-1}}$. This happens in the case of either a low-inclination system where both curtains are visible through the centre of the truncated disk or if the system is eclipsing (edge-on). The amplitude of the radial velocities derived from the spectral emission lines of V407 Lup is around $200\,{\rm km\,s^{-1}}$. This suggests that the system is possibly at a low inclination.

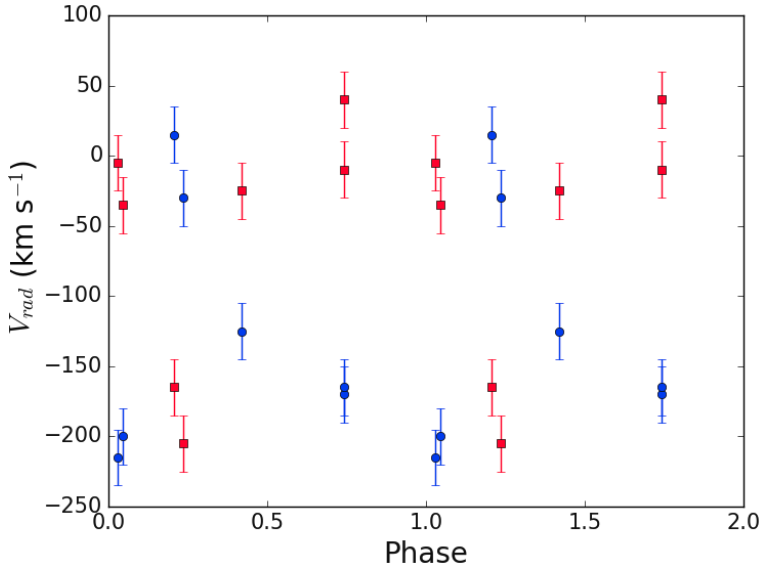

Figure 4.24: Radial velocities of the He II 4686 Å medium width component (MWC; blue circles) and small width component (SWC; red squares) plotted against the orbital phase. The evolution of the velocities is anti-correlated for the two components.

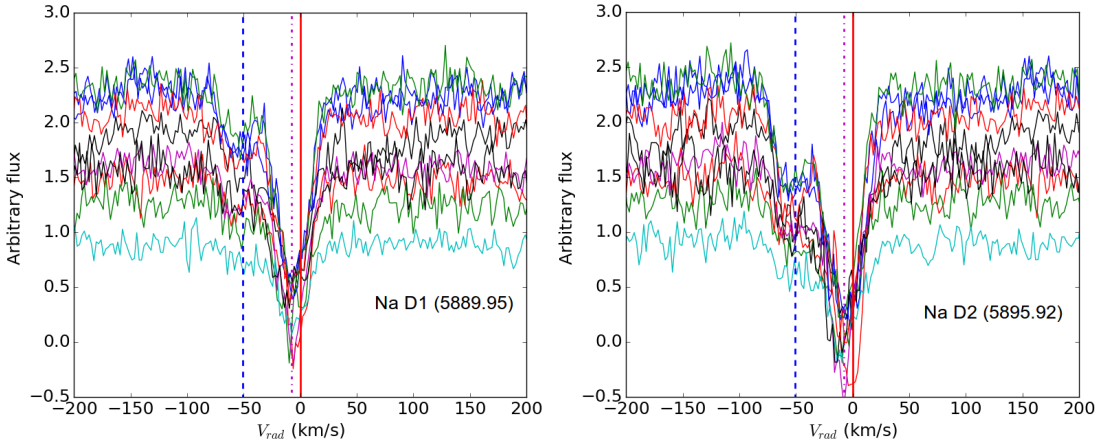

Figure 4.25: The profiles of the Na I D1 (top) and D2 (bottom) absorption lines. Each colour corresponds to a different observation. At least two main components can be identified in the lines. The blue dashed line represents the average radial velocity of the weaker component. The magenta dotted line represents the average radial velocity of the stronger component. The red solid line represents the null radial velocity. A heliocentric correction has been applied to the radial velocities.

4.4.1.5 Sodium D absorption lines

The sodium D absorption lines, D1 (5896 Å) and D2 (5890 Å), are well-known tracers of interstellar material (see e.g. Munari & Zwitter 1997; Poznanski, Prochaska & Bloom 2012). In some cases, circumstellar material around the system can also contribute to Na I D absorption. For recurrent novae this material has been proposed to be due to ejecta from previous eruptions (Patat et al., 2011).

In the high-resolution spectra the Na I D lines are a complex of at least two components, both

blue-shifted (Fig. 4.25). There is a relatively weak component at $\sim -50\pm 3\,\mathrm{km\,s^{-1}}$ and a more prominent one at $\sim -8\pm 3\,\mathrm{km\,s^{-1}}$. Taking into account a suggested systemic velocity of the system ($\sim -100\,\mathrm{km\,s^{-1}}$), both components would be red-shifted. We measure a FWHM of $\sim 35\,\mathrm{km\,s^{-1}}$ for each component. We measure an EW of $\sim 0.94\pm0.02$ Å for the D1 line and $\sim 0.63\pm0.02$ Å for the D2 line. These values are used to derive the reddening in Section 4.5.1.1.

4.4.2 *Swift* UVOT spectroscopy

The UVOT spectra (Fig. 4.8) are dominated by broad emission lines of forbidden O and Ne, along with H Balmer and Mg II resonance lines. A list of the observed lines and identifications is given in Table 4.12. Since the *Swift* UVOT spectra from the grism exposures have an uncertainty in the position of the wavelengths on the image, the individual spectra were shifted to match the [Ne V] 3346 Å and 3426 Å lines. The shifts were at most 15 Å. Any intrinsic shift of the line spectrum is thus undetermined. The emission seen at 1759 Å and 1855 Å in the first order spectrum is uncertain due to the low S/N. However, in the grism image we can see the 1750 Å line in the second order spectrum which lies alongside the first order. The 1860 Å line in the second order is affected by the wings of a nearby first order line, and cannot be confirmed that way. There is no significant line of O II] at 2471 Å, suggesting that the higher ionization state dominates. The He II 2511 Å line may be blended with an unidentified feature around 2533 Å. The line at $\sim$ 2978 Å is possibly Ne VIII 2977 Å (see, e.g., Werner, Rauch & Kruk 2007). A likely identification of the broad blend at 4714 Å has been given with the SALT spectrum (He I 4713 Å; see Section 4.4.1.1). Inspection of the spectrum in Fig. 4.8 shows that the Ne and O lines are much stronger than the H and He lines in this nova, which is consistent with the ONe nature of the WD as concluded by Izzo et al. (2018).

The flux and width of the stronger lines of Mg II, O III, [Ne V], and [Ne III], have been measured for each of the eight UV spectra and the values are shown in Table 4.13. The method used was to plot the line, select the points at which the line merges into the background, and then sum the flux over the line minus the background. The flux uncertainty is around 15% so the forbidden line ratios (Flux [Ne V] 3426/3346 $\sim 2.4-2.7\ \pm0.4$) are close to what is expected in the low density case (ratio ~ 2.7; see the NIST atomic data base)[9]. The Full Width at Zero Intensity (FWZI) clearly depends on the strength of the line. Weaker lines merge earlier with the noise. We also see larger FWZI for longer wavelengths up to $\sim 7000\,\mathrm{km\,s^{-1}}$.

4.4.3 *Swift* X-ray spectral evolution

The initial detection of an X-ray source, once V407 Lup had emerged from behind the Sun (day 150), showed it to be in the supersoft regime already, at a consistently high flux (Fig. 4.27). Therefore, if there was a high-amplitude flux variability phase as seen in some well-monitored novae (e.g. V458 Vul – Ness et al. 2009; RS Oph – Osborne et al. 2011; Nova LMC 2009a – Bode et al. 2016; Nova SMC 2016 – Aydi et al. 2018), it occurred while V407 Lup was behind the Sun and hence unobservable to *Swift*.

[9] https://physics.nist.gov/PhysRefData/ASD/lines_form.html

Table 4.12: Spectral line identifications of the UV-optical grism spectra.

spectrum wavelength (a)	line ID	vacuum lab wavelength	notes
1759	N III]	1750	
1855	Al III	1855,1863	
2141	N II]	2143	
2332	[O III]	2332	
2518	He II	2511	blend?
2635	unid		Ne VI 2626 ?
2801	Mg II	2800	
2978	Ne VIII	2977	
3135	O III	3133	
3346	[Ne V]	3346	
3424	[Ne V]	3426	
3868	[Ne III]	3869	
3970	[Ne III]	3968	
4104	H I	4103	weak
4363	[O III]	4363	
4523	N III	4517	weak
4714	unid		broad feature
4866	H I	4863	
5010	[O III]	4959,5007,5017	blend

(a) after shifting the spectra to best match the [Ne V] doublet.

Table 4.13: UV line measurements for the UV-optical grism spectra. The numbers between brackets are days after t_0.

		10^{-10} Flux ($\mathrm{erg\,cm^{-2}\,s^{-1}}$)							
nominal wavelength (Å)	line ID	MJD 57820 [+165]	MJD 57822 [+167]	MJD 57825 [+170]	MJD 57826 [+171]	MJD 57838 [+183]	MJD 57854 [+199]	MJD 57857 [+202]	MJD 57866 [+211]
2800	Mg II	9.76	14.9	18.4	10.6	7.7	9.6	7.6	11.2
3133	O III	12.1	9.9	7.0	8.1	5.3	5.4	3.2	8
3346	[Ne V]	32.5	28.9	36.1	34.0	23.6	16.1	14.0	15.5
3426	[Ne V]	90.3	76.8	94.4	83.5	59.3	41.1	36.7	36.0
3869	[Ne III]	27.9	28.9	27.9	31.3	19.7	19.6	16.3	17
3968	[Ne III]	13.8	12.6	11.0	14.6	11.5	10.6	8.3	12.4
4363	[O III]	32.7	28.1	31.8	28.5	20.6	22.0	18.4	19.0
		FWZI						(Å)	
2800	Mg II	70.9	90.2	113	55.2	56.6	70.3	66.7	87
3133	O III	90.0	77.3	57.0	57.5	50.8	51.4	40	80
3346	[Ne V]	64.6	73.9	67.0	77.4	64.9	65.9	54.3	58
3426	[Ne V]	79.8	91.1	86.1	86.1	72.1	78.3	71.9	81
3869	[Ne III]	81.3	95.2	74.3	91.7	72.1	85.9	78.6	81
3968	[Ne III]	89.0	77.7	56.1	80.6	82.0	73.4	61.8	98
4363	[O III]	113.6	88.2	116	97.4	95.7	99.5	90.0	103

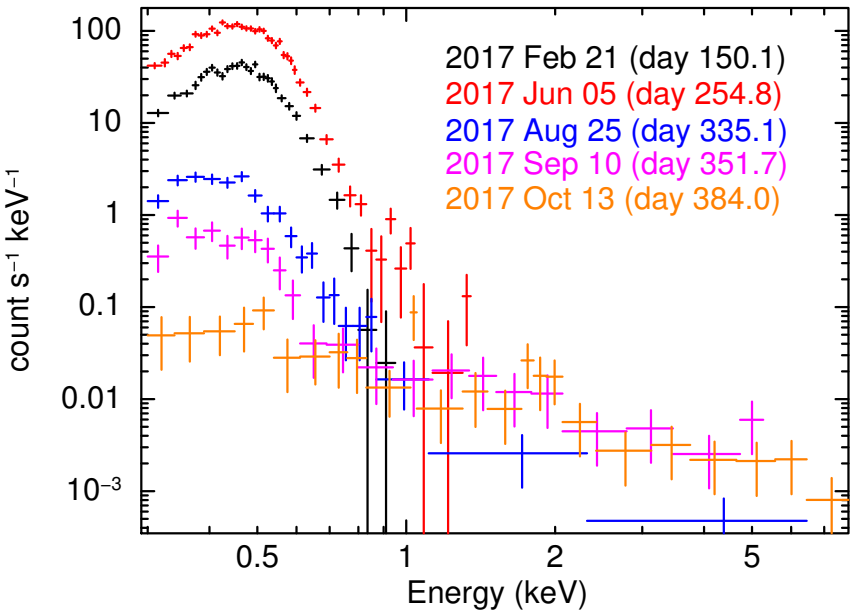

Figure 4.26: A sample of *Swift* X-ray instrumental spectra from days 150.1, 254.8, 335.1, 351.7, and 384.0 since eruption (t_0). Note that the FWHM of the energy resolution at 0.5 keV is $\sim$ 125 eV.

The early X-ray spectra could be acceptably well modelled below 1 keV with a TMAP[10] absorbed plane parallel, static, Non-Local Thermal Equilibrium (NLTE) stellar atmosphere model (Rauch et al. 2010; grid 003 was used). The TBABS absorption model (Wilms, Allen & McCray, 2000) within XSPEC was applied, using the Wilms abundances and Verner cross-sections; this parameter was allowed to vary in the range $(1.15-3.12) \times 10^{21}$ cm^{-2}, based on the analysis of the *XMM-Newton* RGS and *Chandra* LETG spectra (Sections 4.4.4 and 4.4.5). A sample of the spectra obtained during the monitoring is shown in Fig. 4.26, while Fig. 4.27 shows the results of the modelling of the supersoft component. The luminosity was derived using an assumed distance of 10 kpc, which is currently unknown (see Section 4.5.1.2).

We note, however, that an absorbed blackbody (BB) model with a N VII edge at $\sim$0.65 keV provides a statistically better fit than the more physically-based atmosphere model. For example, considering the spectrum obtained on day 200, while a simple BB is a poor fit with Cash-statistic versus the number of degrees of freedom (C-stat/dof) = 611/66, including the oxygen absorption edge decreases this to C-stat/dof = 109/65; the TMAP atmosphere grid leads to C-stat/dof = 533/66, underestimating the observed X-ray flux between 0.8 – 1 keV. Fitting the spectra with the blackbody+edge model, there is no evidence of a temporal trend for the optical depth (τ) of the edge over time, with τ typically lying in the range 1 – 4. The absorbing column required for such blackbody fits is higher than for the atmosphere parameterisation, at $\sim 3 \times 10^{21}$ cm^{-2}. While the blackbody+edge model is statistically preferred, the luminosities from these fits are around a factor of ten higher than those from the atmosphere grids, being $\sim$ a few $\times 10^{39}$ erg s^{-1} between days 150 and 300.

[10]TMAP: Tübingen NLTE Model Atmosphere Package: `http://astro.uni-tuebingen.de/~\protect\kern+.1667em\relaxrauch/TMAF/flux_HHeCNONeMgSiS_gen.html`

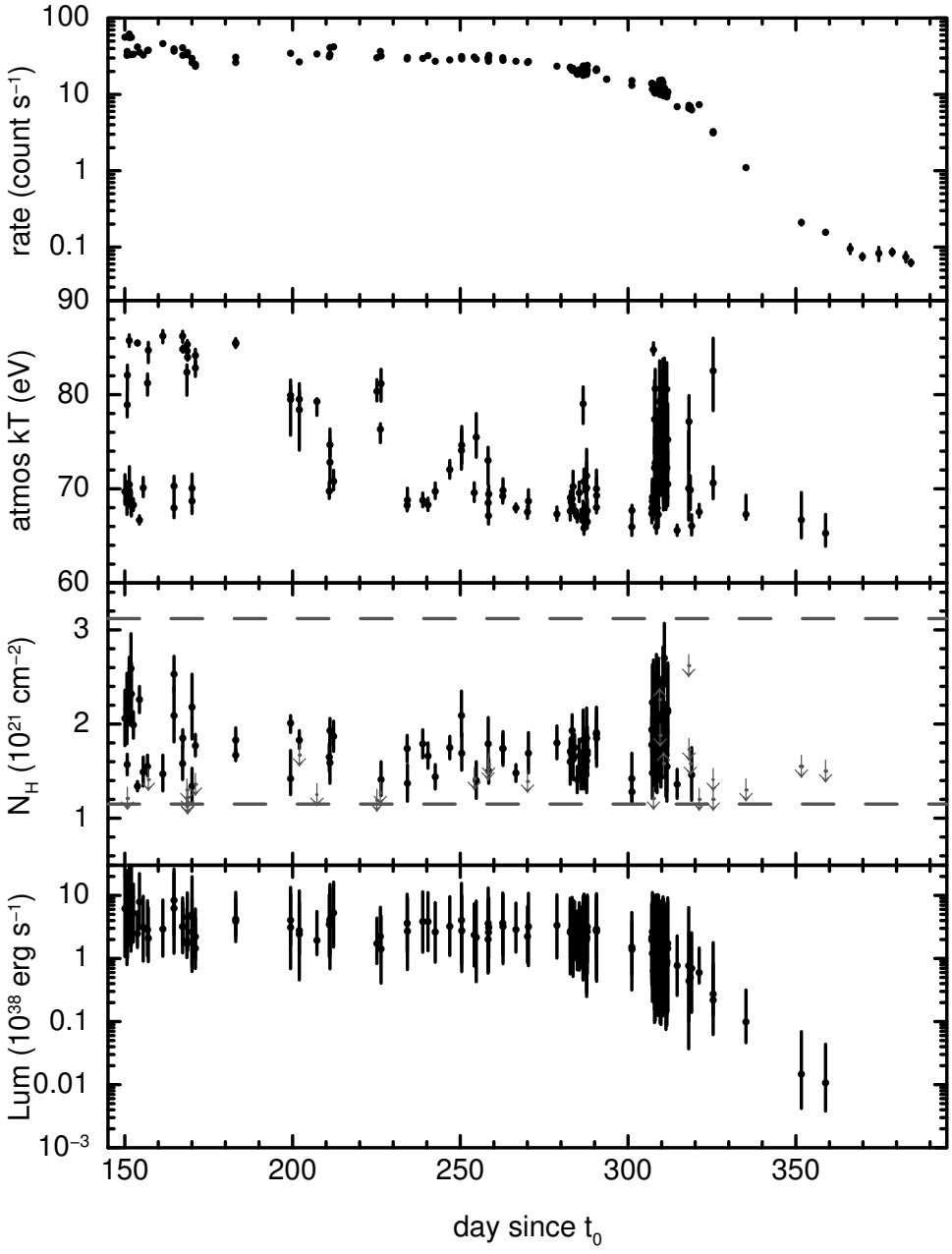

Figure 4.27: Results from fitting the *Swift* XRT spectra (with TMAP atmosphere model; see text for more details), plotted against days since t_0. From top to bottom: the X-ray count rate; the temperature of the SSS emission; the best-fit absorbing column density, constrained to lie in the range of $(1.15-3.12)\times10^{21}$ cm^{-2} from the fits to the *Chandra* and *XMM-Newton* grating spectra, marked by the horizontal dashed lines; bolometric luminosity, for which a distance of 10 kpc is assumed (Section 4.5.1.2 – this value is likely an upper limit for the distance) . For comparison, for a 1.25 $M_\odot$ WD, the Eddington luminosity is 1.6×10^{38} erg s^{-1}.

It is noticeable that the later spectra (day 325 onwards) show evidence for harder X-ray emission above ~ 1.5 keV. This corresponds to the time at which the X-ray source had faded sufficiently that PC mode could be used. The WT mode suffers from a higher background level[11]; in the case of the data collected for V407 Lup, the WT background begins to dominate the source emission around 1 keV, meaning that any such harder component cannot be easily measured.

Using the dataset collected on 2018 January 23 (day 486), at which point the SSS emission has completely faded away, this harder spectral component can be parameterized as optically thin emission with kT > 12 keV, and a $2-10$ keV luminosity of $\sim 4\times10^{33}$ erg s^{-1}, assuming a very uncertain distance of 10 kpc (Section 4.5.1.2). This is the order of magnitude expected for the luminosity from an intermediate polar assuming a typical accretion rate for a CV with a period of ~ 3 hr of $\sim 10^{-8}-10^{-7}$ M$_\odot$ yr^{-1} (Patterson, 1994b; Pretorius & Mukai, 2014). Even at a shorter distance ($d \sim 3-5$ kpc), the hard X-ray luminosity would still be in the right range expected from IPs.

Other novae observed by Swift have also shown harder (>1 keV) emission – see Osborne (2015), as well as the sample of novae discussed by Schwarz et al. (2011). However, these objects typically showed evidence for this harder component from early on in the eruption, before the start of the SSS phase, rather than "switching on" part way through the nova evolution [although V959 Mon (Page et al., 2013a) did reveal a slow rise and fall of the $0.8-10$ keV emission]. In these cases, this harder component was explained as shocks, either within the nova ejecta or with external material, such as the wind from a red giant secondary.

Assuming the same spectral shape as above (optically thin component with kT > 12 keV), we can place a limit on the luminosity of this component during the WT observations of up to a factor of ten below that measured at late times (after day 325). This suggests that this harder X-ray component has turned on significantly after the nova eruption, and could therefore be a signature of restarting accretion. However, with the available data, it is not possible to rule out that the emission may be caused by shocks.

4.4.4 *XMM-Newton* high-resolution X-ray spectroscopy

The absorbed flux at Earth, as measured with the RGS at day 168 over the $14-38$ Å range, was $(1.2\pm0.5)\times10^{-9}$ erg cm^{-2} s^{-1}. The RGS spectrum (Fig. 4.10) is dominated by a bright SSS continuum with relatively weak absorption lines covering most of the spectral range. The most obvious features are absorption edges from N VII at 18.6 Å and O I 22.8 Å and absorption lines from N VII 1s-{2p,3p,4p,5p} (rest-wavelengths at 24.74 Å, 20.9 Å, 19.83 Å, and 19.36 Å), O VII 1s-2p (rest-wavelength at 21.6 Å), and N VII 1s-2p,3p (rest-wavelengths at 28.78 Å and 24.9 Å). These lines are shifted by at most -400 km s^{-1}. In addition, the O VII and N VII 1s-2p lines contain a fast component of -3200 km s^{-1}. A line at 28.5 Å may either be C VI, shifted by -400 km s^{-1}, or N VII, shifted by -3200 km s^{-1}. Further we find interstellar absorption lines of O I 1s-2p (23.5 Å) and N II 1s-2p (31.3 Å).

[11] http://www.swift.ac.uk/analysis/xrt/digest_cal.php#trail shows the typical count rate per column

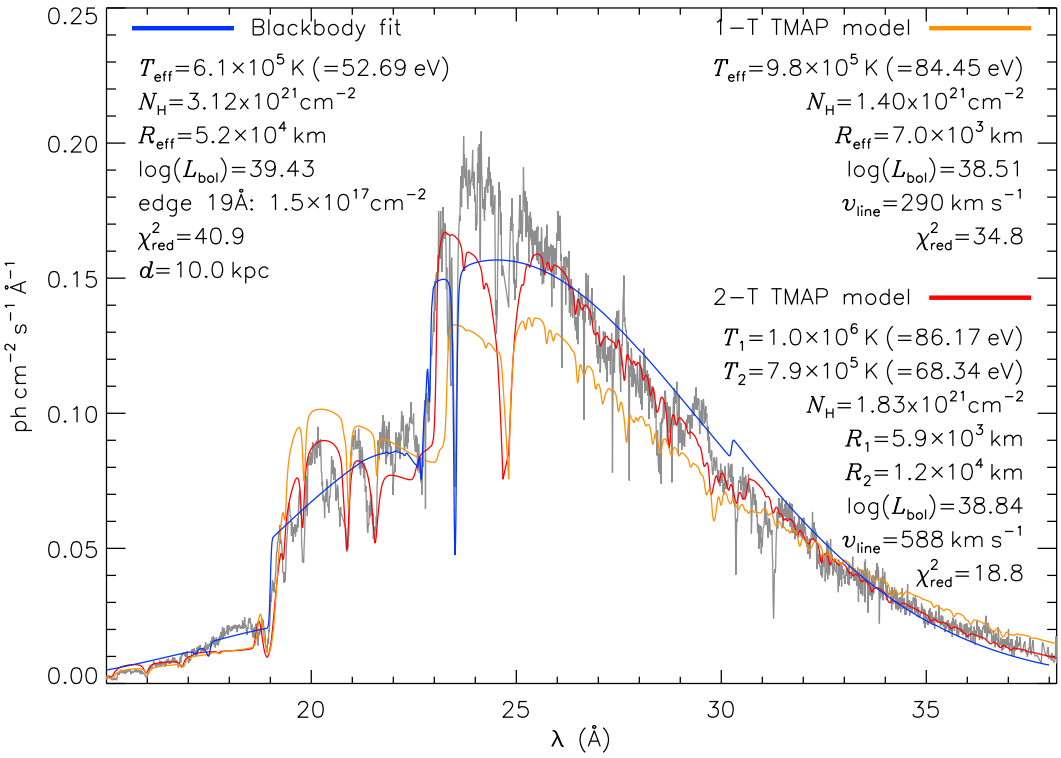

Figure 4.28: This plot represents a blackbody model (blue) including an edge at $\sim$ 18.6 Å (to reproduce the N VII edge; see text for more details), a one-component TMAP model (orange), and a two-components TMAP model (red) all fitted to the *XMM-Newton* RGS spectrum (gray). The parameters of each model are given in the plot. The TMAP models are plane parallel, thus without a radius in the model itself. Therefore, the radii shown in the legend of the TMAP models (1-T and 2-T) were derived assuming spherical symmetry. The bolometric luminosities in the legend were derived using the values of the radii and $T_{\rm eff}$ via Stefan-Boltzmann law. These differ from the luminosities derived in the text based on the X-ray fluxes (see text for more details). The abundances of the interstellar O and N were reduced to 0.6 solar in the blackbody model. The luminosities and radii derived here are distance dependent and therefore a range of these values are presented in Appendix B.1.

The continuum can be parameterized surprisingly well by a blackbody fit plus an absorption edge at $\sim$ 18.6 Å to reproduce the N VII edge (τ=0.94 equivalent to a column density 1.5×10^{17} cm^{-2}), yielding $T_{\rm eff}$=6.1×10^5 K (kT=53 eV), $N_{\rm H}$ = 3.12×10^{21} cm^{-2} (Fig. 4.28). The abundances of the interstellar O and N were reduced to 0.6 solar. The column density of the N VII edge suggests that it arises from a hot plasma (the ionization potential of N VII is $\sim$ 77.5 eV). The presence of such a deep absorption edge, while seeing "shallow" absorption lines, could indicate that the plasma is highly ionized. A high degree of ionization makes the plasma more transparent, and possibly this can explain why the continuum is best fitted by a blackbody model. Note that the *Chandra* spectrum on day 340 shows evidence for even fewer absorption lines (see Section 4.4.5). The continuum normalization corresponds to a radius of 5.2×10^4 km (assuming spherical symmetry; this is an order of magnitude larger than a typical WD radius) at an assumed distance of 10 kpc (Section 4.5.1.2). While a bloated WD is a possible interpretation, overestimates

Table 4.14: The parameters of the two-components TMAP model used to fit the RGS spectrum. $F_{(\rm abs)}$ and $F_{(\rm unabs)}$ represent the absorbed and unabsorbed fluxes, respectively.

Parameter	Value
$N_{\rm H}$ (cm^{-2})	1.83 $\times 10^{21}$
$T_{\rm eff,1}$ (K)	1.016 $\times 10^{6}$
$T_{\rm eff,2}$ (K)	7.930 $\times 10^{5}$
Velocity blue-shift (km s^{-1}	588
$F_{(1,\rm abs)}$ (erg cm^{-2} s^{-1})	6.18 $\times 10^{-10}$
$F_{(1,\rm unabs)}$ (erg cm^{-2} s^{-1})	4.04 $\times 10^{-9}$
$F_{(2,\rm abs)}$ (erg cm^{-2} s^{-1})	5.98 $\times 10^{-10}$
$F_{(2,\rm unabs)}$ (erg cm^{-2} s^{-1})	5.26 $\times 10^{-9}$
Total $F_{(\rm abs)}$ (erg cm^{-2} s^{-1})	1.22 $\times 10^{-9}$
Total $F_{(\rm unabs)}$ (erg cm^{-2} s^{-1})	9.30 $\times 10^{-9}$

of the radius are quite common when using blackbody fits. In Appendix B.1 we present conversion equations for the parameters that are distance dependent (e.g. radii and luminosities). We also present a range of values for these parameters using different distance assumptions.

We also experimented with the NLTE atmosphere models from TMAP (Rauch et al. 2010; Fig. 4.28) and with the synthetic models for expanding atmospheres “wind-type" model (van Rossum 2012; Fig. B.1). Neither of these models reproduced the observed RGS spectrum of V407 Lup. The closest approximation with a plane-parallel, static, NLTE TMAP model yields $T_{\rm eff}$=9.8$\times 10^5$ K (kT=85 eV), $N_{\rm H}$ = 1.4$\times 10^{21}$ cm^{-2}, and an absorption line velocity of 290 km s^{-1} (see Fig. 4.28). The absorbed and unabsorbed X-ray (15 – 38 Å; 0.33 – 1 KeV) fluxes derived from this model are 1.19 $\times 10^{-9}$ erg cm^{-2} s^{-1} and 5.45 $\times 10^{-9}$ erg cm^{-2} s^{-1}, respectively. The X-ray flux derived from the TMAP model is more than 95% the bolometric flux, therefore this flux equates to an absolute bolometric luminosity of $\sim$ 6.5$\times 10^{37}$ erg s^{-1} at a distance of 10 kpc (Section 4.5.1.2). We note that this TMAP model also contains a few weak absorption lines. The comparison with the wind-type atmosphere models suggests $T_{\rm eff}$ between 5.5$\times 10^5$ K and 6.0$\times 10^5$ K (kT=47 – 52 eV).

Due to the complexity of the spectrum, we consider the idea that the atmosphere is not homogeneous, possibly due to hotter emitting regions towards the poles. Therefore, we carried out modelling using two TMAP model components from the grid 003. The parameters of the models are given in Table 4.14. The combination of these two models results in a reasonably good fit to the continuum and it is presented in Fig. 4.28. The total flux derived from the two-component TMAP models is 1.22$\times 10^{-9}$ erg cm^{-2} s^{-1} and the total unabsorbed flux is 9.30$\times 10^{-9}$ erg cm^{-2} s^{-1}. At a distance of 10 kpc (see Section 4.5.1.2 and Appendix B.1), this equates to an absolute bolometric luminosity of $\sim$ 1.1$\times 10^{38}$ erg s^{-1}.

4.4.5 *Chandra* high-resolution X-ray spectroscopy

The observed (absorbed) integrated flux measured with the *Chandra* LETG is 2.89$\times 10^{-10}$ erg cm^{-2} s^{-1}, which is a factor of $\sim$ 45 lower than the observed (absorbed) integrated flux measured with *XMM-*

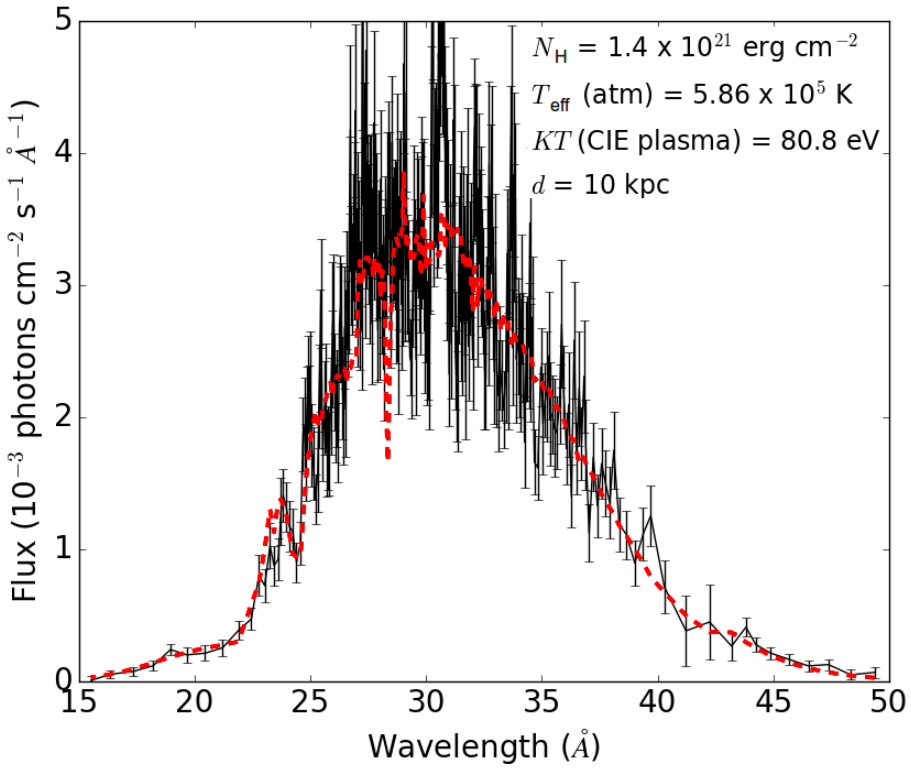

Figure 4.29: Model 1 (red) fit to the *Chandra* LETG spectrum (black). The model consists of two components: a TMAP atmosphere model and a `bvapec` Collisional Ionization Equilibrium (CIE) plasma model. The carbon abundance in the CIE model is enhanced to 19.6 times the solar value. See text for more details.

Newton RGS on day 168 (see Section 4.4.4). It is worth noting that the RGS spectrum is sensitive to a shorter range (6 – 38 Å) compared to the LETG spectrum (1.2 – 175 Å; i.e. a part of the flux is not included in the RGS spectrum). Even if $N_{\rm H}$ has not decreased, this would imply that the effective temperature, which scales as $L^{-1/4}$, has decreased by a factor of 2.6. This is can be ruled out by examining Fig. 4.10 which does not show such a shift in temperature (the peaks of the RGS and LETG spectra show a decrease of temperature by a factor of $\lesssim$1.4). We conclude that we are possibly only observing a small portion of the WD surface. This might be an indication that at this stage ($\sim$ day 340) accretion has resumed and the WD is partially hidden by an accretion disk and/or accretion curtains (see Section 4.5.4 for further discussion) or it may instead mean that the temperature is not homogeneous on the WD surface and supersoft X-rays are emitted only in a restricted region of the surface, possibly on the polar caps (see, e.g., Zemko, Mukai & Orio 2015; Zemko et al. 2016). Another intriguing element in the spectrum is that the N VII absorption feature appears blue-shifted by $\sim -4600\,{\rm km\,s^{-1}}$, which is a larger velocity compared to the blue-shift measured on day 168 in the RGS spectrum (Fig. 4.10).

We tried two models to fit the *Chandra* LETG spectrum. In the first model (Model 1; parameters given in Table 4.15) we assumed that the bulk of the flux comes from the WD surface, with an additional component of plasma in collisional ionization equilibrium. For this purpose we used a TMAP atmosphere model with a `bvapec` model based on the *Astrophysical Plasma Emission Code* (APEC; Smith et al. 2001), with enhanced carbon abundances (19.6 $\times$ solar abundance)

Table 4.15: The parameters of the first model (Model 1) used to fit the *Chandra* LETG spectrum. $T_{\rm bvapec}$ represents the temperature of the collisionally ionized plasma around the nova. $F_{\rm (abs)}$ and $F_{\rm (unabs)}$ represent the absorbed and unabsorbed fluxes, respectively.

Parameter	Value
$N_{\rm H}$ (cm^{-2})	1.4×10^{21}
$T_{\rm eff}$ (K)	5.86×10^{5}
$T_{\rm bvapec}$ (eV)	80.8
Atmosphere $F_{\rm (abs)}$ (erg cm^{-2} s^{-1})	1.13×10^{-11}
Atmosphere $F_{\rm (unabs)}$ (erg cm^{-2} s^{-1})	1.29×10^{-10}
CIE $F_{\rm (abs)}$ (erg cm^{-2} s^{-1})	1.61×10^{-11}
CIE $F_{\rm (unabs)}$ (erg cm^{-2} s^{-1})	3.46×10^{-10}
Total $F_{\rm (abs)}$ (erg cm^{-2} s^{-1})	2.74×10^{-11}
Total $F_{\rm (unabs)}$ (erg cm^{-2} s^{-1})	4.75×10^{-10}

and assuming solar abundances for the other neutral absorbing elements. The fit is not perfect and underestimates the observed flux by 10%, so we conclude that there must be an additional component, possibly a plasma at a different temperature and electron density, since the residual flux seems to be in emission lines. We experimented by varying the abundances or assuming different red-shifted wind velocities, but this did not result in a better fit. The emission lines appear to be broadened by ~ 5000 km s^{-1}, although we had to fix this value to avoid obtaining an unreasonably high velocity. Similarly to the RGS spectrum, we also cannot fit well the shallow absorption line profiles. The total absorbed and unabsorbed X-ray (in the range 15 – 50 Å; 0.248 – 0.827 KeV) fluxes derived from this model are 2.74×10^{-11} erg cm^{-2} s^{-1} and 4.76×10^{-10} erg cm^{-2} s^{-1}. The X-ray flux derived from Model 1 is more than 95% the bolometric flux, therefore this equates to an absolute bolometric luminosity of $\sim 5.7 \times 10^{36}$ erg s^{-1} at 10 kpc. Fig. 4.29 represents the fit of Model 1.

In the second model (Model 2; parameters given in Table 4.16), we assumed that there is a homogeneous WD atmosphere and that due to accretion the polar caps become hotter than the rest of the surface and emit as an additional blackbody component. Because a blackbody energy distribution is broader than just the atmospheric spectral energy distribution, this results in the assumption that there is more absorption of soft flux, partially lifting the discrepancy in $N_{\rm H}$ value (see Section 4.5.1.1). The best fit in this case yields $N_{\rm H}$ =1.87×10^{21} cm^{-2}. The absorbed flux coming from the blackbody component alone would be 2.15×10^{-11} erg cm^{-2} s^{-1} and an unabsorbed flux of 6.53×10^{-9} erg cm^{-2} s^{-1}. At a distance of 10 kpc (Section 4.5.1.2), this would imply an absolute X-ray luminosity of $\sim 7.8 \times 10^{37}$ erg s^{-1} (in the range 15 – 50 Å; 0.248 – 0.827 KeV), which seems absurd because it is four orders too high compared to heated polar caps of magnetic CVs (e.g. Zemko et al. 2017 and references therein; see also Section 4.5.4). It is worth noting that even at shorter distances (3 – 5 kpc; see Appendix B.1) this luminosity is still three orders of magnitude higher compared to heated polar caps of magnetic CVs.

We also experimented with "wind-type" models of van Rossum (2012) for an expanding

Table 4.16: The parameters of the second model (Model 2) used to fit the *Chandra* LETG spectrum. $F_{(\mathrm{abs})}$ and $F_{(\mathrm{unabs})}$ represent the absorbed and unabsorbed fluxes, respectively.

Parameter	Value
N_{H} (cm^{-2})	1.87 $\times 10^{21}$
T_{eff} (K)	6.36 $\times 10^{5}$
$T_{(\mathrm{atm})}$ (eV)	39
Total $F_{(\mathrm{abs})}$ (erg cm^{-2} s^{-1})	2.75$\times 10^{-11}$
Total $F_{(\mathrm{unabs})}$ (erg cm^{-2} s^{-1})	6.94 $\times 10^{-9}$

atmosphere to fit the *Chandra* spectrum. These did not result in a good fit. At a distance of 10 kpc, the best fit parameters are: $T_{\mathrm{eff}} = 4.5 \times 10^{5}$ K, N_{H} = 1.7×10^{21} cm^{-2}, and logarithm of the surface gravity $\log g$ = 8.24. Fig. B.1 shows a sample of the best fit models for various wind asymptotic velocities v_{∞} and mass-loss rates $\dot{M}$.

4.5 Discussion

4.5.1 Reddening, distance, and eruption amplitude

4.5.1.1 Reddening

Estimating the distance to CNe is not straightforward, but it is a crucial step in deriving the properties of the eruption and its energetics. Estimating the reddening is vital for establishing the distance, and we investigate this using various methods below.

The reddening maps of Schlafly & Finkbeiner (2011) indicate $A_V = 0.88$ in the direction of nova V407 Lup ($l = 330.1,\ b = 9.6$), which should be regarded as an approximate lower limit for any object that is sufficiently distant. From the modelling of the X-ray grating spectra, we derived N_{H} ranging between 1.4 and 3.12 $\times$ 10^{21} cm^{-2}. Using the relation between N_{H} and A_V from Zhu et al. (2017), we derive A_V between $\sim$ 0.67 and 1.50 ($\pm$ 0.02). Caution is required when drawing conclusions from these values as they are model dependent.

Poznanski, Prochaska & Bloom (2012) presented empirical relations between the extinction in the Galaxy and the EW of the Na I D absorption doublet. Using these and the measured EW of the Na I D absorption lines at 5990.0 Å (D1) and 5896.0 Å (D2, see Section 4.4.1.5), we derive $E(B-V) = 0.93 \pm 0.25$ and A_V = 2.89 $\pm$ 0.25.

Using colours of novae around maximum has also been suggested as a way to derive reddening (van den Bergh & Younger, 1987). These authors derived a mean intrinsic colour $(B-V)_0$ = +0.23 $\pm$ 0.06 for novae at maximum light and $(B-V)_0$ = -0.02 ± 0.04 at t_2. We lack broadband observations exactly at maximum and t_2, however, we measure $(B-V) \sim 0.8 \pm 0.04$ at $t_{\mathrm{max}} + 0.5$ d using SMARTS. This points towards $E(B-V)$ and A_V values close to that derived from the Na I D EWs. We consider this interpretation as uncertain due to the fast decline and rapid change of the colours around maximum in the case of V407 Lup.

The reddening values we derive from the optical spectroscopy and photometry are much higher than the values derived from the X-ray modelling (Sections 4.4.4 and 4.4.5) and the ones from the reddening maps (see above). This discrepancy suggests that the Poznanski, Prochaska & Bloom (2012) relations are possibly unreliable in the case of this nova. Note that the IP identity of V407 Lup (see Section 4.5.5) also adds to the discrepancy between the reddening derived from the optical and X-ray spectra. If the spin modulation seen in the X-ray data is indeed due to absorption from the system (Section 4.5.4), this means that the X-ray total absorption is due to two components, the interstellar medium (ISM) and the system. Therefore, the absorption due to the ISM is less than the total absorption and the A_V derived from the X-ray spectra might be even smaller.

Izzo et al. (2018) derived an intrinsic extinction of $E(B-V) = 0.24 \pm 0.02$ and therefore $A_V = 0.74$ for V407 Lup, in good agreement with the reddening we derive from the X-ray spectra. These authors have used the diffuse interstellar bands as well as the van den Bergh & Younger (1987) relations to derive the reddening. The assumption of different $t_{\rm max}$, t_2, and the use of the broadband photometry reported in Chen et al. (2016) led Izzo et al. (2018) to derive low values of reddening from the relations of van den Bergh & Younger (1987). The broadband photometry reported in Chen et al. (2016) around maximum are different (by ~ 0.8 mag) from simultaneous SMARTS measurements (see Table 4.1).

For the purpose of our analysis we will use the value of $A_V = 0.67 \pm 0.02$ derived from the fitting of the LETG *Chandra* spectra which is taken at a late epoch (day 340) and is most sensitive to the column density. In some cases we make use of both extreme values (A_V = 0.67 and 2.89) derived from the X-ray and optical spectroscopy.

4.5.1.2 Distance and eruption amplitude

The so-called “Maximum Magnitude-Rate of Decline" (MMRD) relations (see e.g. McLaughlin 1939a; Livio 1992; Della Valle & Livio 1998; Downes & Duerbeck 2000) were considered useful for deriving distances to novae. A physical explanation for these relations has been offered by Shara (1981) and Livio (1992) proposing that the mass of the WD ($M_{\rm WD}$) is the dominant factor that controls the brightness of the eruption. The relations have been questioned theoretically (see e.g. Ferrarese, Côté & Jordán 2003; Yaron et al. 2005) and subsequently proved unreliable following the discovery of faint-fast novae in the M31 (Kasliwal et al., 2011) and M87 (Shara et al., 2016, 2017a). It is now accepted that several factors influence the eruption of a nova, including the accretion rate, the mass of the accreted envelope, the chemical composition and the temperature of the WD, in addition to $M_{\rm WD}$. Buscombe & de Vaucouleurs (1955) have suggested that all novae decline to the same magnitude around 15 days after maximum light. This method is also is also considered uncertain, especially for fast novae (see e.g. Darnley et al. 2006; Shara et al. 2017c and references therein). Using the $M_{V,15}$ method we obtain a distance estimate $d \simeq 3.4^{+1.3}_{-1.0}$ kpc, with A_V = 2.89 $\pm$ 0.25 and $d \simeq 9.4^{+2.3}_{-1.8}$ kpc, with A_V = 0.67 $\pm$ 0.02. We do not adopt any of the distances derived using the methods discussed above, due to their great uncertainty.

The nova is included in Gaia DR1 (data between 2014 July 25 and 2015 September 16) at

$G = 18.95$ and in DR2 (data between 2014 July 25 and 2016 May 23) at $G = 20.66$. DR2 also provides a parallax of 1.27 ± 1.51 which does not contribute anything to our discussion of the distance.

For the purpose of this discussion we assume a distance of 10 kpc, which should probably be regarded as an upper limit. This distance has been adopted to make the conversion of the distance dependent parameters (e.g. radius and luminosity) straightforward once an accurate distance estimate is available (see Appendix B.1). Future Gaia data releases will probably improve the parallax and its associated uncertainty.

Data collection for DR2 stopped just before the nova eruption. The change of $\Delta G \sim 1.7$ between DR1 and DR2 suggests the nova may have faded before the eruption. At maximum, nova V407 Lup was at $V \lesssim 6.0$. Therefore, the amplitude of the eruption is ~ 15 mag. Note that the amplitude of the eruption is determined by both the energetics of the eruption itself and by the luminosity of the donor during quiescence. Such a large amplitude is expected for novae of the same speed class as V407 Lup, with a main-sequence companion (see e.g. fig. 5.4 in Warner 1995). Large amplitude eruptions have been observed in a few other novae, including V1500 Cyg, CP Pup, and GQ Mus (see e.g. Warner 1985; Diaz & Steiner 1989).

4.5.2 Colour-magnitude evolution

In Fig. 4.30 we present a colour-magnitude diagram (CMD) illustrating the evolution of M_V as a function of $(B-V)_0$. Such diagrams have been used to constrain the nature of the secondary star in CNe. Darnley et al. (2012) proposed a new classification system for CNe based exclusively on the evolutionary state of the secondary star: a main-sequence star (MS-Nova), a sub-giant star (SG-Nova), or a red giant star (RG-Nova). Hachisu & Kato (2016a) have shown that there is a difference between the evolutionary track on the CMD of MS- and SG-novae compared to that of RG-novae. For the latter, the track follows a vertical trend between $(B-V)_0$ = −0.03 and $(B-V)_0$ = 0.13. The first value represents the intrinsic colour of optically thin free-free emission (free-free emission from an “optically thin wind" – winds that are accelerated outside the photosphere), while the second value represents the intrinsic colour of optically thick free-free emission (free-free emission from an “optically thick wind" – winds that are accelerated deep inside the photosphere; see fig. 5 in Hachisu & Kato 2014a). Novae with main-sequence or sub-giant companions show a track that evolves blue-ward initially going from maximum light to reach a turning point around the start of the nebular phase. After the turning point, the track evolves red-ward in the opposite direction (see fig. 7 in Darnley et al. 2016).

Fig. 4.30 demonstrates that the evolution of the colours on the CMD follows a similar track to that shown by MS- and SG-novae. Initially, the colours evolve blue-ward between day 2 and day 13, when the broadband observations stopped for more than a hundred days (Sun constrained) and only resumed at day 117, when the colours had already started evolving red-ward. Hence, the turning-point and eventually the start of the nebular phase and the SSS phase have occurred between day 13 and day 117.

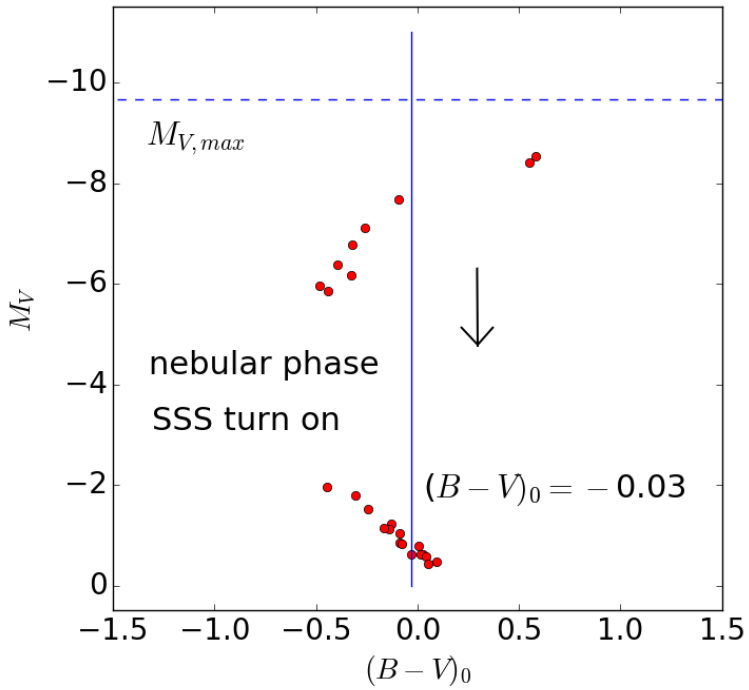

Figure 4.30: Colour-magnitude diagram of V407 Lup showing M_V against $(B-V)_0$ (red dots) at a distance d = 10 kpc and $E(B-V) = 0.22 (A_V = 0.67)$. The direction of the evolution of M_V against time is vertical from top to bottom (as indicated by the black arrow) and it spans from day $\sim$ 2 to day $\sim$ 13 post-eruption and then from day $\sim$ 117 to day $\sim$ 283. Between these two intervals, a turning-point took place in the evolutionary track of the colours, switching from a blue-ward track to a red-ward track. Around this turning point the nova must have entered the nebular phase and the SSS phase must have started, as indicated in the diagram. The blue horizontal, dashed line indicates the estimated maximum absolute magnitude. The blue vertical line indicates the intrinsic colours for an optically thick wind free-free emission (see e.g. Hachisu & Kato 2014a; Darnley et al. 2016 and references therein).

Although we lack broadband observations of the source during quiescence, the evolution of the colour-magnitude track suggests that the companion star is likely to be a main-sequence or a sub-giant star. This is consistent with: (1) the quiescent magnitude measured by Gaia ($G \sim 19$). At this magnitude and with a giant secondary, the distance to the nova would be unreasonable ($d \sim$ 30 – 40 kpc); (2) the short orbital period (3.57 h) of the binary system. Such a short orbital period rules out a giant or sub-giant secondary.

It is worth noting that the first two data points on the CMD, measured at $\sim$ 0.5 - 1.5 d after maximum, represent an intrinsic colour $(B-V)_0 \sim 0.6$. This is inconsistent with the intrinsic colours of novae around maximum and is an indication that the adopted value of $A_V = 0.67$ might be too low a value (see Section 4.5.1.1).

4.5.3 Mass of the WD and ejected envelope

The behaviour of the nova eruption is governed by several factors such as the WD mass, temperature, and chemical composition, as well as the chemical composition of the accreted matter (Yaron et al., 2005; Hillman et al., 2014; Shara et al., 2017a). However, the mass of the WD and consequently the

mass and velocity of the ejected envelope are considered the main factors that control the decline rate of the light-curve. The more massive the WD is, the less accreted material is required to trigger a TNR and hence, the mass of the ejected envelope is small and the light-curve decline time is short. The opposite is equally true. With $t_2 \leq 2.9$ days, the mass of the WD of V407 Lup is expected to be $\gtrsim 1.25\,\mathrm{M}_\odot$ (Hillman et al., 2016).

Shara et al. (2017a) derived an empirical relation between the mass of the accreted envelope and the decline time t_2, using nova samples from M87, M31, the large Magellanic Cloud, and the Galaxy: $\log M_{\rm env} = 0.825 \log(t_2) - 6.18$. Using this relation, we derive $M_{\rm env} \sim 1.6 \times 10^{-6}\,\mathrm{M}_\odot$, typical for very fast novae (Hachisu & Kato, 2016b).

Sala & Hernanz (2005) derived relations between the SSS temperature and the mass of the WD. For $kT \sim 80$ eV (see Fig. 4.27) and for $M_{\rm env} \sim 1.6 \times 10^{-6}\,\mathrm{M}_\odot$, we estimate a $M_{\rm WD} \sim 1.1$ – $1.2\,\mathrm{M}_\odot$ (see fig. 1 in Sala & Hernanz (2005)). We also estimate a value of $M_{\rm WD} \sim 1.2$ – $1.3\,\mathrm{M}_\odot$ based on fig. 1 in Wolf et al. (2014). Note that the temperature values given in Fig. 4.27 are model dependent, therefore caution is needed when interpreting the aforementioned estimates.

The SSS turn-on time is also a useful indication for the mass of the ejected envelope. However, it is not possible to constrain when the SSS emission emerged as the *Swift* monitoring was interrupted due to solar constraints and only resumed after the SSS has already turned on. On the other hand, the SSS turn-off time ($t_{\rm off}$), which is strongly correlated with the WD mass, is better constrained by the X-ray observations ($t_{\rm off} \sim 300$ d). This time is inversely proportional to the WD mass as $t_{\rm off} \propto \mathrm{M}_{\rm WD}^{-6.3}$ (MacDonald, 1996). After an X-ray survey in M31, Henze et al. (2014) derived empirical relations between the SSS parameters. Their relations suggest that very fast novae, such as V407 Lup (with $t_2 < 5$ d), are expected to have $t_{\rm on} \lesssim 25$ d and $t_{\rm off} \lesssim 100$ d. This is much shorter than the observed $t_{\rm off}$ for V407 Lup (see Section 4.5.4 for further discussion).

Based on the optical light-curve decline rate and the temperature of the SSS, we estimate a WD mass between 1.1 and $1.3\,\mathrm{M}_\odot$.

4.5.4 Resumption of accretion

Although the *XMM-Newton* X-ray spectrum (taken on day 168) is originating from H burning on the WD surface, the spin-modulated signal observed in the *XMM-Newton* X-ray data is possibly indirect evidence for accretion restoration onto the polar regions of the WD, as early as 168 days post-eruption. This accretion is either igniting H burning at the poles or resulting in an inhomogeneous atmosphere, leading to the observed modulation.

Typically, the spin-modulated signal seen in the X-ray light-curves of IPs is due to the obscuration caused by the accretion curtains and possibly by the changing projected area of the hard X-ray accretion-shock-regions near the pole of the WD. However, the spin-modulated *XMM-Newton* light-curve of V407 Lup is observed during the SSS, where the energy output is likely to be much higher than what could result from accretion (i.e. the release of gravitational potential energy by accretion on to the WD gives a much lower luminosity per unit mass accreted than nuclear burning does). Hence, there is a possibility that the spin-modulated X-ray emission seen in the *XMM-Newton* RGS

data is not simply due to the supersonic accretion shock (or absorption by an accretion curtain), however it is originating from the burning of the accreting material as it arrives at the WD in magnetically confined regions close to the magnetic poles, possibly making the atmosphere hotter near the poles. This might be responsible for the observed small modulation fraction of $\pm 5\%$ in the RGS data (Fig. 4.16), while simultaneously the post-nova residual H burning on the whole surface of the WD is likely responsible for the majority of the SSS flux. This idea was examined by King, Osborne & Schenker (2002) for a SSS in M31, as IP-like magnetically controlled accretion deposits fuel near to the magnetic poles of the WD, which burns immediately so giving rise to local hot/luminous regions on the WD surface, possibly contributing to the modulation seen in the optical and X-rays.

The $P_{\rm spin}$ modulation seen in the *Chandra* data at day 340 might also be due to localized H burning near the poles of freshly accreted material, while the residual H burning on the rest of the WD surface is fading. This is supported by the little variation in the hardness ratio and the modulation of the harder X-rays (Fig. 4.17), which suggest that the $P_{\rm spin}$ modulation might not be due to typical absorption by an accretion curtain. Lanz et al. (2005) first noticed that the WD model atmosphere that best fitted the spectrum of the non-nova CAL 83 supersoft source indicated a luminosity almost a factor of 10 higher than observed, and they hypothesized that perhaps the emission originated in hot polar caps. In a study of the decline and return to quiescence of novae that are suspected IPs in which the disk is disrupted and a moderately strong (few 10^6 Gauss) magnetic field channels the accretion stream to the WD poles, Zemko, Mukai & Orio (2015) and Zemko et al. (2016) found that such novae seem to decline in flux while remaining SSS, as if the emission region shrinks before any final cooling. These authors have attributed the supersoft-emission to H burning at heated regions near the poles where accreting material impinges. Nova V4743 Sgr in eruption also showed supersoft X-ray flux modulated with the WD $P_{\rm spin}$ (see Dobrotka & Ness 2017 and numerous references therein).

Signatures of accretion have often been found in both optical and X-rays observations of post-eruption novae (e.g. Leibowitz et al. 1992; Retter, Leibowitz & Kovo-Kariti 1998; Beardmore et al. 2012; Ness et al. 2012; Orio et al. 2013) and it has also been hypothesized that the disk may not be fully disrupted in the eruption. It is also possible that nuclear burning is prolonged by renewed accretion, and the supersoft X-ray source lasts for longer because it is refueled by irradiation induced mass transfer (Greiner, Orio & Schartel, 2003). Therefore, we assume that during the SSS phase of V407 Lup, the strongly irradiated secondary is heated by the X-ray emission, leading to an expansion of its outer layers. This will eventually enhance the mass transfer and increase the accretion rate (Osborne, 2015). The material can flow from the L1 Lagrangian point via a ballistic accretion stream to (possibly) a reformed truncated accretion disk. Then it follows the magnetic field lines and finally impacts the WD surface near the magnetic poles, possibly feeding the SSS (see Darnley et al. 2017; Henze et al. 2018 and references therein for a discussion about the surface hydrogen burning feeding from re-established mass accretion in the case of the non-magnetic system M31N 2008-12a). In the case of V407 Lup, this might also explain the long-lasting SSS emission for what is likely a massive WD (see Section 4.5.3).

An X-ray power spectrum with a dominant signal at the frequency of the WD $P_{\rm spin}$, such as the *Chandra* power spectrum (Fig. 4.15) taken on day 340, might be an indication of disk-fed accretion (Ferrario & Wickramasinghe, 1999). Norton et al. (1992b) point out that in this case the spin modulation dominates and the orbital modulation vanishes because "passage through a disk washes out all dependence on the orbital phase from the accretion process". Therefore, it is very likely that a truncated accretion disk has reformed by the time of the *Chandra* observation or even before. Nevertheless, a clear indication of disk-fed accretion would be very-low amplitude variations of the spectral line radial velocities modulated over the spin frequency (Norton, Beardmore & Taylor 1996; Ferrario & Wickramasinghe 1999; see Section 4.4.1.4 for a discussion of the spectral line velocities). It is worth noting that an accretion disk might reform over a few orbital cycles (private communication with B. Warner).

This is consistent with the flux derived from the X-ray grating data at day 340 (see Section 4.4.5). As mentioned previously in this section, there is a possibility that a portion of the WD burning surface is hidden. This might be due to a reformed accretion disk and an accretion curtain around day 340 or due to localized H burning near the poles, as described previously (or both).

The emergence of narrow and moving He II lines around 250 days post-eruption, is another indication that accretion has resumed, as these lines are possibly originating from an irradiated accretion stream/curtain (see, e.g., Warner 1995; Potter et al. 2004; Zemko et al. 2016) or from a reformed accretion disk (see, e.g., Mason et al. 2012; Mason & Walter 2014; Munari, Mason & Valisa 2014). In addition, at day $\sim$ 304, Balmer emission components with a FWHM$\sim$ 500 km s^{-1} emerge on top of the broad nebular lines, showing changes in radial velocity (see Section 4.4.1.3). These lines might also originate from a reformed accretion disk. Few classical or recurrent novae have shown such narrow moving He II and Balmer lines after the eruption when the ejecta become optically thin. Walter & Battisti (2011) suggested that this can be a sign of either the survival of the accretion disk or accretion restoration soon after the eruption.

We conclude that there is a possibility of accretion restoration around 168 days post-eruption causing localized H burning and/or temperature inhomogeneity on the WD surface and leading to the observed spin-modulated signal. The narrow lines observed in the optical spectra, their low velocity amplitude, and the optical/X-ray power spectra dominated by the $P_{\rm spin}$ frequency point towards resumption of accretion and the possibility of a reformed accretion disk. Although it is possible that the accretion has resumed earlier than 168 days after eruption in V407 Lup, it is not possible to constrain when exactly that happened due to the lack of observations between days $\sim$ 17 and $\sim$ 150 (solar constraints). It is also worth noting that features of accretion resumption might only be observable when the ejecta become optically thin.

We showed in Section 4.3.4 that the AAVSO optical and *XMM-Newton* X-ray light-curves are out of phase when folded over the $P_{\rm spin}$. However, caution is required when interpreting this comparison, particularly because: (1) the error (0.5 s) on the WD $P_{\rm spin}$ derived from the RGS data is too large for the ephemeris to be extrapolated to the date of the AAVSO observations ($>$ 150 days later) and for the phase to be known during these observations; (2) the *XMM-Newton* X-ray light-curve was taken during the SSS phase while the AAVSO data were taken when the surface H

burning had started fading considerably.

4.5.5 The IP scenario

Several novae have been suggested to occur in IP systems including V533 Her, GK Per, DD Cir, V1425 Aql, V4743 Sgr, and Nova Scorpii 1437 AD (see e.g. Warner & Woudt 2002; Bianchini et al. 2003; Woudt & Warner 2003, 2004; Zemko et al. 2016; Potter & Buckley 2018 and references therein). These systems either show spin-modulated optical and X-ray light-curves, strong He II emission lines, or spin-modulated circular polarization.

There is a striking similarity between the He II lines of V407 Lup and the complex He II lines seen in mCVs (Rosen, Mason & Cordova, 1987; Schwope, Mantel & Horne, 1997). Zemko et al. (2016) have found multiple components blue and red-shifted with the same velocity in the spectra of V4743 Sgr, which also have been found in GK Per, an old nova and IP, and were attributed to emission from the accretion curtains in the magnetosphere of the WD (Bianchini et al., 2003).

The strong He II 4686 Å line is usually seen in the spectra of IPs, although this line can also be prominent in other CV systems that host a very hot WD. We measure the EW of the narrow component in Hβ in the last three HRS spectra, when the contribution from the broad emission (from the ejecta) is minimal. The ratio of EW(He II 4686 Å) and EW(Hβ) is ~ 2. Such a value is in agreement with the ratio seen in magnetic CVs and IPs which is usually > 0.4 (Silber, 1992).

Belle et al. (2003) detected very narrow lines of O V and N V in the UV spectra of the IP EX Hydra. These high ionization, very narrow (FWHM $\sim 60\,\mathrm{km\,s^{-1}}$) lines are very similar to the very narrow lines that we detect in the optical spectra of V407 Lup. The authors of this study suggest that such high ionization lines should originate from a very high temperature region which increases the probability that the lines are not contaminated by emission from the accretion disk. Therefore, due to their small widths, they suggested that the lines are formed near the surface of the WD.

The main feature that supports the IP scenario in V407 Lup is the detection of the two periodicities in the X-ray, UV, and optical light-curves. These periodicities are very likely to represent the P_{orb} of the binary and the P_{spin} of a highly magnetized WD and therefore are compelling evidence that V407 Lup is an IP.

The detection of a hard X-ray component in the late ($\gtrsim$ day 300) *Swift* X-ray data also favours the IP scenario. In addition, the luminosity of the hard X-ray component in the *Swift* X-ray data taken around the end of January 2018 is in the range observed in IP systems (see Section 4.4.3). However, this has still to be confirmed when a better distance estimate is available.

All of these point towards the scenario of a nova occurring in an IP system and evidence for accretion restoration.

4.6 Summary and conclusions

We have presented multiwavelength observations of nova V407 Lup, which was discovered on HJD 2457655.5 (2016 September 24.0 UT; Stanek et al. 2016). The optical, UV, and X-ray data of this nova have led us to the following conclusions:

1. V407 Lup is a very fast nova. With $t_2 \leq 2.9$ d it is one of the fastest known examples. This is also an indication that the eruption took place on a high mass WD ($\gtrsim 1.25$ $M_\odot$).

2. Based on the evolution of the colours after the eruption and the amplitude of the eruption, the system is very likely to contain a main-sequence companion.

3. Timing analysis of the optical, UV, and X-ray light-curves shows two periodicities of 3.57 h and 565 s. These are interpreted as the $P_{\rm orb}$ of the binary and the $P_{\rm spin}$ of the WD, respectively, suggesting that the system is an IP.

4. The presence of modulation at the $P_{\rm spin}$ of the WD in the X-ray and optical data from 168 days post-eruption suggests that an accretion towards the magnetic poles has resumed leading to localized burning near the polar regions of the WD surface.

5. The high resolution optical spectra exhibit very narrow and moving lines as early as 164 days post-eruption. Such moving, high-excitation lines are most likely associated with very hot regions within the inner binary system.

6. At day 250, relatively strong, narrow, and moving lines of He II emerge in the optical spectra. Their profiles are complex, similar to those observed in mCVs. 285 days post eruption, moderately narrow and moving Balmer emission components also emerge. All of these lines are possibly originating from accretion regions (accretion stream, disk, and curtain) within the inner binary system.

7. Based on the peak temperature of the SSS emission ($\sim$80 eV) and the time taken for the optical brightness to fade by 2 magnitudes ($t_2 \leq 2.9$ d), we conclude that the mass of the WD is in the range of 1.1 – 1.3 $M_\odot$

8. We constrain the turn-off time of the SSS to be around 300 days post-eruption, later than expected for a massive WD. The optical and X-ray data show evidence of some form of accretion restoration while the SSS is still on. The accretion of fresh material onto the WD surface may have been responsible for extending the duration of the SSS.

As the system is evolving back to quiescence, further observations are required to constrain the following: (i) IPs might show optical circular polarization originating from cyclotron radiation (see, e.g., Buckley et al. 1995, 1997; Potter & Buckley 2018), therefore polarimetric observations are encouraged to further investigate the IP identity of V407 Lup; (ii) orbital-period-resolved and spin-period-resolved spectroscopy are both needed to derive any periodicity from the optical emission lines and possibly to reveal the morphology of the system via Doppler tomography; (iii) Gaia might provide an accurate distance estimate allowing us to better constrain the properties of the system, such as the absolute maximum magnitude, luminosities, and evolutionary state of the companion.

Chapter 5

Summary and future work

5.1 Summary

I have presented three detailed studies of two Galactic novae and one nova in the Small Magellanic Cloud. This work was done in collaboration with various people who provided some of the data and in some cases contributed to the analysis and discussion. These studies led to the following conclusions:

Nova V5852 Sgr is a moderately fast nova, showing an Fe II-type spectrum (i.e. optically thick ejecta). We measure a moderate FWHM of $\sim 2300\,\mathrm{km\,s^{-1}}$ from Hα and Hβ. The post-eruption light-curve is unique, showing a combination of several light-curve classes. Estimates of the distance and measurement of the line velocities suggest that the nova might be associated with the Sagittarius stream. If so, it would be the first nova to be discovered in a dwarf spheroidal galaxy.

Nova SMCN 2016-10a is a very fast nova, showing a He/N-type spectrum, indicative of optically thin ejecta. The optical data led us to conclude that the eruption took place on a massive white dwarf ($\gtrsim 1.25\,\mathrm{M_\odot}$). This is consistent with the high temperature of the super-soft X-ray emission and the turn-on/turn-off time of the SSS. A few days after the optical peak, Hα and Hβ show broad profiles (FWHM $\sim 3500\,\mathrm{km\,s^{-1}}$), indicating moderately high expansion velocities. At the distance of the Small Magellanic Cloud, the absolute maximum magnitude of the eruption will be ~ -10.5 in the V-band. This makes nova SMCN 2016-10a the most intrinsically luminous nova ever observed in the Small Magellanic Cloud and one of the most intrinsically luminous on record.

Nova V407 Lup is a very fast nova, showing a He/N-type spectrum, characteristic of optically thin ejecta. The FWHM of Hα and Hβ measured a few days after the visible maximum indicates moderately high expansion velocities. With a decline time $t_2 \leq 2.9\,\mathrm{d}$ it is one of the fastest known examples and the white dwarf is very likely to be more massive than $1.25\,\mathrm{M_\odot}$. Two periodicities were found from the optical, X-ray, and UV light-curves that are presumably associated with the

orbital period of the binary and rotational period of the WD. This means that V407 Lup is an intermediate-polar cataclysmic variable. The optical spectra show relatively narrow and moving lines, possibly associated with accretion regions within the binary system. The optical and X-ray data indicate that the accretion might have resumed around 168 days post-eruption (or even before), while the SSS is still on. Therefore, nova V407 Lup is one of the few novae that shows strong evidence of accretion restoration during the super-soft source phase.

5.2 General conclusions and future work

These studies demonstrate that multiwavelength follow-up of nova events is essential for better interpretation of the different emission processes, evolution of the eruption, accretion mechanisms, and properties of the system. Although most classical novae have similar behaviour, each nova is unique and can show different emission features depending on the properties of the system. Thus, our studies are important both for understanding the eruption of each of these novae and ultimately adding to the wealth of knowledge in the field. This is particularly important in the era of all-sky surveys where an ever increasing number of CNe and optical transients are discovered on a daily basis. Detailed multiwavelength studies have been playing, and will play, a crucial role in identifying the targets and understanding their physical behaviour. The following are general conclusions and potential future work:

1. The SALT high- and medium-resolution spectroscopy, which we obtained for the three novae through the SALT Large Program for Transients, has proved useful to identify these transient events, track the evolution of the eruption, derive the ejection velocity, explore the chemical composition of the white dwarf, and constrain the morphology of the ejecta. Therefore, we aim to make use of this programme to follow-up more optical transients in the future. This is particularly important with the current and new all-sky surveys such as the All Sky Automated Survey for SuperNovae (ASAS-SN)[1] and the Large Synoptic Survey Telescope (LSST[2]; Tyson 2002), which are expected to report a large number of transient events daily.

2. Modelling the lines of the three novae could help constrain the morphology of the ejecta. This should work particularly well for novae SMCN 2016-10a and V407 Lup due to the good sample of high-resolution spectroscopy obtained with SALT.

3. Future imaging follow-up observations of the three novae using SALT might provide more accurate distance estimates via expansion parallax. For the two Galactic novae, Gaia DR2 or DR3 might also provide better distance estimates and thus help constrain several physical properties such as the temperature of the white dwarf and the maximum absolute magnitude, along with the Galactic locations of the systems.

[1] http://www.astronomy.ohio-state.edu/asassn/index.shtml
[2] https://www.lsst.org/

4. If more luminous novae like SMCN 2016-10a are discovered in the future, a new classification of "hyper-luminous novae" might prove useful. These would be rare events that take place every few decades in the Galaxy.

5. As V407 Lup is an intermediate-polar, we expect to detect circular polarization from the system when it returns to quiescence. Therefore, performing polarimetric observations for V407 Lup using the facilities at the South African Astronomical Observatory is essential once the system is observable from Sutherland again.

6. X-ray and UV monitoring of two of our novae were crucial in constraining the temperature of the X-ray emission and the mass of the white dwarf. They also provided strong evidence for the intermediate-polar identification of V407 Lup and for the resumption of accretion. Therefore, collaborations which involve observations from several telescopes covering many wavelength bands, such as SALT, SMARTS, *Swift*, *Chandra*, and *XMM-Newton* are essential to carry out detailed studies of future classical novae. They also represent the essence of scientific research where collaborations and team-work are the route for producing high-quality science and new insights.

7. Monitoring nearby galaxies with the aim of finding ultra-fast and faint novae (Yaron et al., 2005; Kasliwal et al., 2011; Shara et al., 2017a). These (particularly faint, fast novae) are expected to host massive white dwarfs, close to the Chandrasekhar limit and therefore might be candidate supernova type Ia progenitors. If these were to be common, they might contribute to the solution of the supernova type Ia rate problem. Detecting these novae is not straightforward due to their low amplitude and fast brightness decline rate. This would require extensive photometric monitoring of nearby galaxies, such M31 or LMC, using surveys such as ASAS-SN and MASTER, followed by rapid spectroscopic follow up using telescopes such as SALT, SOAR and others in the northern hemisphere.

Appendix A

Appendix for Chapter 3 - Nova SMCN 2016-10a

A.1 Observation logs

In this Appendix we list all the observations log of nova SMCN 2016-10a and a complementary plot. The OGLE time series photometry are also available from the OGLE Internet Archive[1]. The SMARTS time series photometry is available in the SMARTS atlas, at [2]. In Table A.6 we list the line IDs along with the FWHM, Equivalent Widths (EWs), and fluxes for those emission lines for which an estimate was possible.

Table A.1: A sample of OGLE V-band photometry of nova SMCN 2016-10a.

HJD	$t - t_0$ (days)	V (mag)	ΔV
2455399.88	−2270.81	20.60	0.03
2455434.82	−2235.87	20.87	0.12
2455446.70	−2223.99	20.47	0.02
2455456.81	−2213.88	20.58	0.03
2455486.62	−2184.07	20.40	0.06
2455499.63	−2171.07	20.98	0.04
2455503.62	−2167.08	20.72	0.04
2455516.60	−2154.10	20.51	0.06
2455536.58	−2134.11	20.48	0.03

[1] http://ogle.astrouw.edu.pl/ogle4/cvom/smcn-2016-10a.html

[2] http://www.astro.sunysb.edu/fwalter/SMARTS/NovaAtlas/nsmc2016/nsmc2016.html

Table A.2: A sample of OGLE I-band photometry of nova SMCN 2016-10a.

HJD	$t - t_0$ (days)	I (mag)	ΔI
2455346.93	−2323.77	20.14	0.20
2455347.91	−2322.79	20.42	0.23
2455358.90	−2311.80	20.06	0.13
2455364.91	−2305.79	20.35	0.13
2455376.94	−2293.76	20.09	0.13
2455378.94	−2291.76	20.40	0.17
2455380.91	−2289.79	20.35	0.20
2455381.92	−2288.79	20.44	0.21
2455384.89	−2285.81	20.49	0.20

Table A.3: A sample of SMARTS *BVRIJHK* photometry of nova SMCN 2016-10a. The time series photometry is available on the SMARTS atlas.

HJD	$(t - t_0)$ (days)	Band	Magnitude	Instrument uncertainty
2457682.64	11.93	I	10.84	0.002
2457682.64	11.93	H	10.21	0.030
2457682.64	11.93	B	11.73	0.001
2457682.64	11.93	J	9.83	0.037
2457682.64	11.93	K	9.95	0.033
2457682.64	11.93	V	12.14	0.002
2457682.64	11.93	R	10.64	0.001
2457683.73	13.02	I	10.90	0.002
2457683.73	13.02	J	9.95	0.038
2457683.73	13.02	H	10.45	0.034
2457683.73	13.02	B	11.57	0.001
2457683.73	13.02	K	10.05	0.039
2457683.73	13.02	V	12.07	0.002
2457683.73	13.02	R	10.67	0.001
2457684.73	14.02	I	11.10	0.002
2457684.73	14.02	J	10.74	0.043
2457684.73	14.02	H	10.653	0.036
2457684.73	14.02	B	11.73	0.001
2457684.73	14.02	K	10.02	0.04

Table A.4: The SALT spectroscopy and spectropolarimetry observations log of nova SMCN 2016-10a.

Type	HJD	$t - t_0$ (days)	Exposure time (range 1) (s)	Exposure time (range 2) (s)
RSS	2457679.4	8	4×150	3×150 + 4×30
RSS	2457694.3	23	2×150 + 2×30	2×100 + 2×30
HRS	2457679.3	8	3×1200	2×1200
HRS	2457698.3	27	3×1200	2×1200
HRS	2457703.3	32	3×1200	2×1200
HRS	2457716.3	45	3×1200	2×1200
HRS	2457733.2	62	3×1200	2×1200
Spectropol	2457686.3	15	8×120	8×120 + 4×60
Spectropol	2457714.3	43	8×120	8×120 + 4×60

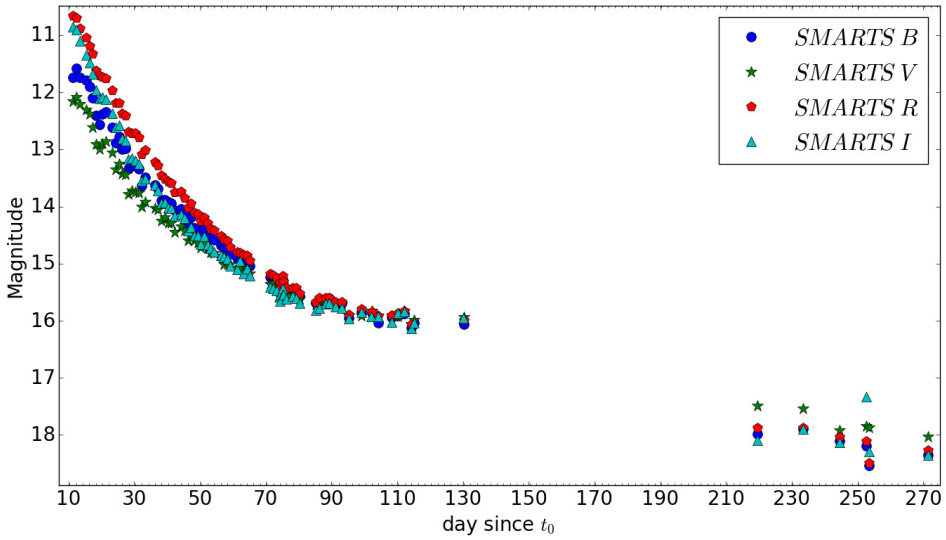

Figure A.1: The full photometric $BVRI$ data from SMARTS as a function of days since eruption, colour and symbol coded as indicated in the legend.

Table A.5: The FLOYDS spectroscopic observations log of nova SMCN 2016-10a.

HJD	$t - t_0$ (days)	Exposure time (s)
2457676.19	5.4	3×60
2457679.10	8.3	3×60
2457680.04	9.3	3×60
2457681.20	10.5	6×60
2457682.00	11.3	3×120
2457684.12	13.4	2×120
2457685.13	14.4	3×120
2457691.11	20.4	3×300
2457693.15	22.4	3×300
2457695.07	24.3	3×450
2457703.20	32.5	3×450

Table A.6: Line IDs, EWs, FWHMs, and fluxes of some emission lines in the nova SMCN 2016-10a spectra.

Line	λ_0	EW (λ) (Å)	FWHM (km s^{-1})	Flux erg cm^{-2}s^{-1}	$(t - t_0)$
[Ne V]	3426	-	-	-	32
Hη	3835	-	-	-	8
Hζ	3889	-11 ± 2	2250 ± 100	-	8
Hϵ	3970	-15 ± 10	2300 ± 100	1.54×10^{-12}	8
Hδ	4102	-85 ± 10	3300 ± 100	2.24×10^{-12}	8
Hγ	4341	-100 ± 10	3450 ± 100	2.48×10^{-12}	8
He I	4388	-	-	-	62
N III	4638	-	-	-	8
He II	4686	-	-	-	8
Hβ	4861	-300 ± 20	3500 ± 100	4.73×10^{-12}	8
[O III]	4959	-	-	-	20
N II	5001	-	-	-	5
[O III]	5007	-290 ± 20	3000 ± 100	1.59×10^{-13}	20
He I	5016	-	-	-	5
Fe II	5018	-	-	-	5
Fe II	5169	-	-	-	5
N II	5679	-	-	-	8
[N II]	5755	-	-	-	8
He I	5876	-	-	-	8
Na I D	5889	-	-	-	8
N II	5938	-	-	-	8
Hα	6563	-1500 ± 100	3500 ± 100	1.82×10^{-11}	8
N I	7452	-	-	-	8
O IV	7713	-	-	-	62
[C IV]	7726	-	-	-	62
O I	7773	-135 ± 10	2400 ± 100	1.83×10^{-12}	8
Mg II	7896	-	-	-	8
N I	8212	-	-	-	8
Mg II	8232	-	-	-	8
O I	8446	-750 ± 50	3000 ± 100	4.00×10^{-12}	8
N I	8617	-	-	-	8
N I	8692	-	-	-	8

Table A.7: A sample of $Swift$ UVOT $uvw2$ photometry of nova SMCN 2016-10a.

HJD	$t - t_0$ (days)	exposure time (s)	$uvw2$ (mag)	$\Delta uvw2$ (mag)
2457682.85	12.15	4.8	9.85	0.14
2457682.86	12.16	4.8	9.68	0.21
2457682.92	12.22	4.8	9.64	0.14
2457682.93	12.23	16.4	9.76	0.18
2457685.18	14.48	4.8	10.65	0.43
2457685.18	14.48	15	10.12	0.15
2457685.24	14.54	15	10.15	0.15
2457685.25	14.55	10.7	9.93	0.215
2457685.57	14.87	4.8	10.07	0.15
2457685.58	14.88	17	10.06	0.19

Table A.8: A sample of $Swift$ UVOT $uvm2$ photometry of nova SMCN 2016-10a.

HJD	$t - t_0$ (days)	exposure time (s)	$uvm2$ (mag)	$\Delta uvm2$ (mag)
2457682.85	12.15	4.8	9.61	0.27
2457682.85	12.15	50	9.91	0.15
2457682.92	12.22	4.8	9.76	0.30
2457685.18	14.48	4.8	10.12	0.15
2457685.25	14.55	4.8	10.26	0.16
2457685.57	14.87	4.8	10.32	0.03
2457703.33	32.63	4.8	12.03	0.05
2457703.33	32.63	46	12.07	0.03

Table A.9: Summed $Swift$ UV grism exposures of nova SMCN 2016-10a.

HJD (start)	HJD (end)	$< t - t_0 >$ (days)	quality notes[1]
2457676.8036	2457678.7299	7.07	2ndO:2870-2950,3308-3390,3890-3980,4400-4500,5080-5150
2457682.8616	2457685.2581	13.36	Good 1700-4500,but rise above 4500-5060
2457685.5775	2457688.7052	16.44	Good 1700-5060,5060-6000 noisy and strange drop in flux
2457699.5597	2457705.4783	31.82	ZOc:1831-1885;2ndO:2824-2945,3235-3375,3843-3947,4375-4530,5050-5170
2457710.9143	2457714.0447	41.78	Good 1700-4800, 4800-5100 shows rising continuum to red
2457715.6864	2457719.7391	47.01	Good 1700-5200, then noisy
2457723.6584	2457734.8146	58.54	Good 1700-5100 then noisy
2457762.1341	2457776.4872	98.61	Continuum level good to 3840
2457788.4264	2457828.3827	137.70	No contamination, bad S/N, very noisy for >4100

[1] 2ndO: second order affects these ranges; ZOc: zeroth order contamination affects these ranges.

Appendix B

Appendix for Chapter 4 - Nova V407 Lup

B.1 Distance dependent parameters

The luminosity and effective radius at a certain distance d (in kpc) can be converted using:

$$L(d) = L(10_{\rm kpc}) \times 0.01\, d^2,$$

$$R(d) = R(10_{\rm kpc}) \times 0.1\, d,$$

where $L(10_{kpc})$ and $R(10_{kpc})$ are the luminosity and effective radius derived assuming a distance d = 10 kpc.

Table B.1 presents the luminosities and effective radii derived from the modelling of the *XMM-Newton* RGS spectrum for different distance assumptions. Table B.2 presents the luminosities derived from the modelling of the *Chandra* LETG spectrum for different distance assumptions.

B.2 Complementary plots

In this Appendix we present complementary plots.

B.3 Observation logs

In this Appendix we list the log of the observations of nova V407 Lup.

Table B.1: The luminosities and effective radii derived from the fitting of the blackbody model (BB), 1 component atmosphere model (1-T), and 2 components atmosphere model (2-T) to the *XMM-Newton* RGS spectrum for different distance assumptions.

d (kpc)	3	5	7
L(BB) (erg s^{-1})	2.4×10^{38}	6.7×10^{38}	1.3×10^{39}
$R_{\rm eff}$(BB) (km)	1.5×10^{4}	2.6×10^{4}	3.6×10^{4}
L(1-T) (erg s^{-1})	2.9×10^{37}	8.0×10^{37}	1.5×10^{38}
$R_{\rm eff}$(1-T) (km)	2.1×10^{3}	3.5×10^{3}	4.9×10^{3}
L(2-T) (erg s^{-1})	9.9×10^{36}	2.7×10^{37}	5.4×10^{37}
R_1(2-T) (km)	1.8×10^{3}	2.9×10^{3}	4.1×10^{3}
R_2(2-T) (km)	3.6×10^{3}	6.0×10^{3}	8.4×10^{3}

Table B.2: The luminosities derived from the fitting of models (1) and (2) to the *Chandra* LETG spectrum for different distance assumptions.

d (kpc)	3	5	7
$L(1)$ (erg s^{-1})	5.1×10^{35}	1.4×10^{36}	2.8×10^{36}
$L(2)$ (erg s^{-1})	7.0×10^{36}	1.9×10^{37}	3.8×10^{37}

Table B.3: A sample of the SMARTS *BVRIJHK* photometry of nova V407 Lup. The time series photometry is available on the SMARTS atlas.

HJD	$(t - t_0)$ (days)	Band	Magnitude (mag)	Instrument
2457657.48	1.98	J	5.245	0.003
2457657.48	1.98	H	4.695	0.002
2457657.48	1.98	K	4.850	0.003
2457657.48	1.98	I	6.909	0.000
2457657.48	1.98	B	7.944	0.000
2457657.48	1.98	V	7.145	0.000
2457657.48	1.98	R	6.953	0.000
2457658.48	2.98	J	5.288	0.003
2457658.48	2.98	H	4.789	0.002
2457658.48	2.98	K	4.629	0.003
2457658.48	2.98	I	6.750	0.000
2457658.48	2.98	B	8.027	0.000
2457658.48	2.98	V	7.260	0.000
2457658.48	2.98	R	6.160	0.001
2457660.50	3.00	J	6.032	0.005
2457660.50	3.00	H	5.409	0.003
2457660.50	3.00	K	5.492	0.004
2457660.50	3.00	I	6.793	0.000
2457660.50	3.00	B	8.107	0.000
2457660.50	3.00	V	7.985	0.001
2457660.50	3.00	R	6.752	0.001

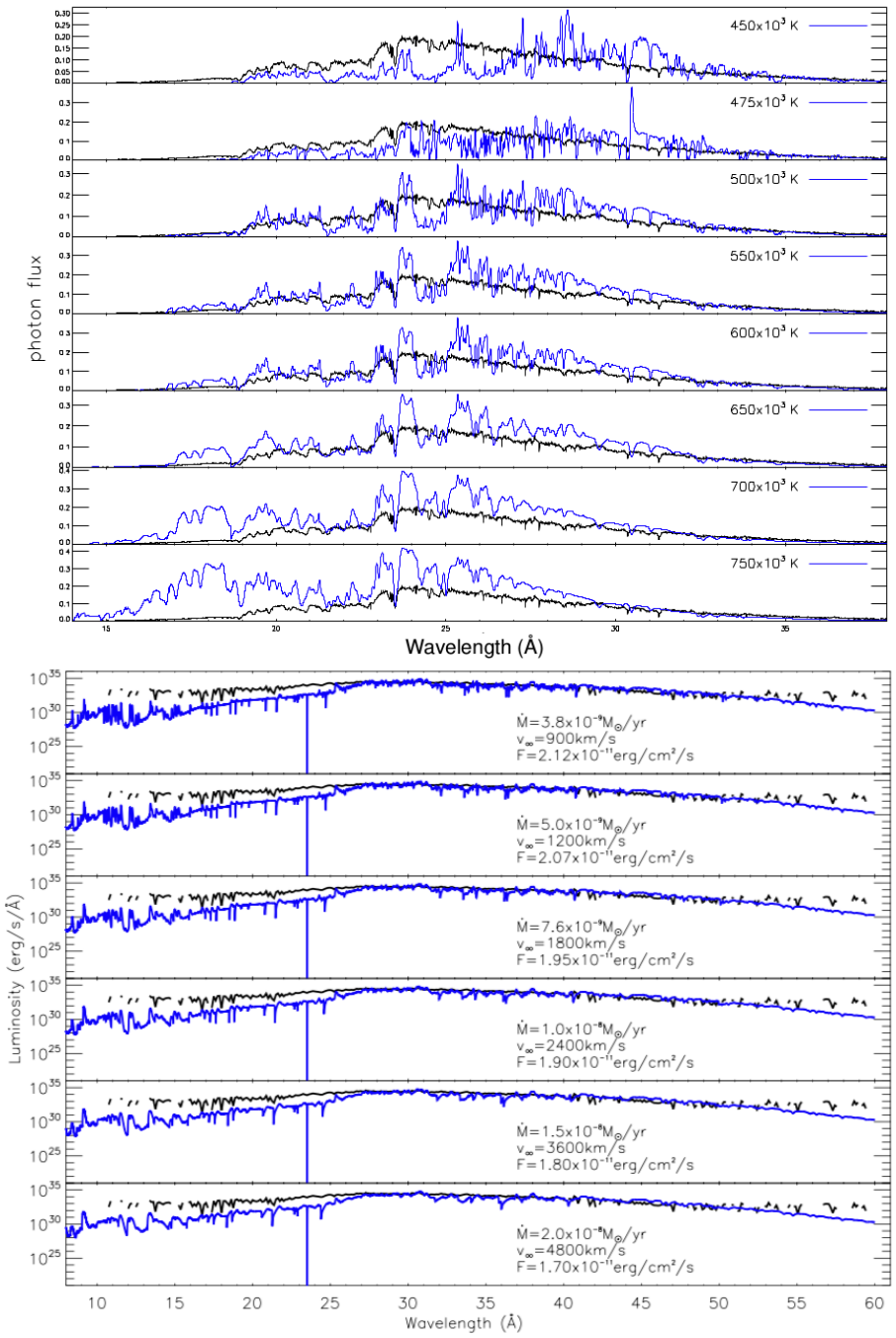

Figure B.1: *Top:* A sample of the wind-type atmosphere models (van Rossum, 2012) fitting to the *XMM-Newton* RGS spectrum. The models in blue compared to the observations in black. The $T_{\rm eff}$ characterizing each model is indicated on the plot. *Bottom:* best fit wind-type atmosphere model to the *Chandra* LETG spectrum for various wind asymptotic velocities v_∞ and mass-loss rates $\dot{M}$ as indicated on the plot. The models in blue compared to the observations in black.

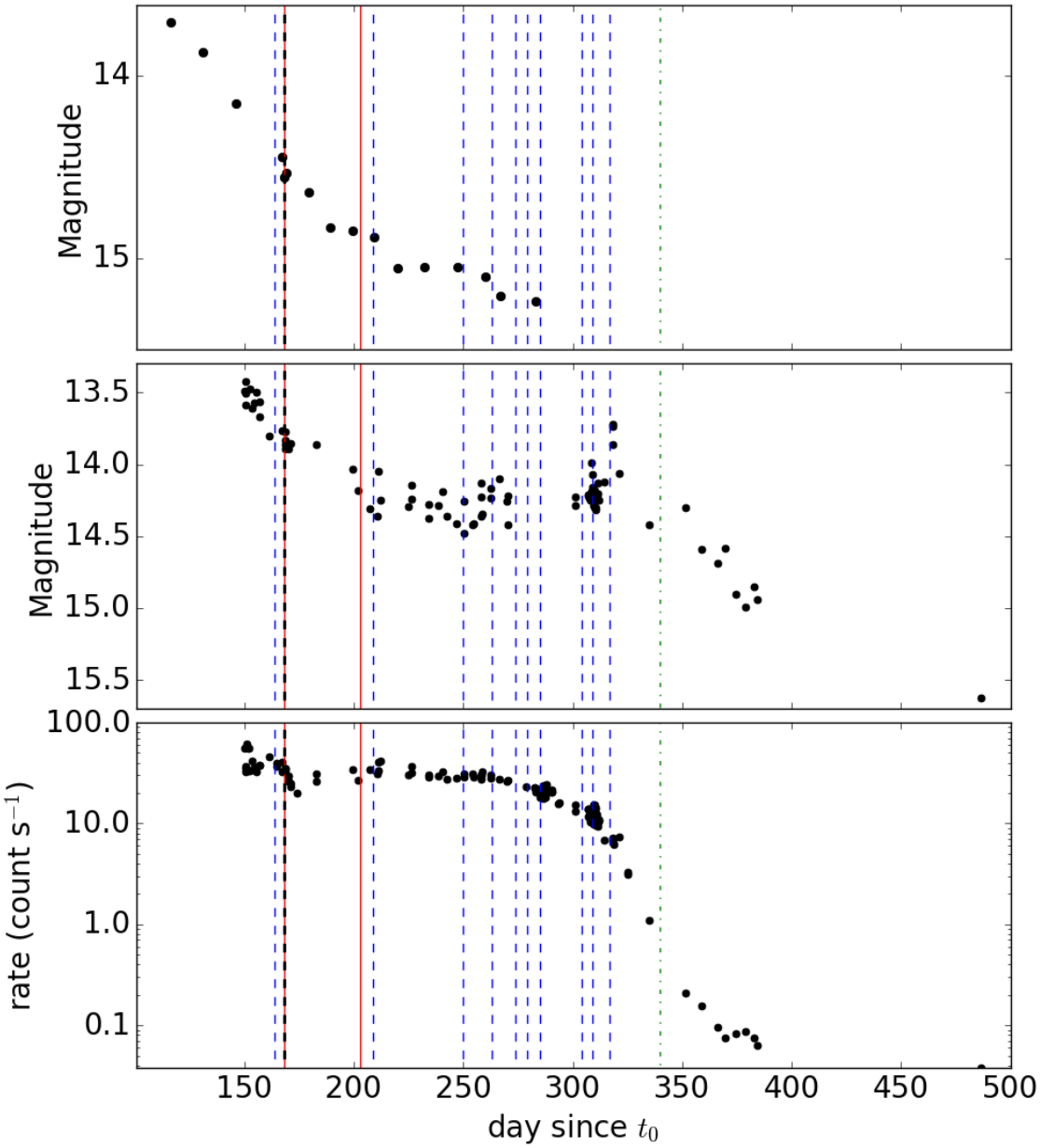

Figure B.2: A direct comparison between the SMARTS V-band (top), *Swift* UVOT *uvw1* (middle), and *Swift* X-ray light-curves (bottom), from day 100. The blue dashed lines represent the dates of the SALT HRS observations respectively. The black dashed line represents the date of the *XMM-Newton* observations. The red solid lines represent the median dates of the first four and second four UV grism spectra. The green dotted line represents the date of the *Chandra* observation.

Table B.4: The SALT HRS spectroscopy observation log of nova V407 Lup.

HJD	$t - t_0$ (days)	Exp. time (blue) (s)	Exp. time (red)	Mode
2457819.49	164	1800	1800	LR
2457864.38	209	1800	1800	LR
2457905.52	250	1800	1800	LR
2457918.47	263	1800	1800	LR
2457929.42	274	—	1800	LR
2457934.43	279	1800	1800	LR
2457940.41	285	1800	1800	LR
2457959.36	304	1800	1800	LR
2457964.35	309	1800	1800	LR
2457972.32	317	1800	1800	LR

Table B.5: A sample of the *Swift* observation log of nova V407 Lup, providing the observation-averaged XRT and UVOT *uvw2* photometric measurements.

ObsID	t-t0 (days)	half-bin width	XRT rate	error	$uvw2$	$\Delta(uvw2)$ (mag)
00034741001	2.916	0.024	< 0.003 *	-	-	-
00034741002	8.210	0.005	< 0.014 *	-	-	-
00034741003	9.141	0.005	< 0.011 *	-	-	-
00034741004	10.300	0.097	< 0.018 *	-	-	-
00034741005	11.492	0.035	< 0.010 *	-	-	-
00034741006	12.162	0.035	< 0.014 *	-	-	-
00034741007	13.595	0.005	< 0.015 *	-	-	-
00034741008	14.392	0.006	< 0.012 *	-	-	-
00034741009	15.157	0.035	< 0.013 *	-	-	-
00034741010	16.383	0.006	6.6 * p	$(+2.6/-1.9) \times 10^{-3}$	-	-
00034741012	19.096	0.066	< 0.039 *	-	-	-
00034741013	150.423	0.371	42.03	0.14	13.48	0.02
00034741014	151.657	0.328	49.74	0.17	-	-
00034741016	152.575	0.002	33.51	0.27	13.47	0.02
00034741017	153.784	0.005	41.82	0.21	13.61	0.02
00034741018	154.381	0.005	35.69	0.20	13.57	0.02
00034741019	155.512	0.002	32.81	0.28	13.49	0.02
00034741020	156.768	0.005	37.62	0.20	13.67	0.02
00034741021	157.025	0.001	37.86	0.51	13.56	0.02
00034741028	161.355	0.001	46.30	0.40	13.80	0.02
00034741030	164.670	0.001	36.88	0.37	-	-
00034741031	164.678	0.005	39.43	0.20	-	-
00034975002	167.261	0.001	40.72	0.46	-	-
00034975001	167.270	0.007	32.51	0.17	13.76	0.03
00034741034	168.628	0.105	37.67	0.10	13.84	0.02
00034975003	170.054	0.001	29.65	0.35	13.89	0.02
00034975004	170.056	0.000	26.09	0.48	-	-
00034975005	171.048	0.001	24.73	0.31	-	-

* Grade 0 events only were considered before the start of the solar observing constraint, because of concern about optical loading (see text for details).

p Possible detection.

Table B.6: UV grism observations of nova V407 Lup with lenticular filters.

date/time (UT)	MJD	$(t - t_0)$ (days)	exposure time (s)	filter	notes
2017-03-07T16:08	57819.67	164.67	892.5	UGRISM	(a)
2017-03-10T06:15	57822.26	167.26	201.1	UVM2	
2017-03-10T06:19	57822.26	167.26	1107.0	UGRISM	(a)
2017-03-10T06:38	57822.27	167.27	103.6	UVW2	
2017-03-13T01:16	57825.05	170.05	240.5	UVW2	
2017-03-13T01:21	57825.05	170.05	103.5	UGRISM	(a)
2017-03-14T01:08	57826.04	171.04	285.5	UVM2	
2017-03-14T01:13	57826.05	171.05	1170.0	UGRISM	(a)
2017-03-14T01:33	57826.06	171.06	98.8	UVW2	
2017-03-26T01:57	57838.08	183.08	202.2	UVM2	
2017-03-26T02:01	57838.08	183.08	839.3	UGRISM	(b)
2017-03-26T02:15	57838.09	183.09	76.6	UVW2	
2017-04-11T09:59	57854.41	199.41	181.4	UVM2	
2017-04-11T10:03	57854.41	199.41	901.3	UGRISM	(b)
2017-04-11T10:18	57854.42	199.42	73.2	UVW2	
2017-04-14T00:15	57857.01	202.01	96.1	UVW2	
2017-04-14T00:17	57857.01	202.01	999.7	UGRISM	(b)
2017-04-14T00:34	57857.02	202.02	92.0	UVW2	
2017-04-23T04:04	57866.16	211.16	222.8	UVM2	
2017-04-23T04:08	57866.17	211.17	889.5	UGRISM	(b)
2017-04-23T04:23	57866.18	211.18	85.4	UVW2	

(a) no offset on detector, roll=$112\mathrm{deg}$; First order contamination < 2050 Zeroth orders contaminate [1750-1865],[1950-2185],[2410-2540]

(b) offset around $5.6\mathrm{arcmin}$ on the detector, roll = $130deg$

Table B.7: The *XMM-Newton* observation log of nova V407 Lup.

Exp.	Instrument	Observing Mode	Filter	Start of exp.	Stop of exp.
001	MOS1	Full Frame	Medium filter	2017-03-11T11:02:17	2017-03-11T17:06:57
002	MOS2	Timing Uncompressed	Medium filter	2017-03-11T11:02:57	2017-03-11T17:02:43
003	pn	Timing	Medium filter	2017-03-11T11:37:25	2017-03-11T17:07:17
004	RGS1	Spectro + Q	N. A.	2017-03-11T11:01:47	2017-03-11T17:08:12
005	RGS2	Spectro + Q	N. A.	2017-03-11T11:01:52	2017-03-11T17:08:12
011	OM	OM Science User Defined	V grism 2	2017-03-11T11:07:29	2017-03-11T12:12:35
012	OM	OM Sci User Def FAST	UVW1	2017-03-11T12:12:36	2017-03-11T13:31:02
013	OM	OM Sci User Def FAST	UVW1	2017-03-11T13:31:03	2017-03-11T14:16:09
014	OM	OM Sci User Def FAST	UVW1	2017-03-11T14:16:10	2017-03-11T15:34:28
015	OM	OM Sci User Def FAST	UVW1	2017-03-11T15:34:29	2017-03-11T16:52:55

Bibliography

Abdo A. A. et al., 2010, Science, 329, 817

Ackermann M. et al., 2014, Science, 345, 554

Adelberger E. G. et al., 2011, Reviews of Modern Physics, 83, 195

Alard C., Lupton R. H., 1998, ApJ, 503, 325

Arnaud K. A., 1996, in Astronomical Society of the Pacific Conference Series, Vol. 101, Astronomical Data Analysis Software and Systems V, Jacoby G. H., Barnes J., eds., p. 17

Aschenbach B., 2002, in Proc. SPIE, Vol. 4496, X-Ray Optics for Astronomy: Telescopes, Multilayers, Spectrometers, and Missions, Gorenstein P., Hoover R. B., eds., p. 8

Ashok N. M., Banerjee D. P. K., 2003, A&A, 409, 1007

Atwood W. B. et al., 2009, ApJ, 697, 1071

Aydi E. et al., 2018, MNRAS, 474, 2679

Baars J. W. M., Hooghoudt B. G., 1974, A&A, 31, 323

Bahcall J. N., May R. M., 1969, ApJ, 155, 501

Ballester P., 1992, in European Southern Observatory Conference and Workshop Proceedings, Vol. 41, European Southern Observatory Conference and Workshop Proceedings, Grosbøl P. J., de Ruijsscher R. C. E., eds., p. 177

Balman Ş., Krautter J., Ögelman H., 1998, ApJ, 499, 395

Barnes S. I. et al., 2008, in Proc. SPIE, Vol. 7014, Ground-based and Airborne Instrumentation for Astronomy II, p. 70140K

Bath G. T., Harkness R. P., 1989, in Classical Novae, Bode M. F., Evans A., eds., Cambridge Astrophysics, Chichester: J. Wiley, p. 39

Bath G. T., Pringle J. E., 1985, Cataclysmic variables: theoretical overview, Pringle J. E., Wade R. A., eds., p. 177

Bath G. T., Shaviv G., 1976, MNRAS, 175, 305

Beardmore A. P. et al., 2010, The Astronomer's Telegram, 2423

Beardmore A. P. et al., 2012, A&A, 545, A116

Beardmore A. P., Page K. L., Osborne J. P., Orio M., 2017, The Astronomer's Telegram, 10632

Belle K. E., Howell S. B., Sion E. M., Long K. S., Szkody P., 2003, ApJ, 587, 373

Bianchi L., Herald J., Efremova B., Girardi L., Zabot A., Marigo P., Conti A., Shiao B., 2011, Ap&SS, 335, 161

Bianchini A., Canterna R., Desidera S., Garcia C., 2003, PASP, 115, 474

Bode M. F. et al., 2016, ApJ, 818, 145

Bode M. F., Evans A., 2008, Classical Novae, Bode M. F., Evans A., eds., Cambridge Astrophysics, Series, Vol. 43 Cambridge Univ. Press, Cambridge

Bode M. F., Harman D. J., O'Brien T. J., Bond H. E., Starrfield S., Darnley M. J., Evans A., Eyres S. P. S., 2007, ApJ, 665, L63

Bode M. F., Kahn F. D., 1985, MNRAS, 217, 205

Bode M. F., Seaquist E. R., Evans A., 1987, MNRAS, 228, 217

Booth R. A., Mohamed S., Podsiadlowski P., 2016, MNRAS, 457, 822

Bowen G. H., 1988, ApJ, 329, 299

Bramall D. G. et al., 2012, in Proc. SPIE, Vol. 8446, Ground-based and Airborne Instrumentation for Astronomy IV, p. 84460A

Bramall D. G. et al., 2010, in Proc. SPIE, Vol. 7735, Ground-based and Airborne Instrumentation for Astronomy III, p. 77354F

Brandi E., Quiroga C., Mikołajewska J., Ferrer O. E., García L. G., 2009, A&A, 497, 815

Brinkman A. C. et al., 2000a, ApJ, 530, L111

Brinkman B. C. et al., 2000b, in Proc. SPIE, Vol. 4012, X-Ray Optics, Instruments, and Missions III, Truemper J. E., Aschenbach B., eds., p. 81

Brown T. M. et al., 2013, PASP, 125, 1031

Buckley D. A. H., 1997, in Astronomical Society of the Pacific Conference Series, Vol. 121, IAU Colloq. 163: Accretion Phenomena and Related Outflows, Wickramasinghe D. T., Bicknell G. V., Ferrario L., eds., p. 420

Buckley D. A. H., Cropper M., van der Heyden K., Potter S. B., Wickramasinghe D. T., 2000, MNRAS, 318, 187

Buckley D. A. H., Haberl F., Motch C., Pollard K., Schwarzenberg-Czerny A., Sekiguchi K., 1997, MNRAS, 287, 117

Buckley D. A. H., Sekiguchi K., O'Donoghue D., Chen A.-L., March C., Haberl F., 1995, in Astronomical Society of the Pacific Conference Series, Vol. 85, Magnetic Cataclysmic Variables, Buckley D. A. H., Warner B., eds., p. 248

Buckley D. A. H., Swart G. P., Meiring J. G., 2006, in Proc. SPIE, Vol. 6267, Society of Photo-Optical Instrumentation Engineers (SPIE) Conference Series, p. 62670Z

Burgh E. B., Nordsieck K. H., Kobulnicky H. A., Williams T. B., O'Donoghue D., Smith M. P., Percival J. W., 2003, in Society of Photo-Optical Instrumentation Engineers (SPIE) Conference Series, Vol. 4841, Instrument Design and Performance for Optical/Infrared Ground-based Telescopes, Iye M., Moorwood A. F. M., eds., p. 1463

Burlak M. A., Esipov V. F., Komissarova G. V., Shenavrin V. I., Taranova O. G., Tatarnikov A. M., Tatarnikova A. A., 2015, Baltic Astronomy, 24, 109

Burrows D. N. et al., 2005, Space Sci. Rev., 120, 165

Buscombe W., de Vaucouleurs G., 1955, The Observatory, 75, 170

Butters O. W., Katajainen S., Norton A. J., Lehto H. J., Piirola V., 2009, A&A, 496, 891

Caldwell J. A. R., Coulson I. M., 1986, MNRAS, 218, 223

Cao Y. et al., 2012, ApJ, 752, 133

Cardelli J. A., Clayton G. C., Mathis J. S., 1989, ApJ, 345, 245

Cash W., 1979, ApJ, 228, 939

Cassatella A., Altamore A., González-Riestra R., 2002, A&A, 384, 1023

Chandrasekhar S., 1931, ApJ, 74, 81

Chen P. et al., 2016, The Astronomer's Telegram, 9550

Cheung C. C., Jean P., Fermi Large Area Telescope Collaboration, Shore S. N., 2015, The Astronomer's Telegram, 7283

Cheung C. C. et al., 2016, ApJ, 826, 142

Chomiuk L. et al., 2012, ApJ, 761, 173

Chomiuk L. et al., 2014, Nature, 514, 339

Ciardullo R., Tamblyn P., Jacoby G. H., Ford H. C., Williams R. E., 1990, AJ, 99, 1079

Clayton D. D., 1983, Principles of stellar evolution and nucleosynthesis, Chicago: University of Chicago Press ., ed.

Clemens J. C., Crain J. A., Anderson R., 2004, in Proc. SPIE, Vol. 5492, Ground-based Instrumentation for Astronomy, Moorwood A. F. M., Iye M., eds., p. 331

Coe M. J. et al., 2011, MNRAS, 414, 3281

Cohen J. G., 1985, ApJ, 292, 90

Crause L. A. et al., 2014, in Proc. SPIE, Vol. 9147, Ground-based and Airborne Instrumentation for Astronomy V, p. 91476T

Crawford S. M. et al., 2010, in Society of Photo-Optical Instrumentation Engineers (SPIE) Conference Series, Vol. 7737, Society of Photo-Optical Instrumentation Engineers (SPIE) Conference Series, p. 25

Darnley M. J. et al., 2006, MNRAS, 369, 257

Darnley M. J. et al., 2016, ApJ, 833, 149

Darnley M. J. et al., 2017, ApJ, 849, 96

Darnley M. J., Ribeiro V. A. R. M., Bode M. F., Hounsell R. A., Williams R. P., 2012, ApJ, 746, 61

Darnley M. J., Williams S. C., 2016, The Astronomer's Telegram, 9688

Darnley M. J., Williams S. C., Bode M. F., Henze M., Ness J.-U., Shafter A. W., Hornoch K., Votruba V., 2014, A&A, 563, L9

De Gennaro Aquino I. et al., 2015, A&A, 581, A134

Della Valle M., Livio M., 1995, ApJ, 452, 704

Della Valle M., Livio M., 1998, ApJ, 506, 818

Della Valle M., Pasquini L., Daou D., Williams R. E., 2002, A&A, 390, 155

Della Valle M. D., 2002, in American Institute of Physics Conference Series, Vol. 637, Classical Nova Explosions, Hernanz M., José J., eds., p. 443

den Herder J. W. et al., 2001, A&A, 365, L7

Diaz M. P., Steiner J. E., 1989, ApJ, 339, L41

Dilday B. et al., 2012, Science, 337, 942

Dobrotka A., Ness J.-U., 2010, MNRAS, 405, 2668

Dobrotka A., Ness J.-U., 2017, MNRAS, 467, 4865

Downes R. A., Duerbeck H. W., 2000, AJ, 120, 2007

Drury L. O., Aharonian F. A., Voelk H. J., 1994, A&A, 287, 959

Duerbeck H. W., 1990, in Lecture Notes in Physics, Berlin Springer Verlag, Vol. 369, IAU Colloq. 122: Physics of Classical Novae, Cassatella A., Viotti R., eds., p. 34

Evans A., Gehrz R. D., 2012, Bulletin of the Astronomical Society of India, 40, 213

Evans E., Rawlings J. M. C., 2008, in Classical Novae, Bode M. F., Evans A., eds., Cambridge Astrophysics, Series, Vol. 43 Cambridge Univ. Press, Cambridge, p. 308

Faulkner J., 1971, ApJ, 170, L99

Ferrarese L., Côté P., Jordán A., 2003, ApJ, 599, 1302

Ferrario L., Wickramasinghe D. T., 1999, MNRAS, 309, 517

Ferrario L., Wickramasinghe D. T., King A. R., 1993, MNRAS, 260, 149

Finzell T. et al., 2018, ApJ, 852, 108

Frank J., King A. R., Raine D. J., 1985, Accretion power in astrophysics

Gallagher J. S., Ney E. P., 1976, ApJ, 204, L35

Gallagher J. S., Starrfield S., 1978, ARA&A, 16, 171

Gehrels N. et al., 2004, ApJ, 611, 1005

Gehrz R. D., 2008, in Classical Novae, Bode M. F., Evans A., eds., Cambridge Astrophysics, Series, Vol. 43 Cambridge Univ. Press, Cambridge, p. 167

Gehrz R. D., Greenhouse M. A., Hayward T. L., Houck J. R., Mason C. G., Woodward C. E., 1995, ApJ, 448, L119

Gehrz R. D., Hackwell J. A., Grasdalen G. I., Ney E. P., Neugebauer G., Sellgren K., 1980, ApJ, 239, 570

Gehrz R. D., Truran J. W., Williams R. E., Starrfield S., 1998, PASP, 110, 3

Gonzales-Riestra R., 1995, in Astrophysics and Space Science Library, Vol. 205, Cataclysmic Variables, Bianchini A., della Valle M., Orio M., eds., p. 21

Gonzalez O. A., Rejkuba M., Zoccali M., Valenti E., Minniti D., Schultheis M., Tobar R., Chen B., 2012, A&A, 543, A13

González-Riestra R., Krautter J., 1998, in ESA Special Publication, Vol. 413, Ultraviolet Astrophysics Beyond the IUE Final Archive, Wamsteker W., Gonzalez Riestra R., Harris B., eds., p. 367

Gorbovskoy E. et al., 2010, Advances in Astronomy, 2010, 917584

Graham J. A., 1979, in IAU Colloq. 46: Changing Trends in Variable Star Research, Bateson F. M., Smak J., Urch I. H., eds., Vol. 46, p. 96

Greiner J., Orio M., Schartel N., 2003, A&A, 405, 703

Hachisu I., Kato M., 2006, ApJS, 167, 59

Hachisu I., Kato M., 2014a, ApJ, 785, 97

Hachisu I., Kato M., 2014b, ApJ, 785, 97

Hachisu I., Kato M., 2016a, ApJ, 816, 26

Hachisu I., Kato M., 2016b, ApJS, 223, 21

Hachisu I., Kato M., Luna G. J. M., 2007, ApJ, 659, L153

Hachisu I., Kato M., Nomoto K., 1999, ApJ, 522, 487

Hanuschik R. W., 2003, A&A, 407, 1157

Haschke R., Grebel E. K., Duffau S., 2011, AJ, 141, 158

Haschke R., Grebel E. K., Duffau S., 2012, AJ, 144, 107

Hatzidimitriou D., Reig P., Manousakis A., Pietsch W., Burwitz V., Papamastorakis I., 2007, A&A, 464, 1075

Hays E., Cheung T., Ciprini S., 2013, The Astronomer's Telegram, 5302

Hellier C., 2001, Cataclysmic Variable Stars, Springer ., ed.

Hellier C., Beardmore A. P., 2002, MNRAS, 331, 407

Henden A. A., Welch D. L., Terrell D., Levine S. E., 2009, in American Astronomical Society Meeting Abstracts, Vol. 214, American Astronomical Society Meeting Abstracts #214, p. 669

Henze M. et al., 2018, ArXiv e-prints 1803.00181

Henze M. et al., 2014, A&A, 563, A2

Hernanz M., 2005, in Astronomical Society of the Pacific Conference Series, Vol. 330, The Astrophysics of Cataclysmic Variables and Related Objects, Hameury J.-M., Lasota J.-P., eds., p. 265

Hillebrandt W., Kromer M., Röpke F. K., Ruiter A. J., 2013, Frontiers of Physics, 8, 116

Hillebrandt W., Niemeyer J. C., 2000, ARA&A, 38, 191

Hillman Y., Prialnik D., Kovetz A., Shara M. M., 2016, ApJ, 819, 168

Hillman Y., Prialnik D., Kovetz A., Shara M. M., Neill J. D., 2014, MNRAS, 437, 1962

Hjellming R. M., Wade C. M., 1970, ApJ, 162, L1

Hounsell R. et al., 2010, ApJ, 724, 480

Hoyle F., Fowler W. A., 1960, ApJ, 132, 565

Humphrey P. J., Liu W., Buote D. A., 2009, ApJ, 693, 822

Hurley J. R., Pols O. R., Tout C. A., 2000, MNRAS, 315, 543

Hyland A. R., Neugebauer G., 1970, ApJ, 160, L177

Ibata R. A., Gilmore G., Irwin M. J., 1995, MNRAS, 277, 781

Iben, Jr. I., Fujimoto M. Y., 2008, in Classical Novae, Bode M. F., Evans A., eds., Cambridge Astrophysics, Series, Vol. 43 Cambridge Univ. Press, Cambridge, p. 34

Iben, Jr. I., Fujimoto M. Y., MacDonald J., 1992, ApJ, 384, 580

Iben, Jr. I., Tutukov A. V., 1989, ApJ, 342, 430

Ikeda Y., Kawabata K. S., Akitaya H., 2000, A&A, 355, 256

Imamura K., Tanabe K., 2012, PASJ, 64, 120

Izzo L. et al., 2016, The Astronomer's Telegram, 9587

Izzo L. et al., 2018, ArXiv e-print 1802.05896

Jablonski F., Oliveira A., 2016, The Astronomer's Telegram, 9684

Jack D. et al., 2017, ArXiv e-prints 1702.01171

Jacoby G. H. et al., 1992, PASP, 104, 599

Jacyszyn-Dobrzeniecka A. M. et al., 2016, Acta Astron., 66, 149

Jansen F. et al., 2001, A&A, 365, L1

José J., Shore S. N., 2008, in Classical Novae, Bode M. F., Evans A., eds., Cambridge Astrophysics, Series, Vol. 43 Cambridge Univ. Press, Cambridge, p. 121

Kaluzny J., Chlebowski T., 1988, ApJ, 332, 287

Kaluzny J., Semeniuk I., 1987, Acta Astron., 37, 349

Kasliwal M. M. et al., 2011, ApJ, 730, 134

Kato M., Hachisu I., 2003, ApJ, 598, L107

Kato M., Hachisu I., Luna G. J. M., 2008, in Astronomical Society of the Pacific Conference Series, Vol. 401, RS Ophiuchi (2006) and the Recurrent Nova Phenomenon, Evans A., Bode M. F., O'Brien T. J., Darnley M. J., eds., p. 308

Kawaler S. D., 1997, in Stellar Remnants, Kawaler S. D., Novikov I., Srinivasan G., eds., p. 1

King A. R., Osborne J. P., Schenker K., 2002, MNRAS, 329, L43

Kniazev A. Y., Gvaramadze V. V., Berdnikov L. N., 2016, MNRAS, 459, 3068

Kobulnicky H. A., Nordsieck K. H., Burgh E. B., Smith M. P., Percival J. W., Williams T. B., O'Donoghue D., 2003, in Society of Photo-Optical Instrumentation Engineers (SPIE) Conference Series, Vol. 4841, Instrument Design and Performance for Optical/Infrared Ground-based Telescopes, Iye M., Moorwood A. F. M., eds., p. 1634

Koester D., Chanmugam G., 1990, Reports on Progress in Physics, 53, 837

Kolb U., Rappaport S., Schenker K., Howell S., 2001, ApJ, 563, 958

Kotze E. J., Potter S. B., McBride V. A., 2016, A&A, 595, A47

Kovetz A., Prialnik D., 1994, ApJ, 424, 319

Kraft R. P., 1962, ApJ, 135, 408

Krauss M. I. et al., 2011, ApJ, 739, L6

Krautter J., 2008, in Classical Novae, Bode M. F., Evans A., eds., Cambridge Astrophysics, Series, Vol. 43 Cambridge Univ. Press, Cambridge, p. 232

Krautter J., Oegelman H., Starrfield S., Wichmann R., Pfeffermann E., 1996, ApJ, 456, 788

Kuin N. P. M. et al., 2015, MNRAS, 449, 2514

Kuin N. P. M., Page K. L., Williams S. C., Darnley M. J., Shore S. N., Walter F. M., 2016, The Astronomer's Telegram, 9635

Kuin P., 2014, UVOTPY: Swift UVOT grism data reduction. Astrophysics Source Code Library

Lamers H. J., M. Levesque E., 2017, in Understanding Stellar Evolution, 2514-3433, IOP Publishing, p. 28

Landau L. D., Lifshitz E. M., 1975, The classical theory of fields

Lanz T., Telis G. A., Audard M., Paerels F., Rasmussen A. P., Hubeny I., 2005, ApJ, 619, 517

Leibowitz E., Orio M., Gonzalez-Riestra R., Lipkin Y., Ness J.-U., Starrfield S., Still M., Tepedelenlioglu E., 2006, MNRAS, 371, 424

Leibowitz E. M., Mendelson H., Mashal E., Prialnik D., Seitter W. C., 1992, ApJ, 385, L49

Li K.-L. et al., 2017, Nature Astronomy, 1, 697

Li X.-D., van den Heuvel E. P. J., 1997, A&A, 322, L9

Liller W., Mayer B., 1987, PASP, 99, 606

Liller W., Shao C. Y., Mayer B., Garnavich P., Harbrecht R. P., Wallentine D., Simmons K., Maley P., 1975, IAU Circ., 2848

Linial I., Sari R., 2017, MNRAS, 469, 2441

Lipunov V. et al., 2016, The Astronomer's Telegram, 9631

Livio M., 1992, ApJ, 393, 516

MacDonald J., 1996, in Astrophysics and Space Science Library, Vol. 208, IAU Colloq. 158: Cataclysmic Variables and Related Objects, Evans A., Wood J. H., eds., p. 281

MacDonald J., Fujimoto M. Y., Truran J. W., 1985, ApJ, 294, 263

Majewski S. R., Skrutskie M. F., Weinberg M. D., Ostheimer J. C., 2003, ApJ, 599, 1082

Marquardt K. S., Sim S. A., Ruiter A. J., Seitenzahl I. R., Ohlmann S. T., Kromer M., Pakmor R., Röpke F. K., 2015, A&A, 580, A118

Mason E., Della Valle M., Gilmozzi R., Lo Curto G., Williams R. E., 2005, A&A, 435, 1031

Mason E., Ederoclite A., Williams R. E., Della Valle M., Setiawan J., 2012, A&A, 544, A149

Mason E., Munari U., 2014, A&A, 569, A84

Mason E., Shore S. N., De Gennaro Aquino I., Izzo L., Page K., Schwarz G. J., 2018, ApJ, 853, 27

Mason E., Walter F. M., 2014, in Astronomical Society of the Pacific Conference Series, Vol. 490, Stellar Novae: Past and Future Decades, Woudt P. A., Ribeiro V. A. R. M., eds., p. 199

Mason K. O. et al., 2001, A&A, 365, L36

Matthews J. H., Knigge C., Long K. S., Sim S. A., Higginbottom N., 2015, MNRAS, 450, 3331

McLaughlin D. B., 1939a, Popular Astronomy, 47, 410

McLaughlin D. B., 1939b, Popular Astronomy, 47, 481

McLaughlin D. B., 1942, ApJ, 95, 428

McLaughlin D. B., 1944, Popular Astronomy, 52, 109

McLaughlin D. B., 1945, PASP, 57, 69

McLaughlin D. B., 1960, The Spectra of Novae, Greenstein J. L., ed., the University of Chicago Press, p. 585

Mellema G., 2004, A&A, 416, 623

Mestel L., 1952, MNRAS, 112, 598

Metzger B. D., Caprioli D., Vurm I., Beloborodov A. M., Bartos I., Vlasov A., 2016, MNRAS, 457, 1786

Mikołajewska J., 2012, Baltic Astronomy, 21, 5

Mikolajewska J., Friedjung M., Kenyon S. J., Viotti R., eds., 1988, Astrophysics and Space Science Library, Vol. 145, The Symbiotic Phenomenon

Miyaji S., Nomoto K., 1987, ApJ, 318, 307

Miyaji S., Nomoto K., Yokoi K., Sugimoto D., 1980, PASJ, 32, 303

Mohamed S., Booth R., Podsiadlowski P., 2013, in IAU Symposium, Vol. 281, Binary Paths to Type Ia Supernovae Explosions, Di Stefano R., Orio M., Moe M., eds., p. 195

Monet D. G. et al., 2003, AJ, 125, 984

Moore C. E., 1945, Contributions from the Princeton University Observatory, 20, 1

Moore K., Bildsten L., 2012, ApJ, 761, 182

Mróz P., Udalski A., 2015, The Astronomer's Telegram, 7179, 1

Mroz P., Udalski A., 2016, The Astronomer's Telegram, 9622

Mróz P. et al., 2015, ApJS, 219, 26

Mróz P. et al., 2016, ApJS, 222, 9

Munari U., Hambsch F.-J., Frigo A., 2017, ArXiv e-prints 1703.09017

Munari U. et al., 2002, A&A, 389, L51

Munari U., Mason E., Valisa P., 2014, A&A, 564, A76

Munari U., Ribeiro V. A. R. M., Bode M. F., Saguner T., 2011, MNRAS, 410, 525

Munari U., Zwitter T., 1997, A&A, 318, 269

Murray S. S. et al., 1997, in Proc. SPIE, Vol. 3114, EUV, X-Ray, and Gamma-Ray Instrumentation for Astronomy VIII, Siegmund O. H., Gummin M. A., eds., p. 11

Nagayama T. et al., 2003, in Society of Photo-Optical Instrumentation Engineers (SPIE) Conference Series, Vol. 4841, Instrument Design and Performance for Optical/Infrared Ground-based Telescopes, Iye M., Moorwood A. F. M., eds., p. 459

Narumi H., Hirosawa K., Kanai K., Renz W., Pereira A., Nakano S., Nakamura Y., Pojmanski G., 2006, IAU Circ., 8671

Nataf D. M. et al., 2013, ApJ, 769, 88

Nataf D. M. et al., 2015, MNRAS, 447, 1535

Nauenberg M., 1972, ApJ, 175, 417

Nelson T. et al., 2014, ApJ, 785, 78

Ness J.-U. et al., 2015, A&A, 578, A39

Ness J.-U. et al., 2009, AJ, 137, 4160

Ness J.-U. et al., 2013, A&A, 559, A50

Ness J.-U. et al., 2012, ApJ, 745, 43

Ness J.-U. et al., 2017, The Astronomer's Telegram, 10756

Neugent K. F., Massey P., Skiff B., Drout M. R., Meynet G., Olsen K. A. G., 2010, ApJ, 719, 1784

Ney E. P., Hatfield B. F., 1978, ApJ, 219, L111

Nishiyama S., Tamura M., Hatano H., Kato D., Tanabé T., Sugitani K., Nagata T., 2009, ApJ, 696, 1407

Nomoto K., 1984, ApJ, 277, 791

Nomoto K., Kondo Y., 1991, ApJ, 367, L19

Nomoto K., Saio H., Kato M., Hachisu I., 2007, ApJ, 663, 1269

Nordsieck K. H., Jaehnig K. P., Burgh E. B., Kobulnicky H. A., Percival J. W., Smith M. P., 2003, in Proc. SPIE, Vol. 4843, Polarimetry in Astronomy, Fineschi S., ed., p. 170

Norton A. J., 1993, MNRAS, 265, 316

Norton A. J., Beardmore A. P., Taylor P., 1996, MNRAS, 280, 937

Norton A. J., McHardy I. M., Lehto H. J., Watson M. G., 1992a, MNRAS, 258, 697

Norton A. J., Watson M. G., 1989, MNRAS, 237, 853

Norton A. J., Watson M. G., King A. R., Lehto H. J., McHardy I. M., 1992b, MNRAS, 254, 705

Norton A. J., Wynn G. A., Somerscales R. V., 2004, ApJ, 614, 349

Ochsenbein F., Bauer P., Marcout J., 2000, A&AS, 143, 23

O'Donoghue D. et al., 2006, MNRAS, 372, 151

Orio M. et al., 2013, MNRAS, 429, 1342

Orio M. et al., 2018, ArXiv e-prints

Osborne J. P., 1988, Mem. Soc. Astron. Italiana, 59, 117

Osborne J. P., 2015, Journal of High Energy Astrophysics, 7, 117

Osborne J. P. et al., 2001, A&A, 378, 800

Osborne J. P. et al., 2011, ApJ, 727, 124

Page K. L., 2013, in IAU Symposium, Vol. 281, Binary Paths to Type Ia Supernovae Explosions, Di Stefano R., Orio M., Moe M., eds., p. 96

Page K. L., Kuin N. P., Osborne J. P., Schwarz G. J., Shore S. N., Starrfield S., Woodward C. E., 2014, The Astronomer's Telegram, 5967

Page K. L., Osborne J. P., 2014, in Astronomical Society of the Pacific Conference Series, Vol. 490, Stellar Novae: Past and Future Decades, Woudt P. A., Ribeiro V. A. R. M., eds., p. 345

Page K. L. et al., 2010, MNRAS, 401, 121

Page K. L. et al., 2015, MNRAS, 454, 3108

Page K. L., Osborne J. P., Wagner R. M., Beardmore A. P., Shore S. N., Starrfield S., Woodward C. E., 2013a, ApJ, 768, L26

Page K. L., Walter F. M., Schwarz G. J., Osborne J. P., 2013b, The Astronomer's Telegram, 4853

Page M. J. et al., 2013c, MNRAS, 436, 1684

Patat F., Chugai N. N., Podsiadlowski P., Mason E., Melo C., Pasquini L., 2011, A&A, 530, A63

Patterson J., 1994a, PASP, 106, 209

Patterson J., 1994b, PASP, 106, 209

Payne-Gaposchkin C., 1964, The galactic novae, New York: Dover Publication ., ed.

Payne-Gaposchkin C. H. P., 1957, The galactic novae., Amsterdam North-Holland Pub. Co.; New York I. P. ., ed.

Perlmutter S., 1999, in Lepton and Photon Interactions at High Energies, Janos J. A., Peskin M. E., eds., p. 715

Perryman M. A. C., 1997, in ESA Special Publication, Vol. 402, Hipparcos - Venice '97, Bonnet R. M., Høg E., Bernacca P. L., Emiliani L., Blaauw A., Turon C., Kovalevsky J., Lindegren L., Hassan H., Bouffard M., Strim B., Heger D., Perryman M. A. C., Woltjer L., eds., p. 1

Pietrukowicz P. et al., 2015, ApJ, 811, 113

Pietsch W., 2010, Astronomische Nachrichten, 331, 187

Pietsch W., Henze M., Haberl F., Hernanz M., Sala G., Hartmann D. H., Della Valle M., 2011, A&A, 531, A22

Poole T. S. et al., 2008, MNRAS, 383, 627

Potter S., Ramsay G., Wu K., Cropper M., 2002, in Astronomical Society of the Pacific Conference Series, Vol. 261, The Physics of Cataclysmic Variables and Related Objects, Gänsicke B. T., Beuermann K., Reinsch K., eds., p. 165

Potter S. B., 2000, MNRAS, 314, 672

Potter S. B., Buckley D. A. H., 2018, MNRAS, 473, 4692

Potter S. B., Hakala P. J., Cropper M., 1998, MNRAS, 297, 1261

Potter S. B., Romero-Colmenero E., Watson C. A., Buckley D. A. H., Phillips A., 2004, MNRAS, 348, 316

Poznanski D., Prochaska J. X., Bloom J. S., 2012, MNRAS, 426, 1465

Pretorius M. L., Mukai K., 2014, MNRAS, 442, 2580

Prialnik D., 1986, ApJ, 310, 222

Prieto J. L., 2016, The Astronomer's Telegram, 9564

Rauch T., Orio M., Gonzales-Riestra R., Nelson T., Still M., Werner K., Wilms J., 2010, ApJ, 717, 363

Retter A., 2002, in Astronomical Society of the Pacific Conference Series, Vol. 261, The Physics of Cataclysmic Variables and Related Objects, Gänsicke B. T., Beuermann K., Reinsch K., eds., p. 655

Retter A., Leibowitz E. M., Kovo-Kariti O., 1998, MNRAS, 293, 145

Ribeiro V. A. R. M., Bode M. F., Darnley M. J., Barnsley R. M., Munari U., Harman D. J., 2013, MNRAS, 433, 1991

Ribeiro V. A. R. M. et al., 2009, ApJ, 703, 1955

Ribeiro V. A. R. M. et al., 2014, ApJ, 792, 57

Ribeiro V. A. R. M., Darnley M. J., Bode M. F., Munari U., Harman D. J., Steele I. A., Meaburn J., 2011, MNRAS, 412, 1701

Ribeiro V. A. R. M., Munari U., Valisa P., 2013, ApJ, 768, 49

Riess A. G. et al., 1998, AJ, 116, 1009

Rodrigues C. V., Cieslinski D., Jablonski F. J., D'Amico F., Steiner J. E., Diaz M. P., Hickel G. R., 2005, in Astronomical Society of the Pacific Conference Series, Vol. 343, Astronomical Polarimetry: Current Status and Future Directions, Adamson A., Aspin C., Davis C., Fujiyoshi T., eds., p. 401

Rodrigues C. V., Magalhães A. M., Coyne G. V., Piirola S. J. V., 1997, ApJ, 485, 618

Roming P. W. A. et al., 2005, Space Sci. Rev., 120, 95

Rosen S. R., Mason K. O., Cordova F. A., 1987, MNRAS, 224, 987

Roy N. et al., 2012, Bulletin of the Astronomical Society of India, 40, 293

Saito R. K. et al., 2012, A&A, 537, A107

Sala G., Hernanz M., 2005, A&A, 439, 1061

Saxton C. J., Soria R., Wu K., Kuin N. P. M., 2012, MNRAS, 422, 1625

Schaefer B. E., 2010, ApJS, 187, 275

Schaefer B. E., 2011, ApJ, 742, 112

Schaefer B. E., 2014, in American Astronomical Society Meeting Abstracts, Vol. 223, American Astronomical Society Meeting Abstracts #223, p. 335.04

Schatzman E. L., 1958, White dwarfs, Amsterdam North-Holland Pub. Co.; New York I. P. ., ed.

Schechter P. L., Mateo M., Saha A., 1993, PASP, 105, 1342

Schlafly E. F., Finkbeiner D. P., 2011, ApJ, 737, 103

Schmidt G. D., Stockman H. S., 1991, ApJ, 371, 749

Schwarz G. J. et al., 2011, ApJS, 197, 31

Schwarz G. J. et al., 2015, AJ, 149, 95

Schwope A. D., Mantel K.-H., Horne K., 1997, A&A, 319, 894

Seaquist E. R., Bode M. F., 2008, in Classical Novae, Bode M. F., Evans A., eds., Cambridge Astrophysics, Series, Vol. 43 Cambridge Univ. Press, Cambridge, p. 141

Serkowski K., Mathewson D. S., Ford V. L., 1975, ApJ, 196, 261

Shafter A. W., 1997, ApJ, 487, 226

Shafter A. W., 2002, in American Institute of Physics Conference Series, Vol. 637, Classical Nova Explosions, Hernanz M., José J., eds., p. 462

Shafter A. W., 2008, in Classical Novae, Bode M. F., Evans A., eds., Cambridge Astrophysics, Series, Vol. 43 Cambridge Univ. Press, Cambridge

Shafter A. W. et al., 2011, ApJ, 734, 12

Shafter A. W., Rau A., Quimby R. M., Kasliwal M. M., Bode M. F., Darnley M. J., Misselt K. A., 2009, ApJ, 690, 1148

Shapiro S. L., Teukolsky S. A., 1986, Black Holes, White Dwarfs and Neutron Stars: The Physics of Compact Objects. p. 672

Shappee B. J. et al., 2014, ApJ, 788, 48

Shara M. M., 1981, ApJ, 243, 926

Shara M. M. et al., 2017a, ApJ, 839, 109

Shara M. M. et al., 2016, ApJS, 227, 1

Shara M. M. et al., 2017b, ArXiv e-prints - 1702.06988v2

Shara M. M. et al., 2017c, ArXiv e-prints 1702.06988V3

Shara M. M. et al., 2018, MNRAS, 474, 1746

Shara M. M., Prialnik D., 1994, AJ, 107, 1542

Shields G. A., Ferland G. J., 1978, ApJ, 225, 950

Shore S. N., 2008, in Classical Novae, Bode M. F., Evans A., eds., Cambridge Astrophysics, Series, Vol. 43 Cambridge Univ. Press, Cambridge, p. 194

Shore S. N., 2014, in Astronomical Society of the Pacific Conference Series, Vol. 490, Stellar Novae: Past and Future Decades, Woudt P. A., Ribeiro V. A. R. M., eds., p. 145

Shore S. N., Augusteijn T., Ederoclite A., Uthas H., 2011, A&A, 533, L8

Shore S. N., De Gennaro Aquino I., Schwarz G. J., Augusteijn T., Cheung C. C., Walter F. M., Starrfield S., 2013, A&A, 553, A123

Shore S. N., Kenyon S. J., Starrfield S., Sonneborn G., 1996, ApJ, 456, 717

Shore S. N. et al., 2016, A&A, 590, A123

Shumkov V. et al., 2016, The Astronomer's Telegram, 9621

Silber A. D., 1992, PhD thesis, MASSACHUSETTS INSTITUTE OF TECHNOLOGY.

Smith R. K., Brickhouse N. S., Liedahl D. A., Raymond J. C., 2001, ApJ, 556, L91

Sokoloski J. L., Rupen M. P., Mioduszewski A. J., 2008, ApJ, 685, L137

Somero A., Hakala P., Wynn G. A., 2017, MNRAS, 464, 2784

Soraisam M. D., Gilfanov M., Wolf W. M., Bildsten L., 2016, MNRAS, 455, 668

Soszyński I. et al., 2014, Acta Astron., 64, 177

Sparks W. M., Starrfield S., Truran J. W., 1976, ApJ, 208, 819

Stahl O., Kaufer A., Tubbesing S., 1999, in Astronomical Society of the Pacific Conference Series, Vol. 188, Optical and Infrared Spectroscopy of Circumstellar Matter, Guenther E., Stecklum B., Klose S., eds., p. 331

Stanek K. Z. et al., 2016, The Astronomer's Telegram, 9538

Starrfield S., 1989, in Classical Novae, Bode M. F., Evans A., eds., Cambridge Astrophysics, Chichester: J. Wiley, p. 39

Starrfield S., Iliadis C., Hix W. R., 2008, in Classical Novae, Bode M. F., Evans A., eds., Cambridge Astrophysics, Series, Vol. 43 Cambridge Univ. Press, Cambridge, p. 121

Starrfield S., Iliadis C., Hix W. R., 2016, PASP, 128, 051001

Starrfield S., Iliadis C., HIx W. R., Timmes F. X., Arnett W. D., Meakin C., Sparks W. M., 2011, in AAS/High Energy Astrophysics Division, Vol. 12, AAS/High Energy Astrophysics Division #12, p. 33.08

Stephenson F. R., 1976, QJRAS, 17, 121

Stockman H. S., Schmidt G. D., Lamb D. Q., 1988, ApJ, 332, 282

Strope R. J., Schaefer B. E., Henden A. A., 2010, AJ, 140, 34

Strüder L. et al., 2001, A&A, 365, L18

Subramanian S. et al., 2017, MNRAS, 467, 2980

Surina F., Hounsell R. A., Bode M. F., Darnley M. J., Harman D. J., Walter F. M., 2014, AJ, 147, 107

Tajitsu A., Sadakane K., Naito H., Arai A., Aoki W., 2015, Nature, 518, 381

Talavera A., 2009, Ap&SS, 320, 177

Thompson A. R., Clark B. G., Wade C. M., Napier P. J., 1980, ApJS, 44, 151

Tody D., 1986, in Society of Photo-Optical Instrumentation Engineers (SPIE) Conference Series, Vol. 627, Instrumentation in astronomy VI, Crawford D. L., ed., p. 733

Torrealba G. et al., 2015, MNRAS, 446, 2251

Truran J. W., Livio M., 1986, ApJ, 308, 721

Turner M. J. L. et al., 2001, A&A, 365, L27

Tyson J. A., 2002, in Proc. SPIE, Vol. 4836, Survey and Other Telescope Technologies and Discoveries, Tyson J. A., Wolff S., eds., p. 10

Udalski A., Szymański M. K., Szymański G., 2015, Acta Astron., 65, 1

van den Bergh S., Younger P. F., 1987, A&AS, 70, 125

van Rossum D. R., 2012, ApJ, 756, 43

Verbunt F., Zwaan C., 1981, A&A, 100, L7

Wagner R. M., Depoy D. L., 1996, ApJ, 467, 860

Walter F. M., Battisti A., 2011, in Bulletin of the American Astronomical Society, Vol. 43, American Astronomical Society Meeting Abstracts #217, p. 338.11

Walter F. M., Battisti A., Towers S. E., Bond H. E., Stringfellow G. S., 2012, PASP, 124, 1057

Wamsteker W., Gonzalez Riestra R., Harris B., eds., 1998, ESA Special Publication, Vol. 413, Ultraviolet astrophysics beyond the IUE final archive

Warner B., 1985, MNRAS, 217, 1P

Warner B., 1995, Cataclysmic variable stars., Cambridge Astrophysics Series 28 ., ed., Vol. 28

Warner B., 2008, in Classical Novae, Bode M. F., Evans A., eds., Cambridge Astrophysics, Series, Vol. 43 Cambridge Univ. Press, Cambridge, p. 16

Warner B., Woudt P. A., 2002, PASP, 114, 1222

Weisskopf M. C., Tananbaum H. D., Van Speybroeck L. P., O'Dell S. L., 2000, in Proc. SPIE, Vol. 4012, X-Ray Optics, Instruments, and Missions III, Truemper J. E., Aschenbach B., eds., p. 2

Wenger M. et al., 2000, A&AS, 143, 9

Werner K., Rauch T., Kruk J. W., 2007, A&A, 474, 591

Whitelock P. A., Carter B. S., Feast M. W., Glass I. S., Laney D., Menzies J. W., Walsh J., Williams P. M., 1984, MNRAS, 211, 421

Whitelock P. A., Feast M. W., van Leeuwen F., 2008, MNRAS, 386, 313

Wilking B. A., Lebofsky M. J., Kemp J. C., Martin P. G., Rieke G. H., 1980, ApJ, 235, 905

Willcox D. E., Townsley D. M., Calder A. C., Denissenkov P. A., Herwig F., 2016, ApJ, 832, 13

Williams R. E., 1992, AJ, 104, 725

Williams R. E., 1994, ApJ, 426, 279

Williams R. E., 2012, AJ, 144, 98

Williams R. E., Hamuy M., Phillips M. M., Heathcote S. R., Wells L., Navarrete M., 1991, ApJ, 376, 721

Williams S. C., Darnley M. J., 2016, The Astronomer's Telegram, 9628

Wilms J., Allen A., McCray R., 2000, ApJ, 542, 914

Wolf W. M., Bildsten L., Brooks J., Paxton B., 2013, ApJ, 777, 136

Wolf W. M., Bildsten L., Brooks J., Paxton B., 2014, ApJ, 782, 117

Wonźiak P. R., 2000, Acta Astron., 50, 421

Woosley S., Janka T., 2005, Nature Physics, 1, 147

Woudt P. A., Warner B., 2003, MNRAS, 340, 1011

Woudt P. A., Warner B., 2004, in Astronomical Society of the Pacific Conference Series, Vol. 315, IAU Colloq. 190: Magnetic Cataclysmic Variables, Vrielmann S., Cropper M., eds., p. 39

Wyrzykowski L., Udalski A., Kozlowski S., 2012, The Astronomer's Telegram, 4483

Yaron O., Prialnik D., Shara M. M., Kovetz A., 2005, ApJ, 623, 398

Young P. J., Corwin, Jr. H. G., Bryan J., de Vaucouleurs G., 1976, ApJ, 209, 882

Young P. R., Feldman U., Lobel A., 2011, ApJS, 196, 23

Yungelson L., Livio M., Tutukov A., 1997, ApJ, 481, 127

Zaritsky D., Harris J., Thompson I. B., Grebel E. K., Massey P., 2002, AJ, 123, 855

Zemko P., Mukai K., Orio M., 2015, ApJ, 807, 61

Zemko P., Orio M., Luna G. J. M., Mukai K., Evans P. A., Bianchini A., 2017, MNRAS, 469, 476

Zemko P., Orio M., Mukai K., Bianchini A., Ciroi S., Cracco V., 2016, MNRAS, 460, 2744

Zhu H., Tian W., Li A., Zhang M., 2017, MNRAS, 471, 3494

Zwicky F., 1936, PASP, 48, 191